ENVIRONMENTAL INFLUENCES ON DWARF GALAXY EVOLUTION: THE GROUP ENVIRONMENT

A Dissertation

Presented to the Faculty of the Graduate School

of Cornell University

in Partial Fulfillment of the Requirements for the Degree of

Doctor of Philosophy

by

Sabrina Renee Stierwalt

February 2010

ENVIRONMENTAL INFLUENCES ON DWARF GALAXY EVOLUTION: THE GROUP ENVIRONMENT

Sabrina Renee Stierwalt, Ph.D.

Cornell University 2010

Galaxy groups are a rich source of information concerning galaxy evolution as they represent a fundamental link between individual galaxies and large scale structures. Nearby groups probe the low end of the galaxy mass function for the dwarf systems that constitute the most numerous extragalactic population in the local universe [Karachentsev et al., 2004]. Inspired by recent progress in our understanding of the Local Group, this dissertation addresses how much of this knowledge can be applied to other nearby groups by focusing on the Leo I Group at 11 Mpc. Gas-deficient, early-type dwarfs dominate the Local Group (Mateo [1998]; Belokurov et al. [2007]), but a few faint, HI-bearing dwarfs have been discovered in the outskirts of the Milky Way's influence (e.g. Leo T; Irwin et al. [2007]). We use the wide areal coverage of the Arecibo Legacy Fast ALFA (ALFALFA) HI survey to search the full extent of Leo I and exploit the survey's superior sensitivity, spatial and spectral resolution to probe lower HI masses than previous HI surveys. ALFALFA finds in Leo I a significant population of low surface brightness dwarfs missed by optical surveys which suggests similar systems in the Local Group may represent a so far poorly studied population of widely distributed, optically faint yet gas-bearing dwarfs. The morphological segregation seen in the Local Group is also reflected in Leo I and further suggests a significant population of gas-bearing dwarfs may be missed by surveys narrowly focused around more massive systems. The Leo I HI mass function is

dominated by low mass objects yielding a steeper low-mass slope than found for luminosity functions of the group. However, the slope still falls short of that predicted by simulations of structure formation. Further contributors to this gap may be dwarf systems formed from tidal material (TDGs), the fraction of which, even in the Local Group, remains unknown. We find that TDGs can be identified from the ALFALFA survey based on their proximity to tidal remnants and from optical spectroscopic followup via their high gas fractions and high metallicities given their luminosities. However, despite the two large tidal remnants found in Leo I, our search results in only two TDGs for the group. If most dwarfs are instead formed from small dark matter haloes as suggested by the ΛCDM framework, different classes of dwarf may reflect early versus late stages of evolution. Dwarfs of mixed morphologies, like the six so-called transition dwarfs in the Local Group, may represent the evolutionary link between gas-rich and gas-poor classes, but when constrained by the requirement of HII regions, we find only one such candidate in Leo I. The work presented here lays the groundwork for future HI-based group studies which will be made possible with rich ALFALFA dataset.

BIOGRAPHICAL SKETCH

Sabrina Stierwalt was born in Indiana, spent her early childhood in southern California, and grew up in Norwalk, Connecticut. Before moving to upstate New York to do her PhD work at Cornell, she earned her undergraduate degree in physics and astronomy from the University of California, Berkeley. Ithaca and Berkeley share many of her favorite things, from drum circles and open-minded people to some of the best locally grown, vegetarian food. She will miss walks through the Plantations, the barbeque tofu 'n' grits at Maxie's, and the movies at Fall Creek. However, she is happy to be giving up her winter clothes and to no longer have to worry whether or not her car doors will be frozen shut. She begins a postdoctoral position at the California Institute of Technology in August working with Spitzer observations of luminous infrared galaxies. She plans to drive out there with her two good friends, Ann Martin and Betsey Adams, and with her two bulldogs, Bella and Chewie.

This thesis is dedicated to my brother, Trent. No one else has believed in me so unconditionally as he has. I love you, buddy.

ACKNOWLEDGEMENTS

I just want more than one membership to more than one club and I owe my life to the people that I love.

- Ani DiFranco

To my collaborators, Amélie Saintonge, Becky Koopmann, Andrew West, Sarah Higdon, Ann Martin, Brian Kent, Betsey Adams, John Salzer, Noah Brosch, and Barbara Rojas Ayala: your thoughts, suggestions, and patience were all very much appreciated.

To my fellow EGGs, past and present, Ann, Betsey, Amélie, Brian, Karen, Kristine, Chris, Kelley, Drew, Manolis, Shan, Nancy, Katie, Kim, Lamarr, and Jae: I have learned so much from all of you. Thank you for making the Camuy Cave such a fun place to work and for taking over the ALFALFA observations throughout the past year so that I could finish my dissertation.

To Tom Shannon: Thank you for keeping hatillo alive long enough for me to complete my dissertation and for responding kindly when I called you in a panic on a Saturday night after a power outage.

To the telescope operators, Jean, Carl, Norberto, Israel, Willy and Ed: Thank you for your guidance and for humbling me with your far superior knowledge of some of the largest telescopes in the world.

To Gary Brinson and the Brinson Foundation: Thank you for promoting my work as a young researcher. Your contributions have allowed me the opportunities to travel to conferences to learn from other astronomers and to share my own results.

And to my family and friends who supported me in more ways than I could ever ask for

To my mom: you are a caring, patient goddess of a woman who has taught me always to look for the good in people (although, Im sorry, you are much better at it than I am). You never pushed me to study harder or even suggested that I go to grad school, but your example taught me never to underestimate myself.

To my brother, Trent: you have such a good heart. Thank you for always supporting me, making me laugh, and for helping me with many of the images that went into this dissertation. Most of all, thank you for being the only person in the whole wide world that understands the madness we call our family.

To my sister, Rachel: you showed me that theres no point in watching movies with sad endings and that even though I think I look cool, I totally dress like a scientist. Thank you for allowing my shameless attempts to turn my nieces and nephew into little astronomers.

To my father: you passed to me a very valuable skill for an astronomer being able to exist for months at a time with only four hours of sleep per night. Thank you also for helping me to travel the world so that I could see the stars from over two dozen countries.

To Kim: you are so clever and you think that I can write a book. If I ever do, it will certainly be inspired by your curiosity as to what I actually do with my time and your endless patience with my long explanations. Thank you for your frequent reminders that astronomy is totally awesome.

To Lauren: I cannot believe you trekked all the way to Ithaca to witness my defense. Weve known each other for 15 years, ever since I got caught trying to beat you up during study hall. I love you (and fight with you) like a sister so your support over these last few years has encouraged me to work harder.

Alicia: you are the reason I am an astronomer. I followed you into astro lab

and never looked back. Thank you for being my partner in lab and partner in crime for four years at Berkeley. You make me smarter, and you make my life more interesting.

Molly: you are fearless. Thank you for making my grad school years easier by allowing me to rest assured that you would some day have it all figured out and would fix the worlds problems.

Nozomi: you are brilliant, fun, and as I see it, amazingly talented at everything you try. Your constant encouragement, even when you had your own dissertation to write, has been so important to me these past few years. Thank you for letting me crash your defense so that I could see how it's done right!

To my activist friends, Laura, Liana, Hannah, Claire, Ariela, Erica, Aly, Molly, Jenny, Graham, Julie, Morgan, Leyla, Jaime and Ashwin: Thank you for constantly reminding me that one driven person (or an awesome-sauce group of people!) can make a difference. Also, always be careful of the hole in the ground outside of Pixel!

To Randall Pants: Even though you left me to face my last years in Ithaca alone, you always encouraged me when I needed it with your stories and your care packages from Finland. Remember, that inappropriate is in the eye of the beholder, or in our case, in the eye of the one wearing the zebra pants.

To Yanling: Despite your complete and utter failure at all attempts to teach me Chinese, I am entirely confident that you are one day going to take over the world, and I cant wait to watch you do it from up close again.

To Dave: Almost every day for these past few months you came by my office to say with a smile, hows the thesis? and even though I am sure I was less than polite at the time, I appreciate you keeping me on track. I am also forever indebted to you for making the impossible task of formatting my thesis properly

a piece of cake. Any friend who will learn basic macro programming in LaTeX to help you out is definitely a keeper.

To Betsey: This dissertation would not have been possible without the 300 cups of coffee youve made me over the past two years. I know you will do great things in astronomy so, you know, dont forget the little people when you are chair of a department somewhere. Thank you for all of the afternoons of peace you gave me by taking my puppy for hikes. Also, you manage to climb ice so theres really no excuse for you not making it out to California for a visit.

To Ann: I am going to miss you Bananna! I tried to think what grad school would have been like without you but it started to give me nightmares. You have done so much for me over these past few years that Ill probably have to take a bullet for you to pay it back. Every single sentence in this dissertation derives from some conversation we had in the office, over coffee, while watching trash television, at the zoo, at the movies, on an airplane, or when I was dropping my bulldogs off to stay with you. I hope your calling plan can handle my moving across the country. May your last two years be full of jelly, trips to the SPCA, and shows about time travel on disappearing islands, but free of edge corrections, zombies, and people who think you cant possibly be correct. As you wish.

To Barbara: Babs, mi chuletita, you taught me that real pisco comes from Chile and never from Peru, and that I will never, ever beat you at anything Nintendo related. Thank you for supporting me in my crazy teaching adventures outside of astronomy and for dragging me out of my office to go belly dancing every week.

To Leon, Jacob, Mike, and Patrick: I have lots of photos just waiting to resurface when you gentlemen are up for tenure. Mike, thanks for braving dinners at

vegetarian restaurants after 8pm (gasp!) on my birthday every year. Patrick, the duck and the cheese are going to be in Cali so bring on the rabbit. Thank you for helping me survive our first two years of classes both by being my study partner and by leaving hand-drawn cartoons for me every day. Jacob, you drive me crazy (and on purpose, Im pretty sure), but I know youll always be there for me, whether you like it or not. Leon, if I were told to pick one of my friends who would revolutionize the medical industry with cotton candy, it would have been you. Thank you for offering me your insights when I was fed up with the boys club.

To Gordon and Ira: Thank you for taking the time to be members of my committee and for actually reading my dissertation! Although I did not appreciate it at the time, thank you for forcing me out of my comfort zone during all of my graduate exams.

To Riccardo: I have managed to sneak by without ever having seen North by Northwest(!), but I value the cinematic education you have given me. Grazie per essere stato sempre disponibile e di grande aiuto e il primo mentore maschile che ho avuto mai. (I hope that comes close to what I think it says!)

To Martha: You have been gently pushing me in the right direction while at the same time encouraging me to find my own path since day one and I didnt even know it. Thank you for not laughing at me when I started bringing a bulldog to all of my observations or when I decided to defend my dissertation, move across the country, and start a new job in one week. You have supported my pursuit of interests outside of research from teaching writing and founding the Women in Physics group to years of Spanish class. In all of your former students (and even some students who werent yours!) I see the lasting impact you make on so many people, and I am lucky and honored to be one of them.

TABLE OF CONTENTS

LIST OF FIGURES

CHAPTER 1

INTRODUCTION

Nothing will work unless you do. - Maya Angelou

From the vantage point of the Milky Way, astronomers have a unique view of the Local Group of galaxies which is home to the lowest mass and faintest known dwarf systems. Although the Milky Way's extragalactic backyard has been studied throughout nearly the entire history of astronomy, our understanding of the evolutionary processes at work and even of the population of galaxies within the Local Group is far from complete. Over the last 10 years alone, huge progress has been made in our understanding of the group's dwarf population. Simulations of structure formation in the early universe based in the Λ Cold Dark Matter framework [Diemand et al., 2007] have improved due to the increased precision of cosmological parameters provided by WMAP (Spergel et al. [2007a]; Komatsu et al. [2009]) and with the help of increased computing power [Diemand et al., 2007]. The Sloan Digital Sky Survey has uncovered a population of ultrafaint dwarf galaxies that has nearly doubled the number of known Milky Way satellites (Belokurov et al. [2007]; Willman et al. [2005]). The combination of these improvements in theory and observation has significantly narrowed the gap between the number of low mass dark matter haloes predicted by ΛCDM and the consistently lower number of observed dwarf galaxy satellites, one of the biggest obstacles to the success of the standard cosmological model known as the substructure problem [Simon and Geha, 2007]. A common mass scale has been determined based on the new dwarf detections of $M_{dyn} \sim 10^7 M_{\odot}$which may suggest a lower limit to the mass of dark matter haloes that have evolved to form galaxies or that they were all

formed at the same epoch [Strigari et al., 2008].

In his overview of the Local Group, Mateo [1998] reported ~ 30 dwarf satellites surrounding the Milky Way and the nearby Andromeda galaxy. In the ten years since this review, 15 additional Local Group dwarfs have been discovered, in most cases by scanning the Sloan Digital Sky Survey for ultrafaint, nearby stellar associations. An update to the compilation[1] of known Local Group satellites found in Mateo [1998] is given in Table 1. Only the three large spirals (the Milky Way, the Andromeda Galaxy, and M33) are excluded.

As shown in Table 1, all but one of the recent detections are dwarf spheroidals (dSphs) or dwarf ellipticals (dEs). These early-type dwarfs have faint stellar populations dominated by old stars and are usually devoid of recent star formation and neutral hydrogen. They dominate the Local Group sample as a whole and constitute 60% of the dwarf population. Late-type dwarf irregulars (dIrrs) which contain neutral gas as well as evidence of current or at least recent star formation make up only $\sim 20\%$ of the known Local Group dwarfs. Comparable in number to the late-type dIrrs are those dwarfs with mixed morphologies (labeled dIrr/dSph). The origin and evolution of this class of so-called transition dwarfs is not well understood and remains a highly contentious topic (see Chapter 5). The only recent dwarf discovery found to have some associated neutral gas content, Leo T [Irwin et al., 2007], is considered a transition dwarf because older stellar populations dominate the galaxy's recent star formation.

The dwarf galaxies of the nearby Leo I group offer a basis for comparison to the Local Group dwarf population and reveal how much of what we know about our own galactic neighborhood may apply to other nearby groups. At

[1]The reference given for each galaxy cites the source of the distance and morphology information found in the table and not necessarily the source for the original detection.

Table 1.1. Satellite Galaxies of the Local Group

Name	Dist (kpc)	Morph Type	log(M_{HI}) ($M_\odot$)	Reference
Sagittarius	24 ± 2	dSph		Mateo 1998
Ursa Major II	31 ± 5	dSph		Belokurov et al. 2007
Coma	45 ± 4	dSph		Belokurov et al. 2007
LMC	51 ± 2	Irr	> 10	Mateo 1998
SMC	60 ± 5	Irr	> 9	Mateo 1998
Bootes	61 ± 3	dSph		Belokurov et al. 2006
Ursa Minor	67 ± 3	dSph		Mateo 1998
Sculptor	80 ± 4	dSph	4.41	Mateo 1998
Draco	83 ± 6	dSph		Mateo 1998
Sextans	87 ± 4	dSph		Mateo 1998
Ursa Major I	101 ± 30	dSph		Wilman et al. 2005
Carina	102 ± 5	dSph		Mateo 1998
Fornax	140 ± 8	dSph		Mateo 1998
Hercules	142 ± 13	dSph		Belokurov et al. 2007
Canes Venatici II	152 ± 14	dSph		Belokurov et al. 2007
Leo IV	162 ± 15	dSph		Belokurov et al. 2007
Leo II	207 ± 12	dSph		Mateo 1998
Canes Venatici I	223 ± 25	dSph		Zucker et al. 2006
Leo I	253 ± 31	dSph		Mateo 1998
Leo T	422 ± 20	dIrr/dSph	5.00	Irwin et al. 2007
Phoenix	450 ± 31	dIrr/dSph	5.30	Mateo 1998
NGC 6822	471 ± 26	Irr	8.12	Mateo 1998
NGC 185	623 ± 19	dSph/dE	5.11	Mateo 1998
Andromeda II	671 ± 12	dSph		Mateo 1998
Leo A	698 ± 101	dIrr	6.90	Mateo 1998
IC 1613	733 ± 16	Irr	7.75	Mateo 1998
Andromeda X	710 ± 37	dSph		Zucker et al. 2007
NGC 147	735 ± 16	dSph/dE		Mateo 1998
Andromeda III	760 ± 16	dSph		Mateo 1998
Andromeda VII	764 ± 29	dSph		van den Bergh 2000
Cetus	770 ± 20	dSph		Whiting et al. 1999
Andromeda IX	777 ± 23	dSph		Zucker et al. 2004
Andromeda I	781 ± 19	dSph		Mateo 1998
LGS 3	781 ± 22	dIrr/dSph	5.59	Mateo 1998
Andromeda V	794 ± 25	dSph		van den Bergh 2000
Andromeda XI	794 ± 16	dSph		Martin et al. 2006

Table 1.1 (continued)

Name	Dist (kpc)	Morph Type	log(M_{HI}) ($M_\odot$)	Reference
Andromeda XII	794 ±101	dSph		Martin et al. 2006
Andromeda XIII	794 ±101	dSph		Martin et al. 2006
Andromeda VI	804 ± 16	dSph		van den Bergh 2000
M32	814 ± 36	dE		Mateo 1998
NGC 205	834 ± 25	dSph/dE	5.87	Mateo 1998
IC 10	834 ± 51	dIrr	8.20	Mateo 1998
Tucana	890 ± 40	dSph		Mateo 1998
Pegasus	930 ± 25	dIrr/dSph	6.72	Mateo 1998
WLM	936 ± 25	Irr	7.78	Mateo 1998
Aquarius	1037 ± 31	dIrr/dSph	6.28	Mateo 1998
SagDIG	1073 ±161	dIrr	7.94	Mateo 1998
Antlia	1249 ± 65	dIrr/dSph	5.98	Mateo 1998
NGC 3109	1263 ±167	Irr	8.86	Mateo 1998
Sextans A	1349 ± 37	dIrr	7.90	Mateo 1998
Sextans B	1359 ±101	dIrr	7.65	Mateo 1998
NGC 55	1480 ±150	Irr	9.15	Mateo 1998
GR 8	1590 ±600	dIrr	6.65	Mateo 1998
IC 5152	1590 ±200	dIrr	7.78	Mateo 1998

only 11 Mpc away, Leo I offers an opportunity to search for low mass, low surface brightness systems. By studying a nearby group with an associated 10 known primary distances, we minimize distance errors associated with calculations of HI mass and luminosity. We also narrow the search area needed to adequately cover the entire group and remove the need for corrections like those applied to the Local Group dwarf sample to account for the parts of the sky not covered by SDSS [Simon and Geha, 2007].

1.1 Near-field Cosmology with Dwarf Galaxies

Low mass, dwarf galaxies constitute the most numerous extragalactic population in the local universe [Karachentsev et al., 2004] and are thus a rich source of information for addressing questions concerning galaxy evolution. By the nature of their defining characteristics of low gas and stellar mass, dwarf systems can only be detected nearby and so place constraints on theories of galaxy formation and evolution from the perspective at $z = 0$.

1.1.1 Substructure problem

The widely accepted framework for the formation of structure in the universe is that predicted by the Λ cold dark matter (ΛCDM) paradigm. In this picture, the hierarchical build up of slight overdensities in the mass distribution of the early universe leads to the formation of increasingly massive haloes. Large numbers of dwarf galaxies, born out of the smaller haloes and left behind in the merging process, are predicted to surround the massive galaxies seen at the current

epoch. However, the number of observed dwarf satellites falls short of that predicted by ΛCDM for the low-mass halos (Kauffmann et al. [1993]; Klypin et al. [1999]), a discrepancy known as the "missing satellites" or "substructure" problem. Despite strong agreement between ΛCDM simulations with large-scale observations like the cosmic microwave background [Spergel et al., 2007b] and galaxy clustering [Percival et al., 2007], the predictions fail on the scale of individual galaxies.

Even for the Local Group, where the most is known about the dwarf galaxy population simply due to proximity, the numbers of observed dwarf satellites fail to meet the number of predicted haloes. For the simulations of Klypin et al. [1999] based in the ΛCDM framework, 281 dwarf satellites are predicted for galaxies like the Milky Way and Andromeda but fewer than 60 Local Group dwarfs have actually been observed (Willman et al. [2005]; Belokurov et al. [2007]; Mateo [1998]; also see Table 1). Recent studies of the Local Group have both narrowed and widened the gap between observations and predictions. The wide sky coverage of the SDSS has inspired successful searches for extremely faint and gas poor neighboring dwarf spheroidals, finding 15 dwarfs in the last few years alone (Willman et al. [2005]; Belokurov et al. [2007]; see Table 1). Conversely, an analysis of the spatial distribution of these newly discovered dwarfs in relation to the disk of the Milky Way suggests a significant percentage of Local Group dwarfs may be of tidal rather than primordial origin (Metz et al. [2009a]; Metz et al. [2009b]). Such tidal dwarf galaxies (TDGs; see Chapter 5) form from recycled material after galaxy mergers or interactions and so are not associated with the merged dark matter haloes of simulations.

Within the ΛCDM framework, dwarf galaxies are born out of small mass-

density fluctuations and originally exist as low mass dark matter haloes. Since simulations of structure formation most directly trace the existence of dark matter haloes, while observations trace baryon-rich, luminous systems, understanding the mechanisms that affect baryons, and thus regulate star formation in dwarfs, is of paramount importance to reconcile the gap in observed versus predicted satellites. However, studies have shown the evolution of the baryon content in dwarfs to vary strongly from dwarf to dwarf. Recent dwarf detections in the Local Group found near the galactic plane have been gas-deficient systems dominated by old stellar populations. Of the previously known gas-poor, Local Group dwarfs studied by Grebel and Gallagher [2004], no two had the same star formation histories. More widespread searches in the outskirts of the Milky Way's influence reveal a few faint, HI-bearing dwarfs with evidence of recent star formation (i.e. Leo T from the SDSS; Irwin et al. [2007]) which may represent an entire population of so far poorly studied, optically faint yet gas-bearing dwarfs.

If numerical predictions are assumed to be correct, the so-called "missing" satellites may form a population dwarfs missed by current optical surveys. If the dwarf systems lack baryons, then astronomers cannot hope to find them without a deeper understanding of what constitutes dark matter. However, if the missing dwarfs are simply too faint for the detection limits of current optical surveys or if they are truly 'dark' galaxies (i.e. lack stars altogether) they may be detectable via their neutral gas content.

If a significant population of optically faint yet HI-bearing dwarfs does exist, physical processes must then be invoked to remove enough (but not all) cool gas from dwarfs to make them inefficient stellar factories. Proposed gas-depleting

mechanisms have been the photoheating of gas by the ultraviolet background radiation [Efstathiou, 1992], the suppression of gas accretion during reionization [Gnedin, 2000], or ram pressure stripping [Mori and Burkert, 2000]. Dwarf galaxies tend to be very metal-deficient when compared to more massive systems (Lequeux et al. [1979]; Skillman et al. [1989]) in support of the idea that their star formation is somehow inhibited. Alternatively, their low metallicities may be due to gravitational potential wells too shallow to retain metals once they are formed. Supernovae-driven winds could cause outflows of significant amounts of gas and thus remove heavier metals and inhibit future star formation (Dekel and Silk [1986]; Mac Low and Ferrara [1999]).

1.1.2 Nature versus Nurture: the role of environment

Another uncertainty in galaxy evolution is the role of environment in the presence of early versus late galaxy morphologies. A majority of galaxies can be placed into one of two categories: red, gas-poor, and passively evolving galaxies dominated by older stellar populations (i.e. early types) or blue, gas-rich, star forming galaxies (i.e. late types). As can be seen for the Milky Way satellites in Table 1 which is ordered by distance from the Milky Way, Local Group dwarfs show a trend with gas-poor systems (dSphs) always found within close proximity of massive galaxies, in contrast to the widespread gas-rich star forming population (dIs) [Grebel, 2005]. Environmental mechanisms invoked to drive the segregation, such as tidal and ram-pressure stripping, affect the amount of cool gas and thus the star formation potential in dwarfs.

This evidence for morphological segregation inspires the classic argument

of nature versus nurture, especially for dwarf galaxies whose formation mechanisms are poorly understood. All dwarf systems may originate as a similar type but are then transformed into different morphologies depending on the density of their location (the ”nurture” argument). Alternatively, galaxies of different morphological type may be born into separate evolutionary tracks from the onset of formation (the ”nature” perspective).

Another key consequence of environment is the possibility for galaxy interactions which are known to promote star formation in more massive galaxies [Kennicutt, 1998] and may also be important for the formation of dwarfs. Some authors suggest the majority of Local Group dwarfs may have originated in gas left behind after past tidal encounters (Metz et al. [2009a]; Metz et al. [2009b]). The more substantial the fraction of observed dwarf galaxies found to be of tidal origin (and thus not associated with a dark matter halo), the wider the gap between observed and predicted satellites. A better understanding of the prevalence of tidal dwarf galaxies is needed to ascertain the contribution galaxy interactions make to dwarf galaxy evolution.

1.2 Challenges of dwarf galaxy studies

Even in the nearby universe, studies of dwarfs are limited by our ability to detect very faint, low mass systems. Incompleteness in the identification of the lowest luminosity systems hampers the census of dwarfs discovered both by optical and HI 21cm line surveys. In both cases, the intrinsic low luminosity or low HI mass renders the flux emitted by these objects very faint, so that sensitivity is a stringent requirement for their discovery is wide area surveys. In

addition to being low mass, dwarfs are also expected to have narrow HI line widths and thus are not detected by HI surveys of insufficient spectral resolution.

The faintest known systems at the low end of the galaxy luminosity function are only detectable in the Local Group, but a census of Milky Way satellites requires full sky coverage. Searches of nearby groups thus offer more efficient opportunities to probe populations of faint, low mass dwarfs. In imaging photometric studies of groups, distance estimates are very difficult to determine for faint, low surface brightness systems, and thus group membership is often established based on galaxy properties of morphology, optical surface brightness, or color (Mahdavi et al. [2005]; Karachentsev et al. [2004]). These methods are plagued by uncertainties, the largest of which being background interlopers mistaken for member dwarfs. In a recent study of dwarf satellites surrouding M81, Chiboucas et al. [2009] found 22 new dwarf galaxy candidates in a sample proposed to be complete down to $M_R = -10$. At a distance of 3.6 Mpc, M81 is close enough to allow distance estimates using stars at the tip of the red giant branch and thus allows for more confident membership statistics.

With nearer groups, however, comes the need for more extended sky coverage. In a deep optical imaging study of the faint end of the luminosity function, Trentham and Tully [2002] uncovered dwarfs also down to $M_R = -10$ in five nearby groups. In order to detect such faint objects, however, their search covered only the very innermost regions of each group which was less than 10% of the full extent of the group in some cases. While scaling corrections can be applied to account for missing dwarfs outside a survey's coverage, such corrections can only be based on the dwarfs that are found within the surveyed area

and may fail to sample intrinsically different, more widespread populations. If morphological segregation exists in other galaxy groups as has been observed for the Local Group [Grebel, 2005] and for the NGC1023 group [Trentham and Tully, 2009], surveys focused only on group centers fail to accurately sample the gas-bearing dwarfs with more widespread distributions and instead overestimate the contribution of gas-poor, early-type dwarfs.

By searching for dwarfs via their gas content rather than their stars, HI spectroscopic surveys do not require the same optical surface brightness sensitivity to detect optically diffuse galaxies; however, HI line surveys do require that the dwarfs contain neutral gas. A significant advantage of spectroscopic surveys is that group membership is confirmed immediately by HI or optical emission lines since redshifts are automatically determined for all detections. HI searches of the nearby Ursa Major (UMa; Verheijen et al. [2001]) and Canes Venatici (CVn; Kraan-Korteweg et al. [1999]; Kovac et al. [2009]) groups have been successful at finding faint, low surface brightness, gas-bearing dwarfs that would have been missed by optical surveys. Surveys like that of Kovac et al. [2009], however, are still limited by their spectral resolution. With an HI-line velocity resolution of 33 km s^{-1} before Hanning smoothing, sources of the lowest velocity widths are missed in the Westerbork survey of CVn. Although the studies of CVn and UMa span far larger areas of sky than most optical searches for dwarfs, they are still limited in scope to the coverage of only a portion of their target groups. To adequately probe the gas-bearing dwarf populations of nearby groups requires a truly blind HI survey with wide sky coverage and superior spectral resolution and sensitivity.

1.3 ALFALFA: searching for dwarfs in HI

Among the first generation blind HI surveys were the Arecibo HI Strip Survey (AHISS, Zwaan et al. [1997]), the Arecibo Dual Beam Survey (ADBS, Rosenberg and Schneider [2000]), and the HI Parkes All-Sky Survey (HIPASS, Meyer et al. [2004], Wong et al. [2006]). Both AHISS and ADBS utilized the Arecibo radio dish and so had beam sizes of $3.3'$, as well as similar velocity ranges (out to $\sim$8000 km s^{-1}). However, ADBS had less than half the velocity resolution of AHISS (34 km s^{-1} compared to the 16 km s^{-1}of AHISS). AHISS made 66 HI detections in 65 deg^2 while ADBS yielded 265 extragalactic detections in non-contiguous strips of northern sky covering a total of $\sim$430 deg^2. With velocity resolution similar to that of AHISS but a larger velocity range (out to 12,700 km s^{-1}), HIPASS found 4315 and 1002 objects in its southern and northern catalogs respectively which together covered 71$\%$ of the sky. However, the spatial resolution of HIPASS was limited by the much larger beam size ($15.5'$ versus $3.3'$) of the Parkes telescope compared to the Arecibo dish.

By combining the superior sensitivity of the Arecibo telescope and its new multi-beam L-band feed array (ALFA), the Arecibo Legacy Fast ALFA Survey (ALFALFA; Giovanelli et al. [2005b,a]) improves on previous efforts both in its higher angular resolution, in sensitivity and in spectral bandwidth and resolution. The ALFALFA survey aims to obtain a thorough census of neutral hydrogen in the local universe and will eventually cover 7000 deg^2 of sky over a redshift range of $-$2000 to 18,000 km s^{-1} with a velocity resolution of 11 km s^{-1} after Hanning smoothing.

The survey's ability to detect objects of extremely narrow HI line width

with masses down to $\sim 10^6 M_\odot$ makes ALFALFA well-suited for the study of nearby, low-mass objects [Giovanelli et al., 2005a]. In only 30% of the survey's intended coverage, ALFALFA has already made more than 300 detections with $M_{HI} < 10^8 M_\odot$, many of which were previously uncatalogued (Giovanelli et al. [2007], Kent et al. [2008], Saintonge et al. [2008]). Because these objects are selected by their gas content, they are also commonly of very low surface brightness. The survey is ongoing and so the sample is constantly growing, but the distribution of low-mass galaxies from the ALFALFA survey current as of the Spring 2009 observations is shown as an open histogram in Figure 1.1. For comparison, the low-mass end of the first generation the HI Parkes All-Sky Survey (HIPASS; Meyer et al. [2004]; Wong et al. [2006]) is shown as a shaded histogram. HIPASS covered a total of 71% of the sky in its northern and southern catalogs but with only one-eighth the sensitivity and one-fourth the spectral resolution of ALFALFA. With 4900 deg^2 still to cover, ALFALFA is already dramatically increasing the number of known dwarfs in the local universe. However, at the lowest masses ($M_{HI} < 10^6$) the Local Group dwarfs dominate the sample. Since the Local Group galaxies probe the lowest detectable masses and are found in equal numbers above and below 10^6 $M_\odot$, a population of HI-bearing dwarfs outside of the Local Group may still remain untapped, lying just below the detection limit of the ALFALFA survey.

To probe the lowest mass galaxies detectable outside of the Local Group and take advantage of the dwarf-rich ALFALFA dataset, the work in this dissertation explores the nearby Leo I group. Of the 365 low mass ALFALFA detections presented in Figure 1.1, 45 are found in Leo I. At the Leo I distance of roughly 11 Mpc (Tully et al. [2008]; Karachentsev et al. [2004]), ALFALFA can detect objects down to a mass of $\sim 5 \times 10^6$ M$_\odot$ for an HI line width of 25 km s^{-1}.

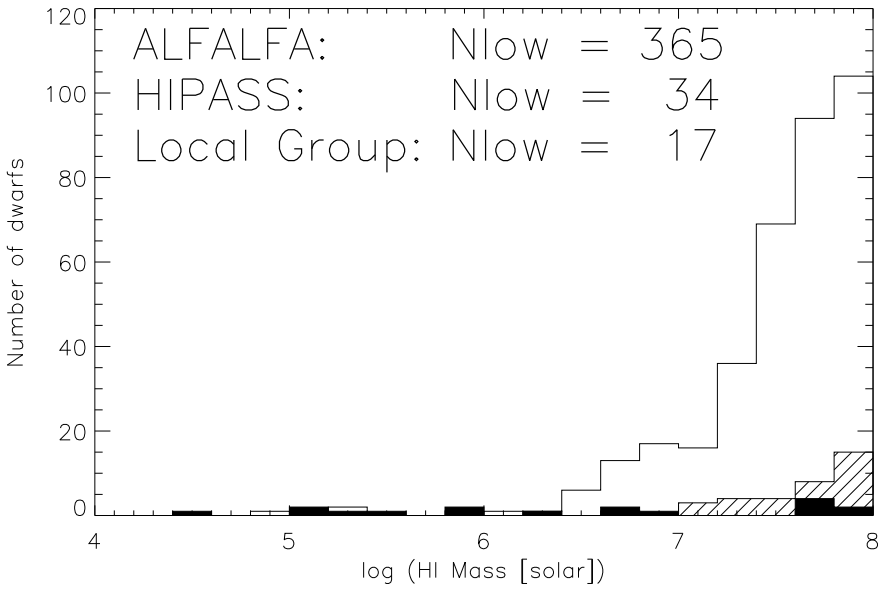

Figure 1.1 Distribution of low mass (i.e. $M_{HI} < 10^8\ M_\odot$) galaxies for the current (Spring 2009) ALFALFA sample of HI-selected dwarfs (open histogram), the HIPASS sample of HI-selected dwarfs (Zwaan et al. [2005]; hashed histogram) and the Local Group dwarfs (see Table 1; solid histogram).

Relative to other nearby groups, Leo I is poor in terms of overall luminosity and number of L* galaxies [Trentham and Tully, 2002, Ferguson and Sandage, 1991], but it is the nearest group to contain giant ellipticals, lenticulars, and spirals [de Vaucouleurs, 1975]. a complex collection of structures crowded in velocity space. Leo I represents a uniquely intermediate density environment as it is characterized by a low crossing time and velocity dispersion (1.7×10^{10} years and ~ 175 km s^{-1} respectively; see Chapter 3), but has a total luminosity that is still higher than that of the Local Group [Pritchet and van den Bergh, 1999] where the local density enhancement is not thought to be large enough to support large and luminous early-type galaxies. Intermediate density locations like Leo I which shows no evidence of ram pressure stripping, but where interactions with other group members clearly occur, are key to understanding the effects of

environment on galaxy evolution.

The work in this dissertation will exploit the Leo I group of galaxies to address several unanswered questions in dwarf galaxy evolution:

Can gas-bearing dwarfs solve the substructure problem?

If optical searches fail to uncover the numbers of observed satellites neccessary to match the predictions of ΛCDM, the possibility remains that these objects still exist but have few to no stars. Such "dark" galaxies may have neutral gas components that have somehow failed as stellar factories. Although there have been a few peculiar cases of completely dark galaxy candidates (Giovanelli and Haynes [1989]; Kent et al. [2007]), ALFALFA, nor any other HI survey, has not uncovered a population of such HI-bearing, optically deficient dwarf galaxies in clusters (Giovanelli et al. [2007]; Kent et al. [2008]) or in voids [Saintonge et al., 2008]. As discussed in Chapter 2, none are found in the Leo I group.

However, as we show in Chapter 3, Leo I is found to be home to a population of low optical surface brightness, gas-bearing dwarfs, many of which were missed by previous optical surveys.Studies of the luminosity function of galaxies in a range of galaxy environments including Leo I [Trentham and Tully, 2002, Liu et al., 2008] have consistently found shallower faint end slopes α than the value of -1.8 predicted by ΛCDM [Press and Schechter, 1974, Blumenthal et al., 1984]. Most recently Chiboucas et al. [2009] found a slope of $\alpha = -1.27$ for the M81 group, and Trentham and Tully [2009] determined $\alpha = -1.27$ to -1.12 for the group containing NGC1023. Similar examinations of the low-mass end of the HI mass function (HIMF) can determine whether or not these objects instead exist as a population of low-mass, gaseous haloes that either lack

stars entirely or are very low surface brightness. Previous determinations of the HIMF have been limited by very small number statistics at the low mass end. The HIPASS survey of the entire southern sky found only 44 objects with $M_{HI} < 10^8 M_\odot$ ($< 1\%$ of their sample; Zwaan et al. [2005]) and ADBS detected only seven [Rosenberg and Schneider, 2000]. We present in Chapter 3 the first HIMF dominated by low-mass objects and derived from the ALFALFA dataset: the HIMF for the Leo I group of galaxies. Although the low-mass end of the Leo I HIMF is made steeper than previous optical LFs for the group by the population of low optical surface brightness, gas-bearing dwarfs, we find there are still not enough to fill the gap with simulations.

What fraction of dwarfs have been formed in tidal debris?

The wide sky coverage of the ALFALFA survey provides a unique opportunity to search for HI tidal streams and remnants. Two large systems have already been discovered in the vicinity of the Virgo Cluster (Haynes et al. [2007]; Koopmann et al. [2008]). Dwarfs of tidal origin are suspected to lack a dark matter component and to have higher metallicities for a given luminosity like the tidal dwarf candidate VCC2062 [Duc et al., 2007]. By locating dwarfs found in and around the tidal remnants easily identified by ALFALFA and obtaining metallicity measurements, we can test the hypothesis of Metz et al. [2009a] that a significant number of the Local Group dwarfs may have formed from tidal debris that has since dispersed. These tidal dwarfs would not be associated with primordial dark matter haloes and thus a significant fraction of known dwarfs being of tidal origin would further widen the gap between observations and simulations. In Chapter 5 we present the beginnings of a candidate tidal dwarf sample derived from the ALFALFA catalog, and we derive a metallicity-

luminosity (Z-L) relation to test their tidal origins.

What fraction of dwarfs have gas?

If gas loss is to blame for the high mass-to-light ratios observed for many dwarfs, several mechanisms have been suggested to remove gas from dwarfs, including ram pressure stripping, suppression of gas accretion during reionization, and photoheating by the UV background. Similarly, opposing ideas exist for why some dwarfs are observed to be gas-rich: they may have retained their gas due to an inability to form stars efficiently, or they may have recently acquired their gas from a past interaction or may even be of tidal origin. To help differentiate between these scenarios, knowing at what epoch dwarfs are formed is crucial. Also of utmost importance is understanding whether dwarfs of different morphologies have entirely different evolutionary tracks or if they represent early and late stages of dwarf galaxy evolution. In Chapter 5 we introduce a sample of dwarfs with mixed morphologies: HI-bearing systems with older, smoothly distributed stellar populations usually typical of early-type galaxies. However, we do not find an offset in the Z-L relation for these transition systems as compared to ordinary dwarf irregulars as was seen for Local Group dwarfs (see Chapter 6) and so cannot rule out the possibility of linked evolutionary histories for late-type and transition dwarfs.

Does evidence exist for morphological segregation outside of the Local Group?

If environment dictates galaxy morphology for dwarf galaxies as is seen for more massive systems, the morphological segregation seen for Local Group dwarfs should be present in other groups as well. Otherwise, special circum-

stances will have to be invoked to explain the trend seen for Milky Way and Andromeda satellites, such as the possibility of a massive merger leading to the formation of most of the low mass satellites as suggested by Metz et al. [2009a]. In Chapter 6 we present clear evidence of morphological segregation amongst Leo I group dwarfs which suggests that environment plays an important role in dwarf galaxy evolution.

The existence of morphological segregation in Leo I also suggests the large number of dSph systems found in the Local Group may reflect a selection bias based on survey coverage rather than true population statistics. Just as surveys focused on the centers of groups miss a population of more widely distributed gas-bearing systems, searches for Local Group dwarfs are biased toward nearby dwarfs. Given the difficulty of distance measurements for nearby objects where peculiar motions outweigh Hubble flow, Milky Way satellites found in the outskirts of the Local Group are hard to discern from free floating, non-group members. Future wider searches for Local Group dwarfs may find numbers of late-type dwarfs matching or even outnumbering those of early-type systems like those found with optical surveys like the SDSS.

CHAPTER 2

HI PROPERTIES OF LEO GROUP GALAXIES: DATA AND METHODS*

The learning process is something you can incite, literally incite, like a riot. - Audré Lorde

2.1 The Leo Galaxy Groups: a lab for galaxy evolution

In an effort to probe the lowest mass galaxies detectable in an intermediate density, group environment outside of the Local Group, early coverage of the ALFALFA survey crosses the Leo region, a complex collection of structures crowded in velocity space. At the foreground of the region is Leo I, the nearest group to contain giant ellipticals, lenticulars, and spirals [de Vaucouleurs, 1975]. At the Leo I distance of roughly 11 Mpc (Tully et al. [2008]; Karachentsev et al. [2004]), ALFALFA can detect objects down to a mass of $\sim 5 \times 10^6$ $M_\odot$ for an HI line width of 25 km s^{-1} at a signal-to-noise level of 6. Relative to other nearby groups, Leo I is poor in terms of overall luminosity and number of L^* galaxies [Trentham and Tully, 2002, Ferguson and Sandage, 1991] and is characterized by a low crossing time and velocity dispersion (1.7×10^{10} years and ~ 175 km s^{-1} respectively; see Section 3.1.4). However, the total luminosity of Leo I is still higher than that of the Local Group [Pritchet and van den Bergh, 1999] where the local density enhancement is not thought to be large enough to support large and luminous early-type galaxies like the E/S0 galaxies found in Leo I. Intermediate density locations like Leo I which shows no evidence of ram pressure stripping, but where interactions with other group members clearly occur, are key to understanding the effects of environment on galaxy evolution.

*This chapter is published in Stierwalt et al. (2009)

Evidence of interactions among Leo I group members is most obvious in the previously identified extended HI features known as the Leo Ring and in the region of the Leo Triplet. An intergalactic ring of neutral hydrogen roughly 225 kpc in diameter surrounds M105 and NGC 3384 and contains $1.67 \times 10^9 M_\odot$ of HI gas [Schneider, 1989]. A spur connects the gas cloud with the warped disk of the M96 spiral galaxy, suggesting the gas may have been swept out after an interaction involving NGC 3384 and M96 [Rood and Williams, 1985]. However, the central bars and dust rings of the three brightest nearby galaxies (NGC 3384, M96 & M105) which all have similar spatial orientations to the Ring [Sil'chenko et al., 2003] and the Ring's Keplerian rotation [Schneider et al., 1989] together suggest the gas could instead be primordial and left over from the formation of the galaxy group.

Another tidal encounter in Leo I is thought to have occurred between the large spirals NGC 3628 and M66 (NGC 3627) to create one of the largest known tidal tails extending $\sim$100 kpc off of NGC 3628 [Rots, 1978, Haynes et al., 1979, Wilding et al., 1993]. In M66, an asymmetric HI disk and a recent (less than 1 Gyr ago) burst of star formation coinciding with the time of the suspected encounter both suggest that an interaction between NGC 3628 and M66 led to NGC 3628's extensive gas loss [Zhang et al., 1993, Afanasiev and Sil'chenko, 2005]. Despite being morphologically similar to M66, the third member of the Triplet, NGC 3623, has had a quiescent star formation history in the more recent past and appears to have escaped any direct collisions [Afanasiev and Sil'chenko, 2005].

In the following section, we present the results from an ALFALFA survey catalog that spans 118 deg^2 of sky and cuts through the southern half of the

Leo region. After combining these results with other ALFALFA catalogs to gain coverage of the entirety of the Leo I groups, the statistics for the Leo region are presented. We end this chapter with a discussion of the ALFALFA detections in the Leo region that have not been associated with optical counterparts.

2.2 Presentation of the ALFALFA catalog in the Leo region

The fifth catalog installment of the ALFALFA survey covers the southern portion of the Leo region defined here as $9^h36^m < \alpha < 11^h36^m$ and $+08^\circ < \delta < +12^\circ$. In this 118 deg^2 of sky, ALFALFA has produced 549 good quality detections. In this same region of the sky, ADBS detected a total of 45 objects, while the northern extension to HIPASS (NHICAT: Wong et al. [2006]) found only 23 sources.

Detailed descriptions of the 2-pass, fixed-azimuth, drift mode strategy exploited by the ALFALFA survey are given in the papers Giovanelli et al. [2005b,a], Saintonge [2007a], Kent et al. [2008]. With the backend correlator set to a bandwidth of 100 MHz spanned by 4096 channels, the resulting spectral resolution is 24.4 kHz ($\sim$5.3 km s^{-1} at a redshift of 0 before the Hanning smoothing that is applied to all of the data presented here). The observations required to construct the dataset in the Leo region catalog were acquired over the months of February and March in 2005, 2006, and 2007.

Once all of the necessary observations are completed, data are gridded into cubes of 2.4° by 2.4° covering the survey's full spectral bandwith, corresponding to $-$2000 km s^{-1} to +18000 km s^{-1}, with 1′ sampling. All HI detections determined to be definitely, likely, or possibly real are immediately cross-referenced with SDSS, DSS2, NED, and the Arecibo General Catalog (AGC; a private

database of extragalactic objects maintained by Martha Haynes and Riccardo Giovanelli). The median pointing accuracy, defined here as the difference between the HI centroid and its corresponding optical counterpart, is 25″ for the lowest signal-to-noise sources ($S/N < 6.5$). With even smaller pointing errors for higher signal-to-noise detections, the corresponding optical galaxy for each HI detection can be identified with a very low margin of error (see Figure 2.1). For comparison, the positional uncertainty for sources detected with HIPASS is $1.3'$ [Meyer et al., 2004]. See Giovanelli et al. (*in prep*) for a complete explanation of the gridding and data reduction process.

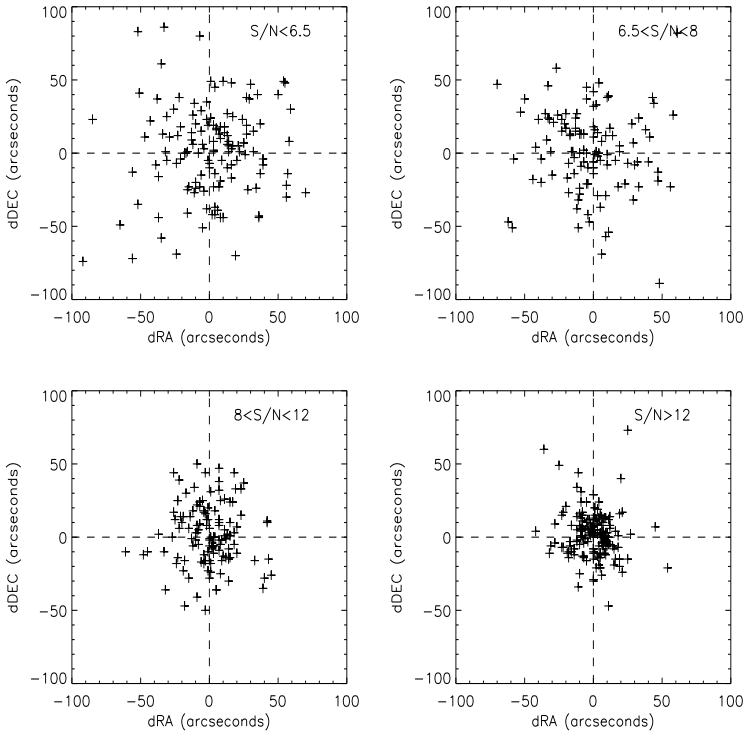

Figure 2.1 Pointing offsets between the HI centroid and the position of the associated optical counterpart as given for each ALFALFA detection given in Table A.1. The sources are separated into bins over a range of signal-to-noise ratios to show the improved pointing for higher S/N sources.

The ALFALFA catalog covering $09^h36^m < \alpha < 11^h36^m$ and $+08^\circ < \delta < +12^\circ$

is given in Table A.1. Similar to catalogs presented in all of ALFALFA data releases so far, the content for the different columns is as follows:

- Col. 1: an entry number for this catalog
- Col. 2: the source number in the AGC
- Col. 3: centroid position (J2000) of the HI source after correction for systematic telescope pointing errors (see Kent et al. [2008] for a description of how pointing errors vary with declination for the Arecibo telescope). The accuracy of HI positions depends on source strength.
- Col. 4: centroid position (J2000) of the optical galaxy found to provide the most reasonable optical counterpart to the HI detection. Assignments of optical identifications are made via the *Skyview* website and are based on spatial proximity, morphology, color, and redshift. Accuracy of centroids is estimated to be $\leq 25''$. For cases with lacking or ambiguous optical counterparts, comments are provided as alerted by an asterisk in Col. 14.
- Col. 5: heliocentric velocity of the HI source in km s^{-1}, $cz_{\odot}$, measured as the midpoint between the channels at which the flux density drops to 50%. The error on $cz_{\odot}$ can be estimated as half the error on the width, as tabulated in Col. 7.
- Col. 6: velocity width of the source line profile measured at the 50% level. Corrections for broadening but not turbulent motions, disk inclination, or cosmological effects are applied. In parentheses we show the estimated error on the velocity width, estimated by the sum in quadrature of two components: a statistical error, principally dependent on the S/N ratio of the feature measured, and a systematic error associated with the observer's subjective guess at the quality of the chosen spectral extent of the

feature. In the majority of cases, the statistical error is significantly larger than the systematic error; thus the latter is ignored.

- Col. 7: integrated line flux of the source, F_c, in Jy km s^{-1}. This is measured on the integrated spectrum, obtained by spatially integrating the source image over a solid angle of at least $7' \times 7'$ and dividing by the sum of the survey beam values over the same set of image pixels (see Shostak & Allen 1980).

- Col. 8: signal-to-noise ratio S/N of the detection, as estimated by

$$S/N = (\frac{1000F_c}{W50})\frac{\omega_{smo}^{1/2}}{\sigma_{rms}} \tag{2.1}$$

  where F_c is the integrated flux density, as listed in Col. 7, the ratio of $1000F_c/W50$ is the mean flux across the feature in mJy, ω_{smo}, the smoothing width expressed as the number of spectral resolution bins of 10 km s^{-1} bridging half of the signal width, is either $W50/(2 \times 10)$ for $W50 < 400$ km s^{-1} or $400/(2 \times 10) = 20$ for $W50 \geq 400$ km s^{-1}, and σ_{rms} is the r.m.s. noise figure across the spectrum measured in mJy at 10 km s^{-1} resolution, as tabulated in Col. 9.

- Col. 9: noise figure of the spatially integrated spectral profile, σ_{rms}, in mJy. The noise figure is the r.m.s. as measured over the signal- and rfi-free portions of the spectrum, after Hanning smoothing to a spectral resolution of 10 km s^{-1}.

- Col. 10: adopted distance in Mpc, D_{Mpc}. For objects with $cz_{cmb} > 6000$, the distance is simply cz_{cmb}/H_o, where cz_{cmb} is the recessional velocity measured in the Cosmic Microwave Background reference frame and H_o is the Hubble constant, for which we use a value of 70 km s^{-1}Mpc^{-1}. For objects of lower cz_{cmb}, we use the multiattractor, peculiar velocity model for the local Universe presented in Masters [2005]. Objects which are thought to be

parts of clusters or groups (for group membership assignments Springob et al. [2007]) are assigned the cz_{cmb} of the cluster or group. A detailed analysis of group and membership of Leo objects is presented in Section 3.1.

- Col. 13: logarithm in base 10 of the HI mass, in solar units. That parameter is obtained by using the expression $M_{HI} = 2.356 \times 10^5 D^2_{Mpc} F_c$.
- Col. 14: object code, defined as follows:

  Code 1 refers to sources of S/N and general qualities that make it a reliable detection: an approximate S/N threshold of 6.5, a good match between the two independent polarizations, and a spatial extent consistent with the characteristics of the telescope beam. Thus, some candidate detections with S/N 6.5 have been excluded on grounds of polarization mismatch, spectral vicinity to RFI features or peculiar spatial properties. Likewise, some features of $S/N < 6.5$ are included as reliable detections if the source's optical characteristics clearly resemble typical galaxies found at the redshift of the HI feature. We estimate that detection candidates with $S/N < 6.5$ in Table will be confirmed in follow-up observations in better than 95% of cases [Saintonge, 2007a].

  Code 2 refers to sources of low S/N (< 6.5), which would ordinarily not be considered reliable detections by the criteria set for code 1. However, those HI candidate sources are matched with optical counterparts with known optical redshifts which, within their respective errors, coincide with those measured in the HI line. We refer to these sources as "priors".

  Code 9 refers to objects assumed to be high velocity clouds (HVCs) based on their low heliocentric velocities ($<$200 km s^{-1}) and their lack of an op-

tical counterpart; no estimate for their distance is made.

Notes flag. An asterisk in this column indicates that a comment is included for this source in the text below.

Only the first few entries of Table 1 are listed here. The full content of Table 1 can be found in Appendix A and will be made available also through our public digital archive site[1].

2.3 Statistics of the ALFALFA sample in the Leo region

In addition to the catalog presented in Table A.1, the current ALFALFA dataset extends both north and south from $+04^\circ$ to $+16^\circ$ over the same range of right ascension. To place the catalog data in the context of the surrounding large-scale structure, we use the entire available ALFALFA dataset in the "Leo region", defined here as $09^h36^m < \alpha < 11^h36^m$ and $+04^\circ < \delta < +16^\circ$ for calculating the statistics in this section and for determining group membership in the next chapter. The limits in right ascension safely span known Leo I members, while avoiding the Virgo cluster at higher RA, and the limits in declination reflect the currently available survey dataset. Figure 2.2 shows the distributions of sources according to redshift, velocity width, integrated flux, signal-to-noise ratio, and HI mass for this 354 deg^2 and over the entire survey bandwidth (-2000 to 18,000 km s^{-1}).

The contribution of the Leo group to large scale structure is evident in the spike between cz $\sim$ 500 km s^{-1} and cz $\sim$ 2000 km s^{-1} in Figure 2.2a. Also

[1]http://arecibo.tc.cornell.edu/hiarchive/alfalfa/

Table 2.1. HI Candidate Detections

Source	AGC #	HI Coords (2000) hh mm ss.s+dd mm ss	Opt. Coords (J2000) hh mm ss.s+dd mm ss	$cz_\odot$ km s^{-1}	$W50$ (ϵ_w) km s^{-1}	F_c Jy km s^{-1}	S/N	rms mJy	Dist Mpc	log M_{HI} $M_\odot$	Code
5- 1	192008	09 36 03.2 +10 54 08	09 36 02.5 +10 54 14	8518	163 (9)	0.59	4.7	2.18	126.2	9.35	2 *
5- 2	193842	09 36 10.0 +11 41 10	09 36 08.6 +11 41 21	8949	38 (5)	0.59	11.6	1.79	132.4	9.39	1
5- 3	190385	09 36 25.3 +11 20 08	09 36 26.0 +11 19 44	8654	338 (11)	2.99	18.2	2.00	128.2	10.06	1 *
5- 4	192364	09 36 27.1 +09 36 00	09 36 26.8 +09 36 22	5602	121 (4)	1.20	13.3	1.83	82.3	9.28	1
5- 5	198344	09 36 46.6 +09 02 45	09 36 46.4 +09 02 42	3316	106 (15)	0.62	5.8	2.31	50.4	8.57	1
5- 6	192145	09 36 53.0 +11 42 44	09 36 53.4 +11 43 01	8627	49 (6)	0.86	15.4	1.77	127.8	9.52	1 *
5- 7	191046	09 37 00.2 +09 06 37	09 37 02.0 +09 06 07	3058	93 (11)	0.46	5.5	1.92	46.7	8.37	2
5- 8	198335	09 37 00.4 +09 57 54	09 37 04.4 +09 57 59	1517	53 (8)	0.37	6.5	1.73	24.2	7.71	1
5- 9	191735	09 37 02.4 +09 32 45	09 37 02.3 +09 32 24	5586	273 (14)	1.83	12.7	1.94	82.1	9.46	1
5- 10	192365	09 37 09.5 +09 27 49	09 37 09.0 +09 27 50	6719	199 (4)	2.31	21.2	1.73	100.6	9.74	1
5- 11	192510	09 37 24.6 +08 41 42	09 37 26.1 +08 41 21	3308	37 (20)	0.47	6.8	2.44	50.3	8.45	1
5- 12	191860	09 37 56.1 +08 10 45	09 37 55.9 +08 10 47	6201	53 (6)	0.49	7.6	1.95	93.2	9.00	1
5- 13	5134	09 38 07.3 +09 31 35	09 38 07.9 +09 31 23	3339	341 (3)	18.43	130.5	1.71	48.2	10.00	1
5- 14	190408	09 38 20.1 +09 26 52	09 38 19.3 +09 26 46	5514	175 (19)	0.87	9.0	1.62	81.1	9.13	1
5- 15	192369	09 38 33.9 +09 31 22	09 38 32.7 +09 31 16	5640	293 (44)	0.80	5.9	1.79	82.9	9.11	2 *
5- 16	191861	09 38 41.1 +08 07 23	09 38 40.3 +08 08 10	3366	103 (10)	1.56	17.8	1.92	51.2	8.98	1
5- 17	193832	09 38 48.1 +11 28 26	09 38 52.2 +11 29 18	5883	21 (6)	0.34	6.7	2.35	88.6	8.80	1
5- 18	190417	09 38 54.5 +09 45 25	09 38 53.5 +09 45 01	5672	180 (16)	1.07	8.8	2.02	83.3	9.24	1
5- 19	192371	09 39 14.2 +09 21 54	09 39 18.4 +09 22 42	14997	44 (8)	0.39	6.5	2.03	218.9	9.64	1
5- 20	192018	09 39 22.6 +10 58 52	09 39 23.0 +10 59 13	10490	193 (6)	0.94	7.2	2.09	154.4	9.72	1

contributing to the structure is the noticeable paucity of sources at a redshift of $\sim$ 2200 km s^{-1} just behind Leo II. The peak in the distribution at velocities just above 3000 km s^{-1} represents the Cancer-Leo Cloud which contains the NGC 3367 group [Tully, 1987]. Further out are three Abell clusters (A1016, A999, and A1142) each with about 35 members and all at nearly the same redshift ($cz_{cluster}$ = 9600 km s^{-1}, 9500 km s^{-1}, and 10500 km s^{-1} respectively) that contribute to the peak near 10,000 km s^{-1}. Two artificial dips in the histogram result from RFI due to the San Juan FAA radar transmitter at 1350 MHz and its harmonic at 1380 MHz as noted by Giovanelli et al. [2007]. The locations and relative strengths of these interferences are represented by downward arrows in Figure 2.2a. Other RFI contributions are negligible when averaged over the whole dataset.

The significant contribution of the ALFALFA survey to the number of known dwarf galaxies in the nearby universe is revealed in the remaining histograms. Because they are of low mass, dwarf galaxies are expected to have small W50. Most previous HI surveys have been limited by their poorer spectral resolution to detection of significantly larger line widths. For example, no objects with W50 $<$ 30 km s^{-1} were found in all of southern HIPASS ($\sim$21,000 deg^2; Meyer et al. [2004]) while, as shown in Figure 2.2b, 55 low width sources are included in the current ALFALFA catalog in the Leo region alone (354 deg^2). Roughly half of these low-W50 HI detections have no associated optical galaxy and are thought to be emission from either the Leo Ring or the extended HI in the Leo Triplet region (see Section 2.4). Of the remaining 30 sources, only ten have signal-to-noise ratios of greater than 10 suggesting that, while ALFALFA clearly has the ability to detect objects of very narrow line widths, dwarf galaxies with W50$<$ 30 km s^{-1} are most likely rarer than dwarfs of higher W50.

New detections of nearby dwarfs are also expected to push the lower limits of HI flux and mass. As shown in Figure 2.2c, nearly half of the objects from the current ALFALFA catalog of the Leo region have integrated fluxes of less than 1.0 Jy km s^{-1}, the completeness limit for broad signals in ALFALFA. (The limit is even lower for narrow signals at ∼0.25 Jy km s^{-1}.) In more than 60 times the areal sky coverage, the southern HIPASS catalog contains only one source below 1.0 Jy km s^{-1} [Meyer et al., 2004]. The Leo sample also reaches down to $M_{HI} = 10^{6.77} M_{\odot}$ as shown in Figure 2.2e. Of the 1953 good quality detections in the sample, 118 have $M_{HI} < 10^{8} M_{\odot}$ (roughly 6%), and 45 of these low-mass galaxies were determined to be members of Leo I (see Section 3.1). The percentage of low-mass objects in the Leo region is comparable to the 8% found in the much denser Virgo region [Giovanelli et al., 2007, Kent et al., 2008]. Although Virgo at 16 Mpc is larger and more densely populated, Leo is slightly closer to the Local Group at ∼11 Mpc away and thus allows for the detection of even lower mass objects down to $5 \times 10^{6} M_{\odot}$.

Figure 2.3 shows the relation of HI mass to distance and of S/N and integrated flux to velocity width for the sample. The stacking of objects at 11 and 17 Mpc in Figure 2.3a comes from placing nearby objects at a variety of recessional velocities at the distances adopted for Leo I and II (see Section 3.1 for an explanation of how the distances and group members were chosen). The lack of sources seen in Figure 2.2a around 2200 km s^{-1} (which roughly translates to 30 Mpc) is still present. This paucity is also seen in the distribution of the ∼3800 optical redshifts found in the AGC within the same right ascension, declination, and velocity bounds, suggesting the gap accurately reflects the large scale structure in the region. RFI from the San Juan FAA radar transmitter causes the gap in detections near 230 Mpc shown both by the vertical lines in the upper panel

of Figure 2.3 and by the dip at 16,000 km s^{-1} in the redshift histogram of Figure 2.2a.

The middle and lower panels of Figure 2.3 show that while the distribution of S/N appears to be unbiased toward larger velocity widths (i.e. the lower envelope is constant over the entire width range), the integrated flux values do depend on width. The dashed line in the lower panel indicates a constant S/N level of 6.5. This expected trend [Giovanelli et al., 2005a] was also noted in other ALFALFA catalog releases [Giovanelli et al., 2007, Saintonge et al., 2008, Kent et al., 2008]. Only seven objects have W50 $>$ 600 km s^{-1}, and only one of the seven (UGC 6066) has a $S/N > 10$ (UGC 6066, an edge-on galaxy with $cz = 11,807$ km s^{-1} & W50 $= 667$ km s^{-1}). The low number of high-W50 detections in this dataset is partially a reflection of the small area of sky being considered; nineteen additional high-W50 sources are found in the currently available ALFALFA spring-sky catalog, six of which have $S/N > 10$. Despite more high-W50 sources found in the ALFALFA-Leo catalog than in the southern HIPASS one (only 8 objects with W50 $>$ 600 km s^{-1}; Meyer et al. [2004]), the number of galaxies falls off quickly for large widths, W50 $>$ 600 km s^{-1} for both samples. Although an intrinsic rarity of sources of high velocity width and low flux most likely plays a role in this paucity, such objects are also difficult to detect both by eye and with matched-filtering algorithms for fixed rms, resulting in a known survey bias against large widths. (See Chapter 3 for completeness corrections applied to compensate for this bias.)

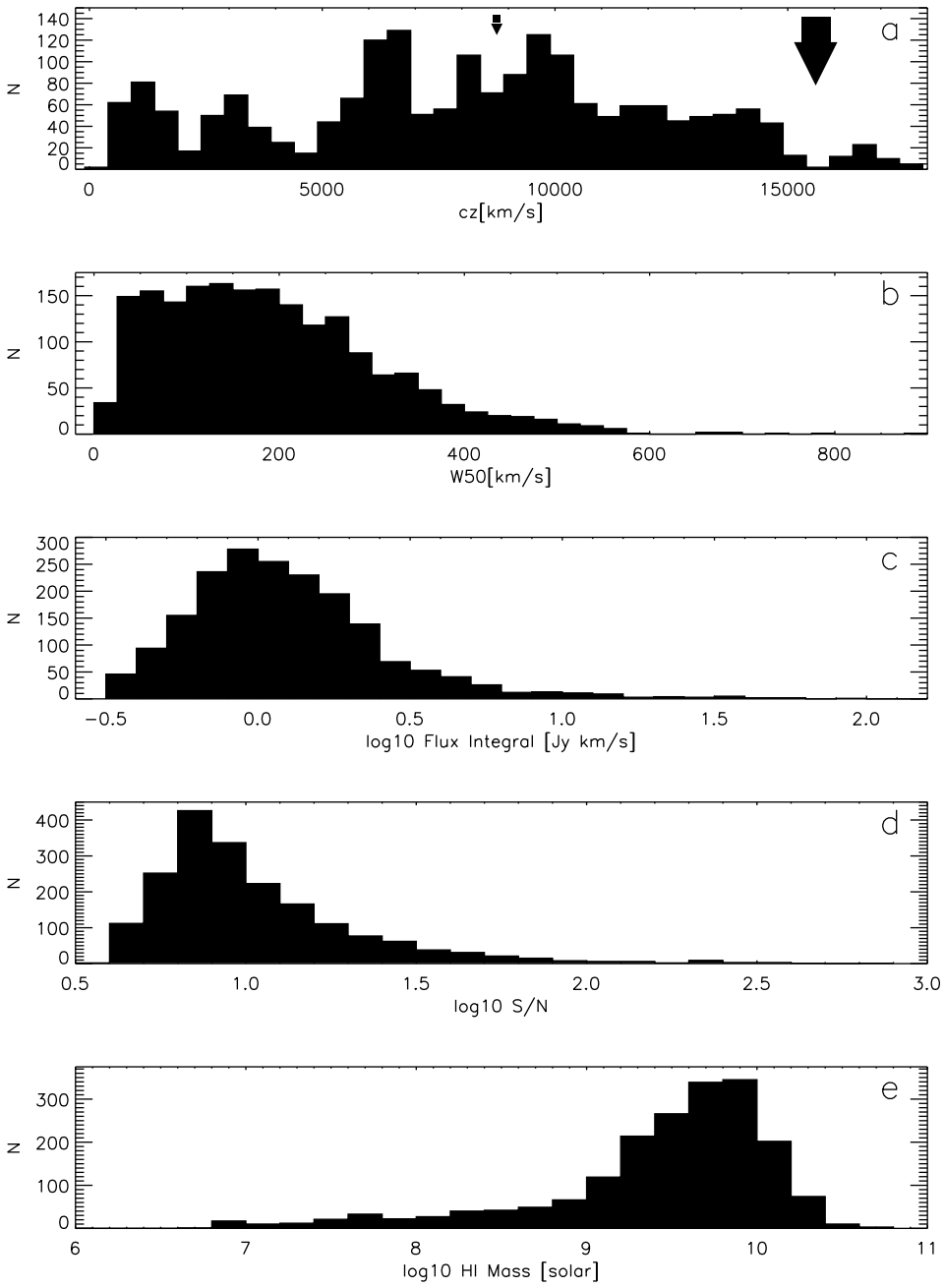

Figure 2.2 Distributions of properties of the sources from the region ($9^h36^m < \alpha < 11^h36^m$ and $+04° < \delta < +16°$. (a) shows the redshift distribution in km s^{-1} with arrows indicating the most significant interruptions due to radio frequency interference (arrow size reflects rfi strength), (b) shows the velocity width distribution in km s^{-1}, (c) shows the integrated flux distribution in Jy km s^{-1}, (d) shows the S/N distribution, and (e) shows the HI mass distribution in solar mass units.

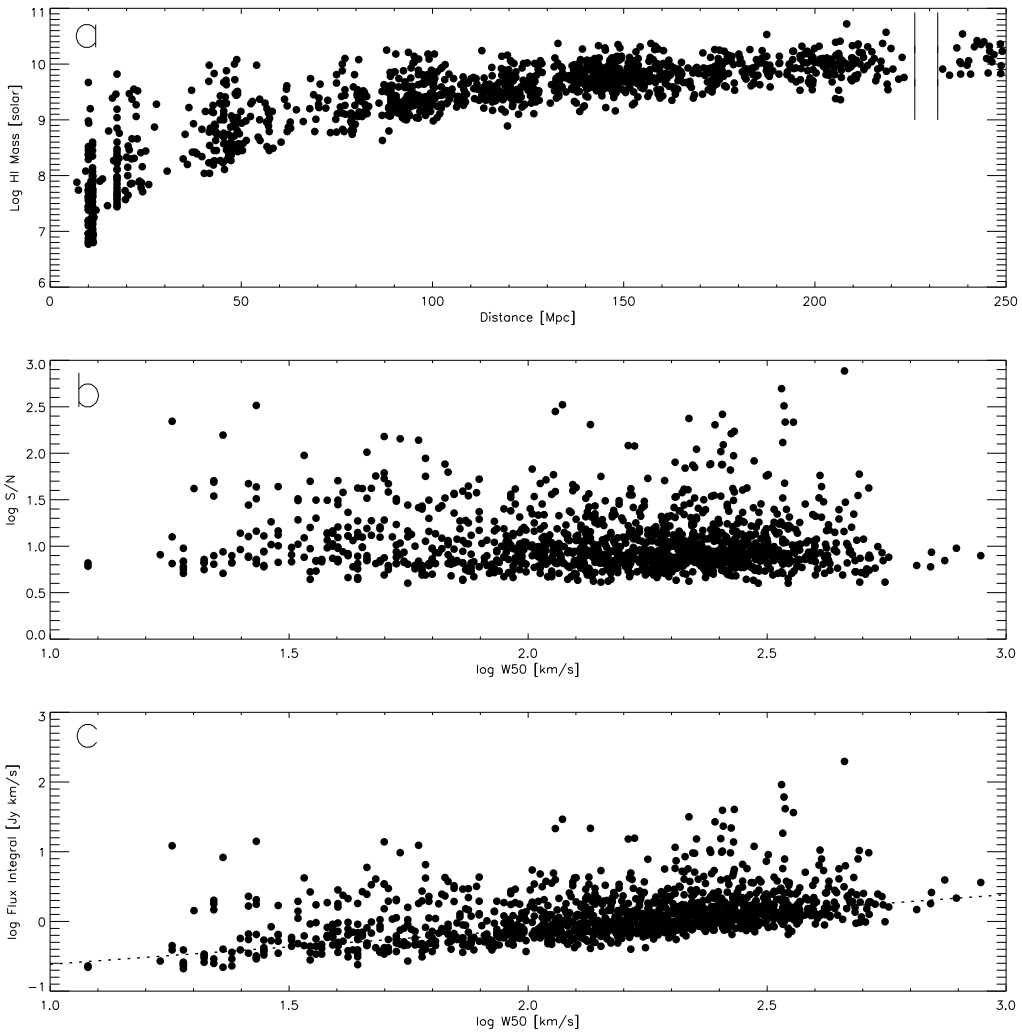

Figure 2.3 Statistical properties of the sources from the region ($9^h36^m < \alpha < 11^h36^m$ and $+04^\circ < \delta < +16^\circ$). The upper panel shows the logarithm of HI mass versus distance. The gap in detections between 220 and 230 Mpc is due to RFI while the gap in sources at 30 Mpc reflects the corresponding large-scale structure. The middle panel shows the logarithm of S/N versus the logarithm of velocity width, W50. The lower envelope is constant over the entire W50 range. The lower panel shows the logarithm of integrated flux versus the logarithm of velocity width. Here the lower envelope is dependent on width and the dashed line indicates a S/N level of 6.5.

2.4 Leo features without optical counterparts

More than 100 detections listed in the ALFALFA catalogs for the Leo region do not have clearly associated optical counterparts. Half of these can be linked to either the Leo Ring, the extended HI in the Leo Triplet, or tidal remnants surrounding NGC 3389. In this section we present detailed maps of these three systems. Another 43 objects are nearby high velocity clouds (denoted by a code '9'). Of the remaining 15 detections with no optical counterparts, 14 have marginal signal to noise and require further followup. The most promising candidate for an independent system without a detectable stellar component is AGC 215416 at a cz of 3371 km s^{-1}. With a signal-to-noise ratio of 17, the putative HI detection is placed at a distance of 50 Mpc by the Masters [2005] flow model and thus at an HI mass of $10^{8.75} M_{\odot}$ but has no visible emission in either SDSS or DSS2 blue images. One very likely possibility is that AGC 215416 is an OH megamaser at z$\sim$0.19. Deeper optical and HI observations are needed to determine the nature of this object.

ALFALFA Survey Map of the Leo Ring

Since its serendipitous discovery [Schneider et al., 1983], the Leo Ring has been studied at 21-cm (Arecibo: Schneider et al. [1983]; VLA: Schneider et al. [1986]), molecular (CO & OH: Schneider et al. [1989]), infrared (IRAS: Schneider et al. [1989]), optical (V and K bands: Skrutskie et al. [1984]; R band: Kibblewhite et al. [1985]; B & V bands: Schneider et al. [1989]; Hα: Reynolds et al. [1986]), and X-ray frequencies [Schneider et al., 1989]. Other than a tentative, 4σ Hα detection by Reynolds et al. [1986], until recently only neutral hydrogen searches in the intergalactic cloud have been successful. However, new GALEX

observations [Thilker et al., 2009] have revealed ultraviolet emission possibly associated with star formation within the Ring's neutral gas.

Schneider [1989] found an integrated flux of $S_{int} = 70.9$ Jy km s^{-1} with an HI mass of $2.06 \times 10^9 M_\odot$ in the Ring for the distance of 11.1 Mpc adopted here. We identify 26 separate clumps which constitute the Ring, yielding a total HI mass of $1.80 \times 10^9 M_\odot$ (24% of the M_{HI} for the entire M96 group), an integrated flux of $S_{int} = 62.14$ Jy km s^{-1}, and a mean velocity of 852 km s^{-1}. The ALFALFA flux budget may not account for some of the low surface brightness components of the Ring, so the 12% flux mismatch is not a source of serious concern. The most massive contribution to the Ring, containing the spur connecting to M96, as well as the additional structures to the north, east, and west found in the Schneider et al. [1989] map are all recovered by the ALFALFA dataset, and no new significant structures are found despite the much larger sky coverage of the ALFALFA map. Both the Schneider et al. [1989] map and the ALFALFA one show a velocity gradient with lower velocities found for the more scattered clumps to the northeast and higher velocities belonging to the larger portions in the southwest.

The ALFALFA survey map of the Ring covering 708 km s^{-1} to 1046 km s^{-1} is shown in Figure 2.4 overlaid on a mosaic of SDSS r-band images. The largest optical galaxies in the M96 group are NGC 3384 and NGC 3379=M105 at the center of the Ring, NGC 3368=M96 which is connected to the Ring by a spur of HI, and NGC 3351 to the west. Six optically-identified galaxies found superimposed on the Ring and thus possibly associated with the HI are noted by filled circles and labeled with their AGC numbers. Three of the optical detections, AGC 201972 (called KK94 in Karachentseva and Karachentsev [1998]), and AGC 202026 and

AGC 201975 from Karachentsev and Karachentseva [2004], have unknown optical redshifts. Thus the HI detected at those locations by ALFALFA cannot be definitively linked to the optical galaxy, but instead may be associated with the Ring. Higher resolution synthesis HI observations and optical redshifts are needed to ascertain the nature of these detections.

In the cases of AGC 202027 and AGC 201970, optical redshifts are reported that match those measured in the HI observations; SDSS gives a redshift of 1013 km s^{-1} for AGC 202027, and Karachentsev and Karachentseva [2004] cite a redshift of 617 km s^{-1} for AGC 201970. For AGC 205505, an independent HI detection was not identified by the signal extraction algorithm [Saintonge, 2007a], and SDSS finds a redshift for the associated optical galaxy of 1146$\pm$50 km s^{-1}, which is slightly higher than the range of HI velocities covered by emission from the Ring. Thus AGC 205505 is considered an M96 group member but the association of the optical galaxy with the Ring is more tenuous. These three dwarf galaxies may have formed out of overdensities in the Ring. A study of their metallicities would determine whether they formed with the other, more massive Leo I group members which may mean the Ring is primordial as suggested by [Schneider, 1989] or whether they are high metallicity tidal dwarf systems which may have resulted from the tidal encounter that produced the Ring.

Two additional optical detections noted by Karachentsev and Karachentseva [2004] as potential Leo I members that overlap with the Ring, AGC 200592 and AGC 201963, were found to be background sources with optical redshifts of 16,775 km s^{-1} and 53,213 km s^{-1} respectively, and are not marked. For details on the comparison of the optically-selected Karachentsev and Karachentseva [2004] sample with the ALFALFA catalog throughout the rest of the M96 group,

see Chapter 3).

ALFALFA Survey Map of the Leo Triplet

Less than 1.5 Mpc away from the Leo Ring is the trio of large spiral galaxies NGC 3623, NGC 3627, and NGC 3628 collectively known as the Leo Triplet. Zwicky [1956] noted a faint optical plume extending from NGC 3628 directed eastward away from the other two galaxies. Subsequent 21-cm observations found an associated neutral hydrogen plume roughly 100 kpc in length, an HI bridge connecting NGC 3628 to NGC 3623, and a distortion in the HI disk of NGC 3627 [Rots, 1978, Haynes et al., 1979].

Despite the appearance of a bridge of gas connecting NGC 3623 to the perturbed NGC 3628, simulations of a collision that is prograde for NGC 3627 and retrograde for NGC 3628 but not involving NGC 3623 match best with the observations of the plume [Toomre and Toomre, 1972, Rots, 1978, Haynes et al., 1979]. NGC 3623 also has a relatively quiescent star formation history [Afanasiev and Sil'chenko, 2005], further suggesting that NGC 3623 was not involved in perturbing NGC 3628. The dust-to-gas ratio in the plume, determined by observations of the plume's infrared component, is also consistent with the tidal model for its formation [Hughes et al., 1991]. No CO has yet been detected in the plume [Young et al., 1983].

The ALFALFA map of the Triplet is shown in Figure 2.5 covering 631 km s^{-1} to 1150 km s^{-1} and overlaid on a mosaic of SDSS r-band images. The main features of the Haynes et al. [1979] map of the region are all recovered: the large plume extending eastward of NGC 3628, a clump of HI between NGC 3628 to NGC 3623 (M65), and the cloud extending to the southwest of NGC 3627. The

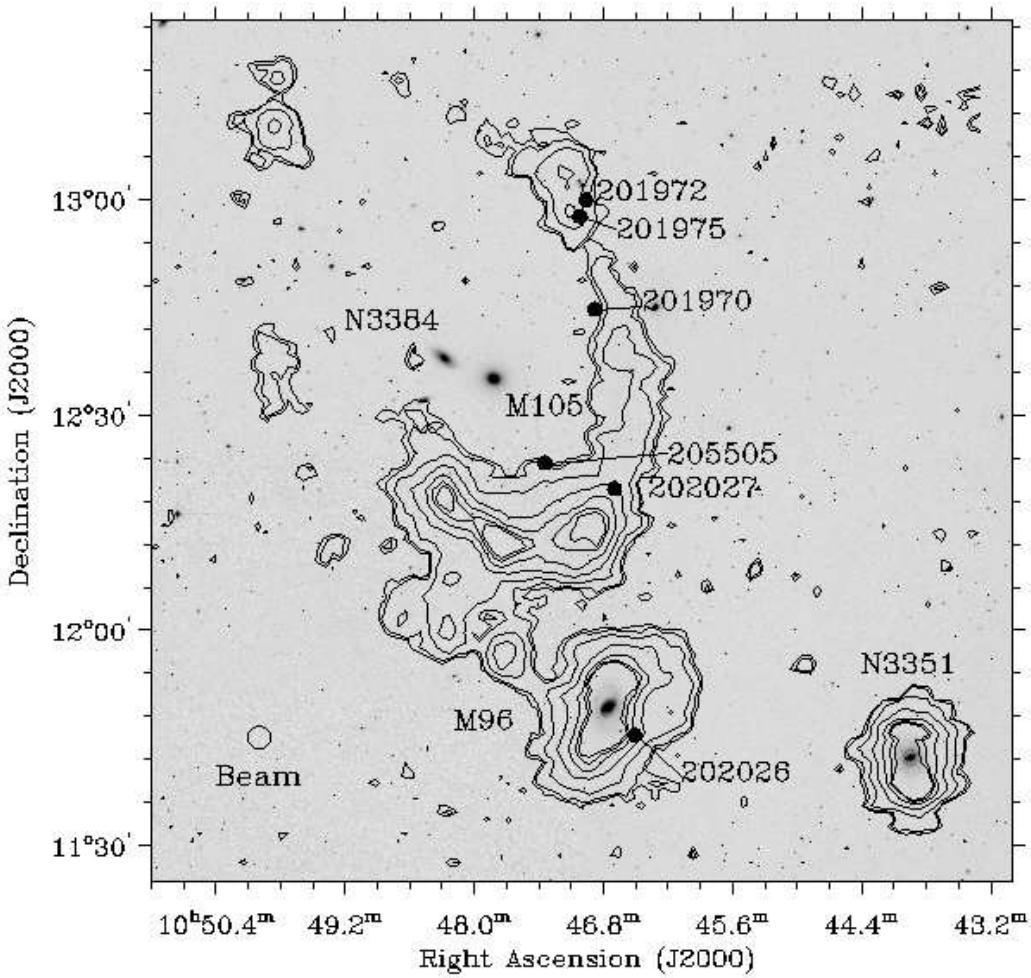

Figure 2.4 The map of the Leo Ring extracted from the ALFALFA dataset over the velocity range 708 km s^{-1} to 1046 km s^{-1}, overlaid on a mosaic of SDSS r-band images. HI contours are drawn at 4.0, 5.0, 9.0, 18, 32, 44, and 50 mJy per beam (units are left in mJy per beam as some of the emission is resolved). The open circle represents the ALFA HPBW of $\sim$4′. Dwarf galaxies noted in optical surveys of the region that lie within the extent of the Ring are shown as filled circles and labeled with their AGC number. Optical redshifts are not known for AGC 202026, AGC 201975, and AGC 201972, so the HI detections at these locations cannot be differentiated from Ring emission and may not be associated with the optical galaxies. For AGC 202027 and AGC 201970, optical redshifts are known that match the measured 21-cm line velocities. These two dwarf galaxies may have formed from overdensities in the Ring. AGC 205505 was not identified by the signal extraction algorithm, and an optical redshift of 1146$\pm$50 km s^{-1} places the optical galaxy at this position just above the range of velocities covered by the Ring. The association of AGC 205505 with the Ring is thus more tenuous. The largest optical galaxies (N3351, N3368=M96, N3384, and N3379=M105) are labeled.

ALFALFA dataset detects $1.0 \times 10^9 M_\odot$ in the plume which contributes 14% of the entire HI mass for the M66 group. The same amount of gas mass is reported in Haynes et al. [1979] for the group distance of 10.0 Mpc adopted here. The earlier map finds a roughly constant velocity field over 50 kpc of the plume's length at ∼900 km s^{-1}. Although the ALFALFA dataset shows emission throughout the plume at that velocity, the ALFALFA map also reveals gas along the entire plume with a larger range of 860 km s^{-1} $< v <$ 920 km s^{-1} as well as gas at low relative velocities (∼840 km s^{-1}) found only at the far end of the plume.

Additional HI located outside the area covered by previous HI observations is found by ALFALFA to extend south of NGC 3627 and northward from NGC 3628. The ALFALFA detection registers $2.3 \times 10^8 M_\odot$ in the southern HI clump which is 3% of the entire HI mass for the M66 group. We identify eight separate clouds within the southwestern clump and they are presented in Table 3.3. Lower velocities (∼650 km s^{-1}) dominate the southernmost part of the clump, and velocity increases as the gas is traced upward until matching the HI velocity of NGC 3627 at 750 km s^{-1}. This newly-detected HI and its spatial and spectral proximity to NGC 3627 furthers the hypothesis that NGC 3627 was responsible for the collision that led to the plume. The ALFALFA data do not reveal any disturbance in the velocity field of NGC 3623 which may suggest it was not involved in the past encounter. The HI clump that appears to connect NGC 3623 with NGC 3628 is actually well separated in velocity from NGC 3623. Thus it is not a bridge between the two galaxies, but instead an extension of NGC 3628.

In Figure 2.5, we note the location of an optical galaxy seen in POSS-II and SDSS (AGC 219303). The irregular galaxy is very low surface brightness with a

B band apparent magnitude of 17.5 and has a morphology consistent with other Leo I dwarfs. An optical redshift is needed to determine whether AGC 219303 is associated with the HI in the plume.

ALFALFA Survey Map of the NGC 3389 System

Located just behind the Leo Ring at a cz of 1301 km s^{-1}, the large SA galaxy, NGC 3389 shows a large central peak in its HI profile, possibly a sign of a prior tidal encounter [Schneider, 1989]. However, de Vaucouleurs [1967] claimed NGC 3389 was not part of the M96 group, and thus unlikely to be interacting with the Ring. After limited mapping of a few points surrounding NGC 3389, Schneider [1989] found a nearby dwarf, CGCG 066-029 (AGC 200603), to be the most likely cause of NGC 3389's centrally peaked profile based on the dwarf's unusual morphology and a slight extension of its HI toward NGC 3389. Hoffman et al. [1987] believed CGCG 066-029 to be part of a binary pair with AGC 200604 with only a 30 km s^{-1} difference in velocity. Neither [Schneider, 1989] nor Hoffman et al. [1987] reported a connection with the dwarf 20 arcminutes to the south, CGCG 066-025 (AGC 200598).

The ALFALFA map of the area surrounding NGC 3389 is shown in Figure 2.6 covering 1123 km s^{-1} to 1487 km s^{-1} and overlaid on a mosaic of SDSS r-band images. A clear connection is seen in position and velocity space between NGC 3389 and CGCG 066-029. A $2'$ displacement is revealed in the direction of NGC 3389 between the centroid of the HI and the stellar component of CGCG 066-029 which furthers the idea that the two galaxies are interacting. However, AGC 200604, originally noted as the binary partner of CGCG 066-029 [Hoffman et al., 1987], does not appear to be part of the system at all, and the optical galaxy lines up with an ALFALFA HI detection at 6941 km s^{-1} instead. A bridge

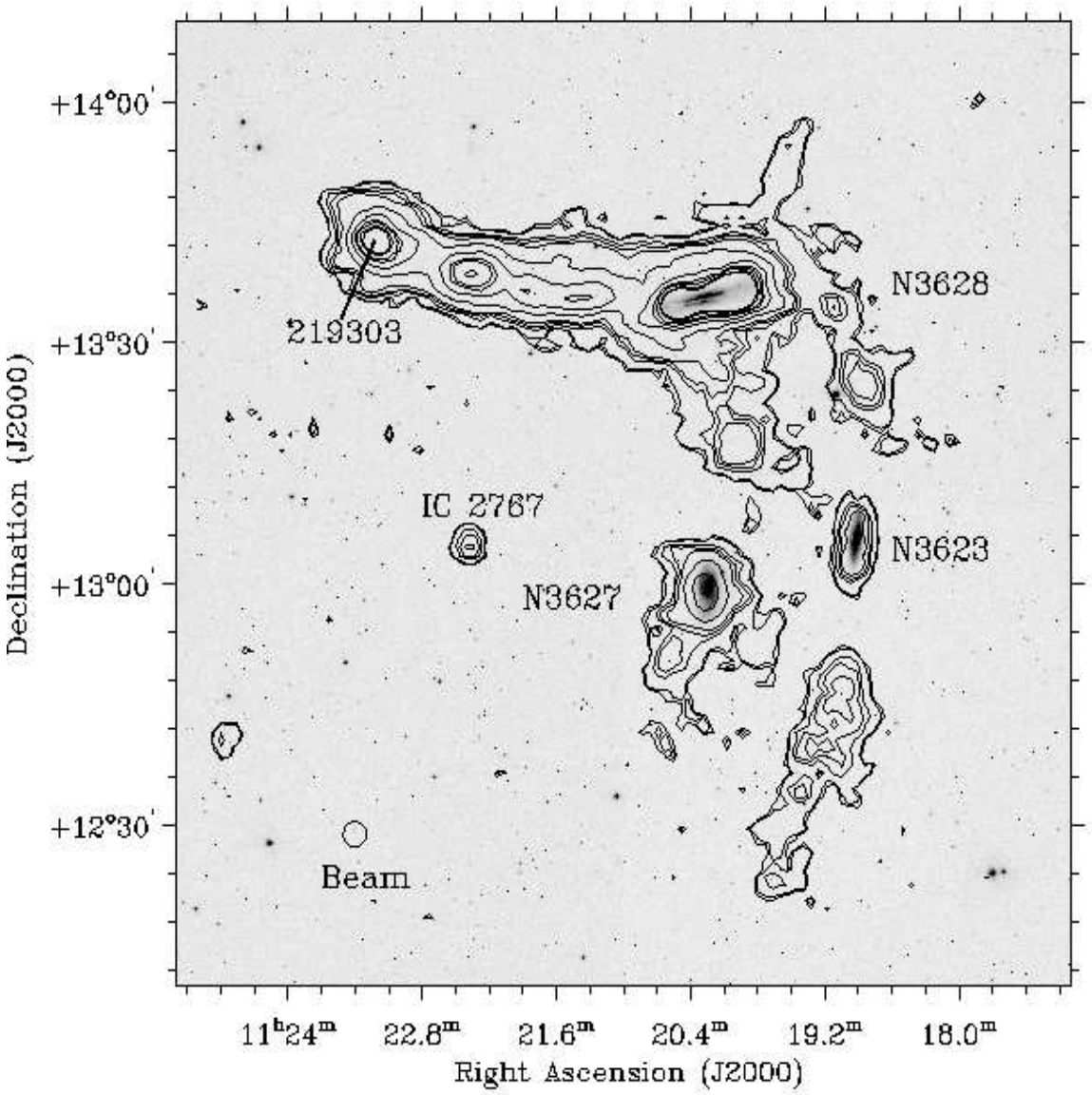

Figure 2.5 The map of the Leo Triplet derived from the ALFALFA dataset over the velocity range 631 km s^{-1} to 1150 km s^{-1}, overlaid on a mosaic of SDSS r-band images. HI contours are drawn at 4.5, 5.0, 8.0, 10, 13, 26, 52, 78, 91, 117, and 130 mJy per beam (units are left in mJy per beam as some of the emission is resolved). The open circle represents the ALFA HPBW of $\sim$4′. All four ALFALFA detections in the field associated with optical galaxies (N3623=M65, N3627=M66, N3628, and IC 2767) are labeled. The location of the optical galaxy AGC 219303 which is possibly associated with the plume but has no optical redshift is indicated.

connecting CGCG 066-025 to the rest of the system is clearly detected suggesting that despite its smooth looking contours, this second dwarf may also be involved in the interaction. This bridge contains $6.3 \times 10^7 M_\odot$ adopting the secondary distance to NGC 3389 of 21.4 Mpc (see Table 3.7). As noted by Schneider [1989] the NGC 3389 system may be similar to the tidal encounter between the Magellanic Clouds and the Milky Way where the dwarfs are distorted by the close encounter with a large spiral neighbor. The only minimally disturbed gas distribution and morphology of CGCG 066-025 may suggest the galaxy became involved in the encounter on more recent timescales.

2.5 Summary

In this chapter we presented the results from the ALFALFA survey's current coverage of the Leo region ($09^h36^m < \alpha < 11^h36^m$ and $+04^\circ < \delta < +16^\circ$) which contribute new spectroscopic detections for 48 previously unconfirmed dwarf galaxies with $M < 10^8 M_\odot$.

Nearby HI-bearing dwarfs are most commonly characterized by low HI flux and narrow HI line width. In the ∼21,000 deg^2 of sky covered by HIPASS, the most extensive previous blind HI survey, HIPASS found 44 objects with $M_{HI} < 10^8 M_\odot$, detected 1 object with an HI flux less than 1 Jy km s^{-1}, and made no detections with HI line widths narrower than 30 km s^{-1}. With its superior spatial and spectral resolution as well as sensitivity, in the 354 deg^2 surrounding the Leo groups ($\sim 1/60$ of the total coverage of HIPASS), ALFALFA finds 118 objects with $M_{HI} < 10^8 M_\odot$, detects 260 objects with HI fluxes less than 1 Jy km s^{-1}, and makes 55 detections with HI line widths narrower than 30 km s^{-1}. Af-

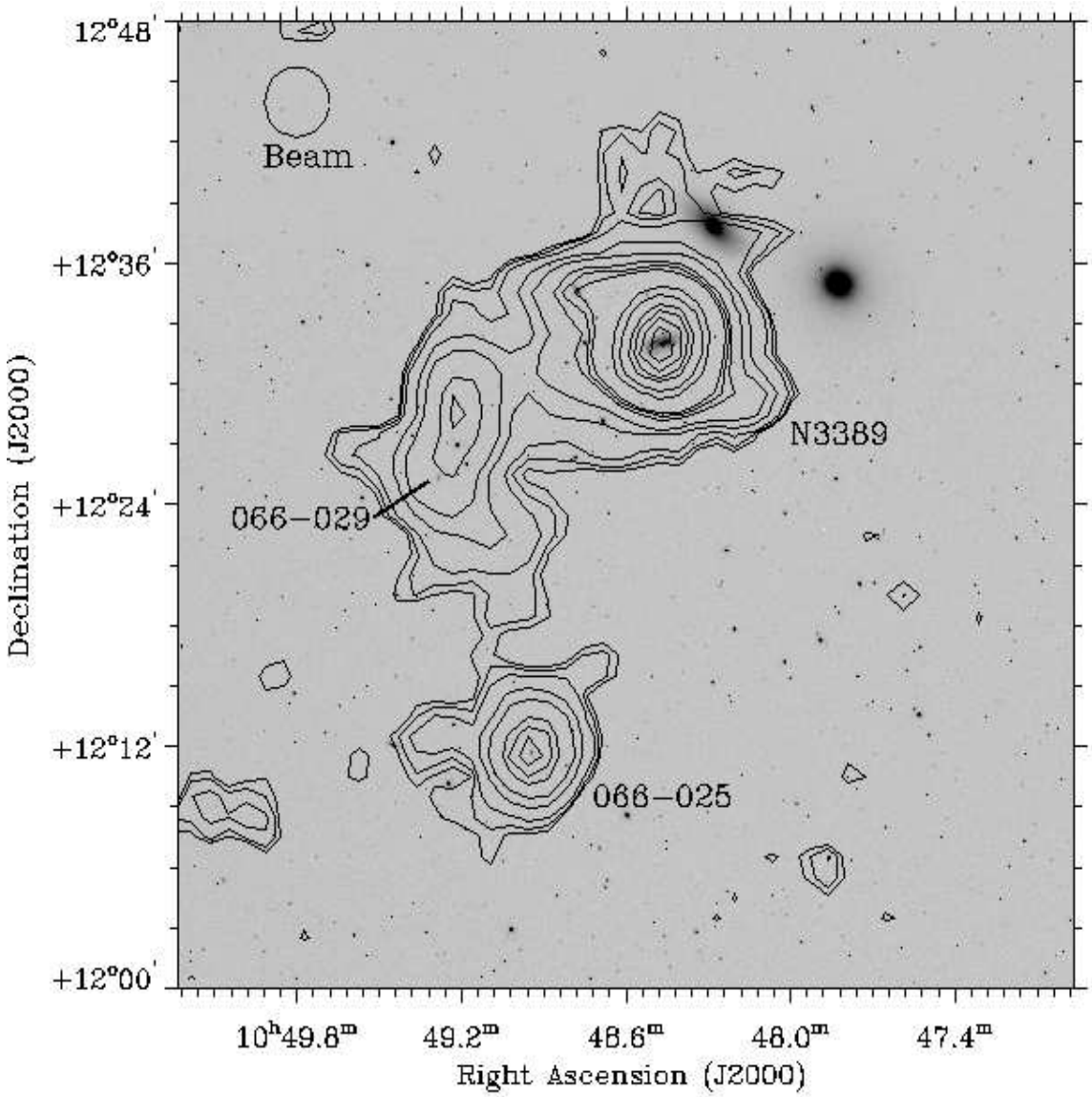

Figure 2.6 Map of the region around NGC 3389 derived from the ALFALFA dataset over the velocity range 1123 km s^{-1} to 1487 km s^{-1}, overlaid on an SDSS r-band image. HI contours are drawn at 0.75, 1.0, 1.45, 2.9, 4.4, 7.3, 8.7, 10, 20, 26, 35, 40, 45, and 50 mJy per beam (units are left in mJy per beam as some of the emission is resolved). The open circle represents the ALFA HPBW of $\sim$4′. The three optical galaxies in the system (N3389, CGCG 066-025, and CGCG 066-029) are labeled. The bright S0 galaxy, NGC 3384, and the bright elliptical galaxy, NGC 3379, seen to the northwest of NGC 3389 are foreground galaxies located in the center of the Leo Ring (see Figure 2.4).

ter membership determinations are made for the Leo I group, ALFALFA finds 45 low-mass group members, which is more than were detected for the entire southern HIPASS sample.

The ALFALFA detection statistics in the Leo region reflect the results of the larger survey. In only 20% of the survey's full intended coverage, ALFALFA has already detected ∼300 objects with $M_{HI} < 10^8 M_\odot$, many of which were previously uncatalogued. The large number of HI-rich dwarfs suggests there may be a significant population of low surface brightness, low-mass galaxies that are missed by optical surveys whether it be due to sensitivity or survey coverage and by HI surveys of lower sensitivity. In the next chapter we derive group membership statistics for the Leo groups and compare this HI-selected sample with an optical survey of the same region.

CHAPTER 3

HIMF FOR THE LEO GROUP*

I don't know that there are any shortcuts to doing a good job.

- Sandra Day O'Connor

3.1 Structure and Dynamics of the Leo Group

The Local Group of galaxies is part of the Local Sheet, a plane-like structure with a spread of only ∼1.5 Mpc about the supergalactic plane SGZ=0 [Tully et al., 2008]. The nearest adjacent structure is Leo I (also called the Leo Spur), a complex grouping of galaxies over a narrow velocity range (roughly 500 km $s^{-1} < v < 1200$ km s^{-1}). Since the earliest references to the Leo group of galaxies [de Vaucouleurs, 1975, Sandage and Tammann, 1975], studies have noted the existence of substructure within the Leo I group, most commonly the M96 group including the Leo Ring and the M66 group including the Leo Triplet [Turner and Gott, 1976, Huchra and Geller, 1982]. Some authors have further separated Leo I into even more distinct groups [Materne, 1978, Tully, 1987], but others suggest that velocity crowding due to the proximity of the Virgo cluster leads to the appearance of more group structure than may actually exist [Schneider, 1989]. Adding further confusion to the Leo I group structure is the more disperse Leo Cloud in the background. [Tully, 1987]. Like Leo I, the Leo Cloud is most likely an assemblage of several smaller groups.

As different authors tend to use the same nomenclature to refer to different groups, the definitions we use are presented in Table 3.1. The centroid position,

*This chapter is published in Stierwalt et al. (2009)

Table 3.1. Hierarchical Structures in the Leo Region

Cloud	Group Name	Centroid (J2000)	$\bar{v}$ (ϵ_v) km s^{-1}	σ (ϵ_σ) km s^{-1}	R_H Mpc	Dist Mpc	N	Notes
Leo I		-	906 (26)	203 (15)	>0.27	-	96	also Leo Spur
	M96	10 46 45.7 +11 49 12	881 (16)	174 (19)	0.13	11.1	41	part of Leo I
	M66	11 20 15.0 +12 59 30	812 (12)	156 (26)	0.06	10.5	19	part of Leo I
Leo Cloud		-	∼1500	∼200	>0.50	-	>100	behind Leo I
	Leo II	∼11 03 +12 24	1423 (24)	181 (20)	0.22	17.5	41	part of Cloud

mean velocity (with error), velocity dispersion (with error), number of members, harmonic mean radius, and assumed distance are listed for each group or subgroup. For the M96 and M66 groups, the centroid positions are M96 and M66 themselves. The center of the background Leo II group is placed approximately along a line of sight between M96 and M66. The mean velocities, velocity dispersions, assumed distances, and number of members are determined in Sections 3.1.1, 3.1.2, and 3.1.3. The harmonic mean radius is calculated using the distance to each group, the number of members, and the angular separation of those members.

3.1.1 Group Membership in Leo I

Nearest neighbor searches and other group finding algorithms for determining group membership are easily confused by the high density of sources and complicated group structure in Leo. Both Leo I and the Leo Cloud are projected on the same small area of sky at very similar redshifts and thus are difficult to separate. Due to Virgo's proximity, the Leo I group's infall velocity to Virgo of > 300 km s^{-1} [Sakai et al., 1997] can counteract pure Hubble flow significantly and thus confuse redshift measurements. Leo I also has at least two distinct

components at nearly the same redshift: the M96 and M66 groups. For M96 and M66 to be part of the same bound structure, the crossing time for such a group would have to be $\tau_{cross} = 2R/\sigma = 1.7 \times 10^{10}$ years, given a σ of 172 km s^{-1} (as calculated in Section 3.1.4). Thus Leo I has not had time to virialize and can still be split into two entities to better understand its dynamics.

For group membership statistics in Leo I, we thus rely on both velocity dispersion calculations and spatial density distributions to determine group assignments. Potential members are pulled from the AGC; that database includes all detections in the current ALFALFA catalog made to date. By experimenting with different velocity cutoffs as a requirement for group membership (i.e. only galaxies within a certain range of velocities can be deemed members), we find the velocity dispersion rises steeply when galaxies with velocities lower than 600 km s^{-1} or higher than 1200 km s^{-1} are included. Thus we require a source velocity of 600 km s^{-1} $< cz <$ 1200 km s^{-1} for a galaxy to be considered a member of Leo I. Next, by placing M96 and M66 at the centers of separate Leo I subgroups, a radius for each subgroup is found beyond which the number of additional group members levels off. We choose a radius of 1.7° for the M66 group or $\sim$ 0.3 Mpc at the M66 distance of 10.0 Mpc and a radius of 4.3° for the M96 group or $\sim$ 0.8 Mpc at the M96 distance of 11.1 Mpc (group distances are determined in Section 3.1.2). The group radius determined for the M96 group does not change if NGC 3384 (found at the center of the Leo Ring) is made the group center instead of M96.

After this analysis, the M96 group is found to have 39 members (not including the detections that make up the Ring) and the M66 group to have 19 members. Included in the M96 members are all of the optically-identified dwarfs

from Karachentsev and Karachentseva [2004] that were spectroscopically confirmed as Leo I members (see Section 3.2). Our membership designations also include all galaxies named as M96 or M66 group members in the Nearby Optical Galaxy catalog of nearby groups (NOG, Giuricin et al. [2000]).

The HI properties for these objects are summarized in Tables 3.2 and 3.3. In the M96 group, 26 HI detections with no optical counterparts are attributed to the Leo Ring. In the M66 group, 22 objects are listed without optical counterparts: sixteen are attributed to either the plume of HI gas extending from NGC 3628 or the extended clump of HI just south of NGC 3627. The remaining six objects are not connected to any of the Triplet galaxies via HI bridges above the ALFALFA survey detection limit, although association is likely. These six detections are treated separately and labeled 'HIonly' in Table 3.3. Parameters for all objects are taken from the ALFALFA catalog unless otherwise noted, and not all objects have associated HI detections.

Thirty-six galaxies remain potential Leo I members but their group membership is unclear. These objects fall within the velocity range of 600 km s$^{-1} < cz < 1200$ km s^{-1} but are outside the group radii determined for the M96 and M66 subgroups. Group distances are not assigned to these objects, and instead distances determined for each individual galaxy by the Masters (2005) flow model are adopted. The parameters for these sources are found in Table 3.4 and are taken from the ALFALFA catalog unless otherwise noted.

Table 3.2. Leo I - M96 Group Membership

AGC #	Other Name	Opt Position[a] (J2000)	HI $cz_\odot$ km s^{-1}	W50 km s^{-1}	F_c Jy km s^{-1}	Dist[b] Mpc	log M_{HI} $M_\odot$
205156		10 30 52.9 +12 26 48	915	21	0.32	11.1	6.91
202248		10 34 56.1 +11 29 32	1177	62	0.64	11.1	7.28
202017[c]	LeG03	10 35 48.9 +08 28 49	1158	70	1.93	11.1	7.75
5761	N3299	10 36 24.0 +12 42 24	604	112	3.54	11.1	8.00
205165		10 37 04.8 +15 20 15	724	27	0.30	11.1	6.93
200499	065-074	10 38 08.0 +10 22 51	1175	178	7.79	11.1	8.35
202019[c]	LeG05	10 39 43.0 +12 38 04	780	22	0.08	11.1	6.37
200512[c]	LeG06	10 39 55.6 +13 54 34	1007	21	0.28	11.1	6.91
5812	065-083	10 40 56.5 +12 28 18	1008	56	1.59	11.1	7.65
200532	065-086	10 42 00.3 +12 20 07	772	36	0.96	11.1	7.46
205268		10 42 52.4 +13 44 28	1145 (opt)	...	...	11.1	...
5850	N3351	10 43 57.6 +11 42 12	777	270	40.41	10.0*	8.98
205445		10 44 35.3 +13 56 23	633 (opt)	...	...	11.1	...
200560[d]		10 44 54.6 +13 54 29	1010	29	0.61	11.1	7.25
202024[c]	LeG13	10 44 57.3 +11 55 01	871	24	0.22	11.1	6.81
202026[c]	FS 15	10 46 30.2 +11 45 19	954	126	3.24	11.1	7.97
205287	Ring	10 46 36.0 +12 37 44	957	78	3.18	11.1	7.94
205289	Ring	10 46 36.4 +12 26 02	1006	48	4.06	11.1	8.06
202027[c]	FS 17	10 46 41.3 +12 19 37	1030	37	1.24	11.1	7.56
205290	Ring	10 46 42.4 +12 46 56	915	50	1.52	11.1	7.63
5882	N3368	10 46 45.7 +11 49 11	893	343	60.81	10.5*	9.20
201970[c]	LeG18	10 46 52.2 +12 44 40	636	38	0.55	11.1	7.20
201972	KK94	10 46 57.3 +12 59 53	834	33	1.94	11.1	7.75
201975[c]	LeG21	10 47 00.8 +12 57 34	843	23	0.48	11.1	7.14
205291	Ring	10 47 02.7 +12 13 36	1018	50	13.86	11.1	8.60
205292	Ring	10 47 09.1 +13 03 11	824	27	1.76	11.1	7.71
205293	Ring	10 47 19.1 +13 09 30	806	51	0.37	11.1	7.02
205505		10 47 20.1 +12 23 15	1146 (opt)	...	...	11.1	...
5889	N3377A	10 47 22.4 +14 04 14	573	46	5.96	9.3*	8.08
205294	Ring	10 47 39.1 +11 55 52	971	27	2.05	11.1	7.79
5899	N3377	10 47 42.3 +13 59 08	689 (opt)	...	...	11.2*	...
205295	Ring	10 47 47.8 +12 13 07	978	59	12.36	11.1	8.55
5902	N3379	10 47 49.6 +12 34 55	911 (opt)	...	...	11.0*	...
205296	Ring	10 47 49.7 +13 07 47	787	30	0.52	11.1	7.20
205297	Ring	10 48 04.3 +13 11 24	794	21	0.26	11.1	6.93
205301	Ring	10 48 12.2 +12 04 14	927	47	3.36	11.1	8.00
205302	Ring	10 48 13.6 +12 08 38	917	46	2.45	11.1	7.76
205303	Ring	10 48 15.6 +12 18 02	910	54	9.69	11.1	8.40
5911	N3384	10 48 16.8 +12 37 42	728 (opt)	...	...	11.6*	...
205304	Ring	10 48 28.1 +12 25 53	854	98	1.17	11.1	7.37
205305	Ring	10 48 30.4 +12 37 43	648	44	0.91	11.1	7.40
205306	Ring	10 48 32.8 +12 30 07	794	75	0.70	11.1	7.23
205307	Ring	10 48 36.0 +12 02 56	924	27	0.65	11.1	7.28
205308	Ring	10 48 42.8 +13 16 05	785	12	0.22	11.1	6.82
200596	066-026	10 48 53.7 +14 07 27	637 (opt)	...	...	11.1	...
205311	Ring	10 49 12.3 +12 11 51	869	18	0.39	11.1	7.01

Table 3.2 (continued)

AGC #	Other Name	Opt Position[a] (J2000)	HI $cz_\odot$ km s^{-1}	W50 km s^{-1}	F_c Jy km s^{-1}	Dist[b] Mpc	log M_{HI} $M_\odot$
201963[e]	Ring	10 49 51.3 +13 09 24	766	20	1.43	11.1	7.60
205313	Ring	10 49 51.5 +12 36 49	774	30	0.64	11.1	7.25
205314	Ring	10 49 51.9 +13 17 21	787	18	0.45	11.1	7.12
205315	Ring	10 49 52.4 +12 32 21	779	33	0.48	11.1	7.13
205316	Ring	10 49 56.7 +12 40 22	776	45	0.62	11.1	7.31
205321	Ring	10 50 02.6 +13 06 30	788	19	0.25	11.1	6.74
205322	Ring	10 50 09.2 +13 00 30	797	23	0.22	11.1	6.79
5944	064-033	10 50 18.9 +13 16 18	1073 (opt)	...	...	11.1*	...
5948		10 50 38.2 +15 45 48	1121	106	4.79	11.1	8.14
5952	N3412	10 50 53.2 +13 24 42	867 (opt)	...	...	11.3*	...
205540		10 51 31.4 +14 06 53	832 (opt)	...	...	11.1	...
205544		10 52 04.8 +15 01 50	828 (opt)	...	...	11.1	...
202456		10 52 19.5 +11 02 36	824 (opt)	...	...	11.1	...
6014	066-058	10 53 42.7 +09 43 39	1133	94	2.90	11.1	7.92
202034[c]		10 55 55.3 +12 20 22	847	22	0.10	11.1	6.46
202035[c]	D640-13	10 56 13.9 +12 00 37	989	30	1.67	11.1	7.69
205278		10 58 52.2 +14 07 46	686	36	0.34	11.1	7.01
6082	N3489	11 00 18.6 +13 54 04	695	113	0.70	12.1*	7.36
210023	066-109	11 04 26.3 +11 45 21	777	44	1.81	11.1	7.70

[a]Positions indicate the centroid of the optical counterpart unless the object is noted as a Ring detection, in which case the position represents the centroid of the HI.

[b]Objects are assigned a group distance except when a * indicates a known primary distance.

[c]HI parameters come from single pixel results (presented in Section 3.2)

[d]HI parameters come from previously catalogued single-pixel Arecibo observations. See the HI archive for details.

[e]Ring detections; optical redshifts from SDSS place optical sources at these locations as background galaxies; ADBS gives v=754 km s^{-1} for AGC 201963

3.1.2 Primary and Secondary Distances in Leo

Primary distances are key to placing galaxy groups like Leo I into the larger context of the surrounding large-scale structure. The primary distances known for the Leo I group are listed in Table 3.5. Heliocentric radial velocities as quoted in the NASA Extragalactic Database[1] and a primary distance with estimated error are given for each galaxy, as well as the method used to obtain the distance and the reference for the measurement. Freedman et al. [2001] used Cepheid variables, Makarova and Karachentsev [1998] measured bright stars, and Tonry et al. [2001] and Rekola et al. [2005] both studied surface brightness fluctuations.

Nine of the ten primary distance measurements quoted in Table 3.5 belong to members of the M96 group. The last entry in Table 3.5 is a Cepheid distance to M66 (UGC 6346/NGC 3627) and is the only primary distance measurement to a member of the M66 group. These primary distances are also reported in Tully et al. [2008], as well as additional secondary distances determined via the Tully-Fisher relation. Potential Leo members with secondary distances are shown in Table 3.6 as calculated from the distance moduli reported in Tully et al. [2008].

For our analysis of Leo I, including both the M96 and M66 groups, we adopt the same distances chosen by Tully et al. [2008]: 11.1 Mpc to the M96 group and 10.0 Mpc to the M66 group. These distances represent a weighted average of the known primary distances in the M96 group (as well as the only primary distance in the M66 group) and agree well with the several distance moduli quoted for Leo I in Ferguson and Sandage [1990]. Group distances are assigned to all members as 11.1 Mpc for the M96 group and 10.0 Mpc for the M66 group unless a primary distance to the object has been measured. Although we favor group

[1] http://nedwww.ipac.caltech.edu/

Table 3.3. Leo I - M66 Group Membership

AGC #	Other[a] Name	Opt Position (J2000)	HI $cz_\odot$ km s^{-1}	W50 km s^{-1}	F_c Jy km s^{-1}	Dist[b] Mpc	log M_{HI} $M_\odot$
215387	HIonly	11 14 14.5 +12 46 55	578	75	2.20	10.0	7.73
6272	N3593	11 14 37.0 +12 49 02	631	254	9.84	10.0	8.36
202256		11 14 45.0 +12 38 51	630	42	0.64	10.0	7.16
210220	I2684	11 17 01.1 +13 05 55	588	25	0.57	10.0	7.09
215386	HIonly	11 17 50.6 +13 59 06	871	27	0.32	10.0	6.86
215389	HIonly	11 18 28.2 +14 18 13	917	28	0.39	10.0	6.95
215392	HIonly	11 18 33.1 +14 32 02	909	17	0.27	10.0	6.79
215393[d]	Plume	11 18 52.4 +13 24 33	862	40	1.80	10.0	7.59
215397	HIonly	11 18 54.4 +14 13 07	909	22	0.29	10.0	6.73
215396[c]	SClump	11 18 53.6 +12 53 50	581	25	0.39	10.0	6.97
6328	N3623	11 18 55.7 +13 05 32	803	493	10.42	10.0	8.37
215398[c]	SClump	11 19 05.2 +12 45 28	753	41	2.37	10.0	7.77
215400[c]	SClump	11 19 08.0 +12 39 16	753	26	1.66	10.0	7.62
215401[d]	Plume	11 19 11.8 +13 35 43	834	49	1.06	10.0	7.35
215286		11 19 12.7 +14 19 40	998	28	0.54	10.0	7.12
215354		11 19 15.9 +14 17 25	728 (opt)	...	...	10.0	...
215402[d]	Plume	11 19 25.7 +13 14 12	772	82	1.02	10.0	7.39
215403[c]	SClump	11 19 30.1 +12 33 57	716	98	1.20	10.0	7.43
215405[c]	SClump	11 19 33.0 +12 31 00	695	76	1.19	10.0	7.50
215406[d]	Plume	11 19 33.5 +13 51 44	984	74	1.52	10.0	7.53
215407[c]	SClump	11 19 37.4 +12 23 44	655	26	0.66	10.0	7.20
215409[c]	SClump	11 19 54.0 +12 52 40	678	47	0.68	10.0	7.17
215410[d]	Plume	11 19 58.6 +13 17 33	785	40	2.83	10.0	7.82
6346	N3627	11 20 15.0 +12 59 21	720	359	36.44	10.0*	8.92
6350	N3628	11 20 16.9 +13 35 13	844	459	197.24	10.0	9.66
215411[c]	SClump	11 20 26.8 +12 52 13	646	67	2.32	10.0	7.43
215412[d]	Plume	11 21 47.4 +13 37 17	908	23	8.29	10.0	8.29
215413[d]	Plume	11 22 23.1 +13 38 55	905	18	12.18	10.0	8.46
211370	I2767	11 22 23.2 +13 04 40	1083	92	1.75	10.0	7.62
213436		11 22 24.0 +12 58 46	626 (opt)	...	...	10.0	...
6395	I2782	11 22 55.5 +13 26 26	999 (opt)	...	...	10.0	...
215414[d,e]	Plume	11 23 11.1 +13 42 30	878	27	14.09	10.0	8.52
6401[f]		11 23 19.1 +13 37 45	883	49	0.94	10.0	7.35
213440	I2791	11 23 37.6 +12 53 45	666	22	0.25	10.0	6.67
215415	HIonly	11 24 33.9 +12 40 48	1004	19	0.39	10.0	6.96

[a]Positions indicate the centroid of the optical counterpart unless the object is noted as a plume, southern clump, or HI-only detection, in which case the position represents the centroid of the HI.

[b]Objects are assigned a group distance except when a * indicates a known primary distance.

[c]Components of the HI cloud just south of N3627 are attributed to N3627 for HIMF determination.

[d]Components of the HI plume in the Leo Triplet are attributed to N3628 for HIMF determination.

[e]possible association with very low surface brightness galaxy at 112313.5+134254 (AGC 219303) found in POSS-II and SDSS

[f]HI parameters come from previously catalogued single-pixel Arecibo observations. See the HI archive for details.

Table 3.4. Probable Leo I members

AGC #	Other Name	Opt Position (J2000)	HI $cz_{\odot}$ km s^{-1}	W50 km s^{-1}	F_c Jy km s^{-1}	Dist[a] Mpc	$\log M_{HI}$ $M_{\odot}$
202171		10 01 09.5 +08 46 56	1167 (opt)	...	...	19.0	...
5453	093-047	10 07 07.2 +15 59 01	839	53	1.99	13.0	7.88
203913	037-033	10 25 46.4 +05 39 13	1155	99	2.77	18.8	8.35
208394		10 28 43.8 +04 44 04	1181	27	0.54	19.2	7.72
202218		10 28 55.8 +09 51 47	1190	39	0.59	19.6	7.73
5708	037-061	10 31 13.2 +04 28 19	1176	169	30.24	19.1	9.41
204139		10 32 01.3 +04 20 46	1147	68	0.45	18.6	7.54
202222		10 34 21.1 +08 11 56	854 (opt)	...	...	12.4	...
208399		10 40 10.7 +04 54 32	747	23	1.00	9.9	7.34
205078		10 41 26.1 +07 02 16	1175	32	0.42	19.4	7.58
5923	038-022	10 49 07.5 +06 55 01	709	142	3.11	9.0	7.76
5962	N3423	10 51 14.4 +05 50 22	1008	156	32.83	11.7*	9.02
5974	038-032	10 51 35.1 +04 34 57	1038	155	16.57	25.1*	9.39
200688	038-054	10 56 09.1 +06 10 22	1014	128	0.69	16.8	7.67
213066		11 12 23.2 +13 42 49	630 (opt)	...	...	7.6	...
211261	I678	11 14 06.3 +06 34 37	968 (opt)	...	...	13.3	...
215282		11 14 25.2 +15 32 02	867	27	0.29	11.3	6.91
6277	N3596	11 15 06.2 +14 47 12	1193	118	29.22	20.7	9.47
215281		11 15 16.2 +14 41 55	1092 (opt)	...	...	19.0	...
215284		11 15 32.4 +14 34 38	1133	23	0.40	19.7	7.54
212132	039-094	11 16 26.3 +04 20 11	1104	155	2.15	18.6	8.24
213006		11 18 03.9 +10 14 40	957 (opt)	...	...	12.7	...
202257		11 19 14.4 +11 57 07	861	51	2.97	10.7	7.90
213074		11 19 28.1 +09 35 44	990	51	1.95	13.7	7.93
215142		11 24 44.5 +15 16 32	1125	123	2.27	20.0	8.29
6438	I692	11 25 53.5 +09 59 13	1156	50	3.46	20.5	8.53
215296		11 26 55.2 +14 50 03	913	44	0.57	11.5	7.23
210340	I2828	11 27 11.0 +08 43 53	1046	45	2.67	17.9	8.30
213091		11 29 34.6 +10 48 36	743 (opt)	...	...	8.6	...
212837	KKH68	11 30 52.9 +14 08 44	880	22	1.79	10.7	7.68
215303		11 31 08.8 +13 34 14	1021	32	0.54	15.0	7.43
215304		11 32 01.9 +14 36 39	1124	115	1.46	20.3	8.13
215306		11 33 50.1 +14 49 28	1129	64	0.45	20.4	7.54
215248		11 33 50.9 +14 03 15	928	19	0.21	11.3	6.88
210459	I2934	11 34 19.3 +13 19 18	1195	61	4.19	21.4	8.65
212838	KKH69	11 34 53.4 +11 01 10	881	22	1.47	10.4	7.57

[a]Objects are assigned flow model distances except when a * indicates a known secondary distance.

Table 3.5. Primary Distances in Leo I

AGC #	Other Name	Opt Position (J2000)	$v_\odot$ km s^{-1}	Dist (ϵ_{dist}) Mpc	Method	Reference
5850	N3351	10 43 57.6 +11 42 12	778	10.00 (0.92)	ceph	Freedman et al. 2001
5882	N3368	10 46 45.7 +11 49 11	897	10.47 (0.96)	ceph	Freedman et al. 2001
5889	N3377A	10 47 22.3 +14 04 13	573	9.30 (1.93)	stars	Makarova and Karachentsev 1998
5899	N3377	10 47 42.3 +13 59 08	665	11.22 (0.47)	sbf	Tonry et al. 2001
5902	N3379	10 47 49.6 +12 34 55	911	10.57 (0.54)	sbf	Tonry et al. 2001
5911	N3384	10 48 16.8 +12 37 42	704	11.36 (0.75)	sbf	Tonry et al. 2001
5944	064-033	10 50 18.9 +13 16 18	1073	11.10 (0.90)	sbf	Rekola et al. 2005
5952	N3412	10 50 53.2 +13 24 42	841	11.32 (0.73)	sbf	Tonry et al. 2001
6082	N3489	11 00 18.6 +13 54 04	677	12.08 (0.83)	sbf	Tonry et al. 2001
6346	N3627	11 20 15.0 +12 59 21	727	10.05 (0.69)	ceph	Freedman et al. 2001

distances over secondary distance measurements, the Tully-Fisher distances are used as a check on the adopted group distances.

3.1.3 Group Membership in the Leo Cloud

The extent and substructure of the slightly more distant Leo Cloud are less clearly defined than those of Leo I. In their catalog of Tully-Fisher distances, Tully et al. [2008] consider potential Leo Cloud members spanning over 50 degrees of right ascension and 45 degrees of declination. Due to the limited declination range of the current ALFALFA catalog and the loose association of the galaxies in the expansive Leo Cloud, our search does not cover the entire structure. In fact, 57 of the 72 objects ($\sim 80\%$) marked as Leo Cloud members in Tully et al. [2008] are outside of the current ALFALFA catalog declination range.

Potential members of the Leo Cloud within the ALFALFA survey limits are found by their velocity. The group velocity dispersion as a function of chosen velocity cut-off begins to rise more steeply after a cz of 2000 km s^{-1}, so any

Table 3.6. Secondary Distances* in Leo I & II

AGC #	Other Name	Opt Position (J2000)	$v_{\odot}$ km s^{-1}	Dist (ϵ_{dist}) Mpc
5271	N3020	09 50 06.6 +12 48 49	1440	21.88 (4.03)
5303	N3041	09 53 07.2 +16 40 40	1408	23.77 (4.38)
5325	N3049	09 54 49.7 +09 16 18	1455	15.28 ($\sim$3.5)
5914	N3389	10 48 28.0 +12 31 59	1308	21.38 (3.55)
6167	N3526	11 06 56.8 +07 10 27	1420	19.77 (3.64)
6209	N3547	11 09 55.9 +10 43 13	1579	18.11 (3.34)
6328	N3623	11 18 55.7 +13 05 32	807	11.97 (1.93)
6387	IC2763	11 22 18.4 +13 03 54	1569	16.60 ($\sim$3.8)
6420	N3666	11 24 26.1 +11 20 32	1060	16.29 (2.63)
6498	N3705	11 30 07.4 +09 16 36	1018	17.22 (2.78)
6594	U6594	11 37 38.3 +16 33 18	1038	21.28 (3.92)
6644	N3810	11 40 58.8 +11 28 17	993	15.35 (2.54)

*All secondary distances are calculated from the distance moduli reported in Tully et al. 2008 from the Tully-Fisher method.

object listed in the AGC within $9^h36^m < \alpha < 11^h36^m$ and $+04^\circ < \delta < +16^\circ$ and having 1200 km s^{-1} $< cz <$ 2000 km s^{-1} is considered a potential Leo Cloud member. The HI parameters for these 103 objects are summarized in Table 3.7 where HI parameters come from the ALFALFA catalog unless otherwise noted.

Although these potential Leo Cloud members are likely to be associated within large scale structure, sources over such a large expanse of sky cannot all be confidently placed at the same group distance. Instead we focus on the substructure within the Leo Cloud directly behind Leo I on the sky which we define as the Leo II group. Choosing an approximate group center located along the line of sight midway between the M96 and M66 groups, the number of additional Leo II members plateaus for group radii larger than 1.1 Mpc. 41 sources are found to be potential Leo II members within a group radius of 1.1 Mpc. The Leo II group includes the NGC 3389 system (see section 2.4).

No primary distances are known for Leo II, so we use as a reference the nine

primary distance estimates placing members of the M96 group firmly at 11.1 Mpc. We adopt a distance of $D = 11.1$ Mpc $\times(\bar{v}_{II}/\bar{v}_{M96}) = 17.5$ Mpc, where $\bar{v}_{II}$ and $\bar{v}_{M96}$ are the mean velocities of suspected Leo II and M96 group members respectively. This value agrees well with the eight potential Leo II members for which Tully et al. [2008] measured Tully-Fisher distances (see Table 3.6). Distances to all other Leo Cloud sources are estimated via the flow model unless a secondary distance is known.

3.1.4 Velocity Dispersion for Leo I

Previous optical and redshift surveys of Leo I have been plagued by interloping background galaxies which have led to large estimates for the group's velocity dispersion. Using grouping algorithms to search for overdensities in the CfA Redshift Survey, Geller and Huchra [1983] found the M96 group (their Group #68) and the M66 group (their Group #78) to have 23 and 9 members respectively. If all of their redshift measurements are weighted equally, they determine a velocity dispersion of 258 km s^{-1} for the Leo I group as a whole. However, when compared to the brightest members of each group (M96 and M66), the velocity distribution of group members is skewed towards higher velocities. Six of the 23 M96 members have recessional velocities less than M96 while only one of the 11 M66 members has a velocity below that of M66. In an examination of optical plates from the Las Campanas Observatory, Ferguson and Sandage [1990] selected 52 members for the M96 group based primarily on morphology as they have redshifts for only 11 of their assigned M96 members. When equally weighted, the 11 Leo group redshifts result in a velocity dispersion of 256 km s^{-1} which is similar to that of Geller and Huchra [1983] and thus potentially too

high an estimate as well.

By limiting the M96 and M66 groups in right ascension and declination, as well as paying close attention to sudden leaps in the groups' velocity dispersions with additional members, we minimize the problem of background contamination. A look at the 39 M96 members and 19 M66 members (not including any Ring, Clump or Plume detections) we find that roughly half of the member galaxies have velocities less than those of the brightest members (M96 and M66). From the group memberships given in Tables 3.2 and 3.3, and using ALFALFA-derived heliocentric velocities, we calculate a velocity dispersion for Leo I of 172 km s^{-1} which excludes the sources whose membership status in Leo I is unclear (see Table 3.4). Including these additional 36 sources, however, only raises the velocity dispersion to 181 km s^{-1}. If our cutoff velocity for group membership ($v_{cut} = 1200$ km s^{-1}) is applied to the groups defined in Geller and Huchra [1983] and in Ferguson and Sandage [1990], their velocity dispersions are reduced to 136 km s^{-1} and 98 km s^{-1} respectively.

The distribution of Leo I and Leo Cloud members in right ascension and declination is shown in Figure 3.1. Filled dark and light gray circles represent members of the M66 and M96 groups respectively. Open circles denote the probable Leo I members found in Table 3.4. M96 and M66 themselves are marked with large crosses, and Leo II members are plotted as small, open triangles. The large circles indicate the group radii of 0.3 Mpc and 0.8 Mpc determined for the M66 and M96 subgroups respectively.

Table 3.7. Probable Leo Cloud Members

AGC #	Other[a] Name	Opt Position (J2000)	HI $cz_{\odot}$ km s^{-1}	W50 km s^{-1}	F_c Jy km s^{-1}	Dist[b] Mpc	log M_{HI} $M_{\odot}$
198335		09 37 04.4 +09 57 59	1517	53	0.37	24.2	7.66
192830		09 39 22.3 +04 57 08	1886	167	3.22	29.5	8.82
192937		09 40 21.1 +04 44 06	1983	44	0.29	30.9	7.75
192833		09 40 56.3 +05 02 41	1871	49	1.21	29.3	8.40
193813		09 42 50.9 +04 53 24	1939	87	0.63	30.3	8.06
198337		09 42 51.2 +09 38 00	1461	34	0.62	23.4	7.90
192835		09 43 02.2 +05 01 45	1963	95	1.32	30.6	8.44
191849		09 44 37.1 +10 00 46	1483	62	1.94	23.7	8.40
191869		09 44 58.9 +08 22 12	1733	163	4.22	27.3	8.86
198456		09 46 42.4 +07 08 07	1886	57	0.62	29.5	8.10
193921		09 49 14.9 +15 48 27	1449	39	0.61	23.3	7.80
5271	N3020	09 50 06.7 +12 48 46	1438	217	31.65	21.9*	9.55
5275	N3024	09 50 27.2 +12 45 55	1418	246	26.82	22.8	9.51
192239		09 50 36.3 +12 48 33	1335 (opt)	...	...	21.6	...
192423		09 54 30.5 +09 52 12	1488	40	0.45	23.8	7.77
192959		09 54 35.7 +04 23 08	1774	77	0.98	27.8	8.22
5325	N3049	09 54 49.7 +09 16 16	1497	203	11.55	15.3*	8.80
5328	N3055	09 55 18.0 +04 16 12	1821	266	11.26	28.5	9.33
190600	063-105	09 55 29.3 +08 23 27	1281	101	2.83	20.7	8.45
192766		09 57 21.1 +06 25 03	1665 (opt)	...	...	26.3	...
192960		09 55 37.8 +04 28 36	1942	61	0.77	30.3	8.15
205283	HIonly	10 01 30.9 +13 21 35	1954	69	0.54	30.6	7.99
204045		10 02 00.0 +04 47 27	1693 (opt)	...	...	26.7	...
200879	036-027	10 04 08.7 +06 30 38	1263	42	0.62	20.4	7.86
202297		10 06 03.8 +10 38 16	1565	258	1.88	25.0	8.43
205108		10 06 40.3 +12 19 00	1487	26	0.55	23.9	7.89
203862		10 07 04.5 +05 00 25	1739	34	0.90	27.4	8.16
203863		10 07 24.1 +05 19 31	1603 (opt)	...	...	25.4	...
205076	FGC120A	10 09 17.4 +05 24 15	1701	83	1.02	26.8	8.21
203432		10 10 20.6 +07 45 13	1268 (opt)	...	...	20.6	...
5504	036-059	10 12 49.0 +07 06 11	1545	147	3.91	24.7	8.74
5522	036-065	10 13 59.0 +07 01 24	1218	211	34.25	19.8	9.50
201993	KKH 60	10 15 59.4 +06 48 16	1620	94	1.53	25.8	8.37
202131		10 17 09.2 +04 20 43	1308 (opt)	...	...	21.1	...
5551		10 17 11.8 +04 19 50	1344	56	4.49	21.7	8.69
208392		10 18 03.7 +04 18 35	1322	34	0.53	21.3	7.75
5633	094-035	10 24 40.0 +14 45 23	1382	167	15.63	22.6	9.27
5646	094-048	10 25 53.0 +14 21 48	1368	221	9.49	22.4	9.05
208295		10 28 27.2 +08 10 26	1491	91	1.06	24.1	8.14
204135		10 31 37.3 +04 34 22	1202 (opt)	...	...	19.6	...
202244		10 31 40.8 +13 50 04	1288	102	1.89	21.3	8.30
202016[c]		10 33 19.2 +10 11 22	1433	32	0.57	23.3	7.82
205161		10 34 05.6 +15 46 50	1218	114	1.03	20.3	8.00
5741	I622	10 34 42.8 +11 11 48	1389	347	3.76	22.8	8.63
202262	FGC125a	10 37 28.7 +12 23 46	1330	59	1.81	22.0	8.31
203080		10 41 41.0 +13 49 30	1271 (opt)	...	...	17.5**	...

Table 3.7 (continued)

AGC #	Other[a] Name	Opt Position (J2000)	HI $cz_\odot$ km s^{-1}	W50 km s^{-1}	F_c Jy km s^{-1}	Dist[b] Mpc	log M_{HI} $M_\odot$
5826	N3338	10 42 07.6 +13 44 48	1298	339	91.69	17.5**	9.82
203082		10 42 26.5 +13 57 26	1277	41	0.52	17.5**	7.58
5832	065-089	10 42 48.6 +13 27 35	1217	102	5.47	17.5**	8.59
200543	065-090	10 43 05.5 +13 30 42	1256	70	2.98	17.5**	8.29
5842	N3346	10 43 38.9 +14 52 16	1258	162	15.20	17.5**	9.03
200552[d]		10 43 57.0 +13 23 14	1210	99	1.51	17.5**	8.04
205270		10 45 09.8 +15 26 59	1230	51	0.42	17.5**	7.43
5914	N3389	10 48 28.6 +12 31 57	1301	266	21.89	21.4*	9.37
200598	066-025	10 48 56.8 +12 11 40	1321	125	4.21	17.5**	8.47
200600	066-024	10 48 59.7 +10 50 07	1939	120	1.33	17.5**	7.97
205309	HIonly	10 49 07.6 +12 22 34	1342	33	1.40	17.5**	8.01
205310	HIonly	10 49 11.5 +12 29 39	1379	50	3.41	17.5**	8.39
200603	066-029	10 49 17.1 +12 25 20	1376	68	3.75	17.5**	8.43
202253		10 49 26.7 +12 15 28	1319 (opt)	...	...	17.5**	...
205197		10 49 42.8 +13 49 41	1332	42	0.38	17.5**	7.38
205198		10 50 01.8 +13 47 05	1322	53	0.62	17.5**	7.71
202260	F640V02	10 57 38.2 +13 58 42	1238	92	2.72	17.5**	8.29
6077	N3485	11 00 02.4 +14 50 28	1432	135	21.66	17.5**	9.19
202040[c]	LeG35	11 03 02.0 +08 02 53	1359	96	1.74	17.5**	8.10
219117		11 03 46.7 +08 34 19	1738	68	0.65	17.5**	7.66
213757		11 05 59.6 +07 22 25	1640	57	0.58	17.5**	7.57
6158	N3524	11 06 32.1 +11 23 06	1321 (opt)	...	...	17.5**	...
215262		11 06 35.3 +12 13 48	1606	63	0.55	17.5**	7.56
6167	N3526	11 06 56.8 +07 10 26	1416	196	8.96	19.8*	8.92
6169	066-115	11 07 03.4 +12 03 34	1551	241	9.80	17.5**	8.84
210082	067-014	11 09 23.2 +10 50 03	1555	66	2.46	17.5**	8.26
6209	N3547	11 09 55.9 +10 43 12	1584	204	7.42	18.1*	8.74
210111	067-022	11 10 25.1 +10 07 34	1320	60	2.72	17.5**	8.29
213064		11 10 54.5 +09 37 19	1604	124	3.26	17.5**	8.36
6233	039-056	11 11 28.3 +06 54 26	1605	212	1.82	26.0	8.45
6245	I676	11 12 39.8 +09 03 21	1421	177	1.29	17.5**	7.94
6248		11 12 51.7 +10 12 00	1286	26	2.29	17.5**	8.21
213796		11 12 52.7 +07 55 19	1412	78	0.55	17.5**	7.57
212097	039-068	11 13 00.1 +07 51 43	1396	118	2.01	17.5**	8.16
215280		11 13 16.3 +15 24 28	1479	93	0.84	17.5**	7.78
215240		11 13 50.8 +09 57 39	1610	34	0.45	17.5**	7.49
219197		11 13 55.2 +04 06 19	1609	63	0.88	25.9	8.14
215186		11 17 01.2 +04 39 44	1455	66	0.27	24.0	7.58
215241		11 17 02.7 +10 08 36	1765	120	1.80	17.5**	8.11
6306		11 17 27.4 +04 36 16	1746	108	4.84	27.8	8.94
6305	N3611	11 17 30.0 +04 33 19	1612	375	14.06	26.0	9.29
215287		11 19 45.1 +15 30 08	1334	103	0.73	17.5**	7.72
214314		11 22 11.1 +04 39 42	1305 (opt)	...	...	22.1	...
6387	I2763	11 22 18.1 +13 03 53	1572	132	2.90	16.6*	8.27
213511		11 22 23.4 +11 47 38	1571	61	0.40	17.5**	7.44
219201		11 22 31.4 +05 31 29	1575	24	0.35	25.7	7.72

Table 3.7 (continued)

AGC #	Other[a] Name	Opt Position (J2000)	HI $cz_{\odot}$ km s^{-1}	W50 km s^{-1}	F_c Jy km s^{-1}	Dist[b] Mpc	log M_{HI} $M_{\odot}$
213512	I2781	11 22 50.7 +12 20 41	1544	72	1.16	17.5**	7.95
215290		11 22 59.1 +12 27 38	1613	42	0.97	17.5**	7.85
6420		11 24 26.2 +11 20 30	1059	255	39.28	16.3*	9.39
214317		11 25 05.4 +04 07 16	1619	130	2.36	26.2	8.59
214318		11 25 40.0 +04 40 36	1527	123	0.46	25.1	7.65
219119		11 26 03.4 +08 04 32	1567	35	0.44	25.8	7.79
214319		11 26 08.3 +04 03 45	1525	49	0.81	25.0	8.09
219202		11 27 10.9 +05 08 56	1518	70	0.69	25.0	7.93
219203		11 27 28.9 +05 37 02	1512	28	0.32	25.0	7.66
6474	N3692	11 28 24.0 +09 24 26	1716	408	10.55	27.8	9.28
213939		11 28 24.3 +06 07 04	1571	45	1.02	15.8	8.20
6498	N3705	11 30 07.6 +09 16 36	1019	345	41.38	17.2*	9.46
213169		11 35 18.4 +04 57 17	1417	37	0.90	23.9	8.08

[a]Positions indicate the centroid of the optical counterpart unless the object is noted as an HI-only detection, in which case the position represents the centroid of the HI.

[b]Objects are given flow model distances except when a secondary distance is known (marked by *) or a group distance was assigned (marked by **).

[c]HI parameters come from single pixel results (see Section 3.2)

[d]HI parameters come from previously catalogued single-pixel Arecibo observations. See the HI archive for details.

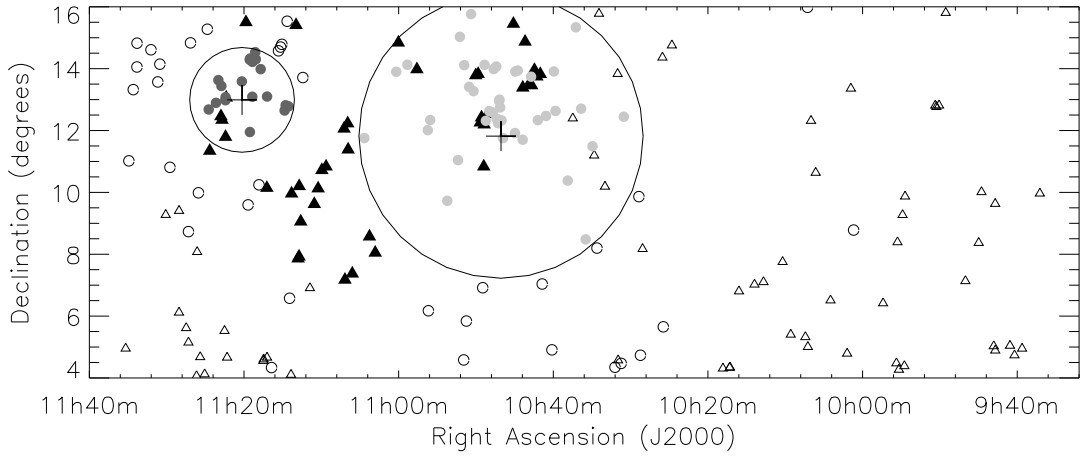

Figure 3.1 Group membership in the Leo region. Filled symbols represent probable group members: dark gray circles for the M66 group (which includes the Leo Triplet), light gray circles for the M96 group (which includes the Leo Ring), and triangles for Leo II. Open symbols represent objects with less clearly defined group memberships: open circles are likely Leo I members and open triangles are probably part of the Leo Cloud. M96 and M66 are marked as large crosses for reference. Large circles surround the M96 and M66 groups at radii of 0.8 Mpc and 0.3 Mpc respectively.

3.2 Comparison with the KK04 Optically-Selected Catalog

To place the ALFALFA catalog in the context of optical surveys, we have compared the catalog of galaxies derived from the ALFALFA observations with that based on the optical identification of galaxies in the Leo region presented in the Catalog of Neighboring Galaxies (Karachentsev et al. [2004]; hereafter KK04). To allow us to compare better the nature of HI selection in Leo, we have also obtained higher sensitivity, single-pixel HI observations of each of the optically-selected potential Leo members. Thirty-five dwarf galaxies optically identified by KK04 as potential M96 group members were observed with the L-band (L-

band wide: LBW) receiver and multi-bit autocorrelation spectrometer. KK04 selected the objects based on visual scrutiny of POS-II/ESO plates; the pointed observations made with the LBW receiver supplied additional redshift information, and, in some cases, confirmation of Leo I group status. The dwarfs range in B-band magnitude from 19.2 to 17.0 and are found in the 160 deg^2 bounded by $10^h30^m < \alpha < 11^h05^m$ and $+08^\circ < \delta < +16^\circ$. This entire region has been included in the ALFALFA survey, and so a direct comparison of optical- and HI-selected galaxies can be made.

Due to instrumental errors, three spectrometer configurations were used resulting in different spectral resolutions. The sources AGCs 202016, 202027, 202035, 200512, 201963, 202028, 201991, 202030, 202032, 202018, 202022, 201990, 202031, and 202038 were observed with a spectral resolution of 12.2 kHz (roughly 2.7 km s^{-1} and 4.5 km s^{-1} at a redshift of 0 before and after Hanning smoothing). The remaining 21 sources were observed with a spectral resolution of 24.4 kHz (roughly 5.3 km s^{-1} and 8.8 km s^{-1} at cz of 0 before and after Hanning smoothing).

All 35 targets were initially observed in total power position-switched mode for 120 seconds on source followed by 120 seconds off source, and nine were immediately detected. The remaining 26 targets were observed for longer periods, with final total integration times ranging from 240 seconds to 1440 seconds on source. Nine additional sources were detected with these longer integration times. All spectra were Hanning smoothed, bandpass calibrated, and when available, both polarizations were averaged. For the sources that were detected, the HI spectra were fit with polynomials, and the central velocity, $cz_\odot$, the full width at half the signal's maximum height W_{50}, and the total integrated flux

under the profile S_{tot} were measured. The rms noise level was calculated for all nondetections to allow the estimation of upper limits to their HI mass and HI mass-to-light ratios.

The results of the targeted single-pixel observations are presented in Table 3.8. The first column gives the galaxy's designation in the AGC, while the second column gives the galaxy's designation in KK04. The third and fourth columns show the optical position of the object in J2000 coordinates and the object's B-band magnitude as quoted in KK04. Columns five through nine give the HI parameters measured for each object by the single-pixel observations: the velocity in km s^{-1} (with error), the velocity width in km s^{-1}, the integrated line flux in Jy km s^{-1}, the rms in mJy, and the signal-to-noise for the detection. For the objects also detected in ALFALFA, the total flux detected by the survey is indicated for comparison. To verify that the data reduction techniques employed for the survey and for the single pixel observations produce consistent results, the velocites, line widths, and integrated fluxes derived from the separate observations are compared in Figure 3.2. The methods are in clear agreement, and only the measured widths have large enough error bars to be visible compared to the size of the plot symbols. A mosaic of the spectra obtained for all 18 detected galaxies is found in Figure 3.3.

The last three columns in Table 3.8 give the derived HI parameters. Suspected members of the M96 group - those objects with 600 km s^{-1} $< v_{helio} <$ 1200 km s^{-1} - were placed at 11.1 Mpc. All other distances were determined using the peculiar velocity model as described for Table A.1. HI masses were calculated using these adopted distances for the targeted detections. For the mass-to-light ratios, luminosities were estimated using apparent B-band magnitudes from KK04 and galactic extinction corrections from DIRBE maps [Schlegel et al.,

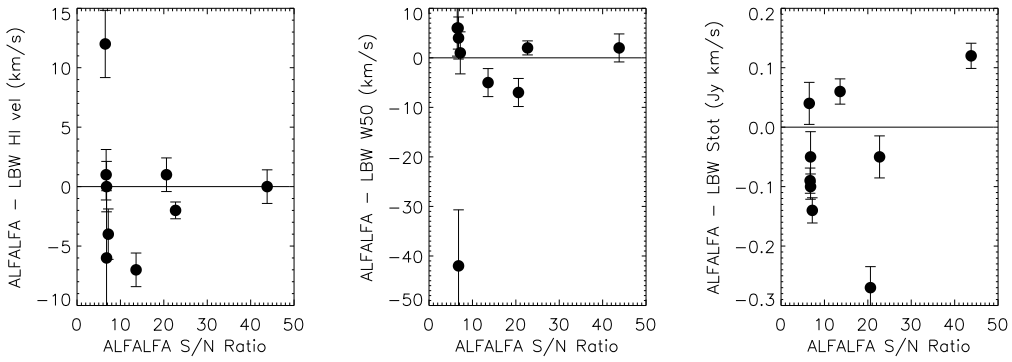

Figure 3.2 Comparison of results for sources detected both with the ALFALFA survey and with single pixel LBW observations. The heliocentric velocities, velocity widths, and the fluxes agree well for the different observations. Only the widths have errors large enough to be visible when compared to the size of the plot symbols.

1998]. For those objects not found in HI, upper limits are calculated for their HI masses and M_{HI}/L_B by placing the objects at 11.1 Mpc and by assuming a peak flux of three times the rms level of each spectrum and a signal width of 50 km s^{-1}. If these galaxies are instead at the adopted Leo II distance of 17.5, the HI mass upper limit should be multiplied by a factor of 2.5.

Table 3.8. Results of Single Pixel, Targeted HI Observations

AGC #	Other Name	Opt Position (J2000)	m_B	HI $cz_\odot$ (ϵ_{cz}) km s^{-1}	$W50$ km s^{-1}	F_c [$F_{c,ALF}$] Jy km s^{-1}	rms mJy	S/N	Dist Mpc	$\log M_{HI}$ $M_\odot$	$\log M_{HI}/L_B$ $M_\odot/L_\odot$
202015	LeG01	10 31 53.8 +12 55 34	18.7	2815 (2)	42	0.36 [0.42]	1.7	10.1	43.1	8.20	2.16
202016	LeG02	10 33 19.2 +10 11 20	19.1	1433 (1)	28	0.57 [0.59]	2.0	17.3	17.5	7.61	2.52
202017	LeG03	10 35 48.9 +08 28 49	17.8	1160 (2)	68	1.97 [1.93]	1.7	45.1	11.1	7.76	2.55
202018	LeG04	10 39 40.2 +12 44 05	18.7	-	-	-	1.9	-	-	< 6.92	< 2.07
202019	FS 01	10 39 43.3 +12 38 03	16.77	780 (3)	22	0.08	0.8	6.6	11.1	6.37	0.75
200512	P031727	10 39 55.6 +13 54 34	18.3	1011 (2)	20	0.42 [0.30]	2.4	13.2	11.1	7.09	2.07
202020	LeG09	10 42 34.6 +12 09 01	18.5	-	-	-	2.5	-	-	< 7.04	< 2.11
202021	LeG10	10 43 55.4 +12 08 06	19.2	-	-	-	1.7	-	-	< 6.86	< 2.21
202022	LeG11	10 44 02.1 +15 35 19	18.8	-	-	-	1.8	-	-	< 6.90	< 2.08
202023	LeG12	10 44 07.3 +11 31 58	19.1	-	-	-	2.0	-	-	< 6.94	< 2.24
202024	FS 09	10 44 57.3 +11 55 01	17.43	870 (2)	18	0.31 [0.23]	2.5	9.2	11.1	6.95	1.60
202025	FS 13	10 46 14.4 +12 57 35	18.7	-	-	-	0.9	-	-	< 6.58	< 1.73
201990	FS 14	10 46 24.7 +14 01 26	18.3	-	-	-	1.6	-	-	< 6.84	< 1.82
202026[a]	FS 15	10 46 30.0 +11 45 20	19.0	954 (7)	126	3.24	1.8	49.3	11.1	7.97	3.24
202027[b]	FS 17	10 46 41.3 +12 19 37	16.98	1030 (2)	37	1.24	2.1	30.9	11.1	7.56	2.03
201970[c]	LeG18	10 46 52.2 +12 44 39	18.9	643 (2)	43	0.49 [0.61]	2.1	11.1	11.1	7.15	2.39
201971	FS 20	10 46 54.8 +12 47 16	18.2	-	-	-	1.7	-	-	< 6.86	< 1.81
201975[a]	LeG21	10 47 00.8 +12 57 34	18.6	843 (1)	23	0.48	2.3	14.0	11.1	7.14	2.25
201959	FS 23	10 47 27.5 +13 53 22	17.79	3009 (3)	61	0.32 [0.26]	1.8	7.2	45.7	8.21	1.76
200592[d]	P032327	10 48 43.3 +12 18 55	17.51	876 (4)	44	0.26	1.1	11.9	11.1	6.88	1.56
202028	FS 40	10 49 37.0 +11 21 04	18.0	-	-	-	2.0	-	-	< 6.95	< 1.81

Table 3.8 (continued)

AGC #	Other Name	Opt Position (J2000)	m_B	HI $cz_\odot$ (ϵ_{cz}) km s^{-1}	$W50$ km s^{-1}	F_c [$F_{c,ALF}$] Jy km s^{-1}	rms mJy	S/N	Dist Mpc	$\log M_{HI}$ $M_\odot$	$\log M_{HI}/L_B$ $M_\odot/L_\odot$
201963[e]	P1424345	10 49 52.2 +13 09 42	20.0	766 (2)	19	1.12 [1.43]	2.1	38.3	11.1	7.51	3.17
202029	LeG23	10 50 09.1 +13 29 00	19.1	-	-	-	1.7	-	-	< 6.86	< 2.16
201991	KK 96	10 50 27.0 +12 21 39	18.3	-	-	-	1.8	-	-	< 6.89	< 1.88
202030[f]	LeG26	10 51 21.1 +12 50 57	17.2	-	-	-	1.7	-	-	< 6.86	< 1.41
202031	LeG27	10 52 20.1 +14 42 25	18.6	-	-	-	1.7	-	-	< 6.86	< 1.98
202032	LeG28	10 53 00.7 +10 22 44	18.3	-	-	-	1.6	-	-	< 6.85	< 1.84
202033	D640-16	10 55 03.6 +14 05 35	18.6	2094 (2)	40	0.22	1.0	10.9	32.5	7.74	1.93
202034	D640-12	10 55 55.3 +12 20 22	18.4	847 (2)	22	0.10	0.8	8.6	11.1	6.46	1.51
202035[g]	D640-13	10 56 13.9 +12 00 37	17.66	989 (2)	28	1.55 [1.69]	2.0	44.7	11.1	7.65	2.40
202036	D640-14	10 58 10.5 +11 59 56	18.5	-	-	-	0.9	-	-	< 6.58	< 1.67
202037	LeG32	10 59 17.4 +15 05 07	18.7	2105 (2)	42	0.67	1.7	19.0	32.9	8.23	2.44
202038	LeG33	11 00 45.2 +14 10 19	18.6	-	-	-	1.7	-	-	< 6.87	< 1.99
202039[h]	D640-08	11 00 51.9 +13 52 51	17.0	-	-	-	0.8	-	-	< 6.52	< 1.01
202040	LeG35	11 03 02.1 +08 02 53	18.1	1358 (1)	103	2.01 [1.77]	2.4	25.5	17.5	8.16	2.65

[a]possible Ring detections; see Figure 2.4

[b]SDSS gives cz=1013 km/s which matches HI cz

[c]NED gives cz=617 km/s which matches HI cz

[d]Ring detection, SDSS gives cz=16,775 km/s for optical galaxy

[e]Ring detection, also in ADBS at 754 km/s, SDSS gives cz=53,213.1 km/s for optical galaxy

[f]SDSS gives cz=1019.29 km/s

[g]SDSS gives cz=629.56 km/s with very low s/n

[h]SDSS gives cz=1588.90 km/s

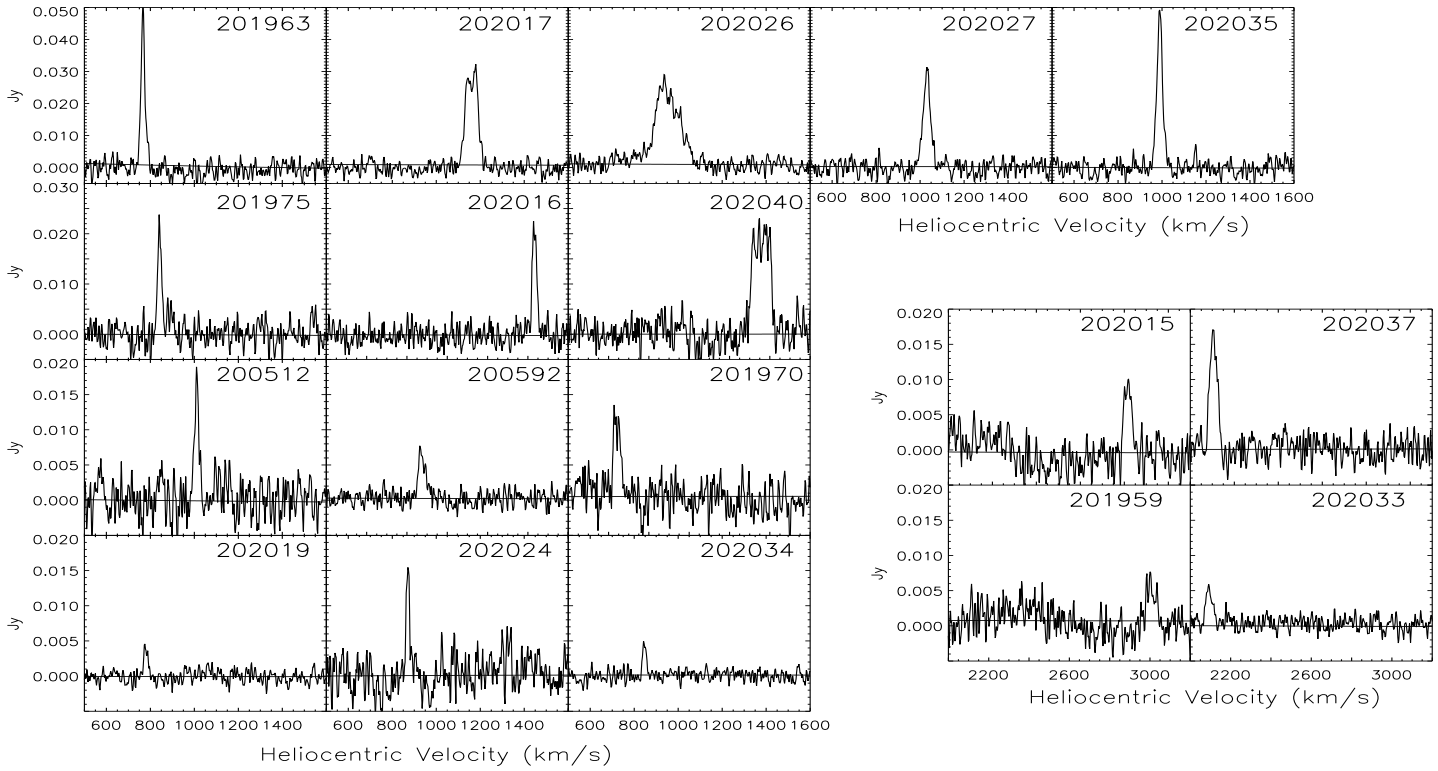

Figure 3.3 Objects successfully detected with the single-pixel L-Band Wide receiver that were originally noted as potential Leo I group members in an optical survey of the region. The values in Table 3.8 were extracted from these 18 spectra. The y-scales are different for each row. Four of the six background galaxies are plotted separately and over a different velocity range.

In the spectroscopic followup, six of the detected objects were found to be background galaxies and the remaining 12 are considered M96 group members. Of these 12, six detections coincide with the Leo Ring as discussed in Section 2.4. Objects not confirmed in the targeted, single-pixel observations either 1) are not actually Leo Group members, 2) lack any HI gas, or 3) contain too little gas to be detected even after several minutes of integration. While the number of objects not detected in ALFALFA but found in the optical survey and vice versa are comparable, all the ALFALFA sources missed by the optical survey were dwarfs. Only a few of the optical galaxies missed by ALFALFA were dwarf-like, and most were L* galaxies ($m_B \sim 10 - 12$) lacking gas including the ellipticals NGC 3377 and NGC 3379 and the lenticulars NGC 3384 and NGC 3412. The HI search also has the advantage of automatic redshift information without the need for the time-consuming spectroscopic followup that is required by optical surveys, and particularly important in searches for dwarfs with unclear morphologies. In the case of Leo I, both types of survey were clearly needed to gain a more complete understanding of the group's population, but the blind, HI search proved more successful at finding low-mass group members.

3.3 HI Mass Function for Leo I

An important aim of the ALFALFA survey is to determine the HIMF to low HI mass, and eventually to compare how the HIMF might vary in different environments. A drawback of earlier determinations of the HIMF has been the lack of statistics at the low HI mass end, especially in wide area surveys where errors in the distances of the nearby systems which populate the low mass bins are significant. Here, we exploit the group membership to examine the HIMF of

the Leo I group alone. Leo I presents an interesting study because of its proximity and because the group also has relatively few bright L* galaxies compared to other groups [Trentham and Tully, 2002].

The distribution of HI masses for Leo I and Leo II members found in the available ALFALFA catalog (Tables 3.2, 3.3, 3.4, and 3.7) is shown in Figure 3.4. The spread of masses peaks at an HI mass of $10^{7.6} M_{\odot}$ with 91 of the 155 sources having an HI mass of less than $M_{HI} < 10^8 M_{\odot}$. The ALFALFA sources that are new HI detections are highlighted by the shaded histogram and clearly dominate the low-mass end. In an effort to use a relatively complete and homogeneous sample, we compute an HIMF only from Leo I members detected by the drift scan technique exploited by the ALFALFA survey. Thus, we do not include the galaxies found via single-pixel Arecibo observations, noted in Tables 3.2, 3.3, 3.4 or any objects from Table 3.7. HI flux from all detections constituting the Leo Ring are combined into one data point for determination of the HIMF. Neutral hydrogen from the eight detections making up the Leo Triplet plume is attributed to NGC 3628, and flux from the eight detections constituting the southern clump in the Leo Triplet is added to that of NGC 3627. The resulting dataset includes 65 HI line sources of which 45 have $M_{HI} < 10^8 M_{\odot}$. Spectra derived from the ALFALFA survey data for all of these sources (with the exception of the Ring) can be found in Figure 3.9. Calculating a group HIMF from a sample consisting of 69% low-mass objects is a marked improvement on the 1% used for the HIPASS HIMF and almost doubles the 36% used by Kovač [2007] for the Canes Venatici group HIMF as well as the 34% used by Verheijen et al. [2001] in their HIMF for the Ursa Major Cluster.

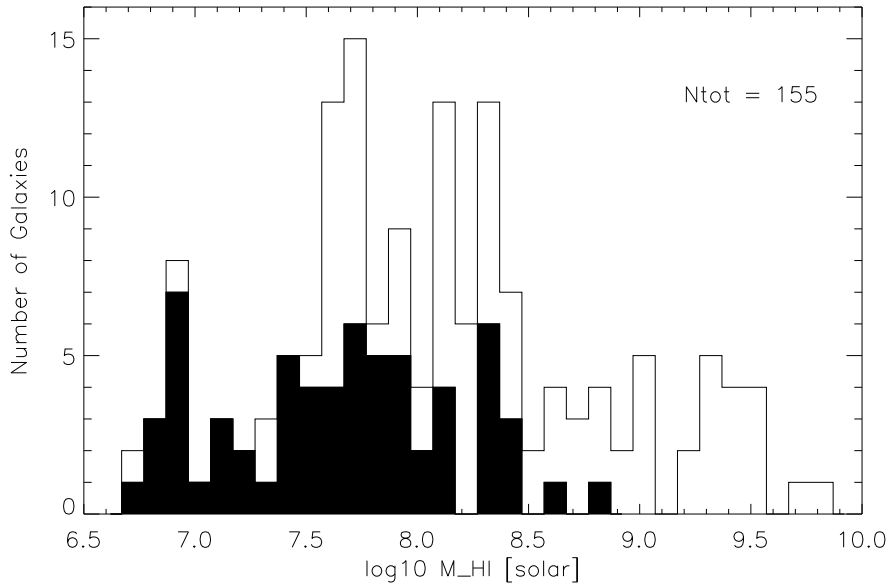

Figure 3.4 Distribution of HI masses for ALFALFA detections in Leo I and in the Leo Cloud. All sources found with ALFALFA from Tables 3.2, 3.3, 3.4, and 3.7 are included. HI flux from all detections constituting the Leo Ring are combined into one entry. Neutral hydrogen from the eight detections making up the Leo Triplet plume is attributed to NGC 3628, and flux from the eight detections constituting the southern clump in the Leo Triplet is added to that of NGC 3627. The distribution peaks at a mass of $10^{7.6} M_{\odot}$. New HI detections are shaded and dominate the low-mass end.

3.3.1 Completeness Corrections & Error Estimates

As is always the case in determinations of luminosity and mass functions, corrections for completeness are critical. The analysis presented here avoids several problems plaguing determinations of HI mass functions for global samples and even for surveys of larger clusters because Leo I is restricted to a small, nearby volume. In wide area surveys like the Rosenberg and Schneider [2002] sample of 265 ADBS galaxies, the Springob et al. [2005] sample of 2771 optically-selected galaxies, or the Zwaan et al. [2005] sample of 4315 southern HIPASS galaxies, the large search volume results in detection of objects in the foreground of the sample that could not have been detected at larger distances. Each source must then be weighted by $1/V_{max}$ where V_{max} is the maximum volume within which it could have been detected. Even in the blind HI surveys focused on the Ursa Major Cluster [Verheijen et al., 2001] and on the Canes Venatici Group [Kovač, 2007], the front and back of the cluster are separated enough to require a $1/V_{max}$ correction. All of the Leo I sources, however, are at roughly the same distance, and the minor volume difference between the foreground of the Leo I cloud and the background where Leo I meets Leo II is not large enough to significantly affect the completeness of our sample in terms of volume.

The proximity of Leo I also results in a galaxy sample that is complete down to a lower flux limit throughout the entire survey volume than is possible for wide area surveys probing more distant galaxy populations. At the Leo I distance, the lowest flux reached is 0.20 Jy km s^{-1} which translates to an HI mass of $\sim\ 10^{6.72} M_{\odot}$. Thus only the lowest mass bin of the Leo I HIMF representing objects with masses between $10^{6.5}$ and $10^{7} M_{\odot}$ needs to be corrected for being populated only down to $10^{6.72} M_{\odot}$.

As was done for the determinations of the HIMF based on other blind HI surveys [Henning et al., 2000, Zwaan et al., 2005, Rosenberg and Schneider, 2002], a correction is needed to account for the dependence of the integrated flux detection limit on the HI line velocity width for ALFALFA detections. As shown in Figure 2.3c, an HI spectroscopic survey such as ALFALFA naturally yields a lack of sources with both low fluxes and large velocity widths. To address this bias without over-correcting for an intrinsically small population, we examine the distributions of velocity width for varying HI mass as determined by a complete sample consisting of all of the currently ALFALFA spring sky catalog detections available to us with integrated fluxes greater than 1.0 Jy km s^{-1}. It should be noted that although the flux completeness limit dips below 1.0 Jy km s^{-1} to $\sim$.25 Jy km s^{-1} for sources of lower velocity widths, these are not the sources in need of the correction we are seeking here. Since the sample is complete, these distributions reflect the intrinsic nature of the ALFALFA sources without a velocity width-integrated flux selection bias. By comparing these 'expected' distributions with those actually observed in Leo I, the deficiency of sources at any given HI mass due to the width-flux selection bias can be corrected.

A plot of the 'expected' distributions of number of galaxies with a given velocity width used to determine the Leo I HIMF is shown in Figure 3.5. Seven mass bins each containing $10^{0.5} M_{\odot}$ are chosen to cover the range of galaxy masses $7.0 < log(M_{HI}) < 10.5$. For each mass bin, the HI mass at the center of the bin (Mc) is noted, as well as the total number of sources that were found in that bin. For example, 103 detections were made with $10^{7.5} M_{\odot} < M_{HI} < 10^{8.0} M_{\odot}$. The total number of 2867 sources used to find the distributions represents the number of ALFALFA detections in the spring sky ($7h30m < \alpha < 14h30m$ and

$+4 < \delta < +16$) with fluxes above 1.0 Jy km s^{-1}. The distributions are fit with six term Gaussians following the equation

$$f(x) = A_0 e^{\frac{-z^2}{2}} + A_3 A_4 x + A_5 x^2 \tag{3.1}$$

where $z = (x - A_1)/A_2$.

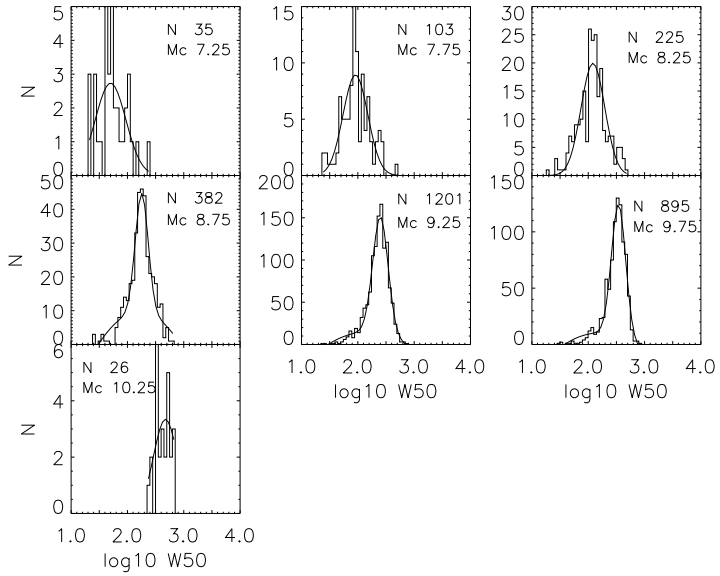

Figure 3.5 Expected distributions (i.e. sources with $F_c > 1.0mJy$) of log(W50) binned by HI mass. The histograms are fitted with six term Gaussians which are overplotted. Due to the small number of galaxies in the first and last mass bins, the parameters determined for those mass ranges are not used in the final fit. Instead a distribution function is fit using the middle five mass bins and interpolated to other velocity width/HI mass pairs.

The two lowest mass bins for detections made by ALFALFA ($10^{6.0} M_\odot < M_{HI} < 10^{6.5} M_\odot$ and $10^{6.5} M_\odot < M_{HI} < 10^{7.0} M_\odot$) as well as the highest mass bin ($10^{10.5} M_\odot < M_{HI} < 10^{11.0} M_\odot$) each contained less than 10 detections, so we were unable to fit expected distributions to these mass ranges. In order to determine the proper fit parameters for these mass bins and for any specific mass

values that do not fall exactly in the center of the bins shown in Figure 3.5, we model the change in fit parameters as a function of mass. The fits for the two most influential fit parameters, the center of the distribution (A_1) and the width of the distribution (A_2), are shown in Figure 3.6. The distributions for A_1 and A_2 are fit with first and second order polynomials respectively.

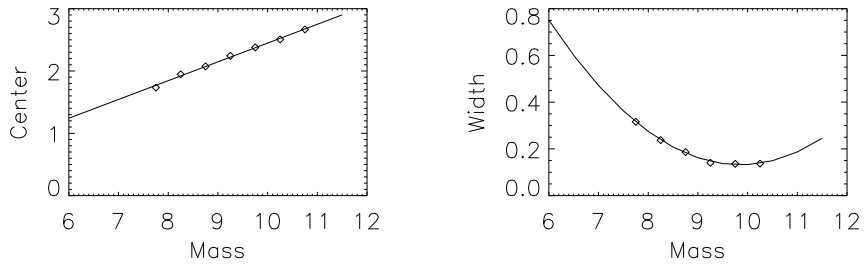

Figure 3.6 The two main fit parameters (Gaussian center and Gaussian width) for the expected distributions of sources for a given HI mass. The circles represent parameters pulled from the six-term Gaussian fits to the distributions in Figure 3.5.

Three separate sources of error contribute to the uncertainties in the determination of the HIMF based on the two completeness corrections discussed above and on Poisson statistics. The error associated with the correction for the flux-width dependence is estimated from the errors associated with each fit to the 'expected' distributions of HI mass versus velocity width. This source of error does not apply for sources of $M_{HI} > 10^{8.5} M_{\odot}$ since the correction is unnecessary for high masses. The second completeness correction only applies to the lowest mass bin and thus so does the additional associated error. The final contribution of Poisson errors affects all HI mass bins and equals $1/\sqrt{(}N)$ where N is the number of galaxies in the bin.

As discussed in Masters et al. [2004], the use of Hubble flow distances leads to large errors in M_{HI} and the HIMF most significantly for nearby galaxies

where peculiar velocites are a more significant fraction of measured recessional velocities. Both Rosenberg and Schneider [2002] and Zwaan et al. [2005] use flow model distances in their HIMF determinations but claim comparisons with Hubble flow distances show no difference. Zwaan et al. [2005] point out that since peculiar motions only affect a small fraction of their sample, they would not expect a different result between the two methods. However, the population of galaxies most important in determination of the low mass slope are the same galaxies whose distances uncertainties are most impacted by peculiar velocities: the lowest mass objects that make up only a very small fraction of both the HIPASS and ADBS samples. Despite being dominated by these low mass, nearby galaxies, the Leo I sample is able to reduce significantly the errors based on distance measurements by using group distances determined with the help of 10 primary distances.

3.3.2 The Leo I HIMF & Comparison with other HIMFs

The Leo I HI mass function is shown in Figure 3.7. There are no objects with HI masses greater than $10^{10} M_{\odot}$ in the Leo I volume; we represent this lack of sources with a downward arrow. The current ALFALFA catalog subtends a volume of $\sim\ 2.5 \times 10^6$ Mpc^3 and contains 6249 high quality (code 1) detections. 1178 of those have masses of $10^{10} M_{\odot} < M_{HI} < 10^{10.5} M_{\odot}$ and 26 have masses of $10^{10.5} M_{\odot} < M_{HI} < 10^{11} M_{\odot}$. When compared to the Leo I volume of $\sim$19 Mpc^3, the fraction of high mass objects in the larger ALFALFA sample translates to an expected $\sim$0.01 objects of $10^{10} M_{\odot} < M_{HI} < 10^{10.5} M_{\odot}$ and an expected $\sim$0.0002 objects of $10^{10.5} M_{\odot} < M_{HI} < 10^{11} M_{\odot}$ within the volume of Leo I. Thus the lack of objects contributing to the HIMF at the high-mass end do not reflect the lack

of such a population but rather the limited volume of our Leo I catalog.

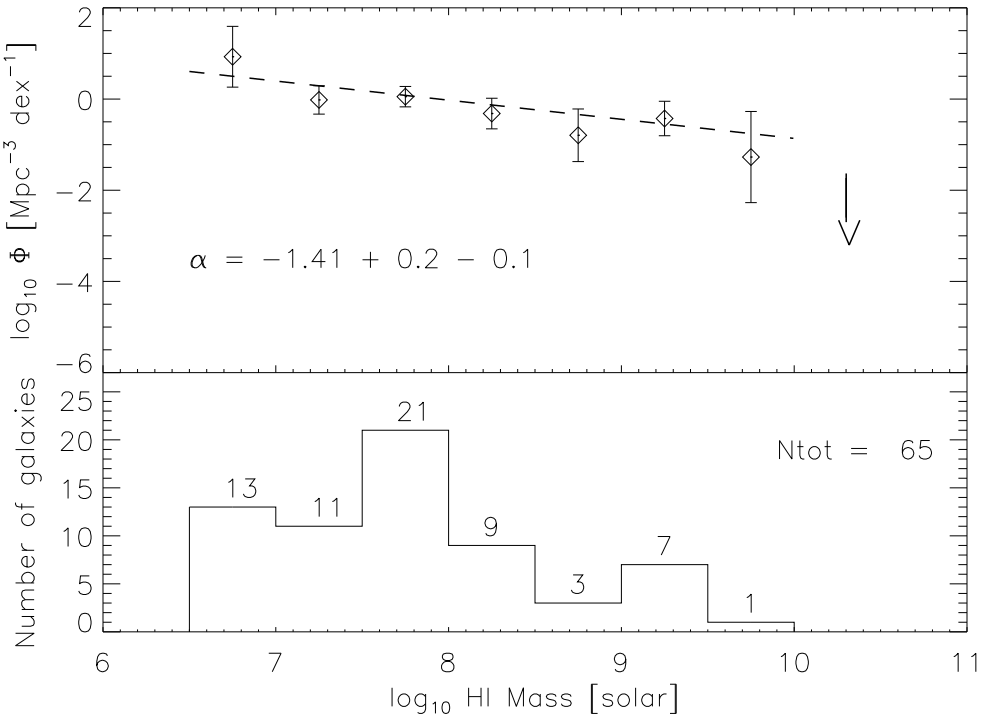

Figure 3.7 The HIMF for Leo I with a linear fit overplotted. The low-mass end slope is well-constrained even given the small sample size due to the large (69%) contribution of low-mass galaxies to the sample. The slope of the linear fit translates to a Schechter function with a low-mass end slope of $\alpha = -1.41 + 0.2 - 0.1$. No objects are found with $M_{HI} > 10^{10} M_{\odot}$. The lack of high-mass galaxies is noted by a downward arrow and suggests that the ϕ^* and log(M$_*$) parameters to the best fit Schechter function should be considered approximations at best.

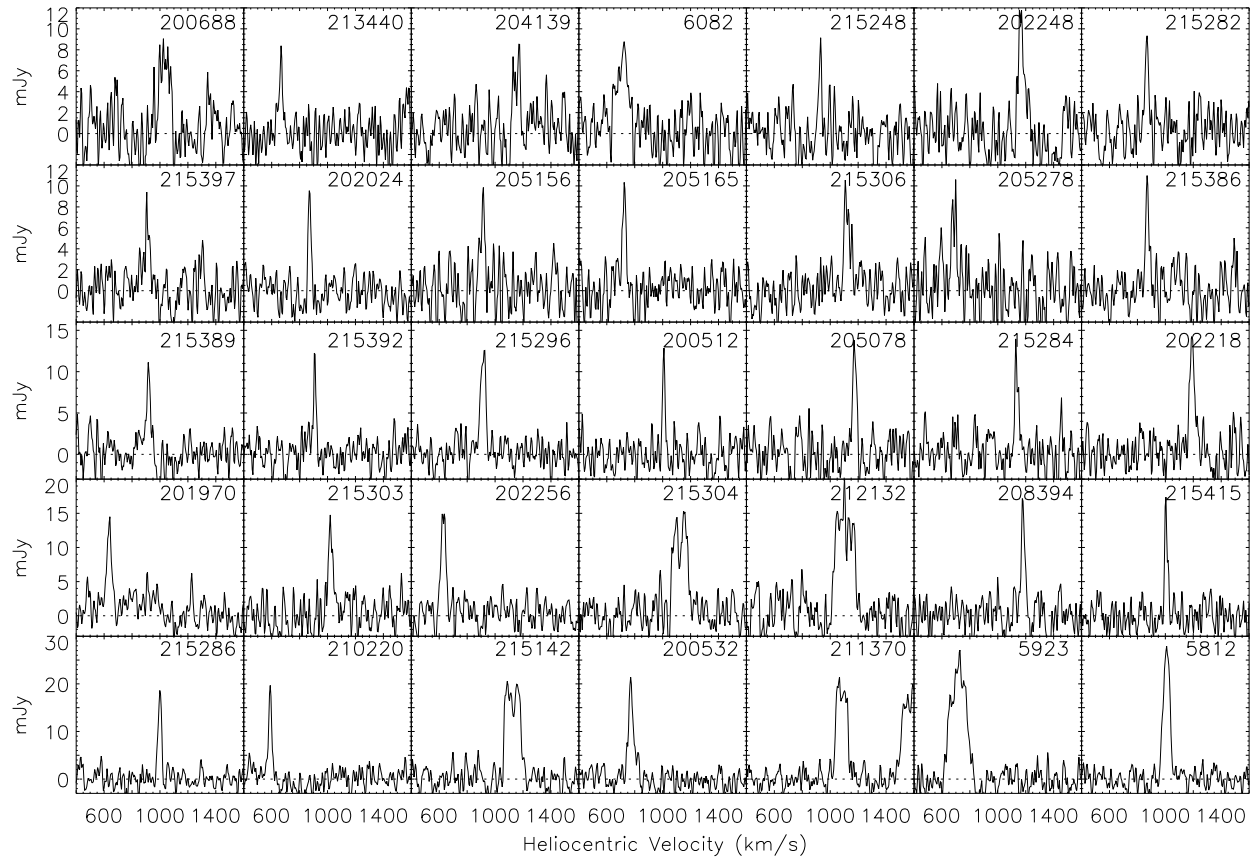

Figure 3.8 The first 35 ALFALFA HI spectra of Leo I members used to determine the HIMF in order of increasing peak flux. The x-axis is the same for every spectrum, but the y-scales are different for each row.

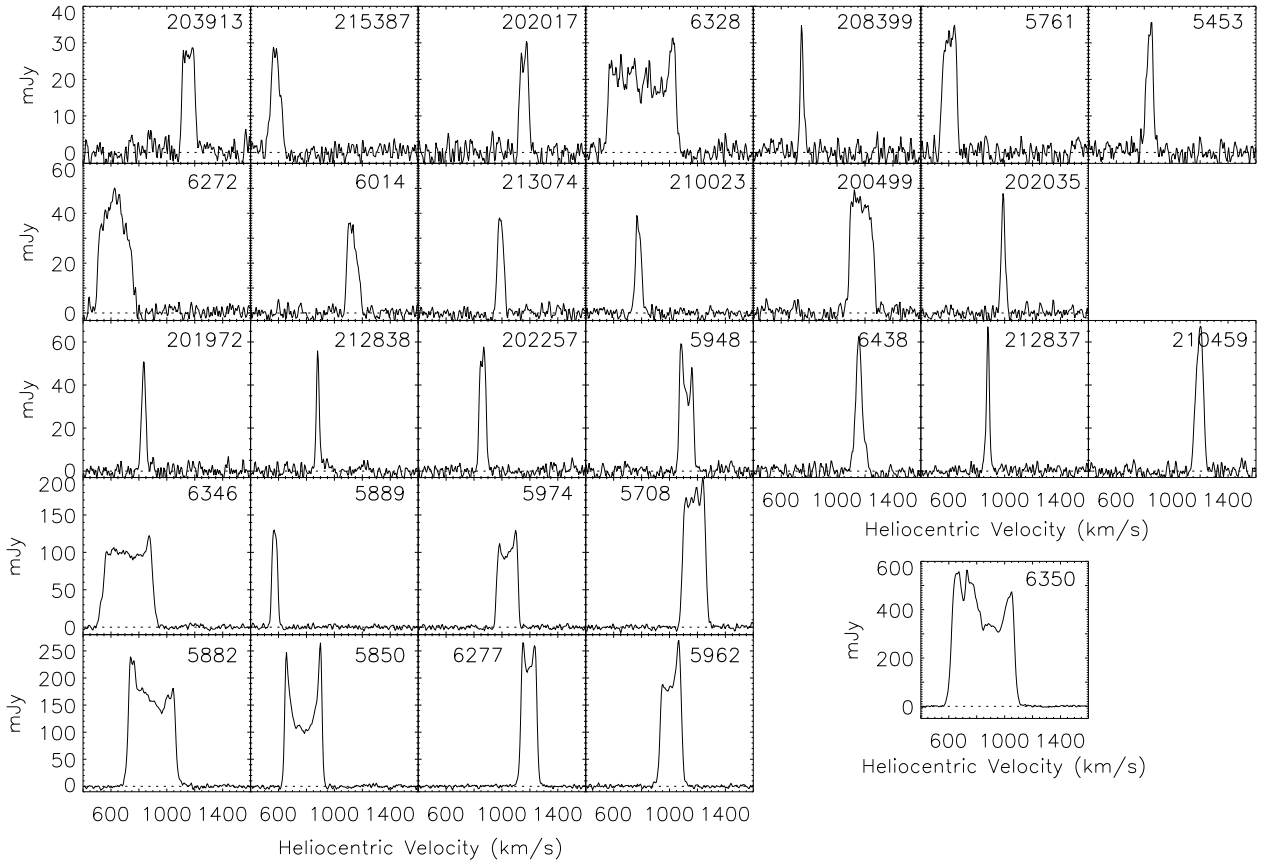

Figure 3.9 The remaining 29 ALFALFA HI spectra of Leo I members used to determine the HIMF in order of increasing peak flux and continued from previous figure. The x-axis is the same for every spectrum, but the y-scales are different for each row. AGC6350 is plotted separately due to its large peak flux value.

For a Hubble constant of $H_0 = 70$ km s^{-1} Mpc^{-1}, a linear fit to the Leo I HIMF gives a slope of -0.41 and a y-offset of 3.33. This slope is identical to that of the best fit Schechter function which has parameters $\phi^* = 0.03$ Mpc^{-3}, $log_{10}(M_*/M_\odot) = 10.7$, and $\alpha = -1.41$. The linear fit is overplotted in Figure 3.7. Our determination of the Leo I HIMF assumes a volume for the Leo I group of 18.7 Mpc^3 with an estimated error of $\pm$ 4 Mpc^3. However this error only affects ϕ^* for the HIMF and does not contribute to errors in α. The inclusion versus exclusion of Leo I objects that were not clearly in the M96 or M66 groups (as described in Section 3.1.1) does affect the low mass end slope. If these objects are placed at the M66 group distance of 10.0 Mpc or the M96 group distance of 11.1 Mpc instead of using flow model distances, α is increased by 0.2 or 0.15 respectively. Thus we estimate that for the Leo I HIMF, $\alpha = -1.41 + 0.2 - 0.1$. The values quoted for ϕ^* and log(M$_*$) are very uncertain given the lack of high mass sources in the Leo I volume and should be considered approximations at best.

The low mass slope of the Leo I HIMF is compared to six other HIMFs in Table 3.9: the Verheijen et al. [2001] sample of 32 members of the Ursa Major Cluster (UMa), the Kovač [2007] survey of 70 objects in the Canes Venatici group (CVn), the Henning et al. [2000] survey of 2347 objects in the zone of avoidance, the Rosenberg and Schneider [2002] sample of 265 ADBS galaxies, the Springob et al. [2005] sample of 2771 optically-selected galaxies, and the Zwaan et al. [2005] sample of 4315 HIPASS (i.e. HI-selected) galaxies. The mean velocities, as well as the number of total and low-mass galaxies in each sample are quoted. Objects of low HI mass are poorly represented in all but the Kovač [2007] sample.

The slope of -1.41 translates to a prediction of 165 galaxies in Leo I with $M_{HI} < 10^8 M_\odot$. To compare the number of low-mass objects expected from the differing HIMFs, the values of ϕ^* for the global HIMFs (i.e. ZOA, ADBS, Springob et al. and HIPASS) must be scaled to account for the fact that Leo I is an overdense region. After scaling the ϕ^* for each global HIMF to match the ϕ^* of the Leo I HIMF, Springob et al. [2005], Zwaan et al. [2005], Henning et al. [2000], and Rosenberg and Schneider [2002] expect 3, 9, 25, and 35 HI detections below a mass of $10^8 M_\odot$ respectively. These estimates are all significantly lower than the prediction of 165 low-mass objects from the Leo I HIMF. Without even correcting for completeness, there are more low-mass objects in the Leo I sample than are predicted for all of the global samples. The Leo I sample thus suggests a population of low HI mass objects in the intermediate density group that was not found by earlier, global determinations of the HIMF.

Since the global HIMFs represent an averaging over a range of galaxy environments and thus are not expected to match the number of low-mass objects found in the overdense Leo I group, a fairer comparison can be made with the HIMF determined for the Canes Venatici group [Kovač, 2007]. A quantitative comparison is not made with the Ursa Major HIMF since precise fit parameters are not quoted in that study. After correcting for completeness, Kovač [2007] expects 61 HI detections below a mass of $10^8 M_\odot$ with a low mass slope of $\alpha = 1.17$. The Leo I and CVn samples are of comparable size, surveyed similar areas on the sky, and both probe nearby groups. (CVn has a group distance of $\sim$4.1 Mpc as determined by primary distances to 17 group members from Karachentsev et al. [2003].) However, the CVn HIMF is a closer match to the global determinations of the HIMF, particularly the optically-selected sample of Springob et al. [2005]. In an optical study of the group, Karachentsev et al. [2003] found

the CVn luminosity function also more closely resembled a luminosity function determined for field galaxies than the same function computed for a sample of nearby groups. The CVn group thus may represent an environment where interactions do not play a significant role in galaxy evolution, in contrast to the Leo I environment where strong evidence exists for previous galaxy encounters.

Despite having the highest percentage of low mass objects, the Leo I HIMF does not have the steepest low-mass slope. However, the two determinations of the HIMF that have higher slopes (Henning et al. [2000] and Rosenberg and Schneider [2002]) use six and seven galaxies respectively to determine those slopes. These samples also have the lowest number of total galaxies with the exception of those focused on specific galaxy groups. These higher slopes are thus more likely to be poorly constrained due to limitations of sample size rather than representative of a significantly larger population of low-mass objects missed by ALFALFA. The slope derived for the HIMF of Henning et al. [2000] also most likely suffers from the largest distance errors of the seven samples presented in Table 3.9 as their distances are based on Hubble flow after correcting measured velocities to the Local Group frame and do not take into account peculiar velocities.

3.3.3 Comparison with Luminosity Functions

Using a deep optical survey covering a small portion of Leo I aimed at studying the faint-end of the optical luminosity function (LF), (Trentham and Tully [2002]; hereafter TT02) determined the Leo I LF to have a flat faint end slope and estimated a dwarf-to-giant ratio of 1.6 ± 0.9, the lowest of the six groups

Table 3.9. Comparison of the low-mass slope α for different HIMFs

Reference	Sample Type	$\bar{v}^*$ km s^{-1}	N_{tot}	$N_{low}{}^{**}$	α
this paper	Leo I Group	931	65	45	-1.41+0.20
Verheijen et al. 2001	Ursa Major Cluster	∼950	32	11	flat
Kovaç 2007***	CVn Group	∼320	70	26	-1.17±0.08
Henning et al. 2000	ZOA	2347	110	6	-1.51±0.12
Rosenberg & Schneider 2002***	ADBS HI-selected	3768	265	7	-1.53±0.12
Springob et al. 2005***	optically-selected	∼5000	2771	15	-1.24±0.17
Zwaan et al. 2005	HIPASS HI-selected	3276	4315	44	-1.37±0.03

*Mean velocities without a '∼' are calculated directly from the publicly-available data.

**Number of objects with $M_{HI} < 10^8 M_\odot$.

***Errors in α are estimated from the 1σ (Kovaç) or 2σ (Springob; Rosenberg & Schneider) contour presented in the reference.

in that study. The TT02 dwarf designation is based on optical properties ($-18 < M_R < -10$) and thus a direct comparison cannot be made to the number of dwarfs presented in the ALFALFA survey's coverage of Leo I. However, as a first order approximation, after labelling all objects with $M_{HI} < 10^8 M_\odot$ and $W_{50} < 100$ km s^{-1} as "dwarfs", the ALFALFA sample, once corrected for completeness, gives a ratio of 9.9 dwarfs for every giant galaxy. The dwarf-to-giant ratio found by ALFALFA does not include lenticular or elliptical galaxies, both of which are found in Leo I and would contribute to the lower ratio found by the TT02 survey. However, given that Leo I has few L* galaxies compared to other nearby groups, these E/S0s may not make up the whole difference in the optically versus HI-selected ratios. The discrepancy may also be indicative of the existence of a population of gas-rich yet optically faint dwarfs that were either discarded as background galaxies or of too low optical surface brightness to be detected by the optical TT02 survey. TT02 report the ratio of dwarf ellipticals (dEs) to dwarf irregulars (dIs) in Leo I to be 40%, a much lower fraction than the ∼80% found for all other groups in their study but one, the very poor NGC

1023 group. A comparatively low percentage of dEs would further enhance the contribution made to the Leo I dwarf sample by a population of optically-faint dIs.

Another factor contributing to the larger number of dwarfs in the HI-selected ALFALFA sample may be that the small portion of the Leo I group covered by the TT02 survey (0.0663 Mpc^2 compared to the 12.8 Mpc^2 surveyed by ALFALFA) did not accurately represent the group as a whole. Although TT02 probe their search area to fainter magnitudes than previous studies, with their limited strip of coverage TT02 are not even able to include M96 as a group member because the galaxy is far outside their survey bounds. Shallower surveys with larger sky coverage of the region have observed 9 deg^2 centered on the core of the M96 group ($\sim$0.3 Mpc^2 at a distance of 11.1 Mpc) and found faint end slopes steeper than that for TT02, but still not as steep as for the Leo I HIMF. Ferguson and Sandage [1991] found $\alpha = -1.36$ and Flint et al. [2003] determined $\alpha = -1.17 \pm 0.04$. These samples may not have the sensitivity needed to detect the gas-rich, low surface brightness galaxies more easily found by a blind HI survey of sufficient sensitivity. Alternatively, by focusing only on the center of the M96 group, these optical surveys may be sampling a different dwarf population than that found by the much wider area ALFALFA strategy.

3.4 Summary

In this chapter, we determined the HI mass function was for the Leo I group, an environment dominated by dwarfs with 69% of the galaxies in the sample having $M_{HI} < 10^8 M_\odot$. The best fit Schechter function and linear fits both give the

Leo I HIMF a low mass slope of $\alpha = -1.41 + 0.2 - 0.1$. With scaling to account for the higher density environment represented by Leo I, this slope is steeper than that for the optically-selected sample of Springob et al. [2005], the HIPASS survey [Zwaan et al., 2005], and the survey of the Canes Venatici Group done by Kovač [2007], but still consistent within the quoted error. Two HIMFs have produced steeper slopes than that for Leo I, the zone of avoidance survey [Henning et al., 2000] and the ADBS, HI-selected survey [Rosenberg and Schneider, 2002], but these surveys have only six and seven total low-mass ($M_{HI} < 10^8 M_\odot$) detections respectively and most likely carry large distance errors; the low mass slope of the Leo I HIMF was more robustly determined.

The Leo I HIMF has a steeper low mass end slope than was found for three luminosity functions based on samples of varying depths and sky coverage. In the deepest of these optical surveys designed to find low luminosity dwarfs in Leo I but most limited in sky coverage, Trentham and Tully [2002] found 1.6 dwarfs for every giant in the group. Using a rough estimate based on HI mass and line width, ALFALFA found a dwarf-to-giant ratio of 9.9, more than six times higher than in the optically-selected sample. This discrepancy may suggest the existence of a population of gas-rich yet optically faint dwarfs not included in the optically-selected sample but is also affected by the lack of E/S0 galaxies in the HI-selected ALFALFA sample. In a direct comparison between an optical survey of the M96 group [Karachentsev and Karachentseva, 2004] and a portion of the ALFALFA survey with the same sky coverage, every group member not found in the optical survey was a dwarf, while only half of the members missed by ALFALFA were dwarfs, and the rest were L^* galaxies (i.e. ellipticals or lenticulars with $m_B \sim 10 - 12$). The widespread population of dIs found by the ALFALFA survey may reflect the trend of morphological segrega-

tion seen in the Local Group.

The next step to understanding this newly uncovered dwarf population is to examine the optical properties of the ALFALFA dwarf sample. A detailed analysis of the optical properties of Leo I group dwarfs is presented in the next chapter.

CHAPTER 4

PHOTOMETRY OF LEO GROUP GALAXIES: DATA AND METHODS

If the shoe doesn't fit, must we change the foot? - Gloria Steinem

In this chapter we test the limits of the photometry from the Sloan Digital Sky Survey (SDSS) at both the low and high luminosity ends of the galaxy luminosity function to investigate the optical properties of the galaxies in the Leo I group. The optical information will then be added to the HI properties derived in the previous two chapters to take a census of the baryonic content of the Leo I galaxies. In later chapters we investigate the properties of gas versus stellar material within the galaxies in the group to look for trends relating galaxy morphology, gas content, and color with location within the group, and we explore the implications for such relationships in different dwarf galaxy formation scenarios.

Even in the nearby universe, dwarfs are hard to detect based on their faint optical luminosities and/or low HI masses. The ALFALFA survey has been successful in finding very low surface brightness dwarfs that have been missed by optical surveys but are also gas-rich and thus easily detected via their gas content (see Chapter 3). In the Leo I sample alone, 19 dwarfs - almost half of the low mass sample - are not identified by SDSS and are instead found via their neutral hydrogen. For such faint, diffuse sources the accuracy of background sky subtraction becomes crucial to the quality of the derived photometric sources.

Extra care has to be taken with the application of measurements (magnitudes, sizes, etc) which make use of the standard SDSS pipeline for extended, nearby objects of both low and high luminosities in the Leo region. SDSS

employs an automated data reduction pipeline to allow the release of large amounts of data in a relatively short time, but at the expense of more specific data processing that is streamlined for particular applications. Of relevance here, large objects are often identified as several separate objects by the automated deblender, and conversely, the light from background objects is sometimes merged with extended but faint foreground galaxies.

For our Leo I sample, we include those galaxies given in Chapter 3 as M96 group members and M66 group members, as well as those mentioned as possible Leo I members (Tables 3.2, 3.3, and 3.4). To more fairly balance the sample we also include the optically-selected dwarf galaxies from Karachentsev and Karachentseva [2004] that were not confirmed as background objects in the deeper, single pixel observations using the L-band Wide receiver (see Table 3.8). These dwarfs were not detected in the 100 MHz bandwidth of the receiver after several minutes of integration and are most likely either at a redshift of $cz > 6000$ km s^{-1} or are found in the Leo I group with little or no neutral gas. We believe the latter scenario to be more consistent with the fact that these galaxies were noted as having morphologies that would likely place them at the Leo I distance of $\sim$10 Mpc [Karachentsev and Karachentseva, 2004]. We suspect this optical sample is not complete as the Karachentsev et al. [2004] catalog from which it is derived only claims $70 - 80\%$ completeness out to 8 Mpc. The methods for obtaining optical photometry for the resulting sample of 105 galaxies are detailed in the following sections.

4.1 Sloan Digital Sky Survey: advantages and problems

The Sloan Digital Sky Survey (York et al. [2000]; SDSS) is a deep, 5-band optical survey of the northern sky which uses a dedicated 2.5-meter telescope at the Apache Point Observatory in New Mexico. The five photometric bands, ugriz, have point source magnitude limits of 22.0, 22.2, 22.2, 21.3 and 20.5 at the 95% completeness level. The survey coverage spans both the M96 and M66 groups in Leo I, and the images used here come from Data Release 3 [Abazajian et al., 2005]. The pixel scale for the detector is $0.''396$/pixel, so the resolution is instead limited by the average seeing which is quoted to be $\sim 1.4''$ [Abazajian et al., 2005].

A subset of photometric objects are chosen for spectroscopic followup based on their Petrosian r-band magnitudes ($r_p < 17.77$; see next section for a description of the Petrosian system). 40 of the 105 Leo I galaxies have optical redshifts in the SDSS database that are compared to the HI redshifts derived from ALFALFA in Figure 4.1.

Discrepancies of more than 50 km s^{-1} are found for both narrow and wide signals, and five sources do not agree within the error (the quadrature sum of the optical and HI errors). In the cases of NGC3623 and NGC3627, at velocity widths of 496 km s^{-1} and 351 km s^{-1} respectively, placement of SDSS spectroscopic fibers (i.e. the location within the galaxy where the optical spectrum is measured) are likely to blame for the differences. For both galaxies, the optical fiber, which has an aperture of only $3''$, was placed more than $\sim$30$''$ from the galaxy's center, and so the optical redshift does not reflect the systematic redshift of the galaxy as a whole. Fiber placement is also an issue for smaller

galaxies, as in the case of LeG03 (AGC202017). Although the HI and optically-derived redshifts for LeG03 agree within the quoted error, the galaxy has an HI redshift of 1158 km s^{-1} and an optical redshift of 1080 km s^{-1}. In this case, the optical fiber, which has an aperture of only $3''$, was placed $\sim$15$''$ from the center of the galaxy (which has a radius of only $\sim$30$''$). For the remaining 3 galaxies with discrepant optical and HI redshifts, AGC202248, CGCG 093-047, and CGCG 066-109, the two redshift measurements differ by 157 km s^{-1}, 90 km s^{-1}, and 211 km s^{-1}, respectively. Although the reason for the different redshift measurements in these cases is less clear given that the signal-to-noise ratios are high for both the optical and HI spectra and the optical fibers are centered on each galaxy, these sources represent only 8% of the sample.

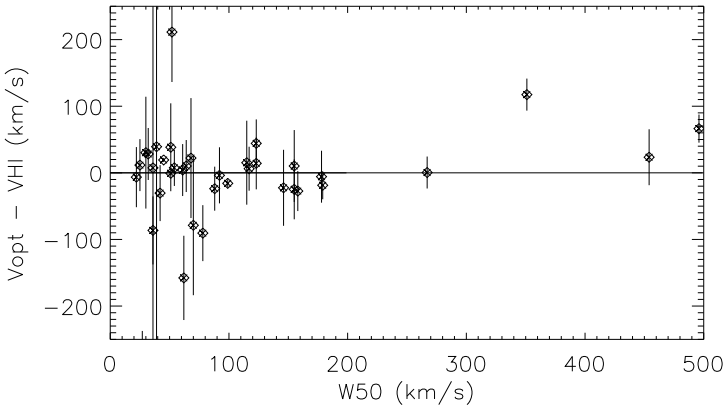

Figure 4.1 Comparison of optical redshifts determined by the SDSS spectroscopic followup survey with HI redshifts from the ALFALFA survey. The difference between the two values are plotted versus the width of the HI profile at half power. Some of the discrepancies occur for cases where the SDSS fiber was placed significantly offcenter. In a small number of cases (3 out of 40), the reason for the discrepancy is unclear. Errors on the y-axis are the quadrature sum of the error provided by SDSS and the error in v_{HI} determined by ALFALFA.

However, Figure 4.1 does not reveal the most significant redshift discrepancies that reflect a larger problem with the deblending of sources in the pho-

tometry and spectroscopy derived from the SDSS. In the instance of NGC3299 (AGC5761), SDSS actually gives two redshifts for the galaxy, both targeted at bright knots more than $20''$ away from the galaxy center; one is nearly matched to the ALFALFA redshift at 570 km s^{-1}, but the second places the galaxy at a z of 0.3. Both spectroscopic measurements for NGC3299 are labeled as galaxies in the SDSS database (rather than as QSOs or stars) and neither have an associated flag to reflect they may be in error. Another case, KKH 68 (AGC212837) which is not shown on the plot due to the large magnitude of its offset, has an HI velocity of 878 km s^{-1}, but an optical redshift of $z = 0.35$ from SDSS. The fiber is placed $\sim$10$''$ offcenter but the spectroscopic measurement has a flag of 'ok' in the database. Similarly large discrepancies are also found for sources where the optical fiber was centered on the galaxy, as in the case of AGC215248. Although the optical spectrum shows the object is clearly a low redshift galaxy, the source is labeled a QSO and assigned a high z.

Ignoring the sources for which the optical and HI redshifts do not agree within the quoted error, $V_{opt} - V_{HI}$ for the Leo I galaxies has a dispersion of 46 km s^{-1} which is comparable to the claimed redshift accuracy of the optical measurements which have a median uncertainty of 42 km s^{-1}. Thus the errors in source classification and redshift measurement resulting from the automated spectral analysis performed by the SDSS are significant in the small sample of Leo I galaxies, and larger samples are necessary so that such discrepancies make up only a small percentage of the overall statistics. The two galaxies at velocity widths near 40 km s^{-1} with error bars spanning the entire plot (AGC202218 and CGCG 065-086/AGC200532) have large errors quoted for their optical redshifts despite having signal-to-noise ratios comparable to the remainder of the sample and no associated warning flags.

All photometric images are also processed through an automated pipeline for source identification, deblending, and photometric reduction before being publicly distributed (Lupton et al. [2001]; Stoughton et al. [2002]). This automation allows for large amounts of uniformly-produced data to be delivered in a reasonably short amount of time, but has the drawback that the automated pipeline does not work well for all situations (Lupton and Ivezić [2005];Blanton et al. [2005b]). As for NGC3299 and KKH 68 mentioned above, the deblender failed to separate high redshift objects that became associated with the foreground galaxy. Conversely, extended nearby galaxies, particularly those with patchy morphologies like the late-type, low surface brightness objects found in Leo I, are often confused by the signal extractor for several different sources.

Another limitation of the automated pipeline for nearby, low surface brightness galaxies, is the accuracy of background sky subtraction (Baldry et al. [2005];West [2005]). An accurate determination of the zero point offset produced by background sky light (and thus to be subtracted from the optical images) requires that a region far enough away from the galaxy be used to determine background levels (Adelman-McCarthy et al. [2008];Abazajian et al. [2009]). For low surface brightness objects, the emission is sufficiently diffuse and faint that the automated photometry pipeline does not always move far enough away from the galaxy before beginning to calculate sky levels, resulting in an oversubtraction of background light. Large scale galaxy studies based on SDSS pipeline data typically place a lower redshift cutoff of $v > 6000$ km s^{-1} on their samples as most of the pipeline's problems occur when dealing with nearby galaxies. This redshift cutoff would eliminate almost one third of the ALFALFA dataset, including the Leo I group.

The New York University-Value Added Galaxy Catalog (NYU-VAGC; Blanton et al. [2005b]) is the result of a large scale effort to address *some* of these calibration issues in the SDSS pipeline and to create an easily downloaded and searchable catalog from the terabytes of data available in the public database. In its initial form, the VAGC contained photometric parameters for $\sim 700,000$ galaxies, mostly below $z \sim 0.3$, based on data from the SDSS Data Release 2. The zero point photometric calibration used by the VAGC improves upon the calibration performed by the SDSS pipeline, reducing systematic errors from 2% to 1% [Blanton et al., 2005b], and has since been adopted by the SDSS. In addition to maintaining an updated catalog (currently the VAGC is up-to-date with data from the most recent SDSS Data Release 7), the authors of the VAGC also visually inspect a large number of galaxy images to add cautionary flags. A variety of potential inaccuracies are noted including bad deblends and contamination from satellite trails, foreground stars, or background QSOs. However, the subset of improved photometry based on these eyeball quality checks does not reflect a complete sample. Thus the flags are not used to correct any of the flux or size measurements presented in the VAGC but instead exist to alert users to the problems associated with blind usage of SDSS pipeline data.

Further improvements to the SDSS pipeline are made for a low redshift catalog (Blanton et al. [2005b]; hereafter called the *lowz* catalog), a subset of the VAGC containing galaxies with spectroscopic measurements placing them between $0.0033 < z < 0.05$. Attempts are made to improve the deblending for galaxies flagged in the VAGC as being bad deblends. For example, if a patchy, extended nearby galaxy is confused by the pipeline for 3-4 separate sources, the flux from the separate objects is combined to give the total flux of the galaxy. In the terminology of the SDSS, *parent* frames are used in place of their *children* to

extract the photometry.

Eighteen of the Leo I galaxies have entries in the *lowz* catalog but only three have updated photometry. The results from the photometry pulled from the VAGC versus that from the *lowz* catalog for these 18 objects are shown in Figure 4.2 for all five bands. For most of the sources, the results agree within 0.05 magnitudes. We suspect this minor offset reflects a slight update to the flux calibration for the most recent data releases. (The VAGC reflects the most recent SDSS sample up to Data Release 7, but the *lowz* catalog only contains sources found in Data Release 4 and earlier. In an earlier (DR4) version of the VAGC, these 15 galaxies have identical entries to those found in the *lowz* catalog.) The three objects for which new photometry was performed for the *lowz* catalog are AGC202248 (circle), IC2934 (AGC210459; square), and IC2828 (AGC210340; triangle). In the first two cases, each galaxy is associated with only one spectroscopic target but with at least two photometric objects. Thus combining the flux from the multiple measurements from within the galaxy gives a more accurate, and brighter, magnitude measurement in all five bands. The largest difference in the two catalogs is seen for IC2828 which was clearly found to be at least two separate objects by the automated pipeline. Several photometric targets as well as two separate spectra are associated with different locations within this galaxy. None of the 15 remaining sources are linked with more than one spectrum, but only two galaxies are represented by only one photometric object. The number of photometric targets per galaxy ranges from 2 (AGC202171 and IC2934/AGC210459) to more than a dozen (NGC3423/AGC5962 and CGCG066-109/AGC210023) suggesting that further deblending issues may still exist in the *lowz* catalog. Although the authors of the VAGC claim to have examined the images for all sources with $z < 0.01$, they

do not include in their catalog galaxies with distances closer than 10 Mpc so the completeness of the eyeball checks at the lowest redshifts is unclear.

The *lowz* catalog improves upon the photometry found in the VAGC, so we use the *lowz* measurements when they are available and the VAGC values otherwise. However, both samples have two significant limitations that result in entries existing for only 68 of the 105 Leo I galaxies.

First, to exclude large resolved galaxies, which are usually shredded into multiple sources by the automated pipeline and thus require special processing, sources closer than $10h^{-1}$ Mpc are not included in the catalogs [Blanton et al., 2005b]. However, this distance cutoff appears to be approximate since 68 of the 105 objects in the Leo sample are found in the VAGC. As described in the previous chapter, the Leo I distance is right on the boundary of this lower limit, and so while the large elliptical UGC5902 and S0 UGC5911 are included in the VAGC, the extended Sab galaxies UGC6346 and UGC6350 are not. All eight of the large UGC galaxies not found in the VAGC (UGCs 5708, 5812, 5850, 5899, 5948, 6328, 6346 and 6350) have B-band magnitudes available from the Third Reference Catalog of Bright Galaxies (RC3; Roman et al. [1991]) and so we instead use the B and V band magnitudes found there to derive the optical properties for these larger galaxies.

The second limitation on the VAGC and *lowz* catalogs is the lower surface brightness cutoff of 24.5 mag arcsec^{-2} as measured at the half light radius in the r-band. Below this limit, the emission is so faint and disperse that the galaxies do not qualify for spectroscopic followup and are rarely even identified by the pipeline as photometric targets. While such low surface brightness objects are not usually optically identified by the SDSS, those bearing gas are easily picked

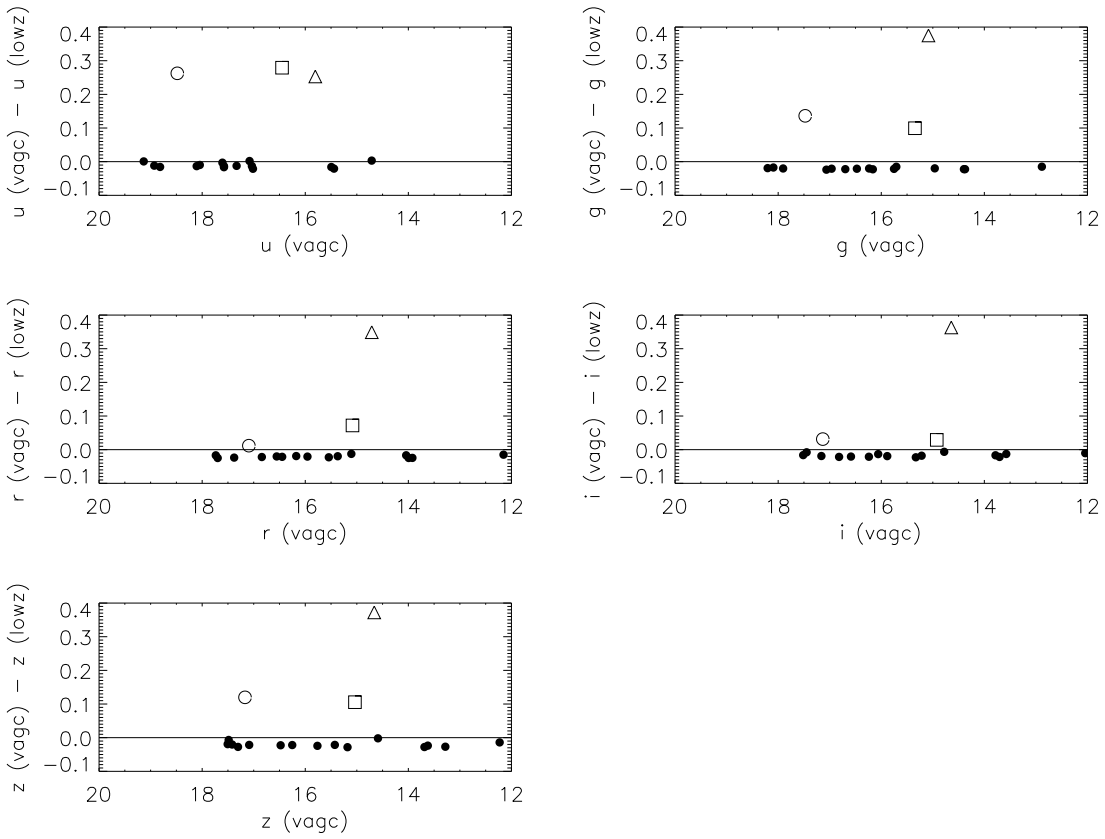

Figure 4.2 Comparison of the 18 Leo I galaxies found in the Blanton et al. [2005b] *lowz* catalog with the photometry given by the NYU-VAGC in the ugriz bands. The difference between the two catalogs is plotted versus the magnitude found in the NYU-VAGC. The photometry is nearly identical (within 0.05 magnitudes) for the majority of the sample (filled circles). The three galaxies with updated photometry in the *lowz* catalog are AGC202248 (open circle), AGC210459 (square), and AGC210340 (triangle), and nearly span the full range of magnitudes. These three objects were identified as multiple sources by the automated pipeline, and the magnitudes found in the *lowz* catalog reflect the combination of the flux from the multiple photometric targets.

out based on their HI content by ALFALFA. Based on the luminosity - surface brightness relationship for bright galaxies, Blanton et al. [2005a] estimate a multiplicative correction factor as high as 2 is neccessary (for galaxies of $M_r = 14$) to correct for incompleteness at low surface brightness levels. In the Leo I sample alone, 19 of the dwarf galaxies are of too low surface brightness to meet the criteria for inclusion in the VAGC.

For the Leo I sample, the photometry for these HI-selected, low surface brightness dwarfs is potentially the most interesting; comparisons of other galaxy properties, like color, gas content or environment, can reveal what factors are most important in regulating their star formation activity or lack thereof. Thus we require a technique independent of surface brightness to examine those dwarfs missed by the automated, optical search performed by the SDSS. For our study of the Leo I dwarfs we use a more interactive method designed by ALFALFA collaborator Andrew West to be better suited for nearby, low surface brightness galaxies (West [2005]; hereafter called the lsb method). The techniques used to obtain photometry for the 20 low surface brightness objects in the Leo I sample are detailed in the following section.

4.2 Measuring magnitudes for low surface brightness galaxies

The differences between the lsb method and automated SDSS pipeline that most significantly applies to our study of low surface brightness dwarfs are the methods of background sky subtraction and of visual deblending. In the lsb method, SExtractor [Bertin and Arnouts, 1996] is run on the r-band image of each object, and a mask is applied to any five adjacent pixels with counts above a threshold

of 1.5σ. The size of each mask is chosen to be 5 times the area determined by SExtractor for stars and galaxies and 20 times the area determined by SExtractor for low surface brightness objects. The masks derived from the r-band image are then applied to the other four bands. The remaining background sky pixels are fit with a tilted plane model and removed from the galaxy images.

The images for each galaxy are then cleaned by hand to remove stars and other foreground or background sources. Using the *IMEDIT* task in *IRAF*, contaminating sources are masked with circular apertures and replaced with background values computed from an annulus surrounding the mask. To remove sources that are either partially overlaid on the target galaxy, the object is masked and then replaced with flux values from an aperture of the same size selected by the user from a different location in the image that most accurately represents the missing flux. This user-defined aperture selection was only performed for three galaxies where light from foreground stars contaminated the emission from the outskirts of the galaxy. A few targets had foreground or background objects that could not be removed without significantly degrading the integrity of the photometry, and those objects were removed from the sample. Due to color variations of foreground and background sources, as well as the galaxies themselves, this editing is performed separately for the ugriz images.

The SDSS documentation[1] recommends that only Petrosian photometry is appropriate for determination of magnitudes for nearby galaxies. The Petrosian system has the advantage of changing as a function of surface brightness in order to adjust for the fact that not all galaxies have the same radial surface brightness profile. Petrosian magnitudes are designed to measure a constant fraction of a galaxy's total light, independent of orientation or distance and have been

[1]http://www.sdss.org/dr7/algorithms/photometry.html

adopted by several other studies of low redshift [Kauffmann et al., 2003] and low luminosity (Blanton et al. [2005a]; Geha et al. [2006]) galaxies. The Petrosian ratio ($R_p(r)$) of the surface brightness within an annulus at radius r within a galaxy to the mean surface brightness for the galaxy as a whole is defined as:

$$R_p(r) \equiv \frac{\int_{0.8r}^{1.25r} dr'\, 2\pi r'\, I(r')/[\pi(1.25^2 - 0.8^2)r^2]}{\int_0^r dr'\, 2\pi r'\, I(r')/(\pi r^2)} \tag{4.1}$$

where I(r) is the azimuthally averaged surface brightness profile. The Petrosian radius for a specific galaxy is then defined as the radius at which $R_p(r) = 0.2$ (Blanton et al. [2001]; Yasuda et al. [2001]). The Petrosian flux for the galaxy is then the flux within 2 Petrosian radii:

$$f_p \equiv \int_0^{N_p R_p} 2\pi r' I(r') dr', \tag{4.2}$$

where $I(r)$ is again the azimuthally averaged surface brightness profile and N_p is the Petrosian number. For the photometry of the SDSS sources and of the low surface brightness galaxies presented here, N_p is set to 2 to measure the flux within 2 Petrosian radii. The goal in the selection of the Petrosian number is to specify an aperture that is large enough to safely contain all of the galaxy's light, rather than to estimate the galaxy's size. The aperture size is also chosen so as not to be so large that the inclusion of additional sky noise becomes problematic.

The Petrosian system can pose problems for faint objects where the surface brightness (and thus the Petrosian ratio) becomes unmeasureable before the limiting value of 0.2 is reached. For these sources an upper limit to the Petrosian radius must be set to avoid unneccessarily large aperture sizes. The SDSS pipeline sets such a limit at $3''$ or, if larger, at the outermost measured point in the radial profile. (Such galaxies are tagged with *PETROFAINT* or *NOPETRO* in the database.) For the low surface brightness photometry described here, we set an upper limit to the radius used for flux measurement by trimming each image

by eye to $\sim$5 times the size of the galaxy as it appears in the r-band. The mask determined for the r-band images is then applied to the other four bands.

Failure to include all of the flux is another potential pitfall of using Petrosian photometry for low surface brightness, patchy sources. Brighter knots of star formation found in the outskirts of these extended, diffuse systems could appear outside the Petrosian radius and would lead to an underestimation of the galaxy's flux. To avoid this issue and to take advantage of our small sample size, the Petrosian radius derived for each low surface brightness galaxy is visually inspected to verify its accuracy, as illustrated in Figure 4.3. A white circle marking twice the Petrosian radius as determined from the r-band image is overlaid on the sky-subtracted, trimmed, and cleaned images from all five filters for LeG05 (AGC202019), one of the Leo I dwarfs. To measure accurate colors for our low surface brightness objects, the same aperture size must be used to measure the flux in all five bands. The Petrosian radius is calculated from the r-band image and then applied to the u, g, i, and zband images. Each image is $2.2'$ in diameter.

Further illustration of the photometry is given in Figure 4.4. For all five bands, the total integrated flux (in nanomaggies, as given by the SDSS) is calculated as a function of radius along the extent of the galaxy and later converted to magnitudes using the relation:

$$m = 22.5 - 2.5log_{10}(flux) \tag{4.3}$$

As seen in the five plots, the flux continues to increase for all radii with a bend in the distribution that occurs near a radius of 120 pixels. The location of this knee matches closely the radius at which the Petrosian flux was determined in each band by the lsb method (overplotted as dashed lines and labeled in units

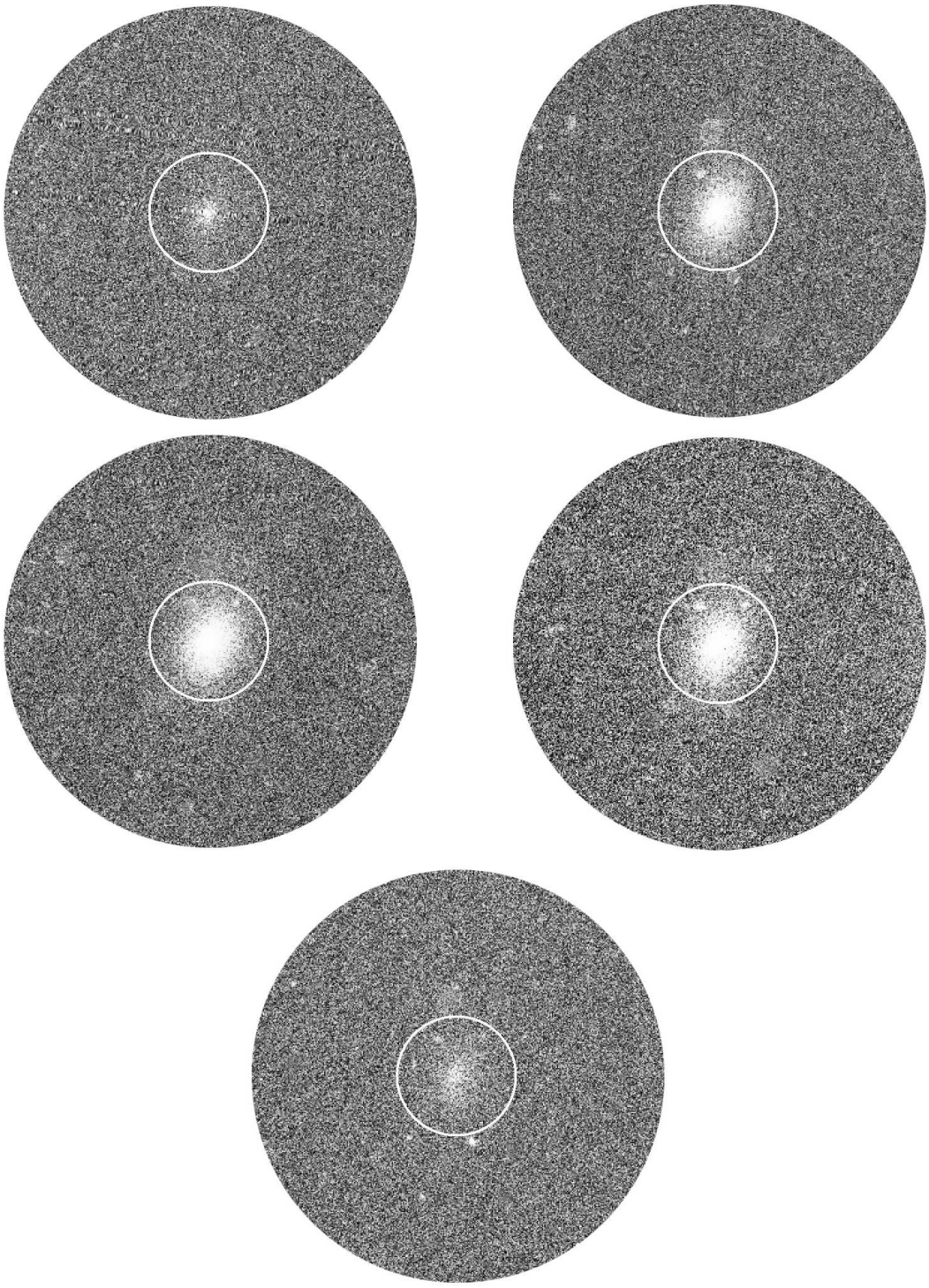

Figure 4.3 Sky-subtracted, trimmed, and cleaned images for LeG05 (AGC202019) in all five bands using the lsb method. Top row: u-band (left) and gband (right). Middle row: r-band (left) and iband (right). Bottom row: zband. Each image is $2.2'$ in diameter, and the white circle marks twice the Petrosian radius as determined in the r-band.

of counts). Ideally, to be sure all the galaxy's flux had been included and the sky perfectly subtracted, the flux would continue to increase with radius within the extent of the galaxy and then flatten out outside of the galaxy where there are only contributions from sky counts (which should fluctuate around zero). However, for the low surface brightness sample, the profiles do not flatten out and the background sky values do have some low value. Since each image is visually inspected to verify that all of the flux has been included as shown in Figure 4.3, the additional flux beyond the knee in the profile may instead represent contributions from nonzero sky counts.

To further test the accuracy of the photometry for the low surface brightness galaxies, we use the same lsb method to obtain photometry for six additional dwarf galaxies with existing magnitude measurements in the *lowz* catalog, AGC202248, CGCG 065-074 (AGC200499), CGCG 065-086 (AGC200532), FS 17 (AGC202027), CGCG 066-109 (AGC210023), I692 (UGC6438), and I2828. Since bad deblends are flagged but not necessarily addressed in the VAGC, the resulting photometry may differ from that derived from the lsb method for the patchy, extended low surface brightness dwarfs. However, the *lowz* catalog may offer a more fair comparison since many more of the nearby galaxies (although certainly not all of the $\sim$28,000 sources) have been visually inspected and corrected for deblending issues.

The comparison of the *lowz* and lsb method photometries for all 5 bands is given in Figure 4.5. If the sky subtraction performed by the lsb method improves upon the subtraction done by the automated SDSS pipeline which tends to overestimate sky background for extended, low surface brightness objects, we expect the magnitudes derived from the lsb method to be brighter. This

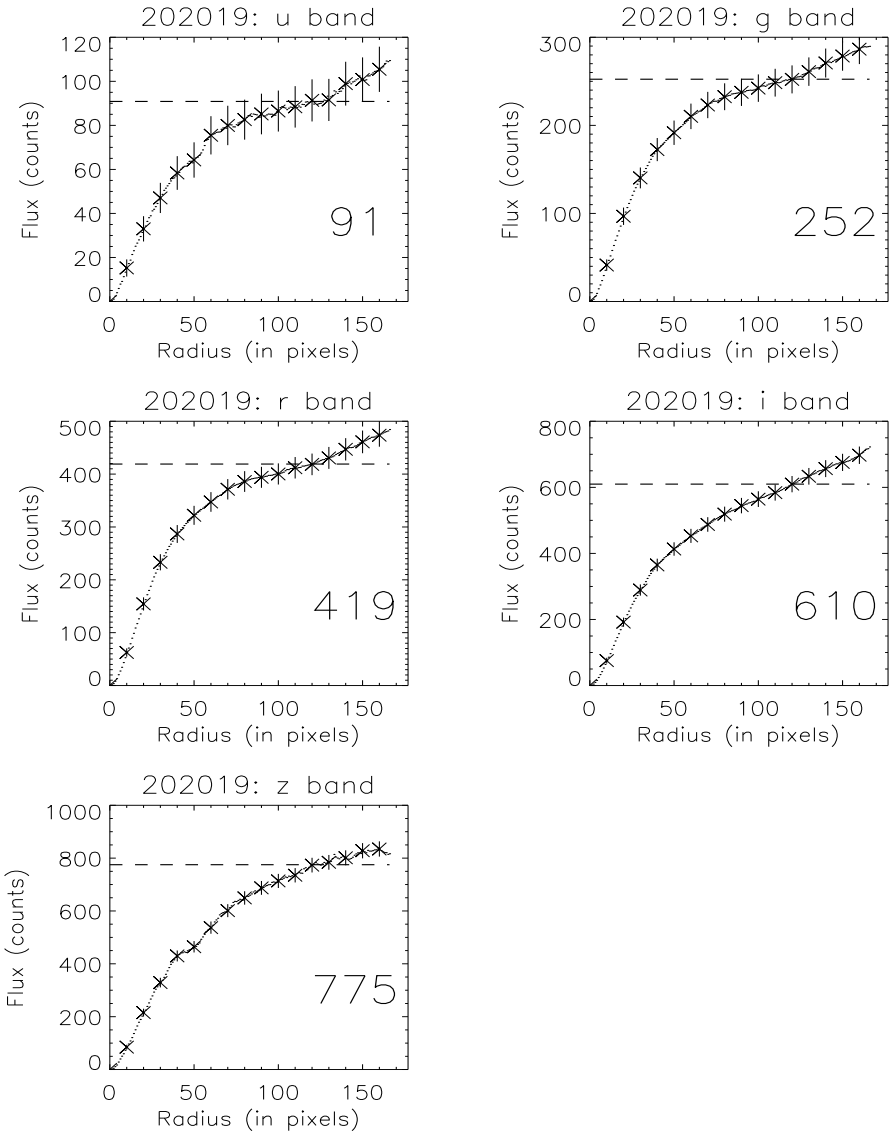

Figure 4.4 Radial profiles (radius versus magnitude) for Leo I dwarf AGC202019 in all five bands. The counts used to determine the Petrosian magnitudes with the lsb method (which are labeled and overplotted as dashed lines) align with the count level at which a knee occurs in the radial profiles. Note that the y-axes have different scales in order to show more detail.

trend is seen for all 6 galaxies in all but the u filter where sky subtraction is known to be more difficult [Baldry et al., 2005]. The results for five of the galaxies agree within 0.5 magnitudes (with $\sigma < 0.3$) for each filter which is a large difference when compared to error estimates claimed by the SDSS pipeline [Lupton et al., 2001], but such an uncertainty may be a reasonable expectation for the low luminosity galaxies in our sample. The galaxy that differs by more than 0.5 magnitudes in each of the 5 bands is CGCG 066-109 which we noted earlier as a candidate for a *lowz* catalog member that may still have deblending problems. Only one spectrum exists for the galaxy, but more than a dozen photometric targets are associated with CGCG 066-109 which could cause the pipeline to leave some flux unaccounted for if not all of the targets are included or, conversely, to include extra flux from foreground or background sources unrelated to the galaxy.

Although Petrosian photometry produces reliable results for most nearby galaxies, particularly those with amorphous and irregular structure, extended and inclined galaxies of high signal-to-noise (some of which are found in the Leo I sample) often benefit from model fitting [Strauss et al., 2002]. Both the VAGC and *lowz* catalogs provide Petrosian magnitudes as well as magnitudes derived from fitting a Sersic function to the radial profile of each galaxy:

$$I(r) = I_0 \, exp[(r/r_e)^(1/n)] \tag{4.4}$$

where I_0 is the central surface brightness, r_e is the radius of the half light isophote, and n, the Sersic index, is 1 for an exponential profile and 4 for a deVaucouleurs profile. As described in Lupton et al. [2001], the best fit profile, convolved with a double Gaussian to account for seeing, is fit to the mean fluxes within annuli starting at the center of a galaxy and extending out to twice the Petrosian radius. Model magnitudes were adopted for the Leo I galaxies with

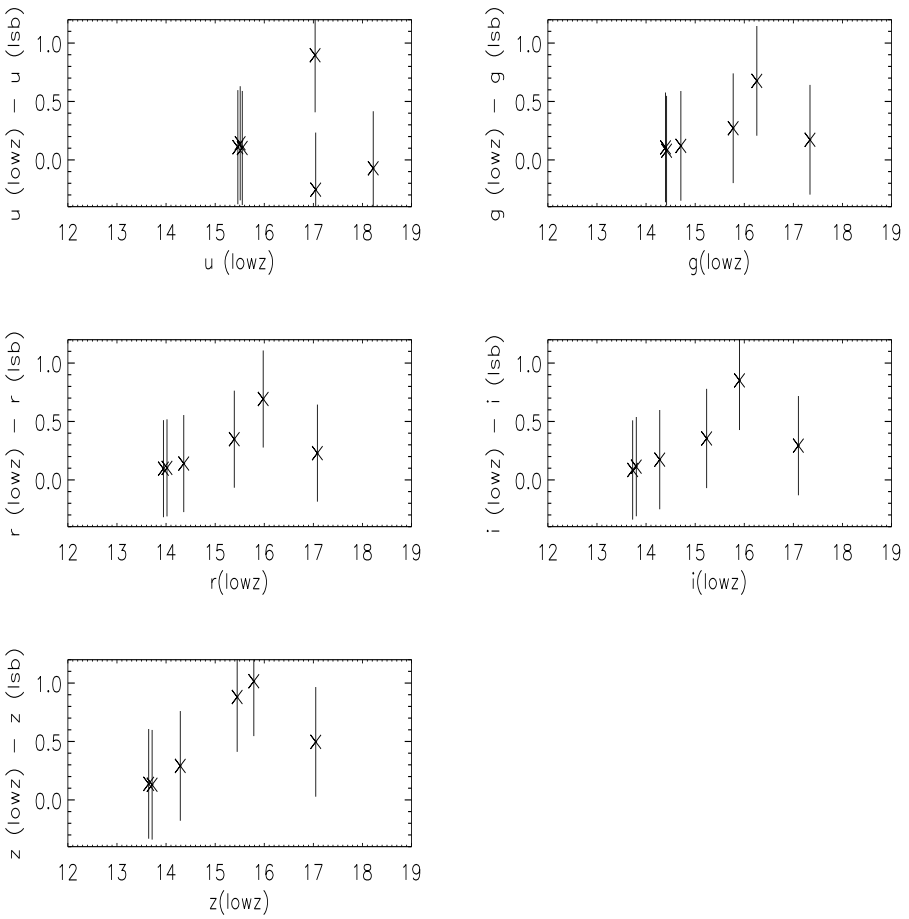

Figure 4.5 Comparison of photometry from the lsb method with the *lowz* catalog measurements for 6 galaxies. In all but the u band, the lsb method returns brighter magnitudes which is consistent with improved sky subtraction. The results for five galaxies agree within 0.5 magnitudes ($\sigma < 0.3$) which may be a reasonable uncertainty to expect for galaxies at the faint end of the galaxy luminosity function. CGCG 066-109 shows the largest discrepancy in each of the filters and may reflect the existence of deblending issues still present in the *lowz* catalog. More than a dozen photometric targets identified by the SDSS pipeline are associated with the galaxy which can lead to an overestimate of the flux (if contaminating sources are included) or an underestimate (if not all of the proper photometric targets are included in the flux determination).

well-defined structure in their r-band images and for which low χ^2 values were returned for the composite model fit. Ten galaxies in our sample fit these criteria: AGCs 5761, 200499, 5882, 5889, 5902, 5911, 5923, 211261, 6272, and 6438.

The Petrosian and model photometries for the 68 Leo I galaxies in the VAGC sample are compared in Figure 4.6. The residuals ($\Delta m = Petrosian\ mag - model\ mag$) are plotted against the Petrosian magnitude in each band. The agreement between the two methods is stronger in the g and r bands where signal-to-noise ratios for galaxy emission are typically highest. For all five filters, the discrepancies between the two methods are similar across the entire magnitude range of the sample (i.e. fainter objects do not necessarily result in larger differences). Without clear trends between the brightness of an object and the resulting difference between the two methods, the choice between model versus Petrosian photometry is best made on a case by case basis through visual inspection of the galaxy's morphology and validation of the axial ratio determined for the best fit model. In Figure 4.6, the ten galaxies for which model magnitudes were adopted over Petrosian values are shown as filled circles.

4.3 Magnitude Corrections and Errors

Before optical properties like stellar masses and mass-to-light ratios can be derived for our sample, corrections for internal extinction, galactic extinction, and k-corrections must be applied to the measured magnitudes.

Internal Extinction

When a galaxy is inclined with respect to a line of sight, the observer must

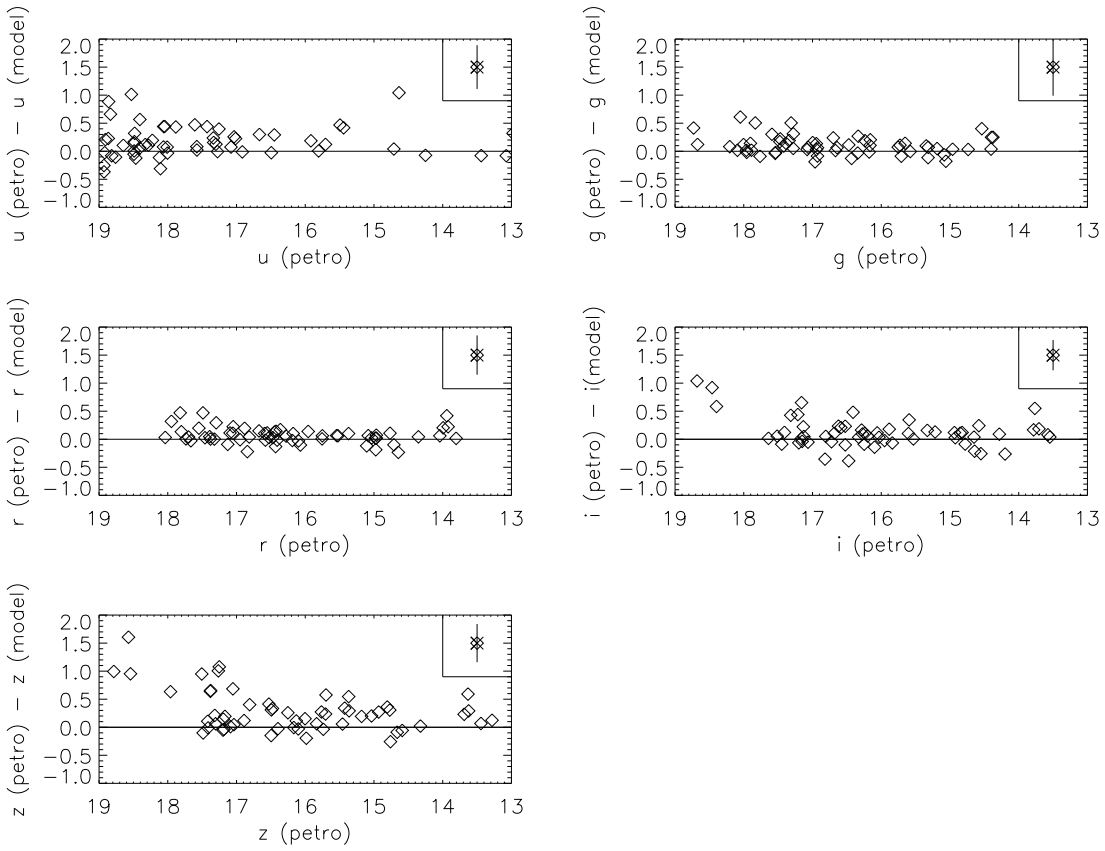

Figure 4.6 Comparison of Petrosian versus model magnitudes given in the VAGC for 68 Leo I galaxies in all 5 bands. In the g and r bands where sky subtraction is most reliable, the methods agree within 0.5 magnitudes. The residuals are similar across the entire magnitude range (i.e. fainter objects do not neccessarily produce larger residuals between the two methods), and thus the choice between the two techniques is best made on a case by case basis comparing galaxy morphology with the parameters determined for the best model fit. The errors are dominated by photometric uncertainties which are the same for every source in each band so we give a mean error bar in the upper right corner of each plot.

look through more gas and dust to see the inner parts of the galaxy. As light from the center of the galaxy travels through the disk, the dust preferentially absorbs blue light and then in turn emits redder photons. Without correcting for this internal extinction, the galaxy will have an underestimated blue luminosity which can lead to significant scatter in the color-magnitude diagram for galaxies [Tully et al., 1998]. Prescriptions for internal extinction corrections, which depend on the band in which the galaxy has been observed, can be deduced from observable galaxy properties such as inclination or luminosity (Giovanelli et al. [1995];Masters et al. [2003]), Hubble type [Gavazzi and Boselli, 1996], or rotation speed [Tully et al., 1998]. However, for galaxies with irregular morphologies that lack a clear inclination angle, the error in the application of such a correction can often outweigh the correction itself. In order to apply internal extinction corrections only for the Leo I galaxies for which they are appropriate (and thus not introduce unnecessary errors), we use the corrections only for those late-type galaxies for which photometry was derived using model magnitudes (see Table 4.1 below). This subset of Leo I galaxies is characterized by well-defined structure, intermediate to high luminosities, and large optical and HI extent.

Following Equations 11-13 in Tully et al. [1998], we determine the internal extinction correction for the B, R and I bands based on the measured HI line width:

$$\gamma_B = 1.57 + 2.75(logW_R - 2.5), \tag{4.5}$$

and

$$\gamma_R = 1.15 + 1.88(logW_R - 2.5), \tag{4.6}$$

and

$$\gamma_I = 0.92 + 1.63(logW_R - 2.5), \tag{4.7}$$

where $W_R = 2v_{rot}$ and v_{rot} is the rotational velocity as determined by ALFALFA. For the two nearly face-on galaxies (AGCs 5889 and 6438) we obtain a non-physical negative value for γ_B and so do not assign those sources a correction for internal extinction. The remaining sources requiring internal extinction corrections are NGC3299, CGCG 065-074, NGC3368, CGCG 038-022 (UGC5923), and NGC3593. Since the prescription for γ_B in Equation 4.5 is derived for B band magnitudes, we are forced to convert the g and r band magnitudes to a B-band measurement, apply the correction, and then convert back to the SDSS filters. The conversions used are those from Blanton and Roweis [2007]. In the SDSS to Landolt filter direction they are:

$$B = g + 0.2354 + 0.3915[(g - r) - 0.6102] \tag{4.8}$$

and

$$V = g - 0.3516 - 0.7585[(g - r) - 0.6102]. \tag{4.9}$$

Galactic Extinction

Just as the disk of an observed galaxy contributes to the reddening of that galaxy's light, so does the disk of the Milky Way affect our extragalactic photometry. We use the galactic dust maps of Schlegel et al. [1998] from the COBE/DIRBE satellite to find the extinction correction to be applied along each line of sight for each SDSS filter. Using the IDL routine *dirbe_bandpass*[2], the average galactic extinction corrections are found to be $A_u = 0.134$, $A_g = 0.098$, $A_r = 0.071$, $A_i = 0.054$, and $A_z = 0.038$.

[2]The corrections found using *dirbe_bandpass* are actually for the test $u'g'r'i'z'$ filters which are not identical to the actual ugriz filters. However, several attempts at improvements and converting to the unprimed system resulted in only subtle differences on the order of 0.01 magnitudes, values smaller than the observational error in the magnitudes themselves. Thus we feel confident, at least for the purposes of the high galactic sky covered by ALFALFA, in applying the corrections derived for the primed system to the unprimed measurements.

K Correction

If a galaxy emits light in a given band, and an observer detects that light in the same band, no correction is needed to accurately determine that galaxy's color and luminosity. However, the redshifting of a galaxy's light usually results in the emission being observed in a different band. A k-correction is necessary to account for the fact that an absolute magnitude can only be determined with the help of a reference or rest frame observation in the same band. We investigate the k-corrections that would be required for the very nearby galaxies in our sample using the extensive code already written for this task [Blanton et al., 2003]. The K-correction ($K_{QR}(z)$)for converting an apparent magnitude in band R (m_R) to an absolute magnitude in band Q (M_Q) is applied following Hogg et al. [2002]:

$$m_R = M_Q + DM(z) + K_{QR}(z) \tag{4.10}$$

where DM(z) is the distance modulus for the galaxy. The difference between the fluxes that would be observed for a particular galaxy in different bandpasses can be completely determined from the galaxy's spectral energy distribution and from knowledge of the bandpass sensitivities. Using the *kcorrect* routines of Blanton et al. [2003], we find the average k-correction to be on the order of $k_u \sim 0.029$, $k_g \sim 0.008$, $k_r \sim 0.010$, $k_i \sim 0.001$, and $k_z \sim 0.008$. Since these corrections are significantly smaller than the other uncertainties in our measurements, we conclude the Leo I galaxies are nearby enough that k-corrections are unnecessary.

Sky subtraction correction for u-band photometry

In a detailed study of the u-band galaxy luminosity function, Baldry et al. [2005] note the presence of a non-astrophysical variation for u - g galaxy color

versus camera column (i.e. the location of the pixels containing the source of interest on the CCD). They conclude that scattered light introduces a more significant systematic error for sky background estimates in the u-band than for the other four bands. Based on an empirical relation fit to the variation, they suggest a correction that increases for decreasing galaxy surface brightness and is on the order of 0.3 to 0.4 magnitudes for the lowest surface brightness objects ($\mu = 28$ mag arcsec^{-2}). They also suggest the use of model magnitudes over Petrosian values since the aperture sizes used in the Petrosian system tend to be larger and thus more likely to include scattered light. Since the corrections are most significant for sources of low surface brightness for which we do not use SDSS photometry but instead the updated pipeline described above, we do not apply the u-band corrections suggested by Baldry et al. [2005]. The different treatment of sky subtraction between the two methods is likely to have different systematic variations. We also still opt for the use of Petrosian magnitdues since we avoid large apertures through the previously described trimming efforts.

Uncertainties

For an accurate assessment of the magnitudes and colors derived for the galaxies in the Leo I sample, we require a careful estimation of the uncertainties associated with each measurement. Three main contributions to the error are considered: calibration errors, photometric zero point errors, and uncertainties associated with the correction factors described above. Since we choose not to apply the corrections with large uncertainties, we assume the latter source of error is negligible when compared to the other two sources.

Poisson statistical errors in the counts associated with a detection, the uncertainty in background sky subtraction, and the dark current and read noise of

the detector all contribute to the uncertainty in the calibration of an image. The inverse variance associated with the calibration error is found using the CCD equation of Mortara and Fowler [1981]:

$$\frac{1}{\sigma} = \frac{N_*}{[N_* + n_{pix}(1 + \frac{n_{pix}}{n_B})(N_S + N_D + N_R^2)]^{(1/2)}} \tag{4.11}$$

where n_{pix} is the total number of pixels in the image and n_B is the number of pixels used to calculate the sky background. In Equation 4.11, four sources of calibration error are added in quadrature: the contribution from Poisson counting errors (using N_*, the total number of source counts), from the uncertainty in the sky background (using N_S, the number of sky counts per pixel from the surrounding sky), from the dark current (using N_D, the total number of dark current electrons per pixel) and finally from the read noise of the detector (using N_R, the total number of electrons per pixel from read noise). The read noise error is indepentent of the integration time and so enters the equation not as a square root.

For the galaxies found in the VAGC and *lowz* catalogs, the inverse variance from calibration uncertainties is given for the flux measurement in each band. A similar error was calculated for the fluxes derived from the lsb method. Propagation of error dictates that errors in flux (ϵ_f) are converted to errors in magnitudes (ϵ_m) following:

$$\epsilon_m = 1.0857\epsilon_f. \tag{4.12}$$

The VAGC gives the errors in the ugriz magnitudes for AGC202222 as 2.93, 21.55, 9.07, 3.43 and 0.30, so we do not use this galaxy in our analysis. Likewise, a reliable magnitude for the extremely faint AGC201970 could only be determined in the i-band (and even then with very large uncertainty), and so we also do not include this galaxy.

The second major sources of error involves the determination of the photometric zero point (i.e. converting relative magnitudes to absolute ones). The current (improved) SDSS photometry is known to within 1.35% for the u and z bands and to within 0.9% for the gri bands [Padmanabhan et al., 2008]. SDSS documentation[3] quotes the following photometric zero points: 24.63 for u band, 25.11 for g band, 24.8 for r band, 24.36 for i band, and 22.83 for z band.

Finally we add an additional error for sources greater than $1'$ to account for possible deblending issues. As previously discussed and as shown in Figure 4.2, bad deblends may still exist in the *lowz* and VAGC catalogs. We estimate the uncertainty associated with possible deblending problems as the standard deviation of the residuals for the three sources that had improved photometry in the *lowz* catalog when compared with that of the VAGC (see Figure 4.2). Thus we find $\epsilon_{deblend} = 0.36$.

The three possible error contributions are added in quadrature to give a final error estimate associated with the magnitude measurement for each galaxy:

$$\epsilon_{tot} = \sqrt{(\epsilon_{cal})^2 + (\epsilon_{phot})^2 + (\epsilon_{deblend})^2} \tag{4.13}$$

The photometry results for the Leo I galaxies for which SDSS data was available are presented in Table 4.1. The first column gives the AGC designation, and the second column presents the optical extent for the galaxy, measured to be the radius of the aperture (in arcseconds) that contains 90% of the galaxy's emission. The third column presents the galaxy's r-band magnitude corrected for galactic extinction and its associated error. The third through sixth columns give the extinction-corrected colors for each galaxy ($u - r$, $g - r$, $r - i$, and

[3]http://www.sdss.org/dr5/algorithms/fluxcal.html

$r - z$ respectively). Although the uncertainties in the g and i bands are well represented by the uncertainty presented for the r band, for the u and z bands the uncertainty is on average 1.5 to 2 times larger. For reference, the seventh column gives the correction for galactic extinction that has been applied to the r-band magnitude based on the DIRBE maps [Schlegel et al., 1998]. The final column lists the method used for determining the photometric parameters. Parameters for galaxies tagged as *VAGC* come from the NYU-VAGC, and those marked *lowz* are pulled from the *lowz* subset of the VAGC. A 'p' means the galaxy has irregular morphology and Petrosian photometry was performed, while an 'm' denotes that the galaxy was fit well by a composite of deVaucouleurs and exponential profiles and so model magnitudes were adopted. The 'LSB' method refers to the West [2005] pipeline described above and is only used for those objects that were too low surface brightness to be found in the VAGC or *lowz* catalogs. Since all of these low surface brightness objects are patchy and lacking clear structure, only Petrosian photometry is used with the LSB method.

SDSS photometry for 22 of the 105 Leo I galaxies are not found in Table 4.1. Eight of the most luminous galaxies (UGCs 5708, 5812, 5850, 5899, 5948, 6328, 6346 and 6350) are too extended to have been accurately processed by the SDSS pipeline and, as previously discussed, B-band magnitudes from the RC3 are used instead. Contamination due to foreground stars made the photometry unreliable for AGCs 205165, 208394, 201972 (KK 94), and 215286. Similarly, high redshift objects projected directly behind AGCs 201975 (LeG21), 202026 (FS 15), 202028 (FS 40), and 213066 produce unlikely red colors. Although the objects most strongly affected by contamination from foreground or background sources are the low mass dwarfs, such unlucky placement on the sky should be random and thus not bias our sample toward a particular galaxy type. In

the case of AGC200688, a problem with the entire g band image, perhaps contamination due to a satellite just out of the frame, made proper photometry impossible. Five galaxies, AGCs 208399, 200560, 201970 (LeG18), 205078 and 202222, were simply too faint to obtain accurate fluxes even after careful sky background subtraction. All but the last of these objects are HI-bearing dwarf irregulars, and thus the lack of photometry places bias against complete representation of HI-bearing dwarfs of extremely low surface brightness. Blank columns in Table 4.1 mark cases where the object was either too faint for reliable photometry (in the cases of u, g and z band blank entries) or the presence of a contaminating satellite trail (in the case of empty i band entries).

4.4 Summary

In this chapter, we investigated the optical photometry for a sample of 105 galaxies from the Leo I group using data from the Sloan Digital Sky Survey. This sample presented a challenge for the publicly available SDSS-based catalogs as it included 19 galaxies that were of too low surface brightness to be identified by SDSS, as well as several extended ($> 1'$) galaxies, both of high and low luminosities, that confused the deblender employed by the SDSS pipeline. Magnitudes were obtained from the NYU-VAGC and *lowz* catalogs when available. For the lowest surface brightness objects not found by the SDSS catalogs, we used a method courtesy of collaborator Andrew West and designed for photometry of nearby, extended galaxies. Petrosian and model-based fluxes were computed using circular apertures and then corrected for galactic extinction and for internal extinction when appropriate.

Table 4.1. SDSS Optical Photometry for Leo I Galaxies

AGC	Other Name	R_{90} arcsec	r (ϵ_r)	u - r	g - r	r - i	r - z	A_r	Method
202171		8.53	17.29 (0.40)	1.33	0.48	-0.20	-0.24	0.11	lowz (p)
5453	093-047	16.72	14.88 (0.24)	1.44	0.31	-0.40	-0.17	0.09	VAGC (p)
203913	037-033	20.84	16.13 (0.24)	1.80	0.27	-0.11	0.34	0.07	lowz (p)
202218		17.71	15.65 (0.25)	1.59	0.55	-0.12	-0.00	0.10	VAGC (p)
205156		5.54	18.09 (0.41)	1.35	0.45	-0.26	-0.36	0.09	LSB
204139		9.04	17.63 (0.37)	1.09	0.31	-0.27	-0.21	0.12	lowz (p)
202248		11.40	17.00 (0.32)	1.06	0.22	0.04	0.01	0.09	lowz (p)
202017	LeG03	21.40	16.59 (0.26)	1.66	0.20	-0.52	-0.48	0.07	lowz (p)
5761	N3299	31.92	13.48 (0.24)	3.01	0.48	-0.12	-0.43	0.07	VAGC (m)
200499	065-074	17.03	13.65 (0.25)	1.10	0.26	-0.10	-0.32	0.08	lowz (m)
202018	LeG04	16.90	17.73 (0.26)	3.99	0.90	0.68	0.19	0.07	VAGC (p)
202019	LeG05	13.84	16.36 (0.32)	1.74	0.55	-0.12	-0.26	0.07	VAGC (p)
200512	LeG06	31.88	16.59 (0.42)	1.77	0.16	-0.12	-0.36	0.10	LSB
200532	065-086	20.44	15.32 (0.24)	1.60	0.36	-0.14	0.09	0.07	lowz (p)
205268		8.81	16.87 (0.33)	1.39	0.44	-0.20	-0.42	0.08	VAGC (p)
202020	LeG09	20.28	17.15 (0.41)	1.68	0.52	-0.30	-0.56	0.07	LSB
202021	LeG10	9.86	18.88 (0.42)	1.70	0.47	-0.19	-0.60	0.07	LSB
202022	LeG11	15.29	17.62 (0.42)	1.35	0.55	-0.49	-0.08	0.09	LSB
202023	LeG12	9.54	18.57 (0.41)	1.06	0.37	-0.04	-0.36	0.08	LSB
205445		15.20	15.98 (0.26)	1.86	0.33	-0.21	-0.20	0.09	VAGC (p)
202024	LeG13	16.83	17.13 (0.41)	1.00	0.45	-0.17	0.06	0.06	LSB
202025	FS 13	18.93	17.83 (0.41)	0.73	0.46	-0.01	0.49	0.07	LSB
201990	FS 14	21.78	16.78 (0.43)	1.50	0.46	-0.26	-0.50	0.08	LSB
202027	FS 17	18.44	16.51 (0.26)	1.49	0.49	-0.30	-0.27	0.07	lowz (p)
5882	N3368	52.88	9.72 (0.24)	2.49	0.66	-0.30	-0.88	0.07	VAGC (m)
201971	FS 20	13.38	18.10 (0.42)	1.72	1.02	-0.48	-0.72	0.06	LSB
205505		38.20	16.35 (0.24)	1.29			1.94	0.06	VAGC (p)
5889	N337A	40.46	14.56 (0.24)		0.44	-0.30	1.71	0.10	VAGC (m)
5902	N3379	22.96	9.98 (0.24)	2.55	0.80	-0.11	-0.72	0.07	VAGC (m)
5911	N3384	24.72	10.39 (0.24)	2.63	0.75	0.35	-0.72	0.07	VAGC (m)
200596	066-026	21.85	14.86 (0.24)	2.28	0.57	-0.29	-0.14	0.11	VAGC (p)
5923	038-022	21.54	13.37 (0.24)	1.57	0.39	-0.18	-0.50	0.07	VAGC (m)
202029	LeG23	8.51	19.48 (0.41)	0.49	0.12	-0.60	-1.84	0.09	LSB
5944	064-033	26.70	14.95 (0.25)		0.66	-0.08	0.36	0.08	VAGC (p)
201991	KK96	30.37	16.57 (0.42)	2.88	0.50	-0.20	-0.79	0.07	LSB
5952	N3412	35.82	10.90 (0.24)	2.40	0.68	-0.42	-0.66	0.08	VAGC (p)

Table 4.1 (continued)

AGC	Other Name	R_{90} arcsec	r (ϵ_r)	u - r	g - r	r - i	r - z	A_r	Method
5962	N3423	69.74	12.09 (0.24)	2.47	0.70	-0.10	0.11	0.08	lowz (p)
202030	LeG26	17.61	16.30 (0.26)	2.41	0.92	0.06	0.92	0.07	VAGC (p)
205540		10.37	17.30 (0.35)	1.46	0.54	-0.30	-0.31	0.09	VAGC (p)
5974	038-032	27.51	14.26 (0.24)	1.48	0.35	-0.05	0.50	0.09	VAGC (p)
205544		15.99	16.41 (0.26)	3.30	0.58	-0.19	0.05	0.06	VAGC (p)
202456		17.39	15.50 (0.26)	1.97	0.60	-0.20	-0.33	0.06	lowz (p)
202031	LeG27	11.81	17.98 (0.34)	2.06	0.61	0.37		0.06	VAGC (p)
202032	LeG28	17.18	16.81 (0.25)	1.55	0.92	0.29	0.20	0.07	VAGC (p)
6014	066-058	23.64	14.88 (0.24)	1.62	0.32	-0.12	0.44	0.09	VAGC (p)
202034	D640-12	25.42	16.67 (0.43)	1.63	0.56	-0.32	-0.54	0.05	LSB
202035	D640-13	19.28	16.42 (0.26)	0.83	0.23	0.15	1.08	0.05	lowz (p)
202036	D640-14	53.54	17.29 (0.46)	1.48	0.45	-0.24	-0.13	0.05	LSB
205278		17.13	16.54 (0.26)	1.86	0.67	-0.05	0.70	0.05	VAGC (p)
6082	N3489	59.16	10.11 (0.67)	2.18	0.64	-0.35	-0.60	0.05	LSB
202038	LeG33	20.08	18.17 (0.41)		0.59	-0.13	-0.33	0.05	LSB
202039	D640-08	15.58	16.54 (0.26)	1.85	0.33	-0.47	-0.39	0.04	VAGC (p)
210023	066-109	21.41	15.94 (0.25)	1.02	0.26	-0.06	-0.17	0.04	lowz (p)
211261	I678	18.78	13.89 (0.24)		0.91	-0.46	-0.76	0.11	lowz (m)
215282		11.00	16.05 (0.31)	1.74	0.22	-0.05	-0.07	0.05	VAGC (p)
6272	N3593	39.02	10.74 (0.24)	1.91	0.41	-0.50	-1.21	0.05	VAGC (m)
202256		10.61	17.00 (0.32)	1.23	0.31	-0.23	0.35	0.05	VAGC (p)
6277	N3596	45.62	11.84 (0.24)	2.28	0.60	-0.23	-0.07	0.07	VAGC (p)
215281		10.61	17.60 (0.33)	1.19	0.32	-0.01	-0.22	0.06	VAGC (p)
215284		8.90	17.26 (0.30)	1.27	0.20	-0.16	-0.10	0.06	VAGC (p)
212132	039-094	19.20	14.98 (0.24)	1.84	0.55	-0.30	-0.46	0.14	lowz (p)
210220	I2684	21.52	15.45 (0.26)	2.94	0.61	0.09	0.21	0.08	VAGC (p)
213006		10.59	17.66 (0.35)	1.36	0.48	-0.18	-0.26	0.06	lowz (p)
202257		13.36	16.99 (0.25)	1.19	0.27	-0.51	-0.13	0.05	VAGC (p)
215354		13.06	16.75 (0.26)	1.62	0.44	-0.12	-0.39	0.06	VAGC (p)
213074		12.29	16.81 (0.25)	0.68	0.10	-0.01	0.49	0.05	lowz (p)
211370	I2767	14.42	16.60 (0.25)	2.13	0.24	-0.03	0.17	0.07	VAGC (p)
213436		16.68	16.12 (0.26)	1.87	0.45	-0.22	-0.42	0.07	VAGC (p)
6395	I2782	21.60	14.58 (0.25)	2.21	0.39	-0.43	-0.29	0.07	VAGC (p)
6401	U6401	25.35	14.91 (0.25)	2.21	0.65	-0.11	-0.02	0.07	VAGC (p)
213440	I2791	16.23	16.45 (0.26)	1.47	0.37	-0.18	-0.51	0.07	VAGC (p)
215142		15.81	16.18 (0.26)	1.70	0.33	-0.06	0.29	0.10	VAGC (p)

Table 4.1 (continued)

AGC	Other Name	R_{90} arcsec	r (ϵ_r)	u - r	g - r	r - i	r - z	A_r	Method
6438	I692	16.47	13.59 (0.24)	1.21	0.38	-0.15	-0.31	0.13	lowz (m)
215296		7.33	18.35 (0.41)	1.19	-0.02	0.04	-0.22	0.10	LSB
210340		20.05	14.21 (0.26)	1.06	0.29	-0.05	-0.00	0.15	lowz (p)
213091		12.48	17.39 (0.34)	0.92	0.52	-0.25	-0.06	0.10	VAGC (p)
212837	KKH68	10.90	17.14 (0.25)	1.24	0.44	-0.26	-0.32	0.11	VAGC (p)
215303		9.56	17.47 (0.34)	1.39	0.31	-0.26	-0.29	0.10	VAGC (p)
215304		16.22	15.65 (0.24)	1.43	0.38	-0.20	-0.25	0.11	VAGC (p)
215306		9.73	16.35 (0.32)	1.51	0.48	-0.16	-0.29	0.08	VAGC (p)
215248		12.20	17.03 (0.25)	1.55	0.37	0.02	0.23	0.09	VAGC (p)
210459	I2934	19.29	14.88 (0.24)	1.04	0.18	-0.09	-0.02	0.13	lowz (p)
212838	KKH69	12.12	17.75 (0.27)	0.53	-0.26	-0.39	0.75	0.07	VAGC (p)

The limitations of the automated data reduction pipeline employed by the SDSS are significant for the small Leo I sample. A blind search of the database would have resulted in 5 out of 40 mislabeled optical redshifts, 19 unidentified low surface brightness dwarfs, and large photometric uncertainties for galaxies at the extreme high and low luminosity ends of the galaxy luminosity function (more than half of the sample). Studies that make the best use of the large SDSS database are thus those that investigate statistics of galaxy properites with large sample sizes that render the small percentage of sources with large uncertainties no longer significant.

The optical properties measured in this chapter will be combined with the knowledge of the HI content of Leo I group galaxies explored in previous chapters to make a complete census of the baryon content of the group and to investigate properties of group dwarfs and the implications for dwarf galaxy formation scenarios. In the next chapter we will present a study of two special classes of dwarf that may represent dwarfs at unique stages in their evolution: transition and tidal dwarfs.

CHAPTER 5

OPTICAL SPECTROSCOPY OF HI-SELECTED DWARF GALAXIES

Success is getting what you want; happiness is wanting what you get.

- Ingrid Bergman

5.1 Formation and evolution of dwarf galaxies

Most dwarf galaxies fall into one of two loosely defined categories reminiscent of classes of more massive systems: passively evolving (early-type) dwarfs with dominant old stellar populations, smooth structure, and little to no neutral gas (dEs/dSphs) versus gas-rich (late-type) dwarfs with recent or ongoing massive star formation and patchy structure (dIs). The gas-poor systems present an evolutionary puzzle since their stellar populations could not have formed without the presence of gas at some time in their histories. Three possible scenarios are considered to cause the gas deficiency: 1) these galaxies have passively evolved to exhaust their gas through star formation; 2) these low mass systems do not have the gravitational potential wells required to retain to their gas; or 3) the gas has been removed by ram pressure stripping or interactions with other galaxies. According to these evolutionary pictures, gas-rich dwarfs then must either follow separate evolutionary tracks or represent earlier incarnations of their gasless counterparts.

If stripped dIs do in fact evolve into dE/dSphs and we assume there is a critical gas density below which star formation cannot proceed, we would expect the existence of a population of dwarfs with old stellar populations but

some neutral gas [Phillipps et al., 1990]. Some authors have suggested a few well-studied galaxies in the Local and Sculptor groups (Grebel et al. [2003a] and Skillman et al. [2003], respectively) may represent such a class of transition dwarf. These systems would be structurally smooth and contain HI gas as well as evidence of localized recent star formation embedded in an older stellar population. While dIs and dSphs show an offset in the slopes of their metallicity-luminosity (Z-L) relations (which some argue suggests separate evolutionary tracks), Grebel et al. [2003a] have found the Z-L relationships for dSphs and transition dwarfs in the Local Group to be similar.

However, the status of these transition objects as evolutionary links remains controversial. Transition dwarfs may also be dEs that have recently acquired their small amounts of neutral hydrogen, or they could represent extreme versions of dIs that are experiencing an interruption in their star formation, or even evolved tidal dwarfs or blue compact dwarfs. Yet another possibility is that transition dwarfs are dIs that are losing gas due to internal mechanisms like supernova blow out [Dekel and Silk, 1986].

While the possibility of dIs evolving into dE or dS0 galaxies after losing their gas is well known (Lin and Faber [1983]; Thuan [1985]), evidence of galaxies currently in the midst of such a transitioning period are rare. Sandage and Hoffman [1991] first noted three galaxies that, based on their optical morphologies and HI gas content, represented a possible evolutionary sequence at three stages of the transition process: NGC 3377A, NGC 4286, and IC 3475. However, further investigation showed the red colors and long gas consumption time scales of NGC 3377A and NGC 4286 made them unlikely progenitors for more gas-poor dwarfs like IC 3475 [Knezek et al., 1999].

Studies of transition dwarfs have disagreed on the definition of what makes a galaxy a transition candidate, but all share the criteria of mixed morphology: an underlying dE or dS0 with evidence of current star formation and some HI gas content. In a study of dwarfs in the Sculptor Group, Skillman et al. [2003] defined transition dwarfs as lacking HII regions (to emphasize the dominance of older stellar populations) but instead required M_{HI}/L_B values typical for dIs. Some of the transition dwarfs identified by Mateo [1998] in his review of the Local Group fit the Skillman et al. [2003] criteria - LGS3 [Young and Lo, 1997], Antlia, DDO210 (McConnachie et al. [2006]; Begum and Chengalur [2004]), and Phoenix (Young et al. [2007]; St-Germain et al. [1999]; Buyle et al. [2006]). However, Mateo [1998] also includes the Pegasus dwarf in his transition sample which is known to have HII knots (Skillman et al. [1997]; Meschin et al. [2009]).

Results from transition dwarf studies have so far been inconclusive due largely to the small sample sizes involved. Of the 14 Local Group satellites discovered in the SDSS in the past four years, only Leo T was labeled a transition dwarf based on its dominant intermediate and old stellar populations mixed with signs of recent star formation and its HI content [Irwin et al., 2007]. Almost by definition, after further study, these mixed morphology objects reveal a wide range of galaxy properties (like Hα flux and metallicity) and thus may not represent one class of galaxy. Skillman et al. [2003] found the transition dwarfs in the Sculptor Group most closely resembled dIs with interrupted or paused star formation due to their low gas content and lack of Hα emission. Grebel et al. [2003b] concluded that transition dwarfs in the Local Group could be progenitors to dSphs based on their similar Z-L and surface brightness-luminosity relationships but that dIs more likely followed separate evolutionary paths. For a sample of five transition dwarf candidates (all of which contained at least one

HII region), Dellenbusch et al. [2007] found the galaxies mimicked evolved (i.e. more metal rich for a given luminosity), low gas content blue compact dwarfs with centrally concentrated ISMs and smooth outer envelopes.

To differentiate between dwarfs evolving from transitional progenitors and those that have been gas stripped due to interactions, dwarf galaxy populations must be examined over a range of different environments. In the Virgo cluster, which is known to foster morphological alterations, a significant fraction of dEs are rotation-dominated [van Zee et al., 2004], suggesting they result from the recent stripping of infalling, gas-rich progenitors. Similarly Lisker et al. [2006] identify a population of Virgo dE/dSphs with disk-like features and blue centers. If instead transition dwarfs are the progenitors of gas-poor dSphs, such transformations are more likely to occur in places where stripping is ineffective. For example, in the Local Group, dwarfs labeled as transitional do not show signs of rotation (for example, LGS 3; see Young and Lo [1997]) and are thus unlikely to be derived from rotating dIs.

The case for separate evolutionary paths for early versus late-type dwarfs in the Local Group may also be supported by the trend of morphological segregation. Passively evolving systems are always found within close proximity of massive galaxies, in contrast to the more widespread, gas-rich and star forming population, suggesting that environmental effects play an important role in dwarf galaxy evolution. More examples of transition dwarf candidates are needed outside of the Local Group to further evaluate where they fit within the framework of morphological segregation as compared to regular gas-bearing dwarfs.

Whether it be their own passive evolution or transformation from gas-rich

progenitors, these proposed dwarf galaxy histories all begin with the same formation scenario, the birth of low mass systems out of small dark matter haloes in the ΛCDM framework. Alternatively, the low mass dwarfs observed in the current epoch may have formed more recently as the result of tidal interactions and mergers among massive galaxies. Numerical simulations have shown that the gravitational collapse of tidal tails can lead to the formation of systems with masses between 10^6 and 10^8 $M_\odot$ (Elmegreen [1993]; Duc et al. [2004]), and objects of similar masses have been found in tidal tails (Duc and Mirabel [1998]; Hibbard et al. [2001]; Mendes de Oliveira et al. [2001]; Higdon and Higdon [2008]). However, only a few known candidates exist for tidal dwarf galaxies (TDGs) that have survived beyond the dissipation of their parent tidal stream (Hunter et al. [2000]; Duc et al. [2007]) due in part to the short lifetimes estimated for such tidal debris (on the order of a few hundred Myrs; Hibbard and Mihos [1995]).

Without a larger sample of TDGs, the fraction of dwarfs that evolve from tidal material remains unknown. Using simulations of TDG formation, Bournaud and Duc [2006] found more than one or two TDGs per massive progenitor to be rare. However, their simulations also showed that TDGs were likely to be found in a flattened distribution favoring the equatorial plane of the progenitor, and based on a statistical analysis of the distribution of Local Group satellites, Kroupa et al. [1993] claim the placement of the majority of the dwarfs are consistent with the tidal origin scenario. In the latter case, the missing satellites problem (see Chapter 1) may be more significant than previously assumed.

Even after the dissipation of their parent streams, TDGs should be distinguished from older generation dwarfs by their lack of dark matter according

to the ΛCDM scenario [Barnes and Hernquist, 1992] and by their strong deviation from the Z-L relationship. Duc et al. [2007] have recently identified VCC 2062, a dwarf galaxy in the outskirts of the Virgo Cluster, as a candidate "old" tidal dwarf because of its strong CO emission and oxygen abundance, a critical indicator of recycled material.

The unique HI-selected sample produced by ALFALFA is perfect for the detection of both transition and tidal dwarf candidates. As discussed in Chapter 2, the survey's superior sensitivity, spectral and spatial resolution produce a rich dataset of nearby, HI-bearing, low-mass dwarf galaxies. Little is known about the controversial class of transition dwarfs, but the fact that there are six candidates in the Local Group (Mateo [1998]; Grebel et al. [2003a]; Irwin et al. [2007]) and three in the nearby Sculptor group (Skillman et al. [2003]; Da Costa et al. [2007]) suggests these objects may be very common among the lowest luminosity, gas-rich dwarfs like those that dominate the Leo I sample. Dwarfs tagged as transitional are typically on the low luminosity end of the range for gas rich dwarfs [Skillman et al., 2003] so selecting by their gas content is advantageous over optical searches that may miss these faint objects. Likewise, interactions among galaxies leave behind the clearest evidence in their HI gas, and so tidal dwarf candidates are most easily identified by starting with the knowledge of the location and structure of HI tidal remnants.

To better understand the formations and transformations of dwarf galaxies, we present in this chapter the careful selection of a set of low-mass ALFALFA galaxies which exhibit the characteristics of transtion or tidal dwarfs. As described in the following sections, these galaxies were targeted for nebular abundance studies to gain insight into their formation mechanisms. The relationship

of transition dwarf galaxy metallicities to other galaxy properties like luminosity may rule out or affirm their potential as a progenitor class of galaxies. The metallicities of tidal dwarf candidates reveal whether these objects were formed from recylced material. The spectroscopic data presented here are derived from observations spanning the past three years and thus are limited by the sample of ALFALFA galaxies in its early stages. The current ALFALFA dataset which is much larger (and still growing), as well as additional telescope time allotted for optical spectroscopy, will offer opportunities for more complete samples.

5.2 Sample selection

5.2.1 Transition dwarf candidates

The transition dwarf candidates in our sample all come from the ALFALFA dataset and thus have known HI gas content. The ALFALFA catalog was searched for objects of low HI mass that resembled early-type galaxies. All objects in the sample have $M_{HI} \lesssim 10^{8.5}\ M_{\odot}$, redder colors (i.e. $g - r > 0.4$ from SDSS) when compared to the average, star-forming ALFALFA dwarf, and smooth stellar distributions lacking disk structure (as seen in SDSS broadband imaging).

Most transition candidates were also determined to have Sersic indices $n > 1.5$ (where higher n values are more typical of elliptical galaxies while disc galaxies favor $n \sim 1$). Sersic indices were taken from the NYU-VAGC (Blanton et al. [2005b]; see Chapter 4) and derived from SDSS photometry. Despite having lower Sersic indices, two objects, AGC191803 with $n = 1.06$ and AGC204301

with $n = 1.16$, were still included in the sample based on their morphologies. Although both galaxies showed a dominant smooth stellar distribution, they lacked an obvious nucleus which may have led to their lower Sersic numbers. In four additional cases, (AGC215306, AGC223407/VCC304, AGC232142, and AGC262737) the objects were too faint to produce reliable photometry so they were included in the sample based on morphology alone (i.e. the derived Sersic indices were ignored).

The basic HI parameters for 32 transition dwarf candidates are given in Table 5.1, and all are pulled directly from the ALFALFA catalog except when otherwise noted. Broadband optical images from SDSS are also given for all 32 candidates in Figures 5.1 and 5.2. Each image is $100''$ by $100''$. We stress the use of the word "candidate" because so little is known about this class of galaxy that their status as evolutionary links (i.e. galaxies actually in "transition") remains controversial. Leo group member NGC 3377A, which was noted among the first references to transition dwarfs [Sandage and Hoffman, 1991], is not included in our list as its status as a transition galaxy has already been explored in detail (Skillman et al. [2003]; Knezek et al. [1999]).

Table 5.1. Transition Dwarf Candidates in the ALFALFA Survey

AGC #	Other Name	Opt Position[a] (J2000)	HI $cz_\odot$ km s^{-1}	W50 km s^{-1}	F_c Jy km s^{-1}	Dist[b] Mpc	log M_{HI} $M_\odot$
191803		09 48 05.9 +07 07 45	535	55	1.62	7.2	7.29
204301[a]		10 16 59.0 +03 42 35	...	...	...	...	...
200496	065-072	10 37 23.3 +12 09 23	2857	176	1.02	45.4	8.69
200499	065-074	10 38 08.0 +10 22 51	1175	178	7.79	11.1	8.35
202019[b]	LeG05	10 39 43.0 +12 38 04	780	22	.08	11.1	6.37
200532	065-086	10 42 00.3 +12 20 07	772	36	0.96	11.1	7.46
202024	LeG13	10 44 57.5 +11 54 58	871	24	0.23	11.1	6.81
215287		11 19 45.1 +15 30 08	1334	103	0.73	17.5	7.72
215306		11 33 50.1 +14 49 28	1129	64	0.45	20.4	7.54
220167	I3025	12 10 23.0 + 10 11 18	485	67	0.81	5.3	6.73
220176	069-072	12 10 57.0 +09 13 09	2240	150	1.41	32.5	8.55
7181	I3033	12 11 09.9 +13 35 15	265	117	4.05	16.2	8.40
223286	I3052	12 13 48.1 +12 41 26	841	50	0.53	17.5	7.58
220257	VCC168	12 15 53.7 +14 01 30	683	60	0.47	16.2	7.47
7285	I3077	12 15 56.3 +14 25 57	1406	51	0.44	16.7	7.44
220282	I3096	12 16 52.4 +14 30 55	1263	74	0.55	16.2	7.53
220286[c]	158-018	12 17 07.3 +30 38 35	(778)	(66)	(0.11)	...	...
220321	I3120	12 18 15.3 +13 44 56	248	32	0.46	16.7	7.46
223407	VCC 304	12 18 43.8 +12 23 08	132	35	0.49	16.7	9.05
223445		12 20 30.7 +13 31 09	2098	111	0.52	33.1	8.13
220510	UA279	12 24 14.5 +04 13 33	1182	173	1.07	16.7	7.84
220555	VCC 841	12 25 47.4 +14 57 08	499	39	0.67	16.7	7.64
223724	VCC1202	12 29 33.6 +13 11 46	1215	286	2.20	16.7	8.15
220739	I3466	12 32 05.7 +11 49 04	909	38	1.37	16.7	7.95
220819	VCC1617	12 35 30.9 +06 20 02	1600	71	0.54	16.7	7.5
7817	I3611	12 39 04.0 + 13 21 49	2737	69	0.94	16.7	7.78
7889	N4641	12 43 07.7 +12 03 02	2021	54	0.71	16.7	7.66
221013	UA298	12 46 55.4 +26 33 51	844	65	0.63	10.4	9.02
232142		13 56 09.4 +05 32 33	1096	38	0.79	20.3	7.88
251419[d]	MTT-124	15 04 08.3 +01 31 28	1845	29	0.25	29.1	...
250103[a]	021-013	15 08 05.8 +01 39 05	...	...	...	...	...
262737[a]		16 40 21.4 +28 45 56	...	...	...	...	...

[a]HI parameters are tentative: awaiting further processing of ALFALFA data in this area of the sky.

[b]Source of HI detection: single pixel observations described in Chapter 3.

[c]Source of HI detection: Arecibo Gregorian feed; HI parameters uncertain so should be used as estimates only and no HI mass is derived.

[d]HI detection noticed in early stages of ALFALFA data reduction but a complete, gridded dataset in this area of the sky is not yet available so only estimates of HI parameters are given.

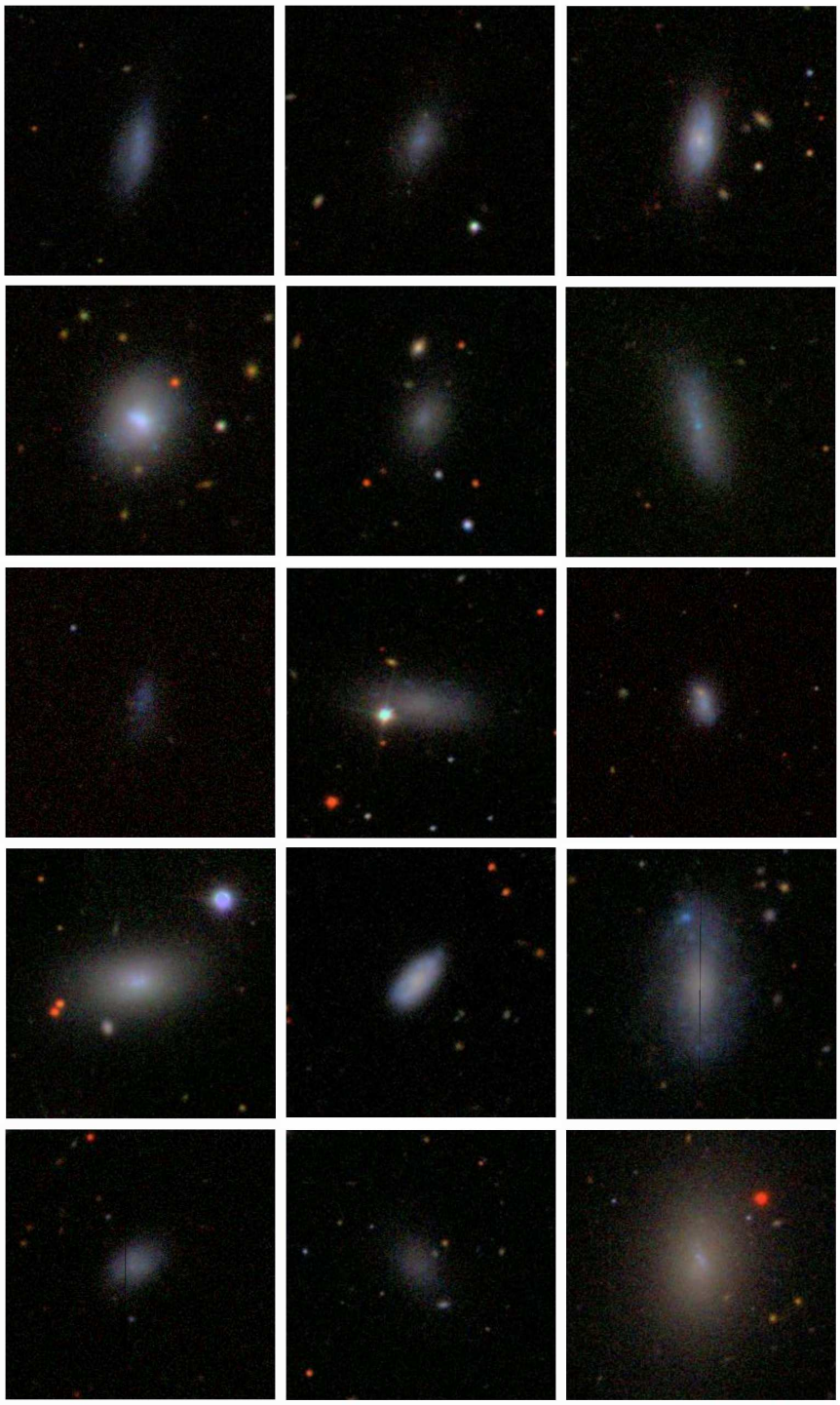

Figure 5.1 SDSS broadband images of 15 transitional dwarf candidates found in the ALFALFA survey. Moving left to right, starting at the top: AGC191803, AGC204301, AGC200496, AGC200499, AGC202019, AGC200532, AGC202024, AGC215287, AGC215306, AGC220167, AGC220176, AGC7181, AGC223286, AGC220257 and AGC7285. Each image is $100''$ by $100''$.

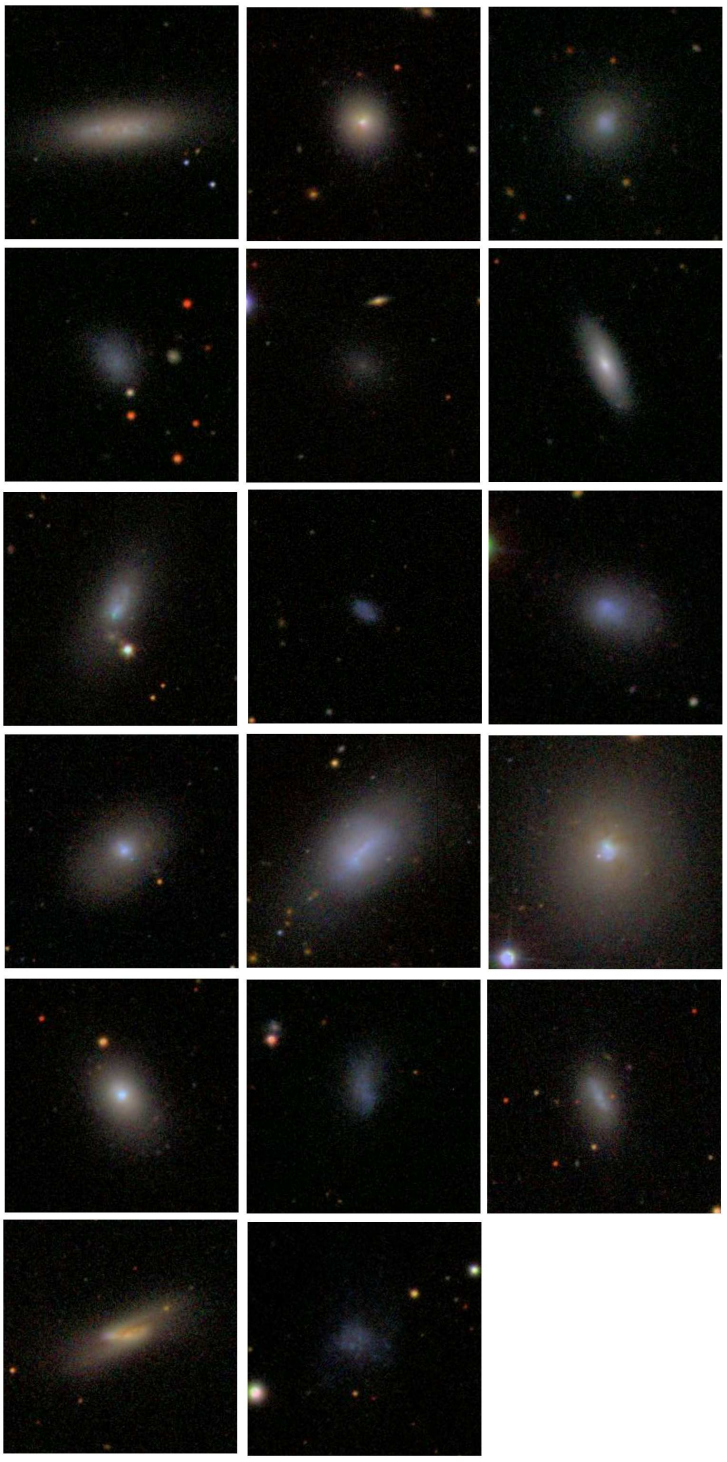

Figure 5.2 SDSS broadband images of 17 transitional dwarf candidates found in the ALFALFA survey. From left to right, starting at the top: AGC220282, AGC220286, AGC220321, AGC223407, AGC223445, AGC220510, AGC220555, AGC223724, AGC220739, AGC220819, AGC7817, AGC7889, AGC221013, AGC232142, AGC251419, AGC250103 and AGC 262737. Each image is $100''$ by $100''$.

Table 5.2. Tidal Dwarf Candidates

AGC #	Other Name	Opt Position[a] (J2000)	HI $cz_{\odot}$ km s^{-1}	W50 km s^{-1}	F_c Jy km s^{-1}	Dist[b] Mpc	log M_{HI} $M_{\odot}$	Tidal Remnant
202026	FS 15	10 46 30.2 +11 45 19	954	126	3.24	11.1	7.97	Leo Ring
201975	LeG21	10 47 00.8 +12 57 34	843	23	0.48	11.1	7.14	Leo Ring
200592[a]	P032327	10 48 43.3 +12 18 55	876	44	0.26	11.1	6.88	Leo Ring
210220	I2684	11 17 01.1 +13 05 55	588	25	0.57	10.0	7.09	Leo Triplet
215286		11 19 12.7 +14 19 40	998	28	0.54	10.0	7.12	Leo Triplet
215354[b]		11 19 15.9 +14 17 25	728	...	...	10.0	...	Leo Triplet
211370	I2767	11 22 23.2 +13 04 40	1083	92	1.75	10.0	7.62	Leo Triplet
213512	I2781	11 22 50.7 +12 20 41	1544	72	1.16	17.5	7.95	Leo Triplet
213440	I2791	11 23 37.6 +12 53 45	666	22	0.25	10.0	6.67	Leo Triplet
6401[a]		11 23 19.1 +13 37 45	883	49	0.94	10.0	7.35	Leo Triplet
224516	Tol1232	12 35 24.4 +05 02 53	1805	37	0.45	29.1	7.95	NGC 4532

[a]Source of HI detection: Arecibo circular feed

[b]no HI detection but may be associated with HI clumps north of the Leo Triplet

5.2.2 Tidal dwarf candidates

The tidal dwarf candidates in our sample are all identified in the vicinities of 3 known tidal remnants in the ALFALFA dataset covering the Leo and Virgo regions: the Leo Triplet and the Leo Ring (see Chapter 2) as well as the tidal stream of NGC 4532 [Koopmann et al., 2008]. In all cases a likely optical counterpart has been identified, but for most of these objects the assigned HI parameters are uncertain as this gas may instead be associated with the tidal stream or remnant. The basic HI parameters for the 11 tidal dwarf candidates are given in Table 5.2, and all are pulled directly from the ALFALFA catalog. We again stress the use of the word "candidate"; this time because the galaxies listed in Table 5.2 are so far only known to be located near tidal remnants, and their tidal origins have not yet been confirmed. Broadband optical images from SDSS are given for all 11 tidal dwarf candidates in Figure 5.3. Each image is $100''$ by $100''$.

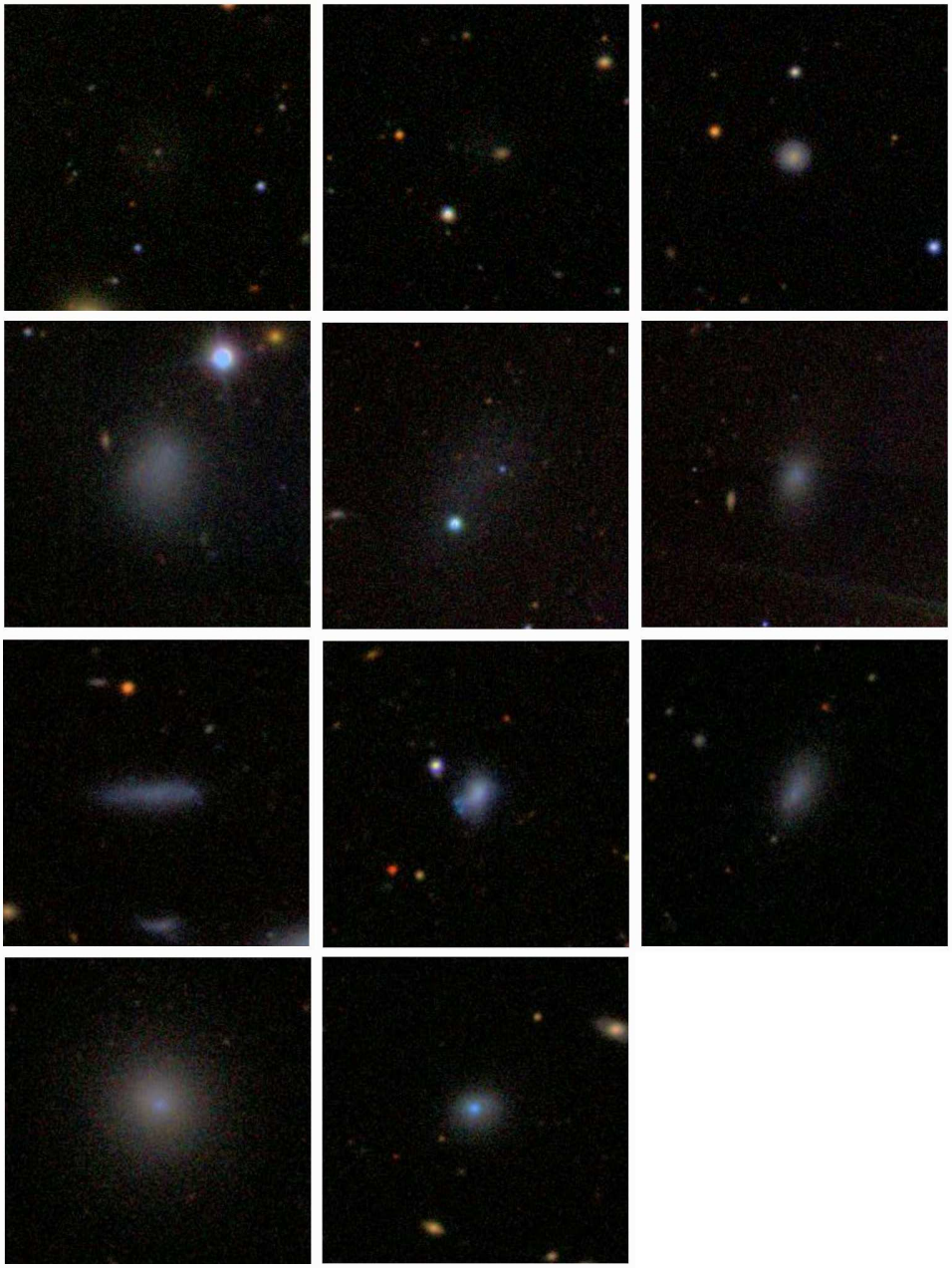

Figure 5.3 SDSS broadband images of 11 tidal dwarf candidates near tidal remnants found in the ALFALFA survey. From left to right, starting at the top: AGC202026, AGC201975, AGC200592, AGC210220, AGC215286, AGC215354, AGC211370, AGC213512, AGC213440, AGC6401 and AGC224516. Each image is $100''$ by $100''$.

5.2.3 Hα Imaging

For the purposes of our study of nebular abundances (as opposed to metallicities based on stellar populations or planetary nebulae), the objects we target for optical spectroscopy must have HII regions. Thus we cannot conduct spectroscopic observations for all of the dwarfs listed in Tables 5.1 and 5.2 and must place an optical bias on the HI-selected sample produced by ALFALFA. A group of collaborators spread all over the world is working on Hα followup observations for the ALFALFA sample starting with the lowest mass objects. The Hα images are then used to determine both the presence and the location of HII regions within our dwarf galaxy targets. The star formation in these low surface brightness systems often occurs in significantly off-center clumps and thus makes pointing directly at the HII region - rather than the center of each galaxy - a necessity.

To maximize the efficiency of our telescope time (i.e. to avoid losing nights that are nonphotometric), we use the Hα images from the WISE and VATT observatories only to map the HII regions within each galaxy. The images are not flux calibrated and so we do not use them to derive Hα fluxes or current star formation rates or to place any limits on the nondetections. More details on the four sources of Hα imaging used for the work presented here are given below.

WISE Observations: The Hα images from the WISE Observatory in Israel are observed with the 40-inch Ritchey-Crétien Telescope by Noah Brosch and his students, Adi Zitrin and Oded Spector. The telescope's Tektronix CCD has 1024 $\times$ 1024 pixels, each covering $0.''696$ per pixel. Depending on the galaxy's redshift (as determined from the ALFALFA observations), one of three narrowband filters is chosen to place the galaxy as close as possible to the center of the

filter's wavelength range and thus to optimize the portion of the bandpass with the highest transmission. Each filter spans 50 Å, and they are centered at 6562 Å, 6586 Å, and 6610 Å. Given that the rest wavelength for Hα is 6562 Å, the filters cover -1188 km s^{-1}$< cz <$ 1097 km s^{-1}, 0 km s^{-1}$< cz <$ 2194 km s^{-1}, and 937 km s^{-1}$< cz <$ 3450 km s^{-1}, respectively. For each target, 2-3 dithered exposures of 1200 seconds each are taken in the narrowband filter along with 2-3 R-band exposures of 300 seconds each.

SMARTS Observations: The Hα images from the Small and Moderate Aperture Research Telescope System (SMARTS) at the Cerro Tololo Inter-American Observatory (CTIO) in Chile are observed with the 0.9-m by Rebecca Koopmann. The telescope's Tek2K_3 detector has 2048 $\times$ 2046 pixels, each covering $0.''396$ per pixel. Depending on the galaxy's redshift, one of two narrowband filters is chosen to place the galaxy as close as possible to the center of the filter's wavelength range and thus to optimize the portion of the bandpass with the highest transmission. Each filter spans 75 Å, and they are centered at 6559 Å and 6598 Å. Given that the rest wavelength for Hα is 6562 Å, the filters cover -1862 km s^{-1}$< cz <$ 1568 km s^{-1}and -69 km s^{-1}$< cz <$ 3321 km s^{-1} respectively. For each target, 2-3 dithered exposures of 900 seconds each are taken in the narrowband filter along with 2-3 R-band exposures of 60 seconds each.

Four of the final, processed Hα images are shown in Figures 5.4 to show the importance of locating the HII regions within each galaxy before attempting spectroscopy. As shown in the images, the Hα emission ranges from being aligned with the galaxy's center (AGC204301) to offcenter by more than $20''$ (AGC202019) to scattered throughout the galaxy (AGCs 191702 and 202024). Each image is $2.5'$ by $2.5'$.

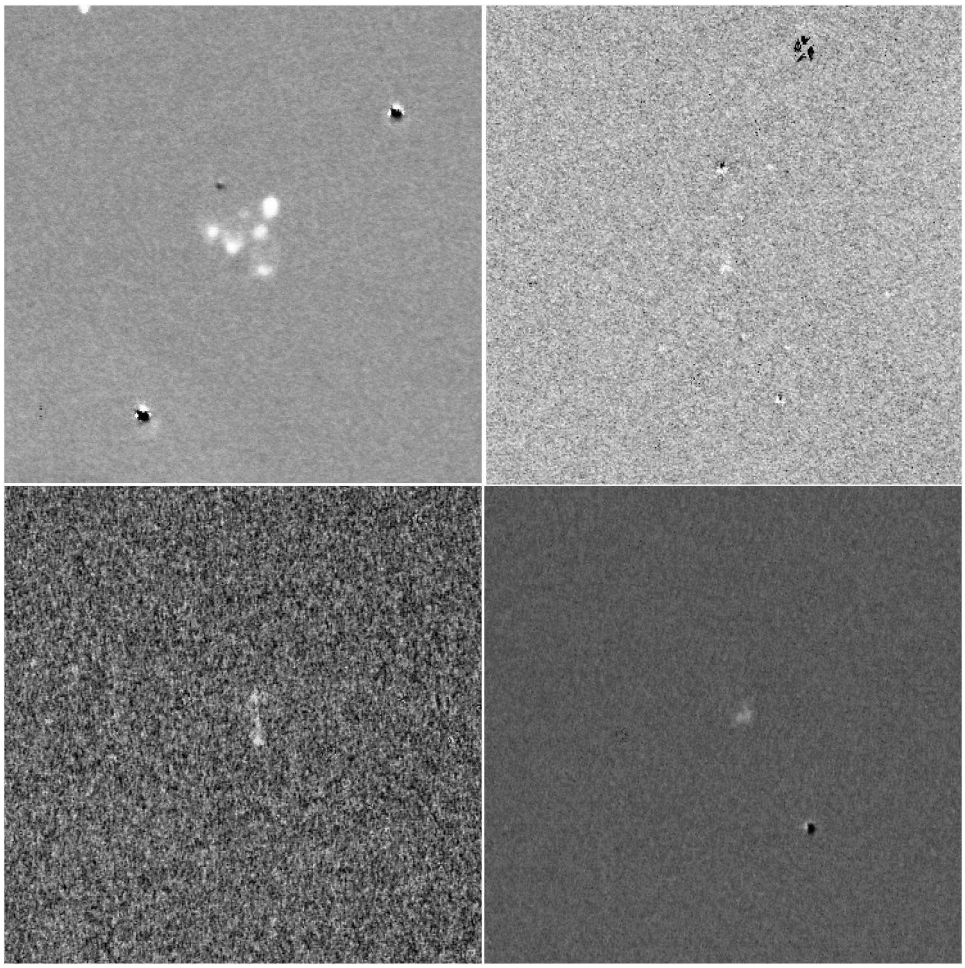

Figure 5.4 SMARTS Hαimaging for AGC191702 (top left), AGC 202019 (top right), AGC 202024 (bottom left) and AGC 204301 (bottom right). Each image is $2.5'$ by $2.5'$.

VATT Observations: The Hα images from the Vatican Advanced Technology Telescope at Mount Graham International Observatory in southeastern Arizona are observed with a 1.8-meter telescope by Aileen O'Donoghue and Chris Corbally. The telescope's VATT4k CCD has 4064 $\times$ 4064 pixels, each covering $0.''375$ per pixel. A narrowband filter with a full width half maximum of 70 Å and centered at 6580 Å was used. The filter covers -779 km s^{-1} $< cz <$ 2402km s^{-1}. For each target, 2 exposures of 1800 seconds each are taken in the narrowband filter along with 2 R-band exposures of 600 seconds each.

GOLDMine Observations: The Hα images from the Galaxy On Line Database Milano Network (GOLDMine; Gavazzi et al. 2003) are either pulled from the public archive or provided by collaborator Giuseppe Gavazzi, the project administrator for the GOLDMine project. The images in the database come from a large team of observers and a number of different telescopes including the 2.1-meter at El Observatorio Astronómico Nacional in San Pedro Mártir, Mexico and the ESO 3.6-m telescope at La Silla Paranal Observatory in Northern Chile. Spectra, narrowband and broadband imaging are available for hundreds of objects, as well as a database of parameters like Hα flux and equivalent width.

Hα imaging for ten of our transition dwarf candidates were pulled from the GOLDMine public archive and the Hα parameters are presented in Table 5.3. The first two columns are the object's AGC number and other names found in the literature. The third and fourth columns give the measured Hα equivalent widths and fluxes as published in the GOLDMine database. The fifth column presents the Hα luminosity as calculated for each source based on the Hα flux

Table 5.3. GOLDMine Hα Observations

AGC #	Other Name	Hα EW (Å)	Hα Flux ($10^{-15} ergscm^{-2}s^{-1}$)	log L(Hα) ($ergss^{-1}$)	Dist (Mpc)
220176	069-072	33	54.95	39.8	32.5
7285	I3077	3	15.85	38.7	16.7
220321	I3120	16	26.30	38.9	16.7
220510	UA279	15	45.71	39.2	16.7
220555	VCC841	29	83.18	39.4	16.7
223724	VCC1202	26	5.01	38.2	16.7
220819	VCC1617	9	25.70	38.9	16.7
7889	N4641	9	79.43	39.4	16.7
220739	I3466	2	4.27	38.2	16.7
7817	I3611	6	44.67	39.2	16.7

in column 4 and the adopted distance given in the last column and as found in Tables 5.1, 5.2, and 5.4. Associated errors for the Hα fluxes and EWs are not given in the online database, but a search of GOLDMine publications shows that they are usually on the order of 10-30%.

The Hα images are delivered in various stages of reduction and all further processing is performed in *IRAF*. Once the images are bias subtracted, flat-fielded, and edited for cosmic rays (please see Chapter **??** for further explanation of these steps), multiple exposures of the same galaxy are aligned using the locations of stars and the *IMSHIFT* task. Using $\sim$10 bright stars, the full width half maximum (FWHM) of the point spread function is determined for each image. Those images with lower values for the FWHM (usually the R-band images) must be smoothed by a scaling factor to match those images with higher FWHMs. The scaling and smoothing can be done using *IMPLOT* and *IMARITH* but we used tasks called *findfwhm* and *getscale* written by John Salzer, a collaborator at Indiana University that streamline the process.

Finally the "OFF" (R-band) exposures can be subtracted from the "ON"

(Hα) exposures to produce a final, continuum-subtracted image. This subtraction removes the stellar continuum and results in an image revealing only the Hα emission from the star forming regions in the galaxy. All of the R-band exposures are combined using the *IMCOMBINE* task, and this final R-band image is subtracted from each Hα exposure using *IMARITH*. The multiple continuum-subtracted exposures are then combined to produce one final continuum-subtracted image.

The final R-band image is also used to determine pointing offsets between the HII regions in the galaxy and nearby bright stars. During the spectroscopic observations, these objects are typically so low surface brightness that they cannot be seen by eye in the slit viewing camera. Rather than wait for the completion of a 20-minute integration to verify that we are pointed at the right position, we instead point at a bright star that is visible in the slit viewing camera and then move by predetermined offsets to the location of the galaxy. Precise locations for the HII regions and nearby stars are found using *MSCGETCATALOG* task and by matching to the NOAO: USNO-A2 star catalog. The tasks *MSCZERO* and *MSCMATCH* are used to shift and rotate the galaxy images to align them with the stellar positions given in the catalog.

5.2.4 Final list of spectroscopy targets

The final list of spectroscopy targets was selected from the objects in Tables 5.1 and 5.2 with detected Hα emission. Four transition-type dwarfs (AGCs 215287, 220167, 220257, and 223445) and six tidal dwarf candidates (AGCs 200592, 210220, 215286, 215354, 213440, 6401) were found to have no Hα emission above

Table 5.4. Low Mass, HI-Selected Dwarfs Targeted for Optical Spectroscopy

AGC #	Other Name	Opt Position[a] (J2000)	HI $cz_\odot$ km s^{-1}	W50 km s^{-1}	F_c Jy km s^{-1}	Dist[b] Mpc	log M_{HI} $M_\odot$
174605		07 50 21.6 +07 47 40	351	24	0.63	4.8	6.53
191702	KKH46	09 08 36.5 +05 17 32	597	27	2.77	8.7	7.70
194068[a,d]		09 40 12.8 +29 35 30	505	77	2.05	7.4	...
5186[b,d]		09 42 59.0 +33 16 00	548	74	1.02	8.3	...
190472	I559	09 44 43.8 +09 36 54	541	67	4.26	7.4	7.74
192402		09 49 37.0 +09 29 42	3101	99	0.53	47.3	8.45
5456	064-068	10 07 19.7 +10 21 43	536	61	6.53	7.0	7.88
213796		11 12 52.7 +07 55 19	1412	78	0.55	23.5	7.86
213333		11 43 27.0 +11 23 54	897	64	0.77	10.3	7.28
238643		13 55 58.3 +08 59 36	1220	45	0.34	22.3	7.60
243852		14 07 04.5 +10 42 46	1178	55	0.70	21.5	7.88
252211[d]	MTT-113	15 03 50.2 +00 58 40	2064	79	1.74	32.0	...
252519[c,d]	KKR15	15 03 55.9 +00 25 44	1588	61	1.44	25.5	...

[a]Source of HI detection: Nancay telescope

[b]Source of HI detection: AO flat feed

[c]Source of HI detection: Bonn 100m

[d]HI detection noticed in early stages of ALFALFA data reduction but a complete, gridded dataset in this area of the sky is not yet available so only estimates of HI parameters are given.

the limits of the detector. Additional targets were needed either for filling in the LST ranges not covered by the targets listed above and for our earliest observing run when the ALFALFA spring sky catalog was not yet complete. These targets are all from the ALFALFA dataset, are expected to have $M_{HI} \lesssim 10^8 M_\odot$, and were detected in H$\alpha$. As they represent typical dwarf irregular galaxies (known HI content and current star formation), these galaxies provide metallicity measurements which we can compare to those derived for the transition and tidal dwarf candidates. The low mass targets are presented in Table 5.4. HI parameters are pulled directly from the ALFALFA catalog unless otherwise noted. Broadband optical images from SDSS are given for the 13 low mass, HI-selected galaxies in Figure 5.5. Each image is $100''$ by $100''$.

A total of 37 galaxies were observed with the Double Spectrograph on the

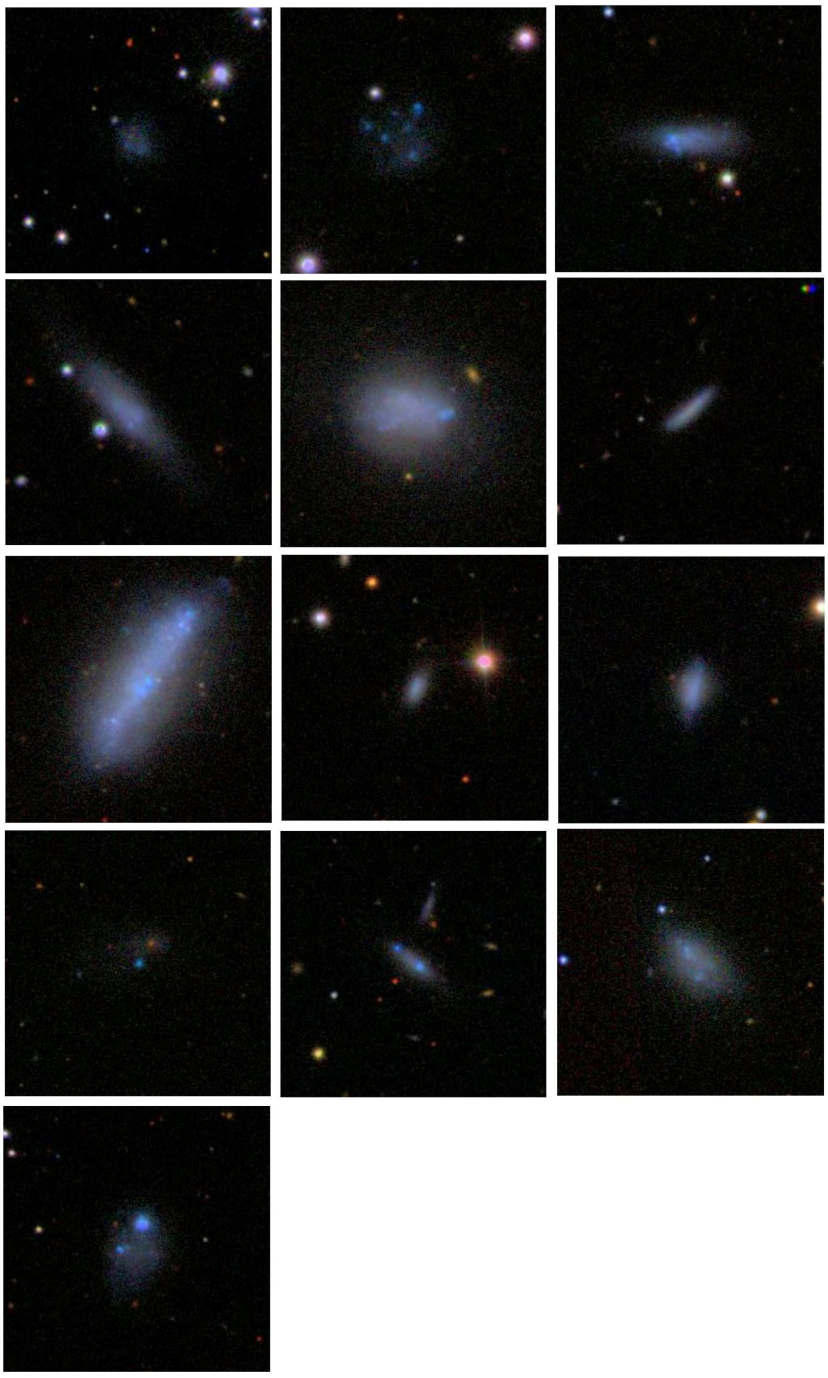

Figure 5.5 SDSS broadband images of low mass galaxies found in the ALFALFA survey and targetted for optical spectroscopy. From left to right, starting at the top: AGC174605, AGC191702, AGC194068, AGC5186, AGC190472, AGC192402, AGC5456, AGC213796, AGC213333, AGC238643, AGC243852, AGC252211 and AGC252519. Each image is 100″ by 100″.

Palomar 200-inch Hale Telescope during three separate observing runs with the help of collaborators Ann Martin, Rebecca Koopmann, Elizabeth Adams, and Shan Huang. An abbreviated observing log is presented in Table 5.5. The first two columns give the AGC number and any other name for the galaxy found in the literature. The third column notes the location of the HII region within the galaxy (i.e. where the spectroscopic observations were pointed). The fourth column gives the position angle at which the telescope was placed for all of the exposures. (Since most of these objects do not have a clearly defined major axis, the position angle was chosen to match the parallactic angle at the midpoint of the total integration time.) The fifth column notes during which run the object was observed, and the sixth column gives the total integration time on source. Note that these integration times only include the exposures used to determine the final spectrum. On a few occassions the seeing degraded over time, and the lower-quality exposures not used in the final stages of data reduction are not documented here. The final column describes whether the dwarf was considered a transition dwarf candidate, a tidal dwarf candidate, or a low-mass target. In the next section, the process of data reduction for the spectra obtained for these 37 galaxies and the resulting line flux and equivalent width measurements are presented.

The final target list presented in Table 5.5 leaves us with a wishlist for future observations. As the ALFALFA dataset grows, more complete samples of transition and tidal dwarfs become available. Additionally, optical spectra were not observed for all of the targets for which we obtained Hα imaging and which revealed Hα emission due to limited telescope time and the loss of a few nights due to nonphotometric conditions. Other transition dwarf candidates with properties matching those of the galaxies in Table 5.1 include AGCs

Table 5.5. Observing Log

AGC #	Other Name	Opt Position[a] (J2000)	P.A. (deg)	Run	T_{int} (s)	Description
200496	065-072	10 37 23.5 +12 09 23	43	2007 May	3 x 1200	trans
220282	I3096	12 16 53.4 +14 30 51	28	2007 May	1 x 1200	trans
7889	N4641	12 43 07.9 +12 03 05	38	2007 May	3 x 1200	trans
250103		15 08 05.9 +01 39 03	5	2007 May	3 x 1200	trans
251419		15 04 08.8 +01 31 28	32	2007 May	2 x 1200	trans
238643		13 55 58.3 +08 59 37	15	2008 March	3 x 1200	low mass
174605		07 50 21.8 +07 47 41	356	2008 March	1 x 1200	low mass
191803		09 48 05.8 +07 07 46	44	2008 March	4 x 1200	trans
200499	065-074	10 38 08.3 +10 22 51	25	2008 March	3 x 1200	trans
211370	I2767	11 22 23.8 +13 04 38	52	2008 March	3 x 1200	tidal
243852		14 07 04.7 +10 42 44	48	2008 March	1 x 1200	low mass
202019	LeG05	10 39 42.9 +12 38 05	330	2008 March	6 x 1200	trans
213512	I2781	11 22 51.4 +12 20 38	43	2008 March	3 x 1200	tidal
224516	Tol1232	12 35 24.8 +05 02 55	30	2008 March	3 x 1200	tidal
262737		16 40 21.0 +28 45 58	290	2008 March	4 x 1200	trans
190472	I559	09 44 43.9 +09 36 54	310	2008 March	3 x 1200	low mass
200532	065-086	10 42 00.2 +12 20 05	313	2008 March	4 x 1200	trans
7285	I3077	12 15 56.1 +14 26 00	309	2008 March	3 x 1200	trans
220321	I3120	12 18 15.2 +13 44 52	327	2008 March	3 x 1200	trans
223407	VCC304	12 18 44.4 +12 23 06	25	2008 March	6 x 1200	trans
220739	I3466	12 32 06.3 +11 48 59	36	2008 March	6 x 1200	trans
192402		09 49 37.0 +09 29 42	313	2008 March	5 x 1200	low mass
215306		11 33 49.9 +14 49 26	311	2008 March	6 x 1200	trans
7181	I3033	12 11 10.2 +13 35 35	332	2008 March	3 x 1200	trans
220555	VCC841	12 25 47.6 +14 57 01	3	2008 March	3 x 1200	trans
232142		13 56 08.8 +05 32 31	29	2008 March	4 x 1200	trans
191702	KKH46	09 08 37.1 +05 17 36	348	2009 March	3 x 1200	low mass
194068		09 40 13.9 +29 35 24	314	2009 March	1 x 1200	low mass
5186		09 42 58.6 +33 15 58	85	2009 March	2 x 1200	low mass
213333		11 43 26.8 +11 23 50	36	2009 March	3 x 1200	low mass
221013		12 46 55.7 +26 33 47	69	2009 March	3 x 1200	trans
252519		15 03 55.8 +00 25 50	21	2009 March	3 x 1200	low mass
5456	064-068	10 07 19.7 +10 21 43	329	2009 March	1 x 1200	low mass
204301		10 16 59.0 +03 42 36	353	2009 March	3 x 1200	trans
213796		11 12 52.5 +07 55 19	22	2009 March	6 x 1200	low mass
220286		12 17 07.4 +30 38 28	76	2009 March	5 x 1200	trans
252211		15 03 50.1 +00 58 37	14	2009 March	4 x 1200	low mass

200879, 5923, 220074, 7305, 220289, 220353, 220354, 220751, 222310, 223913, and 220977. The dynamic Virgo cluster environment is also well known for the presence of other tidal streams (Kent et al. [2007]; Haynes et al. [2007]) which may provide additional tidal dwarf candidates.

5.3 Observations & Data Reduction

All optical spectroscopy was performed at the Palomar 200-inch Hale Telescope using the Double Spectrograph [Oke and Gunn, 1982] over 3 observing runs as detailed in Table 5.5. The 38 galaxies were observed over a total of 7 nights with 3 additional nights lost to weather. All of our observations were during dark time, so moonlight was not an issue. We use a single slit mode with a $128''$ by $2''$ slit. The slit width is chosen to provide high resolution (on the order of R$\sim$3000). The slit length is fixed but is narrow enough not to waste time reading out unused portions of the CCD after every exposure while also wide enough that enough sky is observed in each frame for accurate sky subtraction.

The spectrograph splits the incoming signal into two cameras dubbed the "red" and the "blue". The observer sets where this split occurs by choosing a placement for the dichroic which we set at 5500Å. A grating with 600 lines mm^{-1} and blazed at 27.$^\circ$287 (4000Å) is used for the blue camera which gives a wavelength coverage of 2965 to 5680 Å. The blue camera has 2788 $\times$ 512 15-μm pixels for a resolution of 1.09 Å pixel^{-1} or $0.''390$ pixel^{-1}. A grating with 316 lines mm^{-1} and blazed at 23.$^\circ$742 (7500Å) is used for the red camera which gives a wavelength coverage of 5048 to 7815 Å. The red camera has 1024 $\times$ 1024 24-μm pixels for a resolution of 2.47 Å pixel^{-1} or $0.''468$ pixel^{-1}.

5.3.1 Calibration

Before we can extract one-dimensional spectra from the two-dimensional spectra recorded at the telescope (i.e. dispersion along one axis and the slit size along the other axis), we first need to apply several types of calibration frames also taken during each observing run. Minor editing is performed on the frames first to remove any cosmic rays and to fix any bad pixels. As many cosmic rays as possible are removed using the automated *COSMICRAYS* task, but further editing by hand is always necessary using the *IMEDIT* task. Bad pixels are most clearly seen in dark or lamp frames (see below) and are removed using the *FIXPIX* task. Further explanation of application of calibration frames is given here.

Biases: At the beginning of each night, ten frames are taken each with a zero exposure time so that the shutter is never opened. Even though no light is hitting the CCD, these bias frames still have counts associated with each pixel due to instrumental noise and read-out noise of the detector. In the first stages of data reduction, the ten bias frames are combined using the *ZEROCOMBINE* task and then subtracted from all other frames using the *IMARITH* task so that the zero level of the science frames coincides with roughly zero counts. The bias level falls around 3200 ADU for the blue camera and around 5650 ADU for the red camera. The bias level can also be determined using the overscan region (a portion of the CCD that is read out but not exposed for a non-bias frame), but taking an entire bias frame accounts for pixel-to-pixel variations in the bias level.

Darks: Also at the beginning of each night, an additional three frames are taken without opening the shutter but with integration times typical of the

longest exposure times used for science frames (in our case, 1200 seconds). Any so-called "dark" current due to thermal noise in the detector gets added to a science frame throughout an exposure and then is wiped away when the CCD is read out. If the dark frames show significant dark current, they are combined using *IMCOMBINE* and subtracted from all other frames just as the biases were. Dark frames also aid in the search for "hot" or bad pixels on the CCD. The dark images taken for these three observing runs did not turn up any significant dark current or any hot pixels so we did not need to use them.

Dome flats: Before the dome is opened for the night, we shine a bright white light on the detector and a series of ten exposures are taken for 30 seconds each with the blue camera and for 5 seconds each with the red camera. These dome flats are an attempt to illuminate the CCD as uniformly as possible in order to locate any dust or other imperfections on the CCD and effectively map the illumination pattern over the entire slit. During these exposures some of the light is scattered out of the slit and into the overscan region. Since we know the overscan region should ideally have zero counts, we can estimate the amount of scattered light and correct for this in the illumination pattern we determine using the *BACKGROUND* task.

Once the scattered light correction is applied, the dome flats are combined using the IMCOMBINE task to make a single flat field each for the blue and red cameras. A response function is then fit along the dispersion direction to map any color variations in the combined flat field frame using the *RESPONSE* task. The blue and red dome flats are then divided by their respective response functions. Finally, the illumination patterns are determined for the blue and red dome flats using the *ILLUMINATION* task. These illumination patterns are

then multiplied by the appropriate response function (effectively adding the color variations back in) to produce a final flat field frame each for the blue and red cameras. All other frames are then flat fielded by dividing by these dome flats using the *FLATTEN* task.

Twilight flats: While the dome flats aim to illuminate the CCD as uniformly as possible, the white light is brighter and more uniform at the red end of the spectrum, and so the dome flats are not always a good representation of slit illumination for the blue camera frames. To get a more accurate fit to the illumination function in the blue, we take a series of dithered exposures during sunset. These twilight flats are tricky to obtain because they must be done once the sun is below the horizon but before the sky becomes so dark that bright sky lines overwhelm the uniformity of the exposure. The integration time also varies from exposure to exposure, and usually starts around 1 second at the beginning of sunset but increases to almost 1 minute before the usable twilight time is over. Roughly 20 frames are taken in the span of 10 minutes. These twilight flats are treated in the same way the dome flats are, but dome flats are used for the red frames while twilight flats are used for the blue frames.

Comparison lamps: In order to determine exactly which pixel on the camera corresponds to what wavelength, short exposures are taken throughout the night of lamps with well determined wavelength solutions. For the red camera, a 0.2-second exposure of a helium, neon, and argon lamp is taken, and for the blue camera, a 30-second exposure of an iron and argon lamp is taken. The wavelength solutions for these lamps are so well known, that they are already available in the *IRAF* database to aid with calibration. A new lamp exposure for each camera is taken throughout the night every time the telescope is moved to

a new position as the solution might vary up to 0.5-1Å. The lamp frame taken closest to zenith is chosen for the initial matching of lines in the frame to those in the database using the *IDENTIFY* and *REIDENTIFY* tasks. The solution for that lamp is then applied to all other lamps using *REIDENTIFY* as a first step approximation. The fits for each lamp frame are then viewed individually and a wavelength solution is fit using *FITCOORDS*. This task also helps account for any deviations in the lamp lines from precisely vertical lines. (Usually across the camera a lamp line may shift by up to 1 pixel.) Once the wavelength solution is well-determined for each lamp frame, the fit for each lamp is applied to the corresponding galaxy (or star) frame(s) at the position the lamp frame was taken using the *TRANSFORM* task.

Comparison stripes: Just as we use lamp frames to adjust for any shifts in the spatial direction across the camera, we also want to correct for any shifts along the dispersion axis. Often the continuum emission from low surface brightness targets is not bright enough to trace across the entire frame and a "straight" line across the frame can shift by up to 10 pixels. A trace can be done on a standard star which is bright enough to follow across the whole frame, but the shift might be different along different parts of the CCD. So at the beginning of the night and then again at the end of the night we take five exposures of the same standard star, but with each exposure placing the star at a different spot in the slit. These frames are added together to create a single frame with five stripes parallel to the dispersion axis. The "tiger stripe" frame is treated the same way the lamp frames are using the *IDENTIFY*, *REIDENTIFY*, *FITCOORDS*, and *TRANSFORM* tasks except we are not applying a solution from the database, just tracing the lines across the frame.

Spectrophotometric standards: To translate counts detected by the CCD into flux units of ergs $s^{-1}cm^{-2}$, stars with well-determined spectra are observed throughout the night. Again these spectrophotometric standards are so well-known that their solutions already exist in the *IRAF* database. We use standard stars from Oke [1990] and further explantion of the steps taken in flux calibration is given below.

5.3.2 Extracting a One-Dimensional Spectrum

Once the frames are bias-subtracted, flat-fielded, and wavelength-calibrated, multiple frames of a single galaxy are aligned using the *IMSHIFT* task and co-added using the *IMCOMBINE* task. When combined the different frames are weighted according to the strengths of their brightest spectral line (Hα for the red frames and [OIII] or Hβ for the blue). Night sky lines are then subtracted using the *BACKGROUND* task. The user is asked to pick a region of the frame where the background sky is to be fit, and so we pick the region of sky surrounding the main lines of interest (Hαin the red and [OIII] in the blue) to optimize the fit in that region of the spectrum.

Finally a one-dimensional spectrum is extracted from each two-dimensional spectrum using the *APEXTRACT* task. The most sensitive part of this step is the size of the aperture that is chosen for each galaxy. Too large of an aperture will dilute the signal, but an aperture that is too small will not include all of the signal. The slightly different pixel scales for the red ($0.''468$ pixel^{-1}) and blue ($0.''390$ pixel^{-1}) cameras also must be accounted for so that the spectra extracted from the red frames represents the same portion of the galaxy as is represented

by the blue spectra. The accuracy of the chemical abundances calculated for each galaxy depends on the comparison of lines on the red and blue sides of the spectrum. Aperture sizes are chosen for each galaxy using the red frames and then an equivalent aperture size is calculated and used for the blue frames. If more than one HII knot was placed in the slit for a single pointing, the apertures are chosen not to overlap and the one-dimensional spectra are extracted separately.

In order to extract a spectrum, the *APEXTRACT* task traces the galaxy's continuum across the frame. Since we have straightened the lines in this direction using the comparison stripe images, the trace should be straightforward, but in the cases where the galaxy's continuum is too faint, the trace could "fall off" the galaxy. For these cases we use a standard star as a trace instead of the galaxy's continuum. If more than one HII region was placed in the slit, a separate spectrum is extracted for each one. One-dimensional spectra are extracted for the calibration stars as well.

To set a uniform wavelength range for all of our spectra we run the *DISPCOR* task to resample the spectra over a chosen range of 3500 to 5500 Åfor the blue spectra and 5200 to 7500 Åfor the red spectra. The overlap of 300Åacts as a check that the different frames were properly calibrated to match each other.

The translation of "counts" on the CCD to flux values is then determined by running the *STANDARD* task on each spectrophotometric standard star (usually 3 to 4 per night). In this step, the number of counts within a series of bandpasses $\sim$50Åwide and covering the stellar spectrum is integrated and compared to the flux measurements found in the database for that star. The *SENSFUNC* is then run the combination of all of the standard star spectra to fit the cam-

era's sensitivity as a function of wavelength. This step also takes into account the atmospheric extinction as determined using standard Kitt Peak extinction coefficients also found in the *IRAF* database. Once the sensitivity function of the CCD has been determined using the spectrophotometric standard stars and the conversion from counts (or ADU) to flux units has been found, these fits are applied to the galaxy spectra using the *CALIBRATE* task to produce the final, calibrated spectrum.

5.3.3 Emission Line Measurements

The final, calibrated spectrum for one of the transition dwarf candidates AGC220555 is shown in Figure 5.6 with labeled emission lines. The clean overlap between the blue and red halves of the spectra near 5500 åresults from the careful aperture matching of the different sides of the spectrograph. All 52 spectra can be found in Appedix B. When more than one HII region was observed for a galaxy, the separate extracted spectra are noted with an 'a', 'b', or 'c'.

Emission line fluxes as well as continuum measurements surrounding the Balmer lines in each spectrum (used in calculating equivalent widths) are measured for each galaxy using the $'e'$ option in the *IRAF* task *SPLOT*. A correction must then be applied to account for intergalactic reddening which causes an underestimation of the shorter wavelength lines and an overestimation of the redder lines. To correct for this extinction we use the reddening law of Osterbrock and Ferland [2006] normalized to the $H\beta$ line:

$$\frac{I_\lambda}{I_{H\beta}} = \frac{F_\lambda}{F_{H\beta}} 10^{c_{H\beta}[f(\lambda)-f(H\beta)]} \tag{5.1}$$

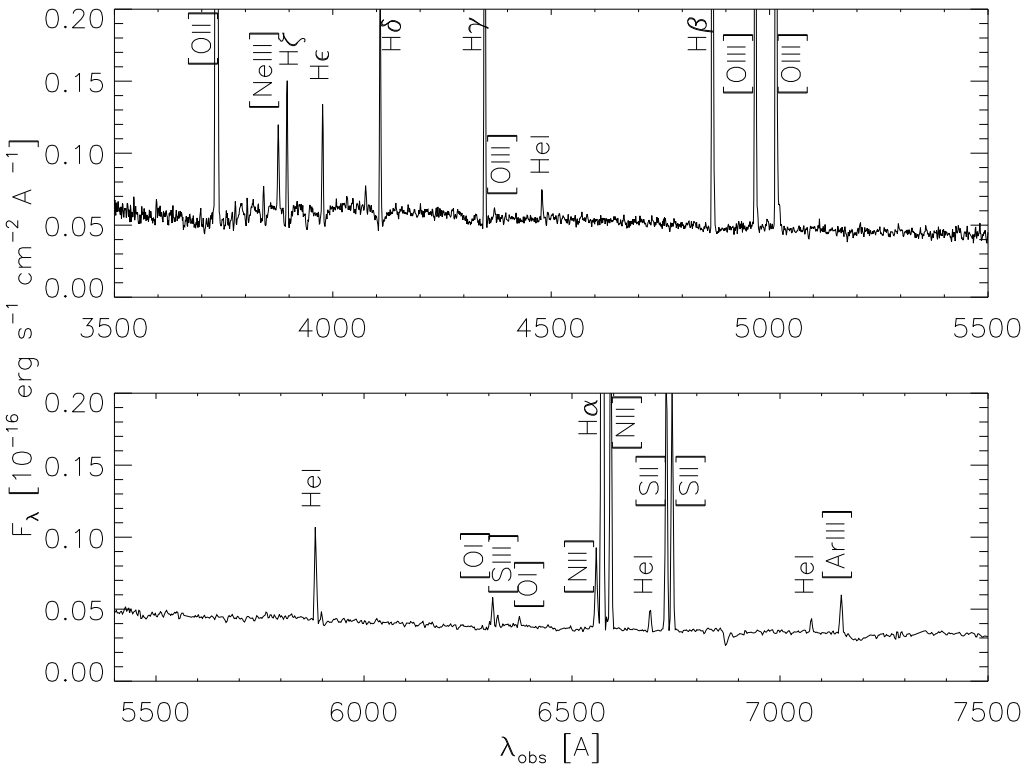

Figure 5.6 Flux calibrated optical spectrum for AGC 220555 with emission lines labeled.

with the reddening function of Howarth [1983]:

$$f(x) = R - 0.236 + 0.462x + 0.105x^2 + \frac{0.454}{(x - 4.557)^2 + 0.293} \tag{5.2}$$

where $c_{H\beta}$ is the reddening coefficient, $x = 1/\lambda$ and $R = A(V)/E(B-V)$, the extinction in the V band divided by the B-V color excess. For R we adopt a value of 3.1 which is derived for the dust grains in the Milky Way [Osterbrock and Ferland, 2006].

To determine the reddening coefficient $c_{H\beta}$ and thus solve the reddening law, we measure the observed Balmer line ratios ($H\alpha/H\beta$, $H\gamma/H\beta$, and, when avail-

able, $H\delta/H\beta$) and compare to theoretical values which can be predicted based on the electron density and temperature of the nebulae. We use the predicted ratios of Storey and Hummer [1995] for Case B (i.e. optically thick) recombination and estimate the electron density at 100 cm^{-3}. Based only on intergalactic reddening, the observed departures from the predicted values for the Balmer ratios in a single spectrum should agree, but sometimes additional correction is needed for stellar absorption from A stars, an effect that varies with wavelength. When the reddening derived for different Balmer ratios from the same spectrum does not agree, we add between 0.5Å and 3Å of stellar absorption needed to obtain the best agreement. The calculated reddening coefficient ($c_{H\beta}$) and the amount of stellar absorption added for each HII region are presented with the derived metallicities in Table 5.4.2 in the next section.

The extinction-corrected line fluxes measured for the blue and red halves of the spectra are found in Tables 5.6 and 5.7, respectively.

5.3.4 Estimation of Uncertainties

To estimate the uncertainties presented in Tables 5.6 and 5.7, we calculate the five main sources of error introduced at the observation, reduction, and calibration stages of the line measurements. Uncertainties inherent to the counts in the spectra, and thus introduced during the observations, include Poisson noise from the photons contributing to both the spectral lines themselves (Δf_ν) and to the continuum (σ_n). At the reduction stage, to measure the flux within an emission line, the level of the continuum surrounding each line must also be measured and contributes an additional uncertainty (ΔC). Finally, the cali-

Table 5.6. Line fluxes for the blue halves of the spectra

HII region	[OII]3727	NeIII[3869]	Hδ	Hγ	[OIII]4363	Hβ	[OIII]4958	[OIII]5007
200496a	5.592±1.006					1.000±0.180	0.818±0.147	2.026±0.364
200496b	3.322±0.513	0.105±0.016	0.207±0.032	0.433±0.067		1.000±0.154	0.856±0.132	2.735±0.422
220282	2.315±0.416		0.177±0.032	0.411±0.074	0.032±0.006	1.000±0.180	0.331±0.060	0.989±0.178
7889	4.858±0.807			0.230±0.038		1.000±0.166	0.224±0.037	0.484±0.080
251419	6.136±1.019					1.000±0.166		1.039±0.173
238643	1.614±0.600	0.170±0.063	0.209±0.078	0.519±0.193		1.000± 0.367	1.054±0.392	2.542±0.946
191803a	3.946±0.710			0.313±0.056	0.249±0.045	1.000±0.180	0.464±0.084	1.885±0.339
191803b	3.484±1.149			0.415±0.137		1.000±0.330	0.289±0.095	0.944±0.311
200499	2.887±1.388	0.213±0.102	0.069±0.033	0.272±0.131		1.000±0.481	0.623±0.300	1.278±0.615
211370	0.658±0.109			0.495±0.082		1.000±0.166	0.507±0.084	1.783±0.296
243852	0.075±0.011	0.315±0.046	0.243±0.035	0.428±0.062	0.044±0.006	1.000±0.146	1.390±0.202	4.378±0.638
213512	0.163±0.025	0.264±0.041	0.239±0.037	0.468±0.072	0.046±0.007	1.000±0.154	1.055±0.163	3.153±0.487
224516	0.527±0.077	0.084±0.012	0.238±0.035	0.452±0.066	0.016±0.002	1.000±0.146	0.843±0.123	2.540±0.370
262737	134.797±10.820	0.239±0.043		0.354±0.064		1.000±0.180	1.081±0.194	3.198±0.575
190472a	3.647±0.656	0.222±0.040	0.113±0.020	0.419±0.075	0.063±0.011	1.000±0.180	0.623±0.112	1.670±0.300
190472b	9.444±2.005					1.000±0.212	0.664±0.141	2.157±0.458
200532	2.310±0.490	0.132±0.028	0.211±0.045	0.408±0.087	0.015±0.003	1.000±0.212	0.923±0.196	2.838±0.602

Table 5.6 (continued)

HII region	[OII]3727	NeIII[3869]	Hδ	Hγ	[OIII]4363	Hβ	[OIII]4958	[OIII]5007
7285	3.292±1.583		0.137±0.066	0.265±0.127		1.000±0.481	0.103±0.049	0.350±0.168
220321	3.123±0.482		0.150±0.023	0.410±0.063		1.000±0.154	0.173±0.027	0.449±0.069
220739	5.368±2.112			0.224±0.088		1.000±0.393	0.725±0.285	1.958±0.771
192402a	3.011±0.809	0.240±0.065	0.151±0.041	0.361±0.097	0.038±0.010	1.000±0.269	0.990±0.266	3.597±0.966
192402b	3.566±0.958	0.331±0.089	0.089±0.024	0.346±0.093		1.000±0.269	1.151±0.309	3.366±0.904
215306	4.881±1.124	0.114±0.026	0.087±0.020	0.364±0.084		1.000±0.230	0.893±0.206	3.002±0.691
7181a	2.291±0.321	0.218±0.031	0.216±0.030	0.449±0.063	0.029±0.004	1.000±0.140	1.065±0.149	3.252±0.455
7181b	4.750±2.284			0.413± 0.238		1.000±0.481	0.605±0.291	1.738±0.836
220555	1.863±0.693	0.074±0.028	0.192±0.071	0.471±0.175	0.009±0.003	1.000±0.372	0.714±0.266	1.747±0.650
232142a	2.758± 0.060		0.230±0.045	0.577±0.113		1.000±0.195	0.688±0.134	2.283±0.446
232142b	4.411±1.098			0.354±0.088		1.000±0.249	0.850±0.212	2.494±0.621
191702a	2.218±0.311	0.135±0.019	0.202±0.028	0.418±0.059	0.020±0.003	1.000±0.140	0.775±0.109	2.321±0.325
191702b	1.713±0.395	0.235±0.054	0.189±0.043	0.449±0.103	0.056±0.013	1.000±0.230	0.958±0.221	2.830±0.652
190468	2.423±0.604	0.145±0.036	0.220±0.055	0.411±0.102	0.031±0.008	1.000±0.249	0.638±0.159	1.946±0.485
5186	6.096±1.404					1.000±0.230	1.703±0.392	4.374±1.007
213333	6.290±1.689	0.246±0.066		0.201±0.054		1.000±0.269	0.828±0.222	2.630±0.706
221013	2.965±0.916	0.193±0.059	0.197±0.061	0.458±0.141	0.022±0.007	1.000±0.309	0.907±0.280	2.874±0.888

Table 5.6 (continued)

HII region	[OII]3727	NeIII[3869]	Hδ	Hγ	[OIII]4363	Hβ	[OIII]4958	[OIII]5007
252519	2.203±0.340	0.329±0.051	0.217±0.034	0.431±0.067	0.031±0.005	1.000±0.154	1.375±0.212	4.007±0.619
5456a	1.528±0.568	0.336±0.125	0.225±0.084	0.443±0.165	0.039±0.014	1.000±0.372	1.645±0.612	4.978±1.852
5456b	2.404±0.399	0.283±0.047	0.232±0.039	0.463±0.077	0.031±0.005	1.000±0.166	1.380±0.229	4.098±0.681
5456c	2.332±0.456	0.381±0.075	0.271±0.053	0.415±0.081	0.016±0.003	1.000±0.195	1.966±0.384	5.055±0.988
204301	5.174±1.191			0.301±0.069		1.000±0.230	0.454±0.104	1.723±0.397
213796	2.660±0.411	0.292±0.045	0.133±0.021	0.395±0.061	0.041±0.006	1.000±0.154	1.086±0.168	3.420±0.528
220286	3.520±1.693			0.830±0.399		1.000±0.481		0.508±0.244
252211a	3.859±0.596	0.311±0.048	0.127±0.020	0.394±0.061	0.021±0.003	1.000±0.154	0.982±0.152	3.023±0.467
252211b	3.894±0.567	0.201±0.029	0.128±0.019	0.359±0.052	0.010±0.001	1.000±0.146	0.695±0.101	2.177±0.317
252211c	4.976±0.769	0.094±0.015	0.124±0.019	0.369±0.057	0.031±0.005	1.000±0.154	0.774±0.119	2.156±0.333

Table 5.7. Line fluxes for the red halves of the spectra

HII region	[NII]6585	Hα	[SII]6716	[SII]6730	[HeI]7065	[ArIII]7136	[OII]7319	[OII]7330
200496a	0.320±0.043	3.833±0.515	0.870±0.117	1.472±0.198	1.091±0.146			
200496b	0.092±0.009	4.032±0.394	0.446±0.044	0.534±0.052	0.369±0.036	0.046±0.004		
220282	0.227±0.030	4.661±0.626	0.834±0.112	0.824±0.111	0.579±0.078	0.063±0.008		
7889	0.347±0.040	3.333±0.384	1.000±0.115	1.633±0.188	2.257±0.260			
251419	0.590±0.068	4.564±0.525	2.008±0.231	2.077±0.239	1.532±0.176			
238643	0.082± 0.048	2.482±0.874	0.142±0.050	0.260±0.092	0.210±0.074	0.078±0.027		
191803a		2.935±0.394		0.686±0.092	0.390±0.052			
191803b		5.159±1.585	0.177±0.054	0.811±0.249	0.639±0.196			
200499	0.054±0.025	1.931±0.899	0.132±0.061	0.153±0.071	0.185±0.086	0.032±0.015		
211370	0.446±0.051	3.285±0.378	0.295±0.034	0.640±0.074	0.487±0.056			
243852	0.046±0.004	2.720±0.226	0.112±0.009	0.203±0.017	0.145±0.012	0.073±0.006	0.028±0.002	0.021±0.111
213512	0.026±0.003	2.986±0.292	0.078±0.008	0.173±0.017	0.122±0.012	0.031±0.003	0.016±0.002	0.113±0.014
224516	0.080±0.007	3.056±0.254	0.209±0.017	0.308±0.026	0.214±0.018	0.095±0.008	0.037±0.003	
262737		2.993±0.402	0.147±0.020	0.304±0.041	0.219±0.029			
190472a	0.066±0.009	3.856±0.518	0.207±0.028	0.528±0.071	0.327±0.044	0.060±0.008	0.160±0.021	
190472b	0.222±0.039	4.565±0.801	0.459±0.081	1.353±0.237	0.964±0.169	0.186±0.033		0.190±0.034
200532	0.084±0.015	3.028±0.531	0.248±0.043	0.240±0.042	0.178±0.031	0.117±0.021	0.029±0.005	

Table 5.7 (continued)

HII region	[NII]6585	Hα	[SII]6716	[SII]6730	[HeI]7065	[ArIII]7136	[OII]7319	[OII]7330
7285	0.258±0.120	3.753±1.747	0.741±0.345	0.638±0.297	0.478±0.223	0.056±0.026		
220321	0.201±0.020	3.280±0.320	0.546±0.053	0.644±0.063	0.474±0.046	0.044±0.004		
220739	0.087±0.033	4.989±1.870	0.347±0.130	0.663±0.249	0.493±0.185	0.096±0.036	0.170±0.064	0.125±0.510
192402a	0.065±0.016	3.390±0.815	0.199±0.048	0.372±0.090	0.246±0.059	0.055±0.013	0.045±0.011	0.044±0.242
192402b	0.063±0.015	3.683±0.885	0.245±0.059	0.464±0.112	0.314±0.076	0.113±0.027		
215306		4.343±0.854	0.202±0.040	0.319±0.063	0.228±0.045	0.086±0.017	0.120±0.024	
7181a	0.081±0.006	3.602±0.262	0.223±0.016	0.403±0.029	0.291±0.021	0.087±0.006	0.038±0.003	0.034±0.082
7181b		3.195±1.488	0.263±0.123	0.493± 0.230	0.327±0.153			
220555	0.112±0.039	1.990±0.701	0.430±0.151	0.366±0.129	0.332±0.117	0.059±0.021	0.034±0.012	0.025±0.483
232142a		4.062±0.627	0.210±0.032	0.558±0.086	0.423±0.065	0.107±0.016	0.122±0.019	0.117±0.162
232142b		4.235±0.925	0.276±0.060	0.899±0.196	0.590±0.129			
191702a	0.064±0.005	2.867±0.209	0.114±0.008	0.255±0.019	0.171±0.012	0.049±0.004	0.050±0.004	0.069±0.053
191702b		2.316±0.456	0.070±0.014	0.175±0.034	0.123±0.024	0.040±0.008		
190468	0.032±0.007	3.192±0.697	0.110±0.024	0.207±0.045	0.152±0.033	0.042±0.009	0.035±0.008	0.021±0.366
5186		5.132±1.010	0.257±0.051	0.672±0.132	0.353±0.069			
213333	0.080±0.019	2.454±0.590	0.336±0.081	0.895±0.215	0.529±0.127	0.113±0.027	0.071±0.017	0.107±0.159
221013	0.120±0.034	3.127±0.891	0.402±0.114	0.251±0.071	0.185±0.053	0.090±0.026	0.048±0.014	0.081±0.168

Table 5.7 (continued)

HII region	[NII]6585	Hα	[SII]6716	[SII]6730	[HeI]7065	[ArIII]7136	[OII]7319	[OII]7330
252519	0.045±0.004	2.735±0.267	0.121±0.012	0.218±0.021	0.155±0.015	0.050±0.005	0.030±0.003	0.018±0.164
5456a	0.040±0.014	2.629±0.926	0.123±0.043	0.166±0.059	0.124±0.044	0.094±0.033	0.029±0.010	0.022±0.469
5456b	0.046±0.005	2.946±0.339	0.130±0.015	0.182±0.021	0.133±0.015	0.074±0.009	0.033±0.004	0.025±0.153
5456c	0.081±0.012	7.004±1.082	0.284±0.044	0.637±0.098	0.438±0.068	0.150±0.023	0.019±0.003	0.032±0.093
204301	0.096±0.019	3.525±0.693	0.365±0.072	0.803±0.158	0.535±0.105	0.037±0.007		
213796	0.042±0.004	3.093±0.302	0.156±0.015	0.314±0.031	0.214±0.021	0.066±0.006	0.042±0.004	0.017±0.240
220286	0.562±0.262	2.460±1.146	1.170±0.545	0.755±0.351	0.784±0.365			
252211a	0.054±0.005	3.094±0.302	0.190±0.019	0.362±0.035	0.259±0.025	0.055±0.005	0.026±0.003	
252211b	0.081±0.007	3.170±0.263	0.256±0.021	0.544±0.045	0.358±0.030	0.045±0.004	0.019±0.002	
252211c		3.218±0.314	0.239±0.023	0.587±0.057	0.395±0.039			

brations applied to account for the sensitivity of the detector across the wavelength range (the sensitivity function) and the extinction correction to adjust for reddening both carry their own associated errors (Δs and $\Delta c_{H\beta}$). These five uncertainties are calculated and then propagated as follows:

The first three uncertainties (Δf_ν, σ_n, and ΔC) contribute linearly to the line flux and so can be added in quadrature to determine the uncertainty associated with the observed line flux:

$$\Delta F_{observed} = \sqrt{(\Delta f_\nu)^2 + (\sigma_n)^2 + (\Delta C)^2} \tag{5.3}$$

Poisson counting statistics dictates that $\Delta f_\nu = \sqrt{N}$, and σ_n is taken as the rms noise surrounding the spectral line to incorporate the Poisson error from the continuum as well as any read noise or errors associated with the flat fielding. The error in the continuum level, ΔC is estimated to be 10% of the continuum as was determined for a sample of gas-rich galaxies [van Zee et al., 1997].

The remaining two sources of uncertainty (Δs and $\Delta c_{H\beta}$) make nonlinear contributions to the line flux, and we calculate their effect according to the error propagation formula:

$$\Delta f(x,y)^2 = (\frac{\delta f(x,y)}{\delta x})^2 \delta x^2 + (\frac{\delta f(x,y)}{\delta y})^2 \delta y^2 \tag{5.4}$$

To determine the sensitivity function, we fit a spline function to the spectra of 3 to 5 standard stars using *IRAF*'s *SENSFUNC* routine. The uncertainty in the sensitivity function (Δs) is then taken to be the error associated with the chosen fit and is the largest contribution to the overall uncertainty in the flux. To incorporate Δs into the total uncertainty, we use Equation 5.4 and the relation between the line flux after the sensitivity function is applied (i.e. F_{cal},

the calibrated line flux) and the line flux before Δs is introduced ($F_{observed}$ from Equation 5.3):

$$F_{cal} = \frac{F_{observed}}{a10^{s/2.5}} \tag{5.5}$$

where s is the sensitivity function and a is a constant that incorporates the contributions of the sensitivity function considered to be error-free because they derive from theoretical values (such as the amount of atmospheric absorption) as opposed to the fit to the standard star data.

The remaining contribution to the error, $\Delta c_{H\beta}$, which derives from the reddening correction is estimated from the spread in reddening coefficients determined from the several Balmer line ratios detected in a single spectrum. $\Delta c_{H\beta}$ has median of 25% but can be as much as 50%. Just as for Δs, we use Equation 5.4 and the relation between the reddening corrected line flux (i.e. F_{cor}) and the line flux before $\Delta c_{H\beta}$ is introduced (F_{cal} from Equation 5.5):

$$\frac{\Delta F_{cor}}{F_{cor}} = \sqrt{\frac{\Delta F_{cal}^2}{F_{cal}^2} + ln(10)^2 \delta c_{H\beta}^2} \tag{5.6}$$

Combining all five sources of uncertainty from Equations 5.3, 5.5, and 5.6 gives the overall uncertainty associated with each line flux measurement:

$$\Delta F_{cor} = F_{cor} \sqrt{\frac{\Delta f_\nu^2 + \sigma_n^2 + \Delta C^2}{F_{observed}^2} + (\Delta s^2 + \Delta c_{H\beta}^2) ln(10)^2} \tag{5.7}$$

The values of ΔF_{cor} calculated for each emission line measurement are presented in Tables 5.6 and 5.7.

5.4 Calculating Oxygen Abundances

Oxygen abundances for 44 HII regions in 33 galaxies were derived using the line fluxes presented in the previous section and the methods described in detail by Osterbrock and Ferland [2006], van Zee and Haynes [2006], and Saintonge [2007b]. Elemental abundances are always calculated as the fraction of each species of the element as compared to hydrogen. The oxygen abundances for our HII regions can thus be calculated as:

$$\frac{O}{H} = \frac{N_{O^0} + N_{O^+} + N_{O^{++}} + N_{O^{+++}}}{N_{H^+}} \tag{5.8}$$

We assume the contribution from O^{+++} is negligible since we do not detect the [OIV] line at 4686Åand so ignore the last term in the above equation [Skillman et al., 1994]. Similarly, we ignore N_{O^0} when [OI] lines at 6300 and 6363 are not detected.

5.4.1 Direct Methods

The direct solution of Equation 5.8 depends on the observed line strengths and emissivities of the oxygen and hydrogen lines. According to Osterbrock and Ferland [2006] the line strengths (I_O and $I_{H\beta}$) are related to the fractional abundance N_O/N_H via the emissivity coefficients (j_O and $j_{H\beta}$) via:

$$\frac{N_O}{N_H} = \frac{j_{H\beta}}{j_O}\frac{I_O}{I_{H\beta}} \tag{5.9}$$

Using the relative line strengths and a numerical solution to a five-level atomic model, the emissivity coefficients are determined by the *ABUND* task in *IRAF*.

However, the temperature and density of the HII region are also required

to solve the atomic model in *ABUND* for the emissivities. The nebulae are unlikely to have a constant temperature throughout the star-forming region, so we assume each HII region has an interior, high temperature zone where oxygen emits mostly as [OIII] as well as an outer, lower temperature zone where oxygen emits mostly as [OII] (i.e. the two-zone model from Melbourne et al. [2004].

To calculate the temperature of each zone, we rely on the certain sets of emission lines that depend directly on the temperature in the nebula. If an ion has two excited states that can emit photons of different wavelengths (but that are still detectable in the same spectrum), the relative strength of the lines reveals the rate of excitation of electrons into those upper levels. The excitation rate can then be directly linked to the temperature of the nebula. As can be seen from Figure 5.6, we could use [NII] or [SII] for the temperature calculation, but instead we choose the stronger [OIII] lines.

The temperature of the region can be determined from the emissivity coefficients and the electron density following Osterbrock and Ferland [2006]:

$$\frac{j_{\lambda 4958} + j_{\lambda 5007}}{j_{\lambda 4363}} = \frac{7.90 e^{3.29 \times 10^4 / T_e}}{1 + 4.5 \times 10^{-4} n_e / T_e^{1/2}} \tag{5.10}$$

All of our HII regions are assumed to be in the low density regime where all excited electrons produce a photon and none are collisionally deexcited. The dependence on density is very weak in the above relation: doubling the electron density produces only a 1% change in the emissivity ratio, and even tripling the density results in only a 14% change for a value of $T_e = 1000$ K. Thus we assume a constant density in both temperature zones and for all of our objects of $n = 100 cm^{-3}$ as was done for the low-metallicity, dwarf irregular samples of Saintonge [2007b] and van Zee and Haynes [2006].

The temperature calculated from Equation 5.10 represents $T_e(O^{++})$, the elec-

tron temperature in the high temperature zone. We use the prescription of Pagel et al. [1992] to relate this temperature to that for the low temperature zone:

$$t_e(O^+) = 2[t_e^{-1}(O^{++}) + 0.8]^{-1} \tag{5.11}$$

where t_e is the temperature in untis of 10^4 K. Since we rely on the emissivities to determine the temperature of the nebula (Equation 5.10), but we need to use the temperature of the nebula as an input into the *ABUND* task to determine the emissivities, the process is done iteratively until the best match is reached.

The direct method described so far for determining oxygen abundance can only be used when the fainter [OIII]4363 line is detected which is the case for only half of our HII regions (see Table 5.6). For the fainter objects, semi-empirical models can be used to relate metallicity to the stronger [OII] and [OIII] lines. Several such models exist (Edmunds and Pagel [1984]; McGaugh [1991]; Zaritsky et al. [1994]; Pilyugin [2001]; Pilyugin and Thuan [2005]), and we detail the parameterizations of McGaugh [1991] and Pilyugin and Thuan [2005] in the next sections.

5.4.2 R23 Methods: McGaugh and Pilyugin models

McGaugh [1991] first noticed that the metallicity (Z) of an HII region could be estimated based on ratios of strong lines known as the R_{23} and O_{32} ratios:

$$R_{23} = \frac{f([OIII]\lambda 4958) + f([OIII]\lambda 5007) + f([OII]\lambda 3727)}{f(H\beta)} \tag{5.12}$$

$$O_{32} = \frac{f([OIII]\lambda 4958) + f([OIII]\lambda 5007)}{f([OII]\lambda 3727)}. \tag{5.13}$$

Plotted against each other, these ratios produce the model grid shown in Figure 10 of McGaugh [1991]. An object's position on the grid determines its ionization

parameter U and its metallicity Z. However, the relation is double-valued so that knowing R_{23} and O_{32} does not uniquely determine values for U and Z; the object must also be assigned to either the high or low metallicity branch of the grid.

We use the parameterizations of Kuzio de Naray et al. [2004] for functional representations of the three-dimensional grid. For the low metallicity branch:

$$Z_{low}(x,y) = -4.93 + 4.25x - 3.35sin(x) - 0.26y - 0.12sin(y) \tag{5.14}$$

and

$$U_{low}(x,y) = -2.95 + 0.17x^2 + 1.02y \tag{5.15}$$

where $x = log(R_{23})$ and $y = log(O_{32})$. Similarly, for the high metallicity branch:

$$Z_{high}(x,y) = -2.65 - 0.91x + 0.12ysin(x) \tag{5.16}$$

and

$$U_{high}(x,y) = -2.39 - 0.35x + 1.29y - 0.15xy \tag{5.17}$$

For comparison, we also use the paramaterization of Pilyugin and Thuan [2005] (called the $p - method$) to obtain metallicities from the strong line ratios. Their parameterization also has low and high metallicity branches:

$$Z_{low} = \frac{R_{23} + 106.4 + 106.8P - 3.40P^2}{17.72 + 6.60P + 6.95P^2 - 0.302R_{23}} \tag{5.18}$$

and

$$Z_{high} = \frac{R_{23} + 726.1 + 842.2P + 337.5P^2}{85.96 + 82.76 + 43.98P^2 + 1.793R_{23}} \tag{5.19}$$

where

$$P = \frac{f([OIII]\lambda 4958) + f([OIII]\lambda 5007)}{f([OIII3727) + f([OIII]\lambda 4958) + f([OIII]\lambda 5007)} \tag{5.20}$$

To place an object on the low versus high metallicity branch of the strong line grid, we use the [NII]/[OII] line ratio. For a sample of HII regions from nearby normal spirals, van Zee et al. [1998] found the boundary between low and high metallicity regions to be around $log([NII]/[OII]) \sim -1$. We use their line ratio cutoffs so that objects with $log([NII]/[OII]) < -1.05$ are considered low Z while objects with $log([NII]/[OII]) > -0.8$ are assigned to the high Z branch. As shown in Figure 5.7, the majority of our HII regions fall on the low metallicity branch with only one being classified as high metallicity. The remaining few objects lie in the turnaround region where the R_{23} methods return ambigous results. In these cases, we use the relation between Z and the [NII]/Hα line ratio derived by van Zee et al. [1998] using their sample of spirals and a set of low surface brightness dwarfs:

$$12 + log(O/H) = 1.02log([NII]/H\alpha) + 9.36 \tag{5.21}$$

van Zee et al. [1998] report the above relation to be good for $Z < 9.1$ within an error of 0.2 dex.

The results are presented in Table 5.4.2. The first column labels the HII region, while the second and column presents the flux in the Hβ spectral line after correction for interstellar reddening. The third and fourth columns give the applied reddening correction factor with its associated error and the assumed Balmer equivalent width used to derive the correction. In the last three columns are the metallicities as derived using the three different methods described in this section.

For 25 HII regions in a sample of dwarf irregulars, van Zee and Haynes [2006] found the metallicities derived from the McGaugh parameterization were offset from those that were calculated directly by 0.07 dex but were found to

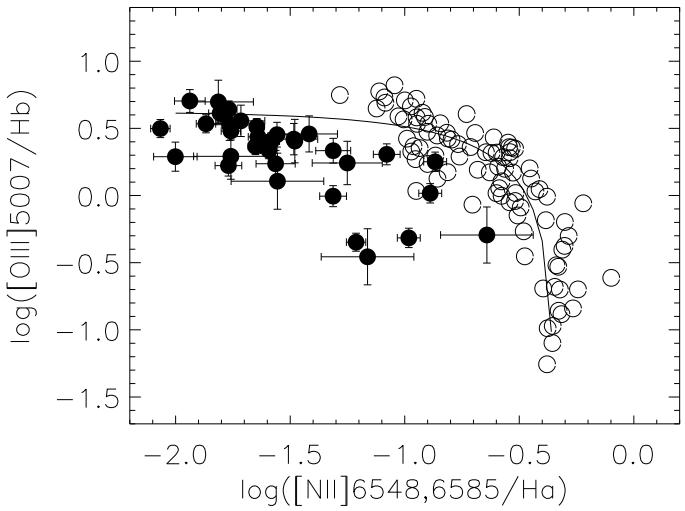

Figure 5.7 Diagnostic diagram for emission line regions for determination of placement of high versus low metallicity branch of the McGaugh grid. The current sample (filled circles) dominate the low metallicity side while the HII regions of normal spiral galaxies from van Zee et al. [1998] (open circles) fill in more of the high metallicity side of the plot. The solid line is the theoretically derived curve from Baldwin et al. [1981].

Table 5.8. Abundances for the HII Regions

HII region	$F_{H\beta} \times 10^{17}$ erg $s^{-1}cm^{-2}$	$c_{H\beta}$	EW_B Å	12 + log(O/H) Mc Gaugh	12 + log(O/H) P-method	12 + log(O/H) Direct
200496a	25.090	0.00 (0.05)	1.0	8.48	8.27	
200496b	51.110	0.00 (0.03)	1.0	8.59	8.02	
220282	127.000	0.00 (0.05)	1.0	8.82	8.42	8.41
7889	84.950	0.00 (0.04)	1.0	8.60	7.88	
251419	22.000	0.00 (0.04)	2.0	8.50	7.72	
238643	69.590	0.00 (0.15)	0.0	7.78	7.65	
191803a	6.3500	0.00 (0.05)	0.5	8.15	7.90	7.75
191803b	7.499	0.00 (0.13)	0.0	8.01	7.50	
200499	42.450	0.30 (0.20)	2.5	7.92	7.66	
211370	13.700	0.00 (0.04)	0.0	8.95	8.72	
243852	796.300	0.00 (0.02)	0.5	8.81	8.56	8.34
213512	125.000	0.00 (0.03)	0.5	8.87	8.65	8.79
224516	461.100	0.00 (0.02)	1.0	8.87	8.67	8.37
262737	3.453	0.00 (0.03)	2.0	8.05	7.79	
190472a	41.100	0.00 (0.05)	0.5	8.09	7.85	7.97
190472b	9.890	0.00 (0.07)	1.0	8.93	9.00	
200532	114.400	0.10 (0.07)	2.5	8.66	7.83	8.08
7285	32.490	0.39 (0.20)	2.0	8.77	8.10	
220321	47.320	0.00 (0.03)	1.5	8.78	8.17	
220739	23.790	0.00 (0.16)	1.0	8.40	8.20	
192402a	29.030	0.23 (0.10)	2.5	8.57	8.08	8.12
192402b	17.180	0.17 (0.10)	2.0	8.53	8.19	
215306	14.840	0.20 (0.08)	2.0	8.40	8.36	
7181a	90.100	0.00 (0.01)	1.5	8.63	7.88	8.06
7181b	3.455	0.39 (0.20)	2.5	8.55	8.01	
220555	285.800	0.00 (0.15)	0.0	8.78	8.51	8.66
232142a	4.660	0.00 (0.06)	0.5	7.98	7.83	
232142b	5.140	0.00 (0.09)	1.0	8.29	8.18	
191702a	44.500	0.00 (0.01)	1.0	7.88	7.74	7.94
191702b	58.300	0.00 (0.08)	1.0	7.83	7.69	8.06
190468	957.300	0.00 (0.09)	1.5	7.88	7.72	7.72
5186	12.230	0.00 (0.08)	1.0	8.72	8.97	
213333	63.280	0.00 (0.10)	2.0	8.57	8.54	
221013	1078.000	0.33 (0.12)	2.5	8.60	8.28	8.46
252519	459.900	0.00 (0.03)	1.5	8.08	7.96	7.86
5456a	4739.000	0.00 (0.15)	2.0	8.06	7.90	7.89
5456b	2115.000	0.10 (0.04)	2.0	8.13	8.03	8.01
5456c	225.300	0.00 (0.06)	2.0	8.51	8.16	8.20
204301	16.990	0.00 (0.08)	1.5	8.34	8.03	
213796	47.070	0.00 (0.03)	2.0	8.09	7.99	8.11
220286	22.290	0.00 (0.20)	0.0	8.74	8.07	
252211a	43.490	0.27 (0.03)	1.5	8.26	8.18	8.23
252211b	34.400	0.08 (0.02)	2.0	8.18	8.00	8.05
252211c	17.500	0.09 (0.03)	2.0	8.35	8.19	8.30

have no degeneracy with ionization parameter. The metallicities resulting from the $p-method$ matched the direct measurements within statistical errors, but showed a residual that was correlated with the ionization parameter. As shown in Table 5.4.2, we found the $p-method$ metallicities more closely matched the direct calculations.

In this chapter we detailed the observations, reduction and analysis resulting in the determination of oxygen abundances for 44 HII regions in 33 galaxies. We follow closely the methods employed by van Zee and Haynes [2006] for a sample of 21 dwarf irregular galaxies and by Saintonge [2007b] for a sample of 12 low surface brightness galaxies so we may directly compare the results. In the following chapter we will place these metallicity measurements in the context of the HI and optical data presented in previous chapters.

CHAPTER 6

DWARF GALAXY FORMATION IN THE LEO GROUP

If it were easy, someone would have done it already.

- Martha Haynes

In the following chapter we combine the HI and optical properties derived in all of the preceeding chapters to better understand the dwarf-dominated sample of galaxies in the Leo I group. First we derive basic properties like gas fraction and mass-to-light ratios to connect the stellar and gas contents of the group. We then explore the environmental influence at work in Leo I in the form of morphological segregation. Next we examine the color magnitude diagram for the group and look for outliers in the distribution's bimodality. Finally, we combine tidal and transition dwarf candidates from the Leo I group, known outliers to the metallicity measurements obtained for "normal" gas-bearing dwarfs, with additional tidal and transition candidates from other environments covered by ALFALFA to relate their gas fractions and oxygen abundances to those expected from different evolutionary scenarios.

6.1 Derived baryonic properties for galaxies in the Leo I group

Stellar Mass and Luminosity Measurements of magnitudes from the Sloan ugriz filters given in Table 4.1 are converted to the Landolt UBVRI system using the conversions from Blanton and Roweis [2007]. For example:

$$m_B = g + 0.2354 + 0.3915[(g - r) - 0.6102] \tag{6.1}$$

and

$$m_V = g - 0.3516 - 0.7585[(g - r) - 0.6102] \tag{6.2}$$

where m_B and m_V are the apparent B and V band magnitudes. The absolute B band magnitude for each galaxy can then be calculated from m_B using the distances determined in Chapter 3 with:

$$M_B = m_B - 5(log_{10}(10^6 d) - 1.) \tag{6.3}$$

where d is the distance to the galaxy in Mpc.

The B band luminosity for each galaxy is then found using:

$$L_B = 10^{(5.48 - M_B)/2.5} L_\odot \tag{6.4}$$

where the factor of 5.48 reflects the use of the absolute magnitude of the Sun in the B band ($M_{\odot,B} = 5.48$) as a reference point.

Stellar masses are typically determined by making assumptions about the mass-to-light ratio (M_*/L) of a galaxy based on the galaxy's color, such as the initial mass function governing the galaxy's star formation, and then multiplying by luminosity. For example, van Zee [2001] derived the following prescription specifically for a sample of dwarf irregular galaxies using the stellar population models of Bruzual A. and Charlot [1993]:

$$log_{10}(M_*/L)_B = -1.26 + 2.84(B - V) \tag{6.5}$$

To accurately treat the variety of morphologies found in the Leo I sample, we use the relation derived from the galaxy evolution models of Bell et al. [2003] for a large SDSS sample of galaxies:

$$log(M_*/L)_B = -0.942 + 1.737(B - V) + log(0.71). \tag{6.6}$$

The factor of 0.71 accounts for the use of a Kroupa et al. [1993] initial mass function.

Also according to Bell et al. [2003], stellar mass-to-light ratios can be derived directly from the magnitudes measured in the ugriz filters. For example, M_*/L in the g and r bands are calculated from the $g-r$ color as follows:

$$log(M_*/L)_g = -0.499 + 1.519(g-r) + log(0.71) \tag{6.7}$$

and

$$log(M_*/L)_r = -0.306 + 1.097(g-r) + log(0.71) \tag{6.8}$$

After multiplying Equations 6.6, 6.7, and 6.8 by the B, g, and r band luminosity respectively for each galaxy, we find the stellar masses derived from the g and r bands agree within 0.03 dex and thus have a negligible difference. However, an offset is found between the B-band stellar masses and those derived from the Sloan filters of 0.4 dex. The B-band stellar masses are systematically lower than the other estimates. This difference most likely derives from the fact that Bell et al. [2003] use a slightly different prescription for relating Landolt and Sloan magnitudes to derive Equation 6.6 (i.e. the relations from Fukugita et al. [1996]). We prefer the relations of Blanton and Roweis [2007] used here (Equations 6.1 and 6.2) as they incorporate updated calibrations to the SDSS photometry.

Gas Mass and Fraction The most significant contributions to a galaxy's gas content are neutral hydrogen (HI), helium (He), and molecular hydrogen (H_2). HI masses are calculated for the Leo I group members using the relation

$$M_{HI} = 2.356 \times 10^5 d^2 F_c \tag{6.9}$$

where d is the distance to the galaxy in Mpc and F_c is the integrated line flux in Jy km s^{-1} (both as given in Chapter 3). Since this relation assumes the gas

is optically thin, the HI mass derived from Equation 6.9 is actually a lower limit. The neutral helium content of a galaxy is not easily measured directly but is commonly assumed to be two-fifths of the neutral hydrogen content. Thus, $M_{atomic} = 1.4M_{HI}$. Molecular hydrogen cannot be measured directly and instead is derived from its correlation with a galaxy's CO content. However, these relations are notoriously poorly constrained [van Zee and Haynes, 2006] and often negligible [Leroy et al., 2005] for the low mass, low surface brightness galaxies like those that dominate the Leo I sample, so we assume $M_{gas} = M_{atomic} = 1.4M_{HI}$.

The gas fraction in a galaxy indicates the galaxy's efficiency at forming stars; a high gas fraction suggests star formation may have somehow been discouraged. We use the previously calculated gas and stellar masses to determine gas fractions for our sample via $f_{gas} = M_{gas}/(M_{gas} + M_*)$.

Optical parameters are not derived for three of the galaxies for which the photometry was incomplete. As discussed in Chapter 4, for 8 of the most extended galaxies in Table 6.1, no SDSS colors were available and so $B - V$ colors were taken directly from the Third Reference Catalog of Bright Galaxies (RC3; Roman et al. [1991]). For UGCs 5708 and 5812, the RC3 reports no V band color, and so for those two galaxies no M_*/L_B (and thus no M_*) can be derived. Reliable photometry was also unavailable for AGC205505 due to a satellite trail in the g-band image.

The entire Leo I region has been mapped by the ALFALFA survey, and so we are able to place upper limits on M_{HI}, f_{gas} and M_{HI}/L_B for those galaxies not detected in HI. The upper bound to the HI mass of a nondetection is calculated in the same way the HI mass is determined for an object that is detected

using Equation 6.9. The integrated line flux F_c is approximated by the peak flux multiplied by the width of the signal. We measure the noise of the integrated spectrum in an area $8' \times 8'$ centered on the position of the optical galaxy in the ALFALFA map (except in the case of AGC205268 for which we used a region of $4' \times 4'$ due to its proximity to NGC3338) and assume a peak flux of 3 times the rms. To estimate the velocity width for each source, we employ a method similar to that of Grossi et al. [2009] for placing lower mass limits on early-type galaxies not detected by ALFALFA: a velocity width of 200 km s^{-1} is assumed for sources with $M_B < -17$ (NGCs 3377, 3379, 3384, and 3412) and for the remaining sources with $M_B > -17$, a velocity width of 50 km s^{-1} is assigned.

6.2 Role of environment

6.2.1 Quantifying environment in the Leo I group

ALFALFA has proven Leo I to be a gas-rich group with a population of low surface brightness yet gas-rich galaxies missed by previous optical surveys (see Chapter 3). The largest contributions to the HI gas density, the Leo Ring and Leo Triplet tidal features, surround the central, massive galaxies. The few early-type galaxies that lack HI entirely have HI-rich, massive galaxies as close neighbors. Thus, unlike in dynamic environments like the Virgo cluster where gas stripping events commonly displace the HI content from the optical content of the group, the HI gas density in Leo I follows the optical luminosity distribution very closely for systems with masses greater than the dwarf level.

Since all of the galaxies in the Leo I sample are already known to be located

Table 6.1. Baryonic Content of Leo I Galaxies

AGC #	Other Name	D Mpc	log(L_B) $L_\odot$	M_*/L_B $M_\odot/L_\odot$	log(M_*) $M_\odot$	log(M_{HI}) $M_\odot$	f_{gas}	M_{HI}/L_B $M_\odot/L_\odot$
202171		19.0	7.57	0.47	7.23	<7.49	<0.71	<0.83
5453	093-047	13.0	8.30	0.21	7.62	7.88	0.72	0.38
203913	037-033	18.8	8.14	0.18	7.40	8.35	0.93	1.62
202218		19.6	8.21	0.63	8.01	7.73	0.42	0.33
205156		11.1	6.80	0.40	6.40	6.91	0.82	1.30
5708	037-061	19.1	9.67			9.41		0.55
204139		18.6	7.50	0.22	6.84	7.54	0.88	1.09
202248		11.1	7.36	0.14	6.52	7.28	0.89	0.83
202017	LeG03	11.1	7.31	0.10	6.32	7.75	0.97	2.74
5761	N3299	11.1	8.58	0.77	8.46	8.00	0.33	0.27
200499	065-074	11.1	8.61	0.23	7.97	8.35	0.77	0.55
202018	LeG04	11.1	6.69	3.21	7.20	<6.92	<0.42	<1.70
202019	LeG05	11.1	7.44	0.63	7.24	6.37	0.16	0.09
200512	LeG06	11.1	7.56	0.11	6.59	7.09	0.82	0.34
5812	065-083	11.1	8.36			7.65		0.19
200532	065-086	11.1	7.96	0.27	7.38	7.46	0.63	0.32
202020	LeG09	11.1	7.14	0.55	6.88	<7.04	<0.67	<0.79
205268		11.1	7.29	0.34	6.88	<7.39	<0.82	<1.27
202021	LeG10	11.1	6.47	0.45	6.12	<6.86	<0.88	<2.45
5850	N3351	10.0	10.08	1.45	10.24	8.98	0.07	0.08
202022	LeG11	11.1	6.93	0.64	6.73	<6.90	<0.67	<0.93
202023	LeG12	11.1	6.65	0.28	6.10	<6.94	<0.91	<1.95
205445		11.1	7.71	0.23	7.07	<7.01	<0.55	<0.20
202024	LeG13	11.1	7.18	0.41	6.79	6.81	0.60	0.42
202025	FS 13	11.1	6.89	0.43	6.53	<6.58	<0.61	<0.49
201990	FS 14	11.1	7.32	0.42	6.94	<6.84	<0.53	<0.33
202027	FS 17	11.1	7.41	0.49	7.09	7.56	0.80	1.42
5882	N3368	10.5	9.77	2.88	10.23	9.20	0.11	0.27
201971	FS 20	11.1	6.48	5.50	7.22	<6.86	<0.38	<2.40
205505		11.1	5.12			<7.13		
5889	N3377A	9.30	8.06	0.40	7.66	8.08	0.79	1.05
5899	N3377	11.2	9.90	2.34	10.27	<7.59	<0.003	<0.005
5902	N3379	11.0	9.84	2.01	10.14	<7.58	<0.004	<0.005
5911	N3384	11.6	9.75	1.61	9.96	<7.62	<0.006	<0.007
200596	066-026	11.1	8.02	0.71	7.87	<7.00	<0.16	<0.10
5923	038-022	9.00	8.31	0.63	8.11	7.76	0.38	0.28
202029	LeG23	11.1	6.43	0.09	5.37	<6.86	<0.98	<2.69
5944	064-033	11.1	7.93	1.08	7.97	<6.98	<0.13	<0.11
201991	KK96	11.1	7.38	0.52	7.09	<6.89	<0.47	<0.32
5952	N3412	11.3	9.56	1.18	9.63	<7.60	<0.01	<0.01
5962	N3423	11.7	9.11	1.28	9.21	9.02	0.47	0.82
202030	LeG26	11.1	7.25	3.61	7.81	<6.86	<0.14	<0.41
205540		11.1	7.06	0.61	6.85	<7.00	<0.66	<0.86
5974	038-032	25.1	9.10	0.25	8.50	9.39	0.92	1.97
205544		11.1	7.39	0.75	7.27	<7.00	<0.43	<0.41
202456		11.1	7.75	0.80	7.65	<7.00	<0.24	<0.18

Table 6.1 (continued)

AGC #	Other Name	D Mpc	log(L$_B$) $L_\odot$	M_*/L_B $M_\odot/L_\odot$	log(M_*) $M_\odot$	log(M_{HI}) $M_\odot$	f_{gas}	M_{HI}/L_B $M_\odot/L_\odot$
202031	LeG27	11.1	6.75	0.85	6.68	< 6.86	< 0.68	< 1.29
202032	LeG28	11.1	7.04	3.61	7.60	< 6.85	< 0.20	< 0.65
6014	066-058	11.1	8.16	0.22	7.50	7.92	0.79	0.58
202034	D640-12	11.1	7.30	0.68	7.13	6.46	0.23	0.14
202035	D640-13	11.1	7.59	0.15	6.76	7.69	0.92	1.26
202036	D640-14	11.1	7.11	0.41	6.73	< 6.58	< 0.50	< 0.30
205278		11.1	7.30	1.11	7.34	7.01	0.39	0.52
6082	N3489	12.1	9.96	0.99	9.95	7.36	0.004	0.003
202038	LeG33	11.1	6.69	0.78	6.58	< 6.87	< 0.73	< 1.51
202039	D640-08	11.1	7.49	0.23	6.86	< 6.52	< 0.39	< 0.11
210023	066-109	11.1	7.76	0.17	7.00	7.70	0.88	0.86
211261	I678	13.3	8.38	3.33	8.90	< 7.20	< 0.03	< 0.07
215282		11.3	7.76	0.14	6.91	6.91	0.58	0.14
6272	N3593	10.0	9.28	1.42	9.43	8.36	0.11	0.12
202256		10.0	7.22	0.22	6.55	7.16	0.85	0.87
6277	N3596	20.7	9.76	0.80	9.66	9.47	0.48	0.52
215281		19.0	7.54	0.22	6.88	< 7.39	< 0.82	< 0.71
215284		19.7	7.77	0.13	6.87	7.54	0.87	0.59
212132	039-094	18.6	8.43	0.65	8.25	8.24	0.58	0.64
210220	I2684	10.0	7.68	0.83	7.60	7.09	0.30	0.26
213006		12.7	7.07	0.46	6.73	< 7.14	< 0.78	< 1.18
6328	N3623	10.0	10.33	1.77	10.58	8.37	0.01	0.01
202257		10.7	7.30	0.18	6.56	7.90	0.97	3.95
215354		10.0	7.25	0.39	6.84	< 6.85	< 0.59	< 0.40
213074		13.7	7.69	0.08	6.60	7.93	0.97	1.75
6346	N3627	10.0	10.54	0.89	10.49	8.92	0.04	0.02
6350	N3628	10.0	10.46	0.70	10.31	9.66	0.24	0.16
211370	I2767	10.0	7.42	0.16	6.62	7.62	0.93	1.60
213436		10.0	7.49	0.41	7.11	< 6.94	< 0.49	< 0.28
6395	I2782	10.0	8.15	0.31	7.63	< 6.89	< 0.20	< 0.06
6401	U6401	10.0	7.87	1.00	7.87	7.35	0.30	0.30
213440	I2791	10.0	7.40	0.29	6.86	6.67	0.47	0.18
215142		20.0	8.14	0.23	7.50	8.29	0.90	1.41
6438	I692	20.5	9.17	0.30	8.63	8.53	0.53	0.23
215296		11.5	6.98	0.05	5.66	7.23	0.98	1.77
210340	I2828	17.9	8.85	0.20	8.14	8.30	0.67	0.28
213091		8.60	6.81	0.57	6.57	< 6.80	< 0.71	< 0.98
212837	KKH68	10.7	7.07	0.28	6.52	7.68	0.95	4.08
215303		15.0	7.45	0.18	6.70	7.43	0.88	0.95
215304		20.3	8.34	0.30	7.81	8.13	0.75	0.62
215306		20.4	8.00	0.47	7.67	7.54	0.51	0.34
215248		11.3	7.28	0.29	6.74	6.88	0.66	0.40
210459	I2934	21.4	8.80	0.12	7.88	8.65	0.89	0.71
212838	KKH69	10.4	7.27	0.02	5.47	7.57	0.99	2.00

in an intermediate density group, useful information cannot be derived from nearest neighbor or fifth nearest neighbor searches usually employed to quantify a galaxy's environment. Instead we assess the environment for a galaxy in Leo I by determining the distance to its nearest massive neighbor. The massive group members are selected as those galaxies with $M_{HI} > 10^9 M_\odot$ (M95, M96, M66, and NGCs 3423, 3596, and 3628), as well as any optical galaxies without associated HI detections with $M_* > 10^{10} M_\odot$, (the large elliptical and S0 galaxies M105 and NGCs 3377 and 3384). We also include NGC3623 with the large galaxies to include all three Leo Triplet members.

6.2.2 Morphological segregation

Clear evidence for morphological segregation exists among Leo I group galaxies as shown in Figures 6.1 and 6.2. The first figure shows the distribution of galaxies detected in ALFALFA (i.e. HI-bearing, open circles) as compared to the locations of gas-poor galaxies not found in the ALFALFA sample (filled circles). The gas deficient systems are more likely to be found clustered around massive galaxies (marked with crosses) than the widespread distribution of gas-bearing systems. Figure 6.2 shows this distribution of low-mass Leo I galaxies in relation to the nearest primary galaxy as compared to the Local Group dwarfs presented in Table 1. The same trend is seen for both groups: the majority of gas-poor systems are found within 300-400 kpc as was seen for Local Group dwarf spheroidals [Grebel et al., 2003b] while the gas-bearing systems are more widely distributed. A similar result was observed for early-type dwarfs in the Sculptor group [Skillman et al., 2003]. The overlaid stars mark the distance bins containing the two transition dwarf candidates from our spectroscopy sample

that are Leo I group members, AGC215306 and CGCG 065-074 (AGC200499) and the six transition dwarf candidates in the Local Group (Leo T, Phoenix, LGS 3, Pegasus, Aquarius, and Antlia). Both transition candidates in the Leo I group are found within the low radial separation from massive galaxies prefered by gas-poor dwarfs thus supporting the possibility of transition dwarfs as progenitors to gas-poor dwarf systems. The same cannot be said, however, for the transition dwarfs in the Local Group.

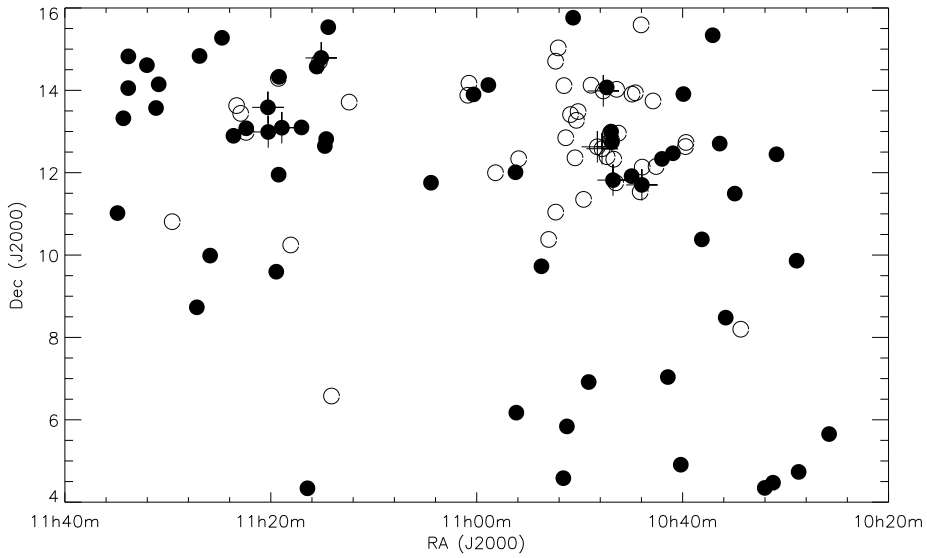

Figure 6.1 Distribution of HI-bearing (filled circles) versus HI-lacking (open circles) galaxies in the Leo I group. Gas-bearing systems detected in ALFALFA are found distributed in regions of both high and low galaxy density, while galaxies not found in ALFALFA (i.e. with little to no neutral gas) are more commonly found clustered around the most massive group members (crosses). The massive members include all Leo I galaxies with $M_{HI} > 10^8 M_\odot$ (M95, M96, M66, and NGCs 3423, 3596, and 3628) or $M_* > 10^{10} M_\odot$ (the large elliptical and S0 galaxies, M105, and NGCs 3377 and 3384). We also include NGC3623 with the large galaxies to include all three Leo Triplet members.

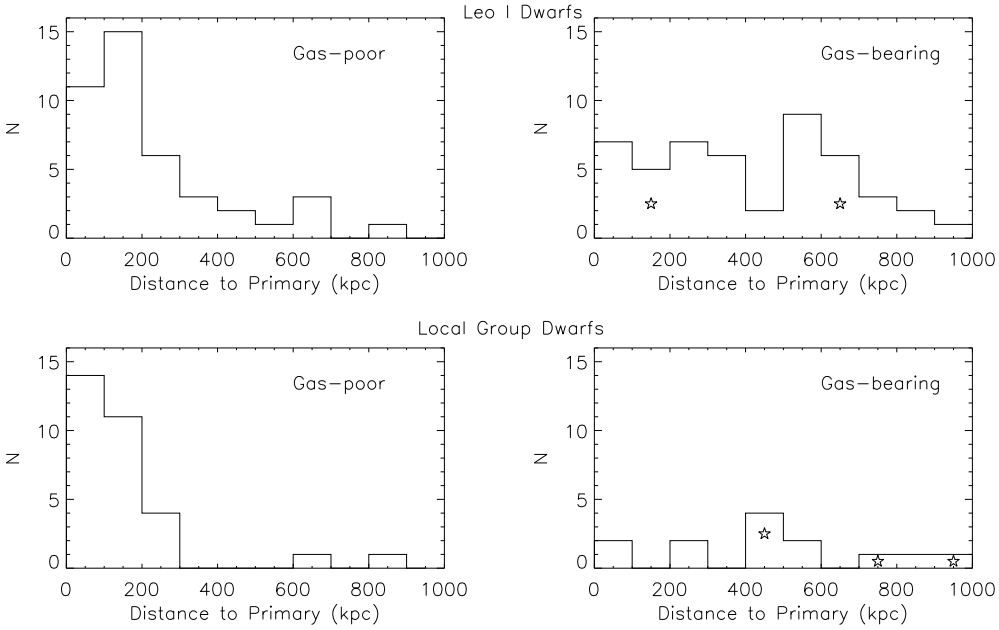

Figure 6.2 Evidence of morphological segregation in Leo I as compared to the same trend seen for Local Group dwarfs. Leo I galaxies not found in ALFALFA (upper left panel) are more likely to be found at a smaller distance from the nearest massive neighbor than the widespread distribution of HI-bearing galaxies found in ALFALFA (upper right panel). A similar distribution is seen in the Local Group as derived from Table 1 (lower left and right panels) suggesting the same environmental effects may be driving morphological segregation in both galaxy groups. The stars mark the bins containing the two transition dwarf candidates in the Leo I group (see Chapter 5) and the six transition dwarfs in the Local Group.

6.2.3 Gas Fraction

The gas fraction (f_{gas}) in a galaxy indicates the galaxy's efficiency at forming stars; a high gas fraction suggests star formation has somehow been discouraged. While studies of large spiral field galaxies have found an average f_{gas} of 0.25 [Haynes et al., 1999], samples of low luminosity dwarfs, like that of Geha et al. [2006] of 101 galaxies pulled from the NYU-VAGC, have found average gas fractions of 0.6 (see Chapter 4 for a description of the NYU-VAGC). The Leo

I dwarf sample (which includes all galaxies with $M_{HI} < 10^8 M_\odot$) has an almost identical value of $< f_{gas} >= 0.61$. These larger gas fractions are evidence that dwarf galaxies have either recently acquired their gas (an unlikely scenario for every single dwarf in such large samples) or are somehow less efficient at forming stars than their more luminous counterparts.

Comparisons of gas fraction to other galaxy properties both internal (such as color or size) and external (such as distance to the nearest massive neighbor) offer clues as to what factors contribute most significantly to a galaxy's ability to form stars. For the Leo I sample which spans the full range of gas fractions, no trend is seen with HI or optical extent. However, a further segregation of dwarfs of different gas contents beyond the morphological segregation described in the previous section is seen for the group's HI-bearing population. As shown in Figure 6.3, HI-bearing dwarf systems (filled circles) found nearest to the massive group members span the full range of gas fractions. Those dwarfs not detected in ALFALFA also have upper limits (marked by arrows) to their gas fractions from almost nothing ($\sim$0.1) to 1.0. However, at larger separations (> 500 kpc from the nearest massive galaxy), no dwarfs of low gas fraction are found and no galaxies without HI detections are found past 600 kpc. The outlying point at a separation of 600 kpc and almost negligible gas fraction is the very luminous yet gas-poor lenticular galaxy, NGC3489 which was noted by Grossi et al. [2009] as being among the faintest HI detections in their sample of early-type galaxies.

If environment is to blame for those HI-bearing dwarfs with low gas fractions, we would expect not to find such systems widely distributed throughout the group. The lack of dwarfs with low gas fractions at large separations is harder to explain, however, if gas-deficient and gas-rich systems represent in-

trinsically different classes without an evolutionary link. Figure 6.3 also offers further evidence that a significant population of dwarfs is missed by surveys that focus only on the inner $1-10\%$ of a group as in the case of previous optical surveys of Leo I (see Chapter 3).

A strong correlation between color and f_{gas} has been observed for the Geha et al. [2006] sample of low luminosity dwarfs. Gas-rich dwarfs tend to be bluer which may indicate more star formation in the recent past. However, none of the galaxies in their sample fall below $M_{HI} = 10^7 M_{\odot}$, and they miss extremely low surface brightness objects which are not included in the NYU-VAGC, but are common in the HI-selected ALFALFA catalog. Thus the Leo I dwarf sample tests this trend at even lower masses and lower surface brightness levels than has been possible with optically-based datasets. As shown in Figure 6.4, the HI-bearing dwarfs in Leo I (shown as filled circles) confirm that the correlation between blue color and higher gas fraction still exists for extremely low surface brightness and low HI mass objects. So although star formation has been stunted in these galaxies for most of their history, they do not appear to have trouble forming stars in the recent past. The dwarfs not detected in ALFALFA (upper limits marked as arrows in Figure 6.4) also follow a similar trend: we are able to place stricter limits on the redder systems.

The only galaxy in the "red" half of Figure 6.4 (i.e. $u-r > 2.0$) found to have a gas fraction greater than 0.5 is AGC211370 (I2767) which was selected in Chapter 5 as a tidal dwarf galaxy candidate based on its proximity to the Leo Triplet. As we will see in the next section, the high metallicity of I2767 given its luminosity may indicate tidal origins and so may the high gas fraction seen in Figure 6.4.

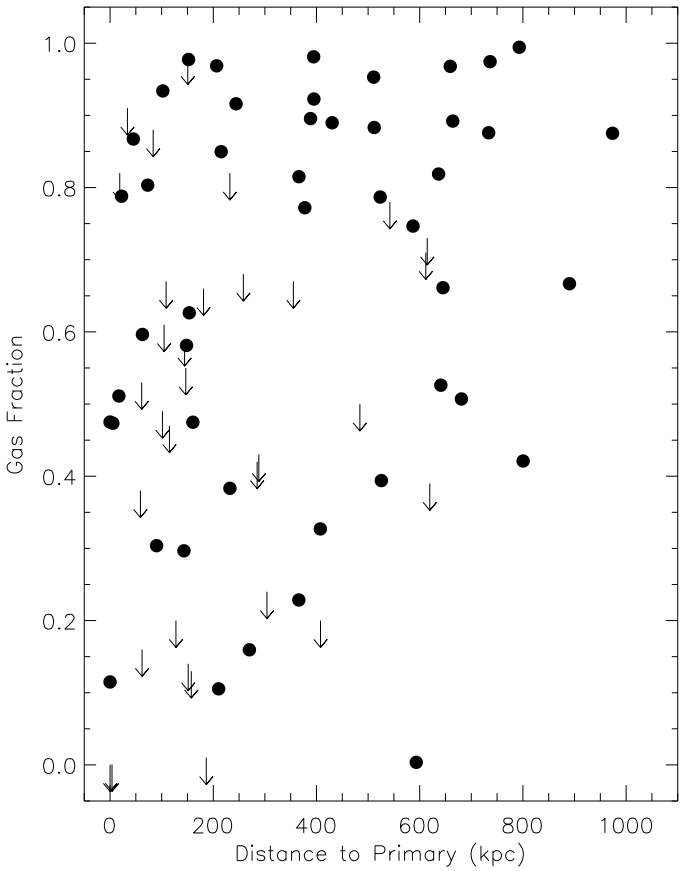

Figure 6.3 Gas fraction for HI-bearing dwarf galaxies in the Leo I sample (filled circles) and upper limits to gas fractions for optical dwarf galaxies not found in ALFALFA (arrows) versus distance to the nearest massive neighbor. At small separations, the HI-bearing dwarfs and upper limits for HI-deficient dwarfs span the entire range of gas fractions, but at separations greater than 500 kpc, no dwarfs with low gas fractions are found. No gas-deficient dwarfs are found past 600 kpc. This segregation of dwarf gas fraction extends the segregation seen for gas-poor versus gas-bearing systems also seen for the group and further suggests a dominant role of environment in dwarf galaxy evolution. The outlying point at a separation of 600 kpc with negligible gas fraction is the luminous yet gas-poor lenticular galaxy, NGC3489.

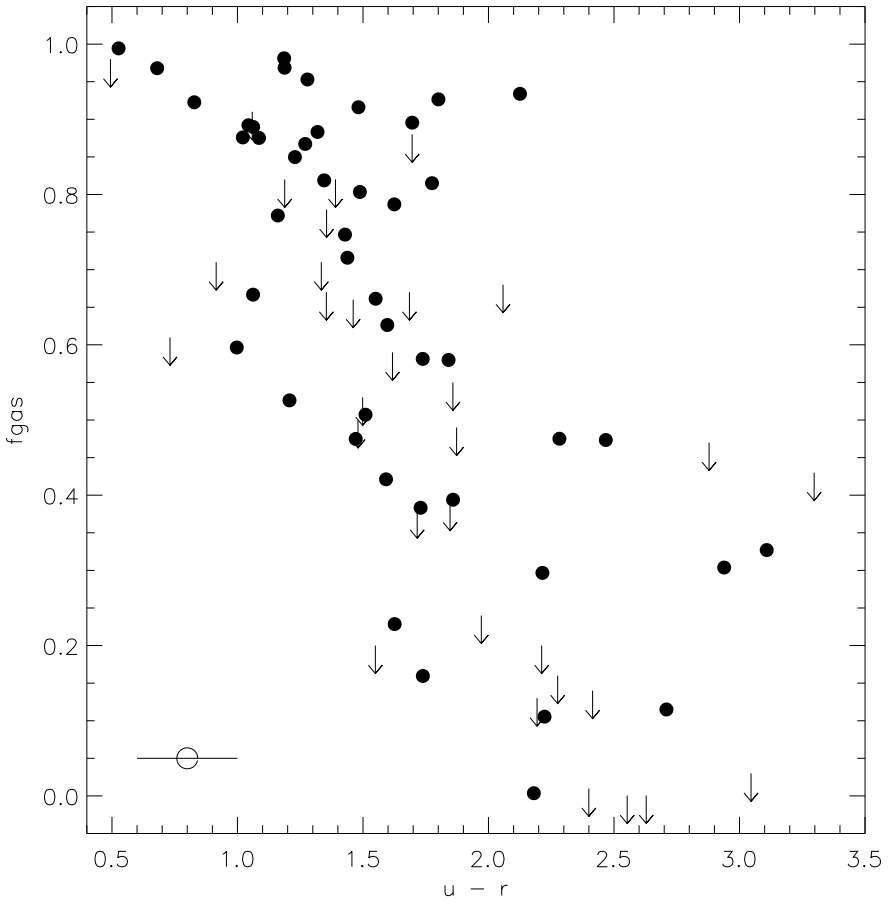

Figure 6.4 u-r color versus gas fraction for HI-bearing dwarfs (filled circles) the Leo I group sample. The tendency for dwarfs of higher gas fractions to be bluer is confirmed for lower HI mass and lower surface brightness dwarfs in the Leo I group. For gas-poor dwarfs not detected with ALFALFA, stricter upper limits (marked with arrows) are found for the redder systems. The errors are dominated by sky subtraction in the uband which has a uniform effect for most sources so a sample color error bar is shown in the bottom left of the plot. For more detailed uncertainty estimates, see Table 4.1.

Another indication of a galaxy's star forming efficiency is it's HI mass-to-light ratio, M_{HI}/L_B. In Figure 6.5, the absolute B band magnitudes are plotted against the HI-mass-to-light ratios for the Leo I galaxies. Detections are shown as filled circles and upper limits are depicted by arrows as in previous figures. The solid line shows the ALFALFA 3-σ detection limit assuming an rms of 2 mJy

and a velocity width of 50 km s^{-1}. Although it is reasonable to assume that the ALFALFA detections will be biased towards gas-rich objects and so the fact that $M_{HI}/L_B > 0.1$ for the entire range of magnitudes is not unexpected, there is a gap between the detection limit depicted by the solid line and the detections for $M_B > -16$. Most likely this lack of detections with low mass-to-light ratios at higher luminosities reflects the small number of L^* galaxies in Leo I (as well as the small volume covered by the group) and does not represent a missing population of luminous, gas-poor galaxies. The outlier to the bottom left of the plot is again the lenticular galaxy NGC3489 as in Figure 6.3.

6.3 Color - magnitude distribution

Historically galaxies have been classified by visual inspection of broadband optical images as early if they have smooth stellar distributions but no disk structure, or as late if they have disk-like or irregular structure with patches of star formation. While such a classification system can be applied to most galaxy studies and is thus a useful metric for comparing different extragalactic observations, the identifications rely ultimately on qualitative galaxy properties.

With large samples like the more than one million galaxies from the SDSS, such visual inspection and identification cannot be performed for every galaxy. Attempts have been made to increase the person-power involved by including the public in this effort (Galaxy Zoo; Lintott et al. [2008]), but the results remain inhomogeneous. A new classification scheme that is more quantitative, and thus potentially a more telling link among galaxies of similar evolutionary tracks, has been derived from the color-magnitude diagrams (CMDs) observed

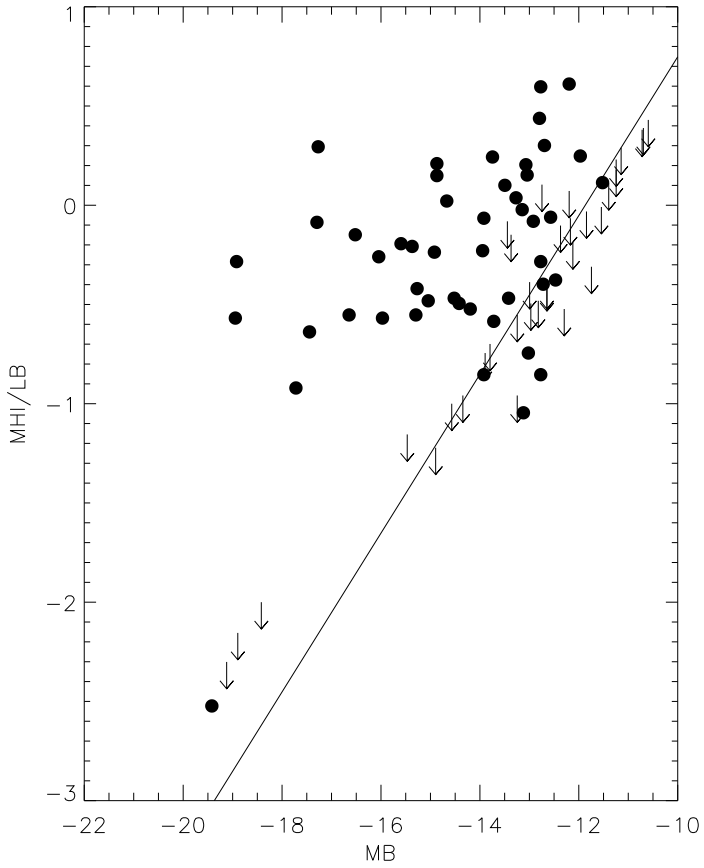

Figure 6.5 HI mass-to-light ratios for the Leo I sample as a function of absolute B band magnitude. $M_{HI}/L_B > 0.1$ for the entire sample except for the lenticular galaxy, NGC3489. Although the ALFALFA detection limit (solid line) suggests there may be a missing population of luminous galaxies with low mass-to-light ratios in the bottom left corner of the plot, this gap most likely reflects the lack of L^* galaxies in Leo I and the small volume covered by the group.

for SDSS galaxies (Strateva et al. [2001]; Baldry et al. [2004]). The relation between absolute r band magnitude and u - r color shows a clear bimodality that separates galaxies into a red sequence and a blue cloud.

For most galaxies, this bimodal color classification based on CMDs (also called Baldry plots) gives the same results as the early versus late type scheme. Early-type galaxies tend to be redder, while late-type galaxies are usually bluer.

However, any exceptions to the categorical matches (i.e. blue cloud galaxies with early-type morphologies or red sequence galaxies with late-type morphologies) may have undergone some sort of transformation in their histories that make them members of a transition class of galaxies similar to that discussed for dwarfs (see Chapter 5). Schawinski et al. [2009] found $\sim 6\%$ of the early-type systems at low redshift ($z < 0.05$) to be blue cloud galaxies using the classification results of the Galaxy Zoo project[1]. The population of blue, early-type galaxies were all found to have super solar metallicites and to avoid groups and clusters with velocity dispersions greater than 200 km s^{-1}. Based on comparisons with numerical simulations, Schawinski et al. [2009] suggest these objects form either via major mergers or cooling events.

Since the Leo I group has both a low velocity dispersion and well-known tidal remnants, we derive the CMD for the Leo I sample and plot the relation in Figure 6.6. The large scatter at low luminosities shows that the bimodal distribution does not exist for $M_r > -15.5$. The boundaries of the box in Figure 6.6 are set to match those of Figure 6 in Baldry et al. [2004] for ease of comparison with the CMD derived for their low redshift sample of SDSS galaxies. At higher luminosities, a separation between the red sequence and blue cloud galaxies is more apparent even given the large uncertainties. However, although distance uncertainties are minimized for Leo I which has 10 members with known primary distances, Figure 6.6 must be used cautiously, as there are still some uncertainties associated with M_r.

Despite the match between the Leo I group and the criteria for environments fostering blue, early-type galaxies proposed by Schawinski et al. [2009], only one such system is found in our sample. In the M96 group, CGCG 065-074

[1]http://www.galaxyzoo.org/

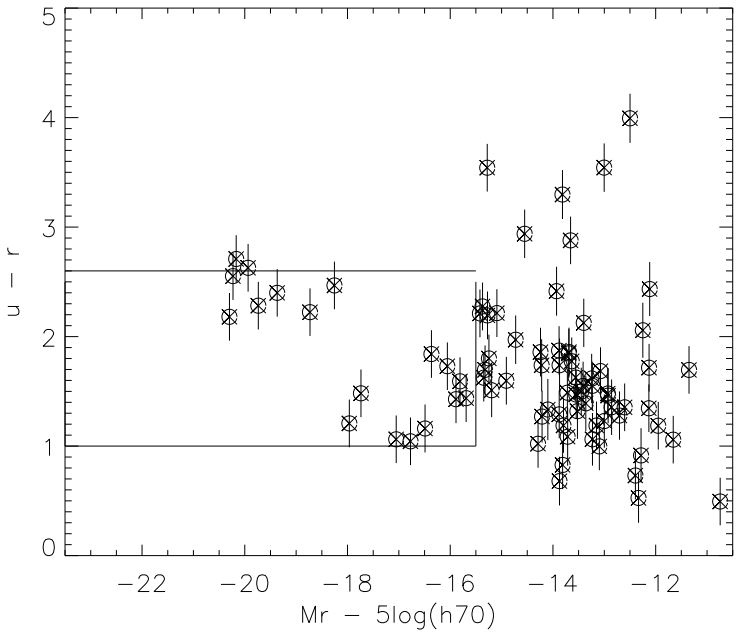

Figure 6.6 u - r color versus absolute r-band magnitude (color - magnitude diagram) for the 83 Leo I galaxies with available SDSS photometry. The box outlines the scale of Figure 6 in Baldry et al. [2004] for comparison. A possible bimodality of red sequence versus blue cloud galaxies is seen in the distribution for luminous galaxies within the box, while the surrounding scatter shows this bimodality does not continue to lower luminosities.

(AGC200499) exhibits clear early-type morphology in broadband optical images, but has an HI mass of $10^{8.35} M_{\odot}$ and a u - r color of 0.32 placing it in the blue cloud. Based on its mixed morphology, CGCG 065-074 was targetted as part of the metallicity study described in Chapter 5 but was not found to have super solar oxygen abundance (given the solar abundance of 12 + log (O/H) = 8.66 from Asplund et al. [2005]) nor to be especially metal-rich given its luminosity (see Section 6.4 below for details). CGCG 065-074 lies at the extreme right of the high luminosity half of the CMD (left panel of Figure 6.6) and thus may represent the boundary where the bimodality of the distribution breaks down.

If future studies determine that other low velocity dispersion groups with

tidal debris are also found to lack blue, early-type galaxies, our Leo I sample may contribute to the idea that major cooling events play a more significant role in the formation of these CMD outliers than tidal interactions. However, if as many as one third of our Leo I galaxies is early-type (an overestimate for such a gas-rich group), we would only expect to find one blue, early-type galaxy in our sample. Thus our null result may only reflect a small search volume.

We also use Figure 6.6 to search for red, late-type galaxies. Of the 8 objects found in the red sequence, three are not found by ALFALFA, exhibit clear elliptical or lenticular morphologies and thus are of no surprise (M105, NGC3384, and NGC3412). A fourth galaxy, NGC3489 has already been discussed as an outlier to the ALFALFA sample with its early-type morphology and very low gas content. The remaining 4 galaxies (NGC3423, M96, NGC3593, and NGC3596) are all classified as SA (normal spiral) or SAB (barred spiral) in the RC3 [Roman et al., 1991]. In particular, NGC3596 and NGC3423 are face-on spirals with obvious knots of current star formation distributed throughout their disks. Rather than having uncovered a population of red, late-type galaxies, we instead fear we have revealed more problems with the photometry derived from the SDSS as mentioned in Chapter 4. Photometry in four of the five cases was derived from the VAGC, and for NGC5962, the photometry came from the lowz catalog which is expected to improve on the deblending issues found in the VAGC. Thus other samples that employ the use of SDSS photometry at low redshift may be plagued by large photometric errors based on poor deblends of extended galaxies.

6.4 Metallicity-Luminosity Relation

The correlation between metallicity and luminosity (Z-L; see Skillman et al. [1989]), originally observed as a trend between stellar mass and luminosity [Lequeux et al., 1979], has been well-established by observations for dwarf spheroidals [Aaronson and Mould, 1985], dwarf irregulars (van Zee and Haynes [2006]; Skillman et al. [1989]) and recently for low surface brightness dwarfs [Saintonge, 2007b], but the origin of the relation remains poorly understood. The possible explanations fall under two scenarios, called open and closed box models. In the first, closed-box scenario, more luminous galaxies have evolved by processing heavier elements through star formation, while the less luminous systems have failed to form stars efficiently. For massive galaxies, a critical mass surface density is observed below which not enough gas is present to incite star formation (Kennicutt [1998]; Schmidt [1959]). A similar, global threshold is not found for dwarf systems, but rather the *local* gas surrounding sites of star formation must reach a certain surface density to allow star formation to proceed (Begum et al. [2006]; van Zee [1996]).

Alternatively, in open box scenarios, low mass systems evolve to form heavier metals just as more luminous systems do, but are somehow unable to retain them. Simulations have shown that for the shallow gravitational potential wells of dwarf systems, a signifcant fraction of the galaxy's gas can be lost to outflows resulting from supernovae explosions [Dekel and Silk, 1986]. However, such significant gas loss is only seen for gas-rich dwarf irregulars and cannot explain the low metallicities of gas-poor dwarf spheroidal systems [Dalcanton, 2007]. Inflows of pristine gas may instead dilute more enriched gas processed via star formation and thus lower the metallicity of a galaxy [Köppen and Ed-

munds, 1999]. Recent simulations show, however, that the infall of metal-poor gas alone is likely insufficient to explain the low metallicities as such systems will once again resemble dwarfs from the closed box models after only very short timescales [Dalcanton, 2007].

Offsets in the Z-L relationship between different dwarf galaxy morphologies have also been argued to represent the separate evolutionary tracks followed by the different populations. Dwarf irregulars were labeled as unlikely progenitors for gas-poor dwarf spheroidal systems in the Local Group because dIs are found to be more luminous for equal metallicities than early-type dwarfs [Grebel et al., 2003b]. The cause of the Z-L relationship is thus intimately linked with the processes by which dwarf galaxies evolve.

We present the Z-L relation for the sample of optical spectroscopy targets in Figure 6.7. The metallicities derived from the McGaugh and Pilyugin methods are displayed in the upper and lower panels respsectively. The solid line gives the best fit slope to the Z-L relation as derived for a set of 67 HII regions in low mass dwarf irregular galaxies [van Zee and Haynes, 2006], and the x's show the metallicities derived for a sample of gas-rich, low surface brightness galaxies found in ALFALFA [Saintonge, 2007b].

No offset is observed between the transition dwarf candidates (open circles) and the collection of low mass, gas-rich targets also detected by ALFALFA (filled circles). A true transition class of galaxy will most likely cover a range of Z-L values and our HI-selected sample may be biased toward similarities with gas-rich dwarfs. We may also be limited by our metallicity determination method which requires the presence of HII regions to obtain nebular abundances. The five crosses mark the transition dwarf sample of Skillman et al. [2003] in the

Sculptor Group, most of which lie at the high metallicity edge of the scatter in the relation. However a clearer offset from the Z-L relation for the dwarf irregulars is needed if the transition dwarfs are to be assigned the status of progenitors for dwarf spheroidal systems. The scatter in the relation shown in Figure 6.7 definitely derives from uncertainties in the determinations of the metallicities and in the distance measurements to each galaxy used to derive M_B. Additionaly, the qualitative nature of our sample selection for the transition dwarfs (defined by HI content and smooth-looking stellar distributions) may also contribute. The ALFALFA dataset has grown significantly since the observations described here, and so we are afforded the luxury of narrowing our criteria using more selective and quantitative methods.

Perhaps the most interesting galaxies seen in Figure 6.7 are the three triangles that represent the three candidate tidal dwarf targets. For both metallicity calibrations, they are the highest metallicity objects of our 37 targets. The location of the faintest tidal dwarf candidate, I2767 (AGC211370), on the lower panel is nearly coincident with that of VCC2062 (marked by a star), a well-studied tidal dwarf candidate in the outskirts of the Virgo cluster Duc et al. [2007]. The tidal dwarf status of VCC2062 is supported by its strong CO emission, its unusually high oxygen abundance given its luminosity, and its low dynamical mass. I2767 can be seen in Figure 2.5 $\sim 45'$ south of the tidal plume associated with the Leo Triplet and may be associated with the surrounding tidal debris.

The oxygen abundances for our dwarf sample can also be compared to their average oxygen yield to test the likelihood of different closed boxed scenarios for their evolution. The yield of the element O, defined as the ratio between the rate at which the oxygen is produced and ejected versus the rate at which

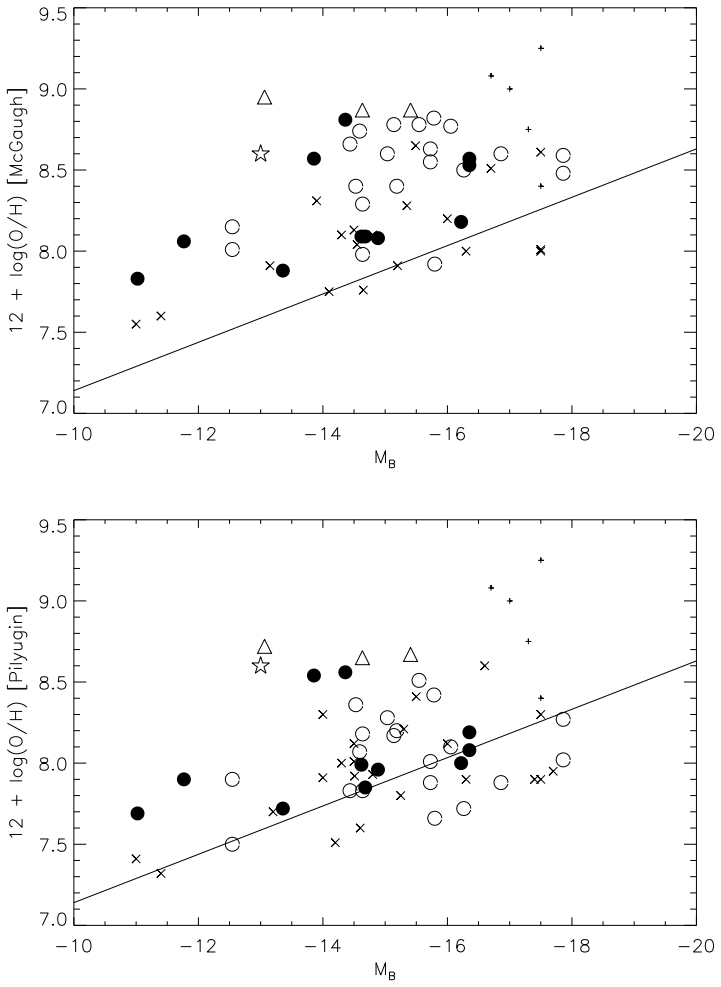

Figure 6.7 Relation between oxygen abundance and absolute B band magnitude (Z-L relation) for our spectroscopic sample using the McGaugh method for metallicity calibration (upper panel) and the Pilyugin method (lower panel). In each panel, the line marks the best fit relation derived for a sample of gas-rich dwarf irregulars [van Zee and Haynes, 2006]. No offset is seen for the relation for the transition dwarf candidates (open circles) and the low mass dwarf irregulars (filled circles) or the HI-selected low surface brightness galaxies of Saintonge [2007b] (x's). The Sculptor group transition dwarfs of Skillman et al. [2003] (crosses) also appear to fall within the scatter. Three tidal dwarf candidates (open triangles) have notably higher metallicities than the rest of the targets, and I2767 almost coincides with a well studied tidal dwarf VCC2062 marked with a star.

hydrogen flows into the galaxy, can be related to the mass ratio of the element to that of hydrogen according to the chemical evolution models of Searle and Sargent [1972] via:

$$M_O/M_H = p(O)ln(1 + \frac{Mstars}{Mgas}) \tag{6.10}$$

where M_O is the mass of oxygen, M_H is the mass of hydrogen, and p(O) is the galaxy's oxygen yield. Using the fact that an oxygen atom has 16 times the mass of a hydrogen atom and assuming the ISM is 75% hydrogen, we can use our previous equation for gas fraction ($f_{gas} = M_{gas}/(M_{gas} + M_*)$) to relate the expected relation between oxygen abundance and gas fraction:

$$12 + log(O/H) = 12 - log(12) + log[p(O)ln(1/f_{gas})]. \tag{6.11}$$

The relation for our spectroscopic targets is given in Figure 6.8. Overplotted are the expected linear relationships derived for different evolutionary scenarios. The upper dashed line represents an oxygen yield of $p(O) = 0.0074$ which is predicted for a Salpter IMF in a closed box system (no inflows or outflows) by Meynet and Maeder [2002]. Although the majority of our sample lie below this line, van Zee and Haynes [2006] point out that allowing for the presence of molecular gas may create more consistency between the data and this model.

The lower, dotted line in Figure 6.8 that follows the data more closely represents an alternate closed box scenario for the origin of the Z-L relationship. In recent simulations of dwarf galaxy formation, Köppen et al. [2007] have shown that an initial mass function that varies with galaxy mass would cause different types of stars to release heavy metals at different rates and lead to a mass-luminosity (and thus a Z-L) relation. A variable IMF is motivated by the idea that more massive clusters are more likely to have more massive stars because gas is more readily available there. Using the derivation of oxygen yield as

a function of baryonic mass and gas fraction from Figure 7 of Köppen et al. [2007], we determine an expected oxygen yield of $p(O) = 0.0022$ for galaxies of $M_{bary} = 10^8 M_\odot$and $f_{gas} = 0.5$. This value of p(O) is shown as the lower, dotted line and is a better fit to the metallicity measurements, including scatter, for all but a few outliers and the tidal dwarf candidates.

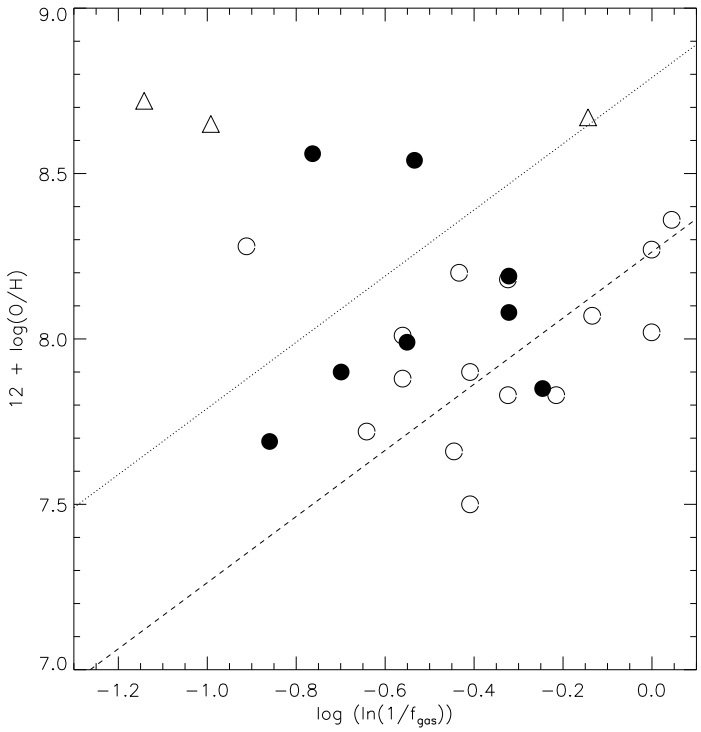

Figure 6.8 Relation between oxygen yield and oxygen abundance for our spectroscopic targets. Symbols are the same as in Figure 6.7. Excluding the tidal dwarf candidates (triangles), the galaxies follow well the relation derived from a closed-box evolutionary scenario in which the Z-L relation derives from a variable IMF (dotted line).

6.5 Summary

Our study of the Leo I group has revealed clear evidence for morphological segregation among passively evolving (gas-poor) versus actively star-forming (gas-bearing) systems, as well as a further segregation among gas-bearing systems of high versus low gas fraction . Despite having a low velocity dispersion compared to more dynamic environments like the Virgo Cluster, a dwarf's location within the Leo I group clearly plays a significant role in the galaxy's evolution.

In Leo I, we have also begun the large scale project of studing the transition and tidal dwarf galaxy candidates uncovered in the ALFALFA sample. The transition dwarf candidates have proven difficult to quantitatively identify. They span a range of gas fractions and are found both near to and far from the more massive group members. They do, however, represent the extreme red end of the blue cloud galaxies. The larger sample of transition candidates outside of the Leo I group presented here are not easily identified as outliers to the Z-L relationship as they show no offset as compared to other samples of gas-rich and low surface brightness dwarf irregulars. An evolutionary link between the two classes thus cannot be ruled out.

The Z-L relationship proves more useful at identifying tidal dwarf galaxy candidates. All three of the dwarf galaxies targeted based on their proximity to tidal features were found to have high metallicities given their luminosities and thus may be born of second generation material. Although a very high gas content ($f_{gas} = 0.93$) is derived for the tidal dwarf candidate from Leo I, AGC211370, this quantity alone does not serve to identify the galaxy as a tidal dwarf candidate as other Leo I dwarfs are found to have similar gas fractions.

CHAPTER 7

CONCLUSIONS AND FUTURE WORK

I have a million ideas. The country can't afford them all.

- Hillary Clinton

Over the last 10 years, huge progress has been made in our understanding of the dwarf population in the Local Group. The wide areal coverage of the Sloan Digital Sky Survey has probed a large volume of the Local Group and in the process discovered a population of ultrafaint dwarf spheroidal satellites (Belokurov et al. [2007]; Willman et al. [2005]). The most recent WMAP data releases have increased the precision of cosmological parameters like H_0 and Ω_{matter} (**?**; Komatsu et al. [2009]) and have consequently allowed for improvements in Λ-Cold Dark Matter simulations of structure formation in low density groups like our Local Group. This greater understanding of our extragalactic neighborhood has inspired the question of how much of this newfound knowledge can be applied to other nearby galaxy groups. Is the dwarf population of the Local Group representative of the dwarf population of all groups at the current epoch? Are the trends among Local Group dwarfs, like morphological segregation and the metallicity-luminosity relationship, unique or do they apply in other groups as well?

The dwarf galaxies of the nearby Leo I group offer a basis for comparison to the Local Group dwarf population and an estimate of how much of what we know about our own galactic neighborhood can be applied to other nearby groups. At only 11 Mpc away, the Leo I group probes the nearest reaches of the Local Super Cluster and thus the some of the lowest mass and lowest surface brightness objects detectable outside of the Local Group. Although both groups

are characterized by low velocity dispersions and are dominated by low mass dwarf galaxies, the Local Group is considered a low density environment based on a lack of massive, early-type galaxies, while Leo I is of more intermediate density with its population of E and S0 galaxies. Leo I is also home to two well-known tidal remnants, the Leo Ring and the Leo Triplet, which allows for a look at the relative role of tides in the formation of dwarf galaxies.

7.1 ALFALFA in the Leo I group: Looking for missing satellites in HI

The Arecibo Legacy Fast ALFA (ALFALFA) survey is a blind, extragalactic, 21 cm HI line survey covering 7000 deg^2 of sky visible to Arecibo out to a distance of 250 Mpc. Exploiting Arecibo's huge collective area, ALFALFA is specifically designed to detect very low mass galaxies in the local universe. Besides its sensitivity advantage, its superior spectral resolution allows detection of HI lines as narrow as 20 km s^{-1}, characteristic of low mass halos. Already, ALFALFA has detected over 300 objects with $M_{HI} < 10^8 M_\odot$ (Giovanelli et al. [2007]; Kent et al. [2008]; Saintonge et al. [2008]) For a distance to Leo I of 11 Mpc, ALFALFA can detect HI-bearing objects down to $\sim 5 \times 10^6$ M$_\odot$.

Previous, optical studies of Leo I claim the group is not only optically poor with only three L* galaxies, but also lacks a significant dwarf population (Trentham and Tully [2002]; Flint et al. [2003]). However, by searching for galaxies via their HI content, the ALFALFA survey finds a significant population of low surface brightness, HI-bearing, low-mass systems. The HI mass function was determined for the Leo I group, an environment dominated by dwarfs with 69% of

the galaxies in the sample having $M_{HI} < 10^8 M_\odot$. The best fit Schechter function and linear fits both give the Leo I HIMF a low mass slope of $\alpha = -1.41 + 0.2 - 0.1$. With scaling to account for the higher density environment represented by Leo I, this slope is steeper than that for the optically-selected sample of Springob et al. [2005], the HIPASS survey [Zwaan et al., 2005], and the survey of the Canes Venatici Group done by Kovač [2007], but still consistent within the quoted error. Two HIMFs have produced steeper slopes than that for Leo I, the zone of avoidance survey [Henning et al., 2000] and the ADBS, HI-selected survey [Rosenberg and Schneider, 2002], but these surveys have only six and seven total low-mass ($M_{HI} < 10^8 M_\odot$) detections respectively and most likely carry large distance errors; the low mass slope of the Leo I HIMF was more robustly determined. However, even though the Leo I HIMF is the first HIMF to be dominated by low-mass galaxies, the low-mass slope still falls short of the $\alpha = -1.8$ predicted by cold dark matter simulations.

The Leo I HIMF has a steeper low mass end slope than was found for three luminosity functions based on samples of varying depths and sky coverage. In the deepest of these optical surveys designed to find low luminosity dwarfs in Leo I but most limited in sky coverage, Trentham and Tully [2002] found 1.6 dwarfs for every giant in the group. Using a rough estimate based on HI mass and line width, ALFALFA found a dwarf-to-giant ratio of 9.9, more than six times higher than in the optically-selected sample. This discrepancy may suggest the existence of a population of gas-rich yet optically faint dwarfs not included in the optically-selected sample but is also affected by the lack of E/S0 galaxies in the HI-selected ALFALFA sample. In a direct comparison between an optical survey of the M96 group [Karachentsev and Karachentseva, 2004] and a portion of the ALFALFA survey with the same sky coverage, every group

member not found in the optical survey was a dwarf, while only half of the members missed by ALFALFA were dwarfs, and the rest were L* galaxies (i.e. ellipticals or lenticulars with $m_B \sim 10 - 12$).

7.2 Morphological Segregation and Gas Fraction in Leo I Dwarfs

Our study of the Leo I group has also revealed clear evidence for morphological segregation among passively evolving (gas-poor) versus actively star-forming (gas-rich) systems. Despite having a low velocity dispersion compared to more dynamic environments like the Virgo Cluster, a galaxy's location within the Leo I group still plays a significant role in the galaxy's evolution. Not only are the gas-deficient systems found preferably closer to massive neighbors, but also within the gas-bearing population, those with higher gas fractions are more widely distributed.

As expected, the ALFALFA sample is found to favor galaxies of high HI mass-to-light ratios. However, given the small volume of Leo I and its lack of L* galaxies, the lack of luminous detections with low mass-to-light ratios alone is not enough to claim a missing population of such systems. Since Leo I has very few luminous galaxies and lacks those with high HI mass, the low surface brightness dwarfs dominate the sample, and the previously observed relation between bluer galaxies and higher gas fractions is confirmed to even lower luminosities.

7.3 Color-Magnitude Diagram and the Metallicity-Luminosity Relation: Identifying dwarf galaxy progenitors

Unsurprisingly, the ALFALFA sample is dominated by blue, star-forming galaxies. The color-magnitude diagram for the Leo I group confirms the lack of a bimodality between red sequence and blue cloud galaxies at low luminosities. Only one ALFALFA detection with reliable photometry was found to lie in the red sequence: the lenticular galaxy NGC3489 which is found to be an outlier in its gas fraction and HI mass-to-light ratio as well. Thus although previous studies have suggested gas-bearing objects in the red sequence may be the result of more recent tidal interactions, we don't find any such galaxies in Leo I despite the two large tidal remnants. This lack of mixed morphology objects could suggest cooling events are more important in the formation of such galaxies, but more likely is a result of the small volume covered by Leo I.

In Leo I, we have also tested the feasibility of a more large scale project of studing the transition and tidal dwarf galaxy candidates uncovered in the ALFALFA sample. The transition dwarf candidates have proven difficult to quantitatively identify when the requirement of HII regions is assumed. They span a range of gas fractions and separations from the more massive group members. They may represent the extreme red end of the blue cloud galaxies, but this characteristic alone cannot identify the galaxy as a transition candidate as other dwarfs occupy similar locations on the color-magnitude diagram. The larger sample of transition candidates outside of the Leo I group presented here are not easily identified as outliers to the Z-L relationship as they show no offset as compared to other samples of gas-rich and low surface brightness dwarf ir-

regulars. An evolutionary link between the two classes thus cannot be ruled out.

The Z-L relationship proves more useful at identifying tidal dwarf galaxy candidates. All three of the dwarf galaxies targeted based on their proximity to tidal features were found to have high metallicities given their luminosities and are thus strong candidates for tidal dwarf galaxies born of second generation material. Although a very high gas content ($f_{gas} = 0.93$) is derived for the tidal dwarf candidate from Leo I, AGC211370, this quantity alone does not serve to identify the galaxy as a tidal dwarf candidate as other Leo I dwarfs are found to have similar gas fractions.

7.4 Future Work

A next step in this exploration of dwarf galaxy evolution is to take a detailed look at the star formation histories (SFHs) for the Leo I dwarfs and compare to those for dwarfs in other higher (and lower) density environments. Both Hα and ultraviolet observations act as high quality star formation indicators for low surface brightness galaxies like those commonly uncovered by ALFALFA. Hα imaging and spectroscopy are sensitive to low levels of star formation and trace the ages and sites of young stellar populations. A large scale effort to obtain Hα images for a large subset of the ALFALFA dwarf sample is currently being undertaken by two members of the ALFALFA team, John Salzer (Indiana University) and Eric Wilcots (University of Wisconsin), at the WIYN telescopes on Kitt Peak.

UV emission traces star formation on even more recent timescales via the

most massive, and thus most short lived, hot O and B stars. A series of proposals to obtain homogeneous near and far UV imaging data for a set of gas-rich low mass ALFALFA galaxies, including those from the Leo I group described in the previous chapters, has been approved and is underway with the Galaxy Evolution Explorer (GALEX; Martin et al. [2005]). A complete HI-selected sample of the lowest mass ALFALFA dwarfs was chosen from the Leo group, the Virgo cluster, and in relative isolation to cover the full range of densities found within the Local Supercluster.

When combined with the knowledge of the HI content, the Hα and UV observations offer key clues to understanding the evolution of these low mass systems. The gas exhaustion time scale, which relates star formation potential (available HI gas) to the rate at which that fuel is being used up (the current star formation rate), reveals whether or not a dwarf is in a short-lived evolutionary phase. For example, short gas exhaustion time scales found for the transition dwarf candidates would argue for their status as galaxies "in transition". However, if they have suitable amounts of neutral gas to maintain their current states for the foreseeable future, we might expect to see more of such objects.

Investigating the star formation histories over a range of galaxy densities will also elucidate the role played by different environment-dependent mechanisms as compared to closed box scenarios applied to field galaxies. In the high density Virgo cluster, ram pressure stripping of spirals is clearly evident in the asymmetric HI distributions seen by the VIVA survey [Chung et al., 2007]. In a comparison of dIs in Virgo and in the field, Lee et al. [2003] suggest that ram pressure stripping is to blame for the gas deficiency in cluster dwarf irregulars. A study of gas-deficient dwarfs in Virgo also found a significant fraction of dEs

to be rotation-dominated, evidence they may have evolved from a gas-rich parent galaxy [van Zee et al., 2004].

The growing ALFALFA dataset will no doubt have a significant impact on many areas of HI extragalactic astronomy. The low surface brightness dwarfs missed by optical surveys but found in Leo I so easily via their HI content offer key insight into the processes that regulate star formation in low mass systems. By surveying a cosmologically significant volume over a range of galaxy densities, the ALFALFA survey results will also place important constraints on the influence of environment on different aspects of galaxy evolution. To better characterize the group environment, the knowledge gained fron this dissertation for the Leo I group can serve as a comparison to similar studies for other groups and eventually a composite group HIMF can be determined. With more than 10,000 sources already detected by the ongoing survey, the census of HI provided by ALFALFA is changing our understanding of galaxies in the local universe.

APPENDIX A

CATALOG OF ALFALFA DETECTIONS IN THE LEO REGION

Catalog of 549 detections from the ALFALFA survey covering $09^h36^m < RA < 11^h36^m$ and $9^\circ < Dec < 11^\circ$. These data are published in Stierwalt et al. [2009].

Table A.1: HI Candidate Detections

Source	AGC	HI Coords (J2000)	Opt Coords (J2000)	$cz_{\odot}$	$W50$ (ϵ_w)	F_c	S/N	rms	Dist	$\log M_{HI}$	Code
	#	hh mm ss.s+dd mm ss	hh mm ss.s+dd mm ss	km s^{-1}	km s^{-1}	Jy km s^{-1}		mJy	Mpc	$M_{\odot}$	
5- 1	192008	09 36 03.2 +10 54 08	09 36 02.5 +10 54 14	8518	163 (9)	0.59	4.7	2.18	126.2	9.35	2 *
5- 2	193842	09 36 10.0 +11 41 10	09 36 08.6 +11 41 21	8949	38 (5)	0.59	11.6	1.79	132.4	9.39	1
5- 3	190385	09 36 25.3 +11 20 08	09 36 26.0 +11 19 44	8654	338 (11)	2.99	18.2	2.00	128.2	10.06	1 *
5- 4	192364	09 36 27.1 +09 36 00	09 36 26.8 +09 36 22	5602	121 (4)	1.20	13.3	1.83	82.3	9.28	1
5- 5	198344	09 36 46.6 +09 02 45	09 36 46.4 +09 02 42	3316	106 (15)	0.62	5.8	2.31	50.4	8.57	1
5- 6	192145	09 36 53.0 +11 42 44	09 36 53.4 +11 43 01	8627	49 (6)	0.86	15.4	1.77	127.8	9.52	1 *
5- 7	191046	09 37 00.2 +09 06 37	09 37 02.0 +09 06 07	3058	93 (11)	0.46	5.5	1.92	46.7	8.37	2
5- 8	198335	09 37 00.4 +09 57 54	09 37 04.4 +09 57 59	1517	53 (8)	0.37	6.5	1.73	24.2	7.71	1
5- 9	191735	09 37 02.4 +09 32 45	09 37 02.3 +09 32 24	5586	273 (14)	1.83	12.7	1.94	82.1	9.46	1
5- 10	192365	09 37 09.5 +09 27 49	09 37 09.0 +09 27 50	6719	199 (4)	2.31	21.2	1.73	100.6	9.74	1
5- 11	192510	09 37 24.6 +08 41 42	09 37 26.1 +08 41 21	3308	37 (20)	0.47	6.8	2.44	50.3	8.45	1
5- 12	191860	09 37 56.1 +08 10 45	09 37 55.9 +08 10 47	6201	53 (6)	0.49	7.6	1.95	93.2	9.00	1
5- 13	5134	09 38 07.3 +09 31 35	09 38 07.9 +09 31 23	3339	341 (3)	18.43	130.5	1.71	48.2	10.00	1
5- 14	190408	09 38 20.1 +09 26 52	09 38 19.3 +09 26 46	5514	175 (19)	0.87	9.0	1.62	81.1	9.13	1
5- 15	192369	09 38 33.9 +09 31 22	09 38 32.7 +09 31 16	5640	293 (44)	0.80	5.9	1.79	82.9	9.11	2 *
5- 16	191861	09 38 41.1 +08 07 23	09 38 40.3 +08 08 10	3366	103 (10)	1.56	17.8	1.92	51.2	8.98	1
5- 17	193832	09 38 48.1 +11 28 26	09 38 52.2 +11 29 18	5883	21 (6)	0.34	6.7	2.35	88.6	8.80	1
5- 18	190417	09 38 54.5 +09 45 25	09 38 53.5 +09 45 01	5672	180 (16)	1.07	8.8	2.02	83.3	9.24	1
5- 19	192371	09 39 14.2 +09 21 54	09 39 18.4 +09 22 42	14997	44 (8)	0.39	6.5	2.03	218.9	9.64	1
5- 20	192018	09 39 22.6 +10 58 52	09 39 23.0 +10 59 13	10490	193 (6)	0.94	7.2	2.09	154.4	9.72	1
5- 21	5148	09 39 32.7 +11 30 42	09 39 33.4 +11 30 33	5904	332(4)	3.81	22.2	2.10	88.9	9.85	1
5- 22	193972	09 39 51.0 +09 29 47	09 39 50.3 +09 29 08	9275	306(10)	0.96	7.3	1.68	137.1	9.63	1
5- 23	190426	09 39 53.7 +11 02 43	09 39 53.7 +11 02 14	6698	232(3)	1.98	14.8	1.97	100.3	9.67	1
5- 24	191515	09 39 56.5 +09 27 58	09 39 54.5 +09 28 30	5625	251(6)	0.97	7.9	1.71	82.6	9.19	1

TableA.1 – Continued

Source	AGC	HI Coords (J2000)	Opt Coords (J2000)	$cz_{\odot}$	$W50$ (ϵ_w)	F_c	S/N	rms	Dist	$\log M_{HI}$	Code
	#	hh mm ss.s+dd mm ss	hh mm ss.s+dd mm ss	km s^{-1}	km s^{-1}	Jy km s^{-1}		mJy	Mpc	$M_{\odot}$	
5- 25	191862	09 39 56.6 +09 35 03	09 39 55.3 +09 35 00	6104	131(5)	0.78	8.2	1.83	91.8	9.19	1
5- 26	192372	09 39 57.7 +09 10 00	09 39 58.0 +09 10 43	6519	95(13)	0.73	7.6	2.21	97.8	9.22	1
5- 27	193833	09 40 12.6 +09 55 33	09 40 13.2 +09 55 31	3381	44(3)	0.69	14.0	1.63	51.3	8.63	1 *
5- 28	191843	09 40 25.9 +10 14 54	09 40 27.0 +10 15 20	17624	42(9)	0.31	4.6	2.28	256.4	9.68	2 *
5- 29	5160	09 40 43.0 +11 53 34	09 40 41.7 +11 53 17	6662	394(3)	3.29	21.9	1.69	99.7	9.89	1
5- 30	5164	09 40 50.1 +11 33 02	09 40 49.7 +11 33 06	6713	461(18)	6.29	29.7	2.05	100.5	10.18	1 *
5- 31	192149	09 40 59.8 +11 40 25	09 40 59.3 +11 40 17	6640	80(17)	0.87	10.7	2.02	99.4	9.31	1 *
5- 32	192025	09 41 02.5 +10 56 43	09 41 01.2 +10 56 42	5541	99(4)	1.38	14.9	2.08	81.4	9.33	1 *
5- 33	198336	09 41 04.3 +08 55 44	09 41 06.1 +08 55 18	3152	87(7)	0.59	6.7	2.09	48.0	8.51	1
5- 34	190438	09 41 08.0 +10 18 54	09 41 07.2 +10 18 48	5898	56(8)	0.91	12.6	2.11	88.9	9.23	1
5- 35	190440	09 41 30.6 +10 39 04	09 41 31.4 +10 38 29	5549	147(9)	0.74	6.1	2.22	81.6	9.06	1
5- 36	5173	09 41 31.9 +11 24 52	09 41 32.2 +11 24 45	6236	490(3)	7.88	35.1	2.05	93.7	10.21	1
5- 37	192152	09 41 46.2 +11 53 10	09 41 46.1 +11 53 21	6827	53(4)	1.13	17.1	2.00	102.1	9.44	1
5- 38	5177	09 41 54.1 +11 38 00	09 41 53.9 +11 37 54	5070	242(4)	4.85	34.4	2.03	74.9	9.81	1
5- 39	198337	09 42 50.6 +09 38 07	09 42 51.2 +09 38 00	1461	34(3)	0.62	12.3	1.88	23.4	7.90	1 *
5- 40	5189	09 42 55.9 +09 29 16	09 42 58.4 +09 28 16	3216	114(3)	21.50	281.3	1.60	48.8	10.08	1 *
5- 41	193782	09 43 02.4 +09 15 05	09 43 01.7 +09 15 11	3217	138(3)	1.96	20.5	1.81	49.0	9.04	1
5- 42	190460	09 43 20.2 +10 04 45	09 43 21.3 +10 05 13	16275	370(19)	1.46	9.1	1.86	237.1	10.29	1
5- 43	5204	09 43 50.8 +09 39 30	09 43 51.0 +09 39 23	3177	142(3)	5.36	56.3	1.78	48.4	9.47	1
5- 44	191867	09 44 03.2 +09 22 52	09 44 02.9 +09 22 27	3098	166(7)	1.41	13.6	1.80	47.2	8.87	1
5- 45	192161	09 44 04.3 +11 03 45	09 44 03.2 +11 03 50	6442	109(6)	0.64	7.1	1.92	96.7	9.15	1
5- 46	192163	09 44 12.7 +11 08 32	09 44 13.1 +11 08 47	11925	192(8)	0.73	5.7	2.07	175.0	9.72	2
5- 47	191848	09 44 22.0 +09 59 22	09 44 19.4 +09 59 05	3107	198(8)	0.67	6.5	1.64	47.3	8.55	2
5- 48	190470	09 44 23.8 +11 13 59	09 44 23.5 +11 13 53	5068	103(2)	3.44	34.2	2.20	74.9	9.66	1

TableA.1 – Continued

Source	AGC	HI Coords (J2000)	Opt Coords (J2000)	$cz_{\odot}$	$W50$ (ϵ_w)	F_c	S/N	rms	Dist	$\log M_{HI}$	Code
	#	hh mm ss.s+dd mm ss	hh mm ss.s+dd mm ss	km s^{-1}	km s^{-1}	Jy km s^{-1}		mJy	Mpc	$M_{\odot}$	
5- 49	192165	09 44 30.0 +11 16 34	09 44 30.3 +11 16 44	8298	111(6)	0.72	7.0	2.17	123.2	9.41	1
5- 50	191849	09 44 37.2 +10 00 59	09 44 37.1 +10 00 46	1483	62(3)	1.94	31.3	1.74	23.7	8.41	1
5- 51	190472	09 44 44.3 +09 36 50	09 44 43.8 +09 36 54	541	67(3)	4.26	76.4	1.51	7.4	7.74	1
5- 52	191869	09 44 58.2 +08 21 47	09 44 58.9 +08 22 12	1733	163(5)	4.22	35.7	2.06	27.3	8.87	1
5- 53	192389	09 45 11.0 +09 55 32	09 45 11.8 +09 55 04	17441	209(13)	0.90	6.8	2.04	253.8	10.14	1
5- 54	5215	09 45 14.5 +09 06 45	09 45 14.3 +09 06 36	5483	411(3)	7.86	43.8	1.95	80.7	10.08	1
5- 55	5216	09 45 21.7 +09 45 59	09 45 22.6 +09 46 02	3282	216(4)	5.67	40.5	2.13	48.8	9.50	1
5- 56	191871	09 45 49.8 +08 54 37	09 45 50.5 +08 54 34	5231	108(7)	0.90	9.8	1.96	77.2	9.10	1
5- 57	191873	09 46 10.2 +08 56 18	09 46 13.4 +08 56 06	5210	83(9)	0.44	5.1	2.09	76.9	8.79	2
5- 58	198338	09 46 10.5 +08 42 56	09 46 08.4 +08 43 05	2581	69(11)	0.59	7.3	2.15	39.7	8.34	1
5- 59	191852	09 46 14.3 +10 10 15	09 46 14.0 +10 09 57	16947	151(9)	1.03	8.8	2.12	246.8	10.17	1
5- 60	190491	09 46 22.4 +09 09 59	09 46 22.5 +09 09 53	5988	281(4)	3.79	23.1	2.18	90.2	9.86	1
5- 61	192036	09 46 46.2 +10 54 27	09 46 45.2 +10 54 14	14131	299(48)	1.29	7.7	2.17	206.5	10.11	2 *
5- 62	192392	09 46 50.0 +09 01 22	09 46 50.6 +09 01 14	14173	228(18)	1.14	8.2	2.08	207.2	10.06	1
5- 63	198342	09 46 55.7 +08 06 00	09 46 56.2 +08 05 38	9482	126(5)	1.17	11.5	2.02	140.2	9.73	1 *
5- 64	193835	09 47 10.4 +11 41 38	09 47 11.3 +11 41 39	12606	301(4)	1.49	10.1	1.90	184.7	10.08	1
5- 65	191854	09 47 16.3 +10 05 22	09 47 16.8 +10 05 28	16816	223(34)	0.90	6.8	1.98	244.9	10.10	1 *
5- 66	190508	09 47 22.6 +08 33 30	09 47 22.8 +08 34 09	9465	360(8)	1.05	5.4	2.31	139.9	9.69	2
5- 67	192039	09 47 28.0 +10 30 10	09 47 31.4 +10 29 32	3112	36(7)	0.44	7.0	2.28	47.4	8.37	1 *
5- 68	192040	09 47 32.5 +10 45 22	09 47 32.8 +10 45 09	14254	223(13)	5.09	33.0	2.30	208.3	10.72	1
5- 69	192042	09 47 42.2 +10 35 12	09 47 42.1 +10 35 12	8052	250(10)	1.61	11.5	1.97	119.7	9.74	1
5- 70	192396	09 47 43.9 +08 59 00	09 47 41.0 +08 58 49	14753	224(8)	1.14	8.0	2.14	215.5	10.10	1
5- 71	190511	09 47 44.1 +09 10 00	09 47 42.1 +09 09 40	5335	196(26)	0.91	6.6	2.19	78.7	9.12	1
5- 72	190512	09 47 45.9 +09 08 10	09 47 45.3 +09 08 23	7761	60(5)	1.97	27.0	2.09	115.6	9.79	1

TableA.1 – Continued

Source	AGC	HI Coords (J2000)	Opt Coords (J2000)	$cz_{\odot}$	$W50$ (ϵ_w)	F_c	S/N	rms	Dist	$\log M_{HI}$	Code
	#	hh mm ss.s+dd mm ss	hh mm ss.s+dd mm ss	km s^{-1}	km s^{-1}	Jy km s^{-1}		mJy	Mpc	$M_{\odot}$	
5- 73	192043	09 47 46.7 +10 52 07	09 47 48.2 +10 52 12	5054	186(5)	0.77	4.6	2.84	74.7	9.01	2
5- 74	190517	09 47 52.5 +08 49 45	09 47 51.7 +08 49 51	5378	261(32)	2.63	17.4	2.09	79.3	9.59	1
5- 75	192178	09 47 58.2 +11 53 42	09 48 01.3 +11 53 21	12596	244(11)	0.75	5.0	2.18	184.6	9.78	2
5- 76	191877	09 48 16.1 +09 11 10	09 48 15.3 +09 10 44	6038	65(8)	0.68	8.5	2.19	91.0	9.12	1 *
5- 77	192400	09 48 22.3 +09 15 18	09 48 22.4 +09 15 05	5489	73(4)	0.89	11.5	2.02	80.8	9.14	1
5- 78	192180	09 48 43.3 +11 46 18	09 48 39.3 +11 46 10	3766	85(12)	0.44	5.8	1.85	56.7	8.52	2
5- 79	192047	09 48 48.9 +10 59 17	09 48 49.8 +10 59 24	14050	539(39)	2.47	9.9	2.07	205.4	10.39	1 *
5- 80	190834	09 49 07.8 +09 05 55	09 49 06.0 +09 05 17	5179	149(10)	0.49	4.4	2.03	76.5	8.83	2
5- 81	193840	09 49 14.5 +10 42 34	09 49 11.4 +10 43 01	6556	168(9)	1.12	8.8	2.18	98.3	9.41	1
5- 82	192402	09 49 36.1 +09 29 52	09 49 37.0 +09 29 42	3101	99(15)	0.53	6.4	1.87	47.3	8.45	1
5- 83	190531	09 49 37.4 +09 00 30	09 49 36.9 +09 00 20	5235	299(32)	1.95	13.5	1.87	77.1	9.44	1
5- 84	191855	09 49 51.1 +10 11 05	09 49 47.3 +10 11 29	10153	224(16)	0.97	7.9	1.84	149.7	9.71	1
5- 85	190539	09 49 52.2 +10 25 52	09 49 51.5 +10 25 55	8910	281(9)	3.12	18.5	2.25	132.0	10.11	1 *
5- 86	5267	09 49 56.0 +09 05 30	09 49 52.8 +09 05 43	5682	399(30)	1.29	6.8	2.12	77.1	9.26	1
5- 87	191879	09 50 15.8 +09 43 52	09 50 15.1 +09 44 05	6342	112(28)	0.90	10.5	1.80	95.3	9.28	1
5- 88	192054	09 50 30.9 +10 17 22	09 50 30.5 +10 17 20	10253	207(7)	1.64	14.5	1.75	151.2	9.95	1
5- 89	191881	09 50 41.7 +08 43 12	09 50 42.4 +08 43 54	2827	124(7)	0.96	8.4	2.30	43.3	8.63	1
5- 90	192055	09 50 43.0 +10 38 38	09 50 45.7 +10 38 47	16132	60(10)	0.48	5.6	2.43	235.2	9.80	2 *
5- 91	191882	09 50 44.2 +09 56 34	09 50 43.2 +09 57 04	2977	105(7)	0.77	9.8	1.70	45.4	8.57	1
5- 92	193836	09 50 54.0 +10 10 32	09 50 52.0 +10 10 24	3807	40(8)	0.36	6.8	1.85	57.3	8.45	1
5- 93	192057	09 50 58.2 +10 48 11	09 50 58.8 +10 48 05	3153	106(9)	1.45	15.3	2.06	48.0	8.90	1
5- 94	5286	09 51 06.4 +09 00 22	09 51 06.1 +09 00 29	5199	318(2)	9.07	58.9	1.93	77.1	10.10	1
5- 95	192182	09 51 11.2 +11 49 22	09 51 11.6 +11 49 06	14455	214(25)	0.62	5.0	1.92	211.2	9.81	2
5- 96	192407	09 51 16.2 +09 08 23	09 51 18.4 +09 08 21	5336	272(9)	0.80	4.8	2.27	78.7	9.07	2

TableA.1 – Continued

Source	AGC	HI Coords (J2000)	Opt Coords (J2000)	$cz_{\odot}$	$W50$ (ϵ_w)	F_c	S/N	rms	Dist	$\log M_{HI}$	Code
	#	hh mm ss.s+dd mm ss	hh mm ss.s+dd mm ss	km s^{-1}	km s^{-1}	Jy km s^{-1}		mJy	Mpc	$M_{\odot}$	
5- 97	191906	09 51 40.7 +11 17 59	09 51 39.7 +11 18 07	3199	119(3)	1.50	14.0	2.18	48.6	8.92	1
5- 98	192183	09 51 55.3 +11 08 52	09 51 55.2 +11 08 31	8110	85(7)	1.38	14.6	2.29	120.5	9.67	1
5- 99	192410	09 52 24.2 +09 53 16	09 52 22.0 +09 53 15	16458	298(8)	0.71	5.5	1.67	239.8	9.98	2
5-100	191885	09 52 32.0 +08 11 47	09 52 35.1 +08 11 57	2711	135(6)	1.48	11.4	2.49	41.6	8.78	1
5-101	191817	09 52 59.4 +08 01 45	09 52 58.7 +08 01 41	2641	124(2)	3.67	46.0	1.59	40.6	9.15	1
5-102	192418	09 52 59.9 +09 19 10	09 52 58.8 +09 19 05	10436	39(4)	0.91	14.6	2.17	153.8	9.71	1
5-103	192071	09 53 25.8 +10 54 54	09 53 29.4 +10 53 30	16842	76(9)	0.49	5.9	2.11	245.3	9.84	2 *
5-104	192525	09 53 32.0 +08 30 30	09 53 29.7 +08 30 46	10740	227(7)	1.56	10.3	2.24	158.2	9.96	1
5-105	192526	09 53 37.7 +08 30 18	09 53 34.0 +08 29 30	12011	116(21)	0.55	5.1	2.22	176.4	9.61	2 *
5-106	190576	09 53 38.7 +09 33 06	09 53 38.2 +09 32 51	12009	158(7)	2.32	18.9	2.18	176.3	10.23	1
5-107	192188	09 53 49.5 +11 20 47	09 53 48.5 +11 20 38	12343	313(8)	0.94	5.4	2.19	181.0	9.86	2
5-108	5314	09 53 51.7 +08 52 52	09 53 51.1 +08 52 39	6410	283(5)	1.93	12.8	2.00	96.3	9.63	1
5-109	191886	09 54 03.1 +08 46 59	09 54 00.6 +08 46 39	3868	77(12)	0.39	4.7	2.08	58.3	8.49	2
5-110	192083	09 54 13.8 +10 15 10	09 54 16.1 +10 13 43	11871	128(11)	0.61	6.2	1.94	174.3	9.64	1 *
5-111	192423	09 54 31.3 +09 51 17	09 54 30.5 +09 52 12	1488	40(16)	0.45	7.2	2.16	23.8	7.78	1
5-112	192424	09 54 39.2 +09 35 00	09 54 45.5 +09 36 15	10372	236(27)	0.97	5.6	2.50	152.9	9.73	2
5-113	5325	09 54 50.0 +09 16 18	09 54 49.7 +09 16 16	1497	203(2)	11.55	80.0	2.26	15.3	8.80	1
5-114	192088	09 54 50.9 +10 43 58	09 54 49.2 +10 43 50	12044	123(13)	0.53	4.7	2.27	176.8	9.59	2
5-115	190595	09 55 07.2 +11 02 42	09 55 07.0 +11 02 22	12066	220(12)	1.86	12.1	2.32	177.1	10.14	1
5-116	190600	09 55 30.4 +08 23 12	09 55 29.3 +08 23 27	1281	101(5)	2.83	25.3	2.47	20.7	8.46	1
5-117	5334	09 56 02.2 +10 30 52	09 56 04.1 +10 29 53	9037	285(16)	1.36	7.4	2.44	133.8	9.76	1 *
5-118	193841	09 56 27.2 +10 54 22	09 56 27.0 +10 54 20	5421	51(5)	0.55	6.1	2.10	79.8	8.92	1
5-119	192092	09 56 34.8 +10 54 52	09 56 36.0 +10 54 22	14711	385(33)	1.53	8.0	2.17	214.9	10.22	2
5-120	192432	09 57 10.1 +09 52 36	09 57 10.6 +09 52 49	5457	183(4)	1.93	15.4	2.08	80.3	9.47	1

TableA.1 – Continued

Source	AGC	HI Coords (J2000)	Opt Coords (J2000)	$cz_{\odot}$	$W50$ (ϵ_w)	F_c	S/N	rms	Dist	$\log M_{HI}$	Code
	#	hh mm ss.s+dd mm ss	hh mm ss.s+dd mm ss	km s^{-1}	km s^{-1}	Jy km s^{-1}		mJy	Mpc	$M_{\odot}$	
5-121	192098	09 57 43.4 +10 07 22	09 57 40.7 +10 07 28	5365	49(12)	0.37	6.8	1.70	79.0	8.74	1
5-122	190626	09 57 46.7 +10 01 13	09 57 47.4 +10 01 38	6400	288(16)	1.02	6.2	2.17	96.2	9.35	1
5-123	192439	09 57 47.4 +09 26 22	09 57 44.0 +09 25 41	12531	239(55)	0.81	5.2	2.26	183.8	9.81	2
5-124	192441	09 57 56.0 +09 51 31	09 57 52.0 +09 51 05	16707	483(53)	1.59	7.0	2.09	243.4	10.35	2 *
5-125	192201	09 57 57.9 +11 23 59	09 57 55.7 +11 23 43	11377	121(12)	0.66	6.1	2.20	167.3	9.64	1
5-126	192530	09 58 04.2 +08 51 14	09 58 08.0 +08 52 26	14874	266(16)	1.02	5.8	2.41	217.3	10.05	2
5-127	192445	09 58 15.8 +09 11 22	09 58 14.2 +09 11 07	9018	164(5)	0.93	8.0	2.01	133.6	9.59	1
5-128	192104	09 58 16.2 +10 39 29	09 58 16.3 +10 39 09	6406	171(1)	1.25	9.1	2.17	96.3	9.44	1
5-129	5358	09 58 46.7 +11 23 27	09 58 47.1 +11 23 17	2913	203(2)	5.77	33.7	2.28	44.5	9.43	1
5-130	190643	09 59 05.1 +10 21 29	09 59 05.1 +10 21 40	5360	58(8)	0.57	6.2	2.01	79.0	8.92	1
5-131	192212	09 59 36.2 +11 32 47	09 59 41.0 +11 31 59	10834	37(9)	0.41	7.2	2.00	159.5	9.39	1
5-132	190651	09 59 41.2 +09 56 38	09 59 42.5 +09 57 06	16866	176(19)	0.84	6.6	2.14	245.7	10.08	1
5-133	192452	09 59 53.9 +09 30 56	09 59 56.2 +09 30 47	5329	118(9)	0.64	6.6	2.01	78.6	8.97	1
5-134	207022	10 00 12.1 +09 38 49	10 00 12.1 +09 38 55	5411	191(4)	1.23	10.1	1.98	79.7	9.26	1
5-135	190657	10 00 21.5 +11 20 11	10 00 20.8 +11 20 09	12480	268(2)	2.29	16.2	1.93	183.0	10.26	1
5-136	190660	10 00 39.6 +11 56 48	10 00 39.6 +11 56 48	7425	390(35)	1.25	7.1	1.98	110.8	9.56	1
5-137	190664	10 00 57.3 +11 10 45	10 00 57.0 +11 10 59	10880	40(6)	1.61	28.0	1.97	160.2	9.99	1
5-138	190666	10 01 03.6 +11 27 54	10 01 03.3 +11 27 40	10893	225(8)	2.85	20.5	2.07	160.4	10.24	1
5-139	202269	10 01 06.7 +10 55 47	10 01 06.8 +10 55 27	10882	142(21)	0.44	4.1	2.03	160.2	9.43	2
5-140	208379	10 01 31.8 +11 25 15	10 01 33.4 +11 24 52	10526	94(8)	0.64	6.7	2.19	155.1	9.56	1
5-141	203135	10 01 36.3 +09 54 22	10 01 40.5 +09 54 32	17091	162(11)	1.17	8.5	2.41	249.0	10.23	1 *
5-142	5396	10 01 39.2 +10 45 44	10 01 40.6 +10 45 22	5403	327(5)	4.31	24.9	2.14	79.6	9.81	1
5-143	202470	10 01 40.5 +11 51 02	10 01 39.3 +11 50 42	7439	196(20)	0.83	8.0	1.65	111.0	9.38	1
5-144	203136	10 01 48.6 +09 52 20	10 01 50.4 +09 52 02	17062	290(12)	1.56	8.6	2.38	248.5	10.36	1

TableA.1 – Continued

Source	AGC	HI Coords (J2000)	Opt Coords (J2000)	$cz_{\odot}$	$W50$ (ϵ_w)	F_c	S/N	rms	Dist	$\log M_{HI}$	Code
	#	hh mm ss.s+dd mm ss	hh mm ss.s+dd mm ss	km s^{-1}	km s^{-1}	Jy km s^{-1}		mJy	Mpc	$M_{\odot}$	
5-145	205067	10 01 56.8 +11 43 00	10 02 00.1 +11 43 13	6863	265(5)	1.14	8.6	1.81	102.8	9.45	1
5-146	202478	10 02 10.9 +11 38 28	10 02 10.4 +11 38 37	3468	129(7)	1.76	16.8	2.05	52.4	9.06	1
5-147	207034	10 02 13.2 +10 48 48	10 02 10.2 +10 48 13	6753	40(7)	0.45	6.9	2.24	101.2	9.04	1
5-148	200006	10 02 49.2 +11 43 46	10 02 49.7 +11 43 43	7118	199(6)	0.82	7.3	1.79	106.4	9.34	1
5-149	202173	10 02 55.5 +08 25 43	10 02 53.0 +08 26 27	9147	321(9)	1.44	5.7	3.18	135.5	9.79	2
5-150	202482	10 03 00.3 +11 50 02	10 03 02.4 +11 49 44	11206	246(19)	0.90	7.9	1.63	164.8	9.76	1
5-151	5409	10 03 02.7 +10 44 59	10 03 03.5 +10 44 44	3007	210(3)	5.24	37.7	2.14	45.8	9.41	1
5-152	202483	10 03 05.8 +11 26 49	10 03 05.6 +11 26 47	3501	70(3)	3.25	36.1	2.39	52.9	9.33	1
5-153	202282	10 03 25.2 +10 27 19	10 03 26.8 +10 27 38	6755	66(5)	0.72	9.4	2.08	101.3	9.24	1
5-154	202042	10 03 50.6 +11 05 54	10 03 51.8 +11 06 00	3301	75(2)	1.46	17.8	2.09	50.1	8.94	1
5-155	202288	10 04 16.7 +10 47 33	10 04 18.4 +10 47 20	8168	92(7)	0.96	10.3	2.17	121.5	9.52	1
5-156	200029	10 04 34.2 +10 24 45	10 04 33.2 +10 24 51	9259	280(73)	2.20	13.5	2.17	137.1	9.99	1 *
5-157	202290	10 04 43.8 +10 25 46	10 04 45.9 +10 25 52	16757	201(10)	1.80	13.2	2.15	244.2	10.40	1 *
5-158	202175	10 04 47.0 +08 21 44	10 04 47.5 +08 21 20	6671	137(3)	1.21	10.5	2.21	100.2	9.46	1
5-159	200036	10 04 50.7 +11 54 22	10 04 49.7 +11 54 46	9293	294(5)	1.72	12.9	1.74	137.5	9.88	1
5-160	207024	10 04 59.5 +08 47 22	10 04 58.9 +08 46 57	5355	58(6)	0.72	10.0	2.12	78.9	9.02	1
5-161	205073	10 05 18.7 +10 48 12	10 05 21.1 +10 47 58	3073	112(11)	0.52	4.7	2.33	46.8	8.43	2
5-162	200042	10 05 24.8 +11 43 47	10 05 22.9 +11 43 44	9284	171(5)	1.69	15.4	1.87	137.4	9.88	1 *
5-163	202486	10 05 28.3 +11 07 14	10 05 27.5 +11 07 16	9357	467(27)	2.34	10.1	2.22	138.5	10.02	1
5-164	203142	10 05 40.5 +09 35 04	10 05 40.4 +09 35 13	9580	221(4)	1.59	10.6	2.26	141.7	9.88	1
5-165	202295	10 05 49.7 +10 33 12	10 05 51.1 +10 32 55	13003	138(9)	0.78	6.7	2.19	190.6	9.82	1
5-166	202297	10 06 03.7 +10 38 05	10 06 03.8 +10 38 16	1565	258(26)	1.88	11.1	2.36	25.0	8.44	1
5-167	207025	10 06 03.8 +10 55 32	10 06 04.7 +10 55 16	7103	110(7)	0.64	6.8	2.03	106.3	9.23	1
5-168	202488	10 06 08.6 +11 05 52	10 06 10.8 +11 06 02	2496	97(8)	0.71	8.0	1.99	38.4	8.39	1

TableA.1 – Continued

Source	AGC	HI Coords (J2000)	Opt Coords (J2000)	$cz_{\odot}$	$W50$ (ϵ_w)	F_c	S/N	rms	Dist	$\log M_{HI}$	Code
	#	hh mm ss.s+dd mm ss	hh mm ss.s+dd mm ss	km s^{-1}	km s^{-1}	Jy km s^{-1}		mJy	Mpc	$M_{\odot}$	
5-169	202184	10 06 32.2 +08 36 04	10 06 29.3 +08 36 19	6696	208(22)	1.58	11.6	2.10	100.5	9.58	1
5-170	203144	10 06 38.6 +09 47 44	10 06 44.4 +09 47 20	13617	127(12)	0.47	4.3	2.17	199.4	9.64	2
5-171	202298	10 06 42.4 +09 58 15	10 06 44.4 +09 58 04	12844	75(9)	0.47	5.4	2.25	188.3	9.59	2
5-172	200075	10 06 46.8 +11 39 45	10 06 46.3 +11 39 49	6888	194(13)	2.08	17.0	1.96	103.2	9.72	1
5-173	202300	10 06 55.4 +10 40 22	10 06 55.4 +10 40 03	12774	156(16)	0.91	6.7	2.42	187.3	9.88	1
5-174	5456	10 07 19.8 +10 21 22	10 07 19.7 +10 21 43	536	61(3)	6.53	88.1	2.10	7.0	7.88	1
5-175	207026	10 07 20.8 +09 52 29	10 07 19.6 +09 51 44	7575	133(9)	0.87	8.0	2.11	113.0	9.42	1
5-176	202144	10 07 33.2 +09 58 22	10 07 33.8 +09 58 16	7564	129(18)	0.94	9.6	1.91	112.9	9.45	1
5-177	207027	10 08 02.7 +11 12 52	10 08 02.6 +11 13 06	9299	46(13)	0.45	7.3	1.96	137.6	9.30	1
5-178	205355	10 08 51.8 +09 28 22	10 08 52.1 +09 28 34	7634	198(3)	1.41	11.1	2.01	113.9	9.63	1
5-179	202193	10 09 27.6 +08 54 32	10 09 27.9 +08 54 53	7981	271(6)	1.43	7.3	2.65	118.9	9.68	1
5-180	200128	10 09 59.8 +11 55 22	10 10 00.2 +11 55 00	8451	269(4)	1.61	11.7	1.86	125.5	9.78	1
5-181	202195	10 10 06.5 +08 08 47	10 10 05.3 +08 09 48	8100	98(9)	0.70	6.6	2.39	120.6	9.38	1
5-182	202196	10 10 19.5 +08 07 43	10 10 18.6 +08 07 23	8079	131(20)	1.15	10.8	2.08	120.3	9.59	1
5-183	200139	10 11 00.4 +09 50 59	10 11 00.0 +09 50 50	8341	268(19)	1.11	7.1	2.14	124.0	9.60	1
5-184	200141	10 11 05.0 +09 45 29	10 11 07.1 +09 45 04	7759	58(8)	0.47	6.2	2.20	115.7	9.17	2
5-185	201757	10 11 07.7 +10 21 26	10 11 07.6 +10 21 29	9609	321(21)	1.49	8.3	2.23	142.1	9.85	1
5-186	208303	10 11 19.7 +10 00 16		-137	55(8)	0.42	6.1	2.03			9 *
5-187	200150	10 11 39.4 +08 36 46	10 11 38.3 +08 36 43	16328	92(8)	0.50	5.1	2.31	238.1	9.82	2
5-188	207038	10 12 24.1 +11 26 34		3641	106(10)	0.60	6.2	2.08	54.9	8.63	1 *
5-189	202322	10 12 29.6 +10 45 48	10 12 31.3 +10 45 56	8344	110(9)	0.53	4.7	2.44	124.0	9.28	2
5-190	200157	10 12 30.8 +11 27 52	10 12 29.2 +11 27 18	12782	192(7)	1.65	11.7	2.27	187.4	10.14	1
5-191	202201	10 13 33.2 +08 35 22	10 13 32.2 +08 35 37	9703	45(4)	0.70	9.8	2.33	143.5	9.53	1
5-192	202510	10 13 57.6 +11 35 07	10 14 00.6 +11 34 44	13979	76(8)	0.49	5.4	2.31	204.5	9.68	2

TableA.1 – Continued

Source	AGC	HI Coords (J2000)	Opt Coords (J2000)	$cz_{\odot}$	$W50$ (ϵ_w)	F_c	S/N	rms	Dist	$\log M_{HI}$	Code
	#	hh mm ss.s+dd mm ss	hh mm ss.s+dd mm ss	km s^{-1}	km s^{-1}	Jy km s^{-1}		mJy	Mpc	$M_{\odot}$	
5-193	200192	10 14 06.9 +10 08 30	10 14 08.0 +10 08 53	8330	276(10)	1.09	6.3	2.31	123.9	9.60	1
5-194	202328	10 14 31.6 +10 58 40	10 14 32.2 +10 58 26	7594	253(12)	1.06	6.8	2.19	113.3	9.51	1
5-195	208309	10 14 33.4 +08 28 15	10 14 33.2 +08 27 42	8346	55(6)	0.51	6.7	2.28	124.1	9.27	1
5-196	200199	10 14 35.1 +11 52 46	10 14 34.6 +11 51 58	8820	40(8)	0.50	9.8	1.76	130.8	9.30	1 *
5-197	200210	10 15 17.3 +10 48 32	10 15 15.6 +10 48 39	9325	287(14)	1.00	7.9	1.68	138.1	9.65	1
5-198	202203	10 15 30.2 +09 15 55	10 15 31.4 +09 16 42	8298	212(4)	1.09	8.8	1.91	123.4	9.59	1
5-199	203168	10 16 20.9 +09 34 52	10 16 16.9 +09 34 21	11849	235(27)	0.85	5.3	2.33	174.2	9.78	2
5-200	203170	10 17 44.0 +09 26 34	10 17 43.9 +09 26 38	11854	91(8)	1.02	10.7	2.22	174.2	9.86	1
5-201	200239	10 17 47.6 +09 08 09	10 17 47.0 +09 08 12	13266	517(28)	1.90	8.0	2.04	194.4	10.23	1
5-202	203171	10 18 13.8 +09 43 52	10 18 13.8 +09 43 19	13317	76(19)	0.53	6.6	2.05	195.1	9.68	1
5-203	203174	10 19 16.8 +09 11 28	10 19 17.6 +09 11 02	15087	176(7)	0.71	5.8	2.08	220.4	9.91	2 *
5-204	207028	10 19 40.0 +10 00 15	10 19 37.1 +10 00 04	6967	139(14)	0.91	8.2	2.09	104.4	9.37	1
5-205	201361	10 20 27.8 +08 02 41	10 20 27.7 +08 02 42	8273	196(5)	1.09	9.4	1.85	123.1	9.59	1
5-206	208312	10 20 39.6 +08 09 06		5336	32(11)	0.44	8.1	2.07	78.7	8.81	1 *
5-207	200262	10 20 50.0 +11 22 52	10 20 49.9 +11 22 20	9619	341(23)	1.90	11.8	1.95	142.3	9.96	1
5-208	208291	10 21 05.1 +08 31 15	10 21 05.9 +08 31 47	8290	59(12)	0.47	6.9	1.99	123.4	9.23	1
5-209	201366	10 21 12.2 +08 07 00	10 21 12.7 +08 06 50	13381	417(7)	1.55	7.8	2.12	196.1	10.15	1
5-210	200267	10 21 32.8 +09 22 22	10 21 32.2 +09 22 25	6817	130(12)	1.59	15.1	2.06	102.3	9.59	1
5-211	200268	10 21 33.5 +11 57 35	10 21 33.5 +11 57 44	7748	171(12)	2.74	23.2	2.02	115.5	9.94	1
5-212	203282	10 21 41.0 +08 45 18	10 21 41.1 +08 45 26	13560	121(10)	0.47	4.4	2.16	198.7	9.64	2
5-213	203284	10 21 57.5 +08 14 23	10 21 57.2 +08 14 23	13395	350(18)	1.37	7.7	2.13	196.3	10.09	1
5-214	202355	10 22 14.3 +10 30 11	10 22 14.0 +10 29 23	9875	306(7)	1.33	6.9	2.45	146.0	9.82	1
5-215	202356	10 22 18.6 +10 22 10	10 22 21.1 +10 22 07	9895	154(15)	1.09	8.5	2.30	146.3	9.74	1
5-216	202360	10 23 05.8 +10 51 12	10 23 05.3 +10 51 01	14113	243(13)	1.21	8.3	2.09	206.5	10.08	1

TableA.1 – Continued

Source	AGC	HI Coords (J2000)	Opt Coords (J2000)	$cz_{\odot}$	$W50$ (ϵ_w)	F_c	S/N	rms	Dist	$\log M_{HI}$	Code
	#	hh mm ss.s+dd mm ss	hh mm ss.s+dd mm ss	km s^{-1}	km s^{-1}	Jy km s^{-1}		mJy	Mpc	$M_{\odot}$	
5-217	200911	10 23 09.4 +08 58 42	10 23 08.6 +08 58 48	4760	175(2)	3.69	30.4	2.05	70.6	9.64	1
5-218	203294	10 23 13.4 +08 24 04	10 23 14.2 +08 23 46	13643	470(15)	2.01	8.6	2.23	199.9	10.28	1
5-219	200912	10 23 16.5 +09 13 34	10 23 16.6 +09 13 30	4733	154(8)	1.43	12.3	2.10	70.3	9.22	1
5-220	5616	10 23 25.1 +09 56 22	10 23 22.0 +09 56 14	9717	411(33)	1.30	20.5	2.00	143.7	9.80	1
5-221	200329	10 23 31.0 +10 57 26	10 23 32.6 +10 57 34	9557	222(12)	2.41	17.1	2.11	141.4	10.06	1
5-222	203296	10 23 43.3 +08 03 30	10 23 43.0 +08 03 17	11785	297(9)	1.16	9.0	1.67	173.3	9.91	1
5-223	202370	10 23 51.7 +09 59 17	10 23 51.9 +09 59 15	4899	65(2)	1.79	25.6	1.92	72.6	9.35	1
5-224	208292	10 24 08.5 +08 41 18	10 24 12.0 +08 41 53	8459	93(7)	0.54	6.1	2.04	125.8	9.30	2
5-225	203183	10 24 18.3 +09 48 22	10 24 19.3 +09 48 20	13756	303(11)	1.28	7.3	2.25	201.4	10.09	1
5-226	201404	10 24 34.0 +08 08 23	10 24 33.2 +08 08 37	6795	152(8)	1.16	10.6	1.98	102.0	9.45	1
5-227	202371	10 24 35.2 +10 17 22	10 24 32.0 +10 17 41	13226	97(8)	0.60	6.5	2.10	193.9	9.73	1 *
5-228	200970	10 24 37.3 +11 54 22	10 24 37.2 +11 54 29	2432	151(2)	2.59	24.3	1.77	37.5	8.93	1
5-229	202210	10 24 38.2 +08 30 32	10 24 35.5 +08 31 01	8231	162(5)	0.92	8.1	1.98	122.5	9.51	1
5-230	200346	10 24 42.3 +11 04 30	10 24 43.1 +11 05 21	14265	197(8)	0.82	6.8	1.91	208.7	9.92	2
5-231	203187	10 25 05.1 +09 31 26	10 25 04.5 +09 31 56	13247	495(42)	1.89	7.4	2.30	194.2	10.23	1
5-232	200917	10 25 13.3 +09 38 04	10 25 13.6 +09 38 00	14545	444(25)	1.23	5.8	2.12	212.7	10.12	2
5-233	202375	10 25 25.5 +10 36 46	10 25 27.6 +10 36 44	15992	62(11)	0.63	6.5	1.98	233.4	9.91	2 *
5-234	200918	10 25 29.6 +09 51 52	10 25 30.0 +09 52 43	13606	63(11)	0.37	5.0	2.07	199.3	9.54	2
5-235	5642	10 25 41.2 +11 44 45	10 25 41.6 +11 44 20	2349	245(4)	5.37	35.2	1.77	36.3	9.22	1
5-236	200365	10 26 14.2 +11 02 34	10 26 13.7 +11 02 32	9494	195(3)	2.11	13.6	2.09	140.5	9.99	1
5-237	208293	10 26 23.9 +08 24 38	10 26 24.8 +08 24 20	8232	91(6)	0.64	7.2	2.08	122.6	9.36	1
5-238	200377	10 26 37.8 +10 55 52	10 26 36.5 +10 56 07	10087	426(50)	3.77	15.0	2.04	149.0	10.29	1 *
5-239	202243	10 26 42.2 +11 53 52	10 26 41.8 +11 53 51	2283	89(4)	1.86	25.2	1.73	35.3	8.74	1
5-240	201440	10 26 45.7 +08 09 46	10 26 44.4 +08 10 56	9714	188(18)	0.91	6.4	2.31	143.7	9.65	1 *

TableA.1 – Continued

Source	AGC	HI Coords (J2000)	Opt Coords (J2000)	$cz_{\odot}$	$W50$ (ϵ_w)	F_c	S/N	rms	Dist	$\log M_{HI}$	Code
	#	hh mm ss.s+dd mm ss	hh mm ss.s+dd mm ss	km s^{-1}	km s^{-1}	Jy km s^{-1}		mJy	Mpc	$M_{\odot}$	
5-241	208315	10 26 58.6 +08 46 59		148	21(2)	4.35	43.9	4.51			9 *
5-242	200394	10 27 11.8 +10 01 27	10 27 11.0 +10 01 26	9712	464(22)	1.53	10.7	2.12	143.7	9.87	1
5-243	203304	10 27 14.4 +08 33 26	10 27 14.9 +08 33 01	13488	396(5)	1.77	9.1	2.19	197.7	10.21	1
5-244	200405	10 27 32.6 +09 54 33	10 27 33.3 +09 54 13	9743	105(10)	0.64	6.1	2.26	144.1	9.50	2
5-245	208294	10 27 44.1 +08 45 11	10 27 43.8 +08 44 52	14307	211(19)	0.86	6.1	2.16	209.4	9.95	2
5-246	200924	10 27 46.4 +09 56 55	10 27 45.5 +09 56 43	14085	511(23)	1.51	5.7	2.33	206.2	10.18	2
5-247	205386	10 28 04.2 +08 14 46	10 28 05.4 +08 14 45	11076	96(14)	0.57	5.6	2.30	163.2	9.55	2
5-248	200876	10 28 09.7 +09 01 02	10 28 09.9 +09 00 46	10045	359(6)	1.54	8.8	2.07	148.5	9.90	1
5-249	208295	10 28 27.4 +08 10 27	10 28 27.2 +08 10 26	1491	91(5)	1.06	11.2	2.19	24.1	8.16	1
5-250	208296	10 28 32.1 +08 33 26	10 28 34.7 +08 33 30	13536	64(9)	0.52	6.5	2.19	198.3	9.68	1
5-251	205092	10 28 48.2 +10 01 48	10 28 51.7 +10 01 07	11768	60(8)	0.45	6.2	2.08	173.1	9.50	1
5-252	202218	10 28 54.5 +09 51 30	10 28 55.8 +09 51 47	1190	39(5)	0.59	10.0	2.07	19.6	7.73	1
5-253	203324	10 29 05.8 +08 14 38	10 29 04.5 +08 14 36	10411	46(8)	0.46	7.0	2.11	153.7	9.41	1
5-254	203325	10 29 15.3 +08 13 03	10 29 15.1 +08 13 01	10250	127(7)	0.73	6.8	2.13	151.4	9.60	1
5-255	202219	10 29 32.4 +08 11 23	10 29 28.5 +08 11 37	9687	296(21)	0.77	4.3	2.33	143.4	9.57	2
5-256	203208	10 29 53.1 +09 53 22	10 29 52.6 +09 54 31	11185	195(8)	0.96	6.5	2.11	164.7	9.79	1
5-257	202551	10 31 14.0 +11 58 25	10 31 15.5 +11 58 42	9805	190(6)	0.75	7.1	1.71	145.0	9.57	1
5-258	202552	10 31 35.4 +11 55 07	10 31 34.7 +11 54 50	9415	99(12)	0.37	5.3	1.57	139.4	9.23	2
5-259	200456	10 33 11.4 +11 53 16	10 33 10.3 +11 53 26	9823	277(12)	1.28	10.7	1.61	145.2	9.80	1 *
5-260	200457	10 33 15.8 +11 50 22	10 33 14.1 +11 50 37	10092	163(7)	1.31	14.2	1.61	149.1	9.84	1 *
5-261	202016	10 33 19.2 +10 11 16	10 33 19.2 +10 11 22	1433	32(6)	0.59	6.8	2.27	23.3	7.88	1
5-262	203341	10 33 26.6 +08 44 18	10 33 23.9 +08 44 27	14763	74(8)	0.46	5.6	2.13	215.9	9.70	2
5-263	200466	10 33 31.2 +11 52 06	10 33 33.4 +11 52 17	10113	475(10)	2.64	16.0	1.56	149.4	10.14	1 *
5-264	200463	10 33 31.5 +11 52 22	10 33 32.6 +11 52 32	10115	173(5)	2.42	25.9	1.59	149.4	10.10	1 *

TableA.1 – Continued

Source	AGC	HI Coords (J2000)	Opt Coords (J2000)	$cz_{\odot}$	$W50$ (ϵ_w)	F_c	S/N	rms	Dist	$\log M_{HI}$	Code
	#	hh mm ss.s+dd mm ss	hh mm ss.s+dd mm ss	km s^{-1}	km s^{-1}	Jy km s^{-1}		mJy	Mpc	$M_{\odot}$	
5-265	202558	10 33 34.1 +11 53 43	10 33 34.6 +11 54 25	10096	175(57)	2.60	27.1	1.62	149.1	10.13	1 *
5-266	712924	10 33 42.9 +11 50 46	10 33 44.3 +11 50 18	10349	49(15)	0.36	7.0	1.63	152.8	9.30	2 *
5-267	5737	10 33 52.6 +11 11 49	10 33 53.4 +11 12 23	14956	351(6)	3.29	16.7	2.14	218.6	10.57	1
5-268	203214	10 34 07.4 +09 35 09	10 34 05.5 +09 35 34	14990	44(13)	0.31	4.6	2.20	219.1	9.54	2 *
5-269	5741	10 34 42.8 +11 11 52	10 34 42.8 +11 11 48	1389	347(4)	3.76	24.9	1.61	22.8	8.66	1
5-270	202248	10 34 56.4 +11 28 55	10 34 56.1 +11 29 32	1177	62(12)	0.64	6.2	2.24	11.1	7.27	1
5-271	202565	10 35 21.0 +11 48 14	10 35 21.5 +11 48 38	14967	162(6)	0.66	5.9	1.72	218.7	9.87	2
5-272	202017	10 35 48.9 +08 28 58	10 35 48.9 +08 28 49	1158	70(2)	1.93	22.7	2.26	11.1	7.75	1
5-273	202566	10 36 02.8 +11 59 36	10 36 03.8 +11 58 59	10390	290(28)	0.85	6.2	1.81	153.3	9.67	2
5-274	205095	10 36 33.7 +10 10 15	10 36 34.7 +10 10 19	9789	226(19)	1.20	7.7	2.32	144.8	9.77	1
5-275	200489	10 36 53.0 +09 40 06	10 36 54.2 +09 40 06	9691	532(29)	1.77	5.8	2.56	143.4	9.93	2
5-276	202410	10 36 55.2 +10 40 40	10 36 54.7 +10 40 08	8181	101(18)	1.65	9.9	2.16	121.8	9.76	1 *
5-277	205164	10 36 57.8 +11 58 43	10 36 55.8 +11 59 16	5946	289(36)	0.91	6.4	1.86	89.9	9.24	1
5-278	203220	10 36 58.1 +09 45 02	10 36 56.0 +09 44 14	11428	60(10)	0.37	4.9	2.18	168.2	9.39	2
5-279	202226	10 36 59.7 +09 33 39	10 36 59.9 +09 33 16	9757	163(7)	0.87	6.2	2.45	144.4	9.63	1
5-280	202569	10 37 13.7 +11 53 22	10 37 14.4 +11 53 18	14342	175(14)	1.05	9.3	1.67	209.8	10.04	1
5-281	202227	10 37 16.1 +09 48 59	10 37 15.7 +09 49 36	9608	122(111)	1.34	11.5	2.33	142.2	9.81	1 *
5-282	200495	10 37 20.0 +09 47 05	10 37 21.7 +09 46 15	9705	328(24)	2.65	14.5	2.26	143.6	10.11	1 *
5-283	203222	10 38 00.0 +09 32 52	10 38 02.3 +09 32 27	17661	70(13)	0.62	6.6	2.51	257.3	9.99	1 *
5-284	200499	10 38 07.9 +10 22 54	10 38 08.0 +10 22 51	1175	178(3)	7.79	53.6	2.09	11.1	8.35	1
5-285	202228	10 38 10.4 +09 19 29	10 38 11.6 +09 19 32	9933	343(2)	2.55	16.7	1.84	146.9	10.11	1
5-286	203224	10 38 35.3 +08 58 28	10 38 37.4 +08 58 33	15183	73(13)	0.46	4.4	2.72	221.9	9.73	2 *
5-287	200502	10 38 38.6 +11 12 05	10 38 37.9 +11 13 03	16308	106(17)	0.82	7.5	1.66	237.9	10.04	2 *
5-288	202576	10 38 52.1 +11 10 10	10 38 51.4 +11 10 19	14342	418(38)	1.25	7.5	1.77	209.8	10.11	1

TableA.1 – Continued

Source	AGC	HI Coords (J2000)	Opt Coords (J2000)	$cz_{\odot}$	$W50$ (ϵ_w)	F_c	S/N	rms	Dist	$\log M_{HI}$	Code
	#	hh mm ss.s+dd mm ss	hh mm ss.s+dd mm ss	km s^{-1}	km s^{-1}	Jy km s^{-1}		mJy	Mpc	$M_{\odot}$	
5-289	202417	10 39 09.7 +10 35 40	10 39 09.2 +10 36 07	9819	158(19)	1.61	12.5	2.14	145.2	9.90	1
5-290	202580	10 39 25.5 +11 48 37	10 39 25.3 +11 48 28	7982	135(3)	0.41	5.4	1.39	119.0	9.14	2
5-291	200510	10 39 44.6 +11 38 28	10 39 45.3 +11 38 49	8965	279(22)	1.31	6.1	2.15	133.0	9.74	1 *
5-292	202230	10 40 08.8 +09 15 59	10 40 08.8 +09 16 29	5433	66(8)	0.79	12.2	1.77	79.9	9.08	1
5-293	208333	10 40 18.2 +11 58 05		87	19(4)	0.74	13.3	2.62			9 *
5-294	203353	10 40 23.2 +08 40 40	10 40 23.7 +08 40 11	16495	91(9)	0.48	5.2	2.18	240.7	9.82	2
5-295	205172	10 40 26.1 +11 59 24	10 40 25.3 +11 59 41	9757	153(39)	0.66	6.9	1.72	144.3	9.51	1
5-296	5807	10 40 27.8 +09 11 47	10 40 28.4 +09 10 56	5834	311(51)	2.19	10.2	2.73	88.3	9.60	1
5-297	202422	10 40 57.8 +10 36 59	10 40 57.1 +10 37 44	14329	85(10)	0.48	5.2	2.13	209.7	9.70	2
5-298	200525	10 41 09.6 +10 34 11	10 41 08.8 +10 33 56	13562	174(8)	0.60	5.6	2.12	198.7	9.75	2
5-299	202233	10 41 10.0 +08 42 42	10 41 11.3 +08 42 54	9913	203(12)	1.61	12.4	2.04	146.6	9.91	1
5-300	202168	10 42 03.7 +10 06 26	10 42 03.0 +10 06 42	10735	327(7)	1.42	8.8	1.99	158.3	9.92	1
5-301	202603	10 42 13.8 +11 21 59	10 42 11.9 +11 21 40	16845	244(56)	1.46	5.4	2.33	245.6	10.32	2
5-302	205413	10 42 18.6 +08 59 44	10 42 18.5 +08 59 14	5728	184(4)	1.84	13.2	2.29	86.8	9.51	1
5-303	205336	10 42 43.0 +10 09 45	10 42 43.7 +10 10 10	10760	77(12)	0.59	6.8	2.19	158.7	9.54	1
5-304	202428	10 43 01.1 +10 40 38	10 43 00.6 +10 40 25	11853	181(2)	0.66	5.8	2.02	174.3	9.67	2
5-305	202606	10 43 01.1 +11 04 49	10 42 59.9 +11 04 24	5941	174(14)	0.85	6.0	2.06	89.8	9.21	1
5-306	205417	10 43 25.8 +08 01 23	10 43 27.4 +08 01 10	11360	257(8)	0.75	5.4	1.96	167.3	9.69	2
5-307	205329	10 43 26.8 +11 06 10	10 43 26.5 +11 05 24	14311	136(3)	0.52	4.7	1.98	209.4	9.73	2
5-308	200551	10 43 46.5 +11 29 50	10 43 46.0 +11 29 37	6584	245(14)	2.15	11.3	2.18	99.0	9.70	1
5-309	5850	10 43 57.6 +11 42 17	10 43 57.6 +11 42 12	777	270(1)	40.41	171.9	2.51	10.0	8.98	1 *
5-310	202613	10 44 24.4 +11 05 08	10 44 24.7 +11 05 35	10783	110(19)	0.48	4.7	1.84	159.0	9.46	2
5-311	205446	10 44 34.2 +08 46 10	10 44 36.6 +08 45 43	10052	170(35)	0.83	7.1	1.99	148.6	9.64	1
5-312	205324	10 44 46.4 +11 19 54	10 44 47.9 +11 19 35	11205	317(30)	1.12	6.4	1.89	165.0	9.86	1

TableA.1 – Continued

Source	AGC	HI Coords (J2000)	Opt Coords (J2000)	$cz_{\odot}$	$W50$ (ϵ_w)	F_c	S/N	rms	Dist	$\log M_{HI}$	Code
	#	hh mm ss.s+dd mm ss	hh mm ss.s+dd mm ss	km s^{-1}	km s^{-1}	Jy km s^{-1}		mJy	Mpc	$M_{\odot}$	
5-313	202024	10 45 00.2 +11 54 46	10 44 57.5 +11 54 58	871	24(6)	0.23	6.7	1.46	11.1	6.82	1
5-314	5864	10 45 04.5 +10 10 40	10 45 04.0 +10 11 05	10001	350(44)	1.73	8.3	2.18	147.9	9.95	1
5-315	205330	10 45 12.9 +10 01 11	10 45 12.2 +10 01 13	14432	316(9)	2.09	12.0	2.19	211.2	10.34	1
5-316	205463	10 45 16.8 +08 30 49	10 45 17.1 +08 30 31	14890	382(5)	2.09	10.9	2.19	217.7	10.37	1 *
5-317	5869	10 45 42.1 +11 20 39	10 45 42.7 +11 20 37	6570	281(1)	6.59	40.2	1.97	98.8	10.18	1
5-318	200566	10 45 51.5 +09 44 11	10 45 51.4 +09 43 21	10059	303(17)	0.98	5.8	2.17	148.7	9.71	2
5-319	205331	10 46 01.8 +10 01 42	10 46 03.4 +10 01 56	16572	361(21)	1.47	8.4	2.05	241.7	10.31	1
5-320	205489	10 46 37.9 +08 43 13	10 46 37.9 +08 43 25	5883	72(5)	1.28	18.7	1.78	89.1	9.38	1
5-321	5882	10 46 45.7 +11 49 25	10 46 45.7 +11 49 11	893	343(2)	60.81	323.4	2.04	10.5	9.20	1 *
5-322	202641	10 47 25.6 +11 08 48	10 47 25.3 +11 09 03	11100	87(10)	0.46	5.4	1.80	163.5	9.46	2
5-323	205294	10 47 39.3 +11 55 43		971	27(3)	2.05	43.4	1.95	11.1	7.77	1 *
5-324	5897	10 47 42.1 +11 04 49	10 47 41.5 +11 04 36	2719	297(1)	11.94	82.7	1.68	41.5	9.69	1
5-325	200581	10 47 53.3 +10 54 00	10 47 53.9 +10 53 52	2799	107(4)	3.15	28.4	2.01	42.7	9.13	1
5-326	200584	10 48 05.6 +09 42 02	10 48 07.8 +09 42 38	9382	269(25)	1.73	10.9	2.16	139.0	9.90	1
5-327	202644	10 48 07.4 +11 59 47	10 48 06.4 +11 59 47	6573	131(6)	0.70	7.6	1.81	98.8	9.21	1 *
5-328	202646	10 48 23.0 +11 05 34	10 48 22.8 +11 05 47	7997	210(1)	1.74	13.4	1.74	119.2	9.77	1
5-329	208297	10 48 37.5 +08 55 22	10 48 37.5 +08 54 40	16890	171(7)	0.77	6.7	1.95	246.3	10.04	1
5-330	205195	10 48 39.6 +11 54 34	10 48 39.1 +11 54 36	9503	156(6)	0.94	9.9	1.55	140.7	9.64	1
5-331	200600	10 49 00.3 +10 50 09	10 48 59.7 +10 50 07	1939	120(6)	1.33	13.3	1.81	17.5	7.98	1
5-332	202653	10 49 11.6 +11 09 14	10 49 11.2 +11 08 57	7979	203(67)	0.86	5.8	1.87	119.0	9.46	2
5-333	208349	10 49 56.6 +08 43 10	10 49 57.0 +08 43 12	2594	162(3)	1.81	16.6	1.91	39.7	8.83	1
5-334	200617	10 49 59.9 +09 04 33	10 50 01.5 +09 04 18	10064	185(6)	2.24	16.2	2.27	148.8	10.07	1 *
5-335	200616	10 50 04.1 +11 02 40	10 50 03.5 +11 02 21	10125	333(10)	1.14	5.1	2.10	149.6	9.78	2
5-336	208351	10 50 07.4 +08 51 42	10 50 08.5 +08 51 41	6343	82(26)	0.51	6.2	2.01	95.7	9.04	1

TableA.1 – Continued

Source	AGC	HI Coords (J2000)	Opt Coords (J2000)	$cz_{\odot}$	$W50$ (ϵ_w)	F_c	S/N	rms	Dist	$\log M_{HI}$	Code
	#	hh mm ss.s+dd mm ss	hh mm ss.s+dd mm ss	km s^{-1}	km s^{-1}	Jy km s^{-1}		mJy	Mpc	$M_{\odot}$	
5-337	200625	10 50 20.8 +08 45 00	10 50 21.3 +08 44 51	5900	364(31)	1.59	10.2	1.82	89.3	9.48	1
5-338	202657	10 50 47.9 +11 58 36	10 50 47.9 +11 58 59	6615	183(8)	0.76	7.7	1.65	99.5	9.25	1
5-339	208352	10 50 47.9 +10 04 22	10 50 50.2 +10 03 35	9490	71(11)	0.55	6.8	2.15	140.6	9.41	1
5-340	202658	10 50 52.3 +11 50 57	10 50 52.7 +11 50 50	6668	164(27)	0.40	5.1	1.44	100.2	8.98	2
5-341	202660	10 51 02.2 +11 37 47	10 51 02.0 +11 37 34	6585	335(16)	2.09	14.0	1.61	99.0	9.68	1
5-342	205332	10 51 20.5 +11 33 57	10 51 17.7 +11 33 45	6700	261(10)	1.06	6.9	1.74	100.7	9.40	1 *
5-343	5966	10 51 22.5 +08 17 41	10 51 26.3 +08 17 55	6350	403(8)	1.11	5.7	2.14	95.8	9.38	2
5-344	5968	10 51 28.7 +09 16 42	10 51 29.5 +09 16 45	8022	480(4)	4.27	22.1	1.80	119.6	10.16	1
5-345	201654	10 51 33.8 +08 09 48	10 51 33.8 +08 09 54	6120	144(10)	1.96	16.7	2.19	92.5	9.60	1
5-346	208353	10 51 45.3 +09 37 52	10 51 44.9 +09 38 28	14516	302(41)	1.48	8.9	2.14	212.4	10.20	1
5-347	201237	10 51 46.3 +10 05 40	10 51 46.8 +10 05 55	8043	220(5)	2.32	16.6	2.10	119.9	9.90	1
5-348	202455	10 51 48.0 +10 51 52	10 51 47.9 +10 51 58	8118	114(7)	0.84	6.8	2.10	121.0	9.46	1
5-349	200639	10 52 00.3 +08 56 44	10 51 59.2 +08 56 42	6660	119(4)	1.02	9.9	2.10	100.2	9.38	1
5-350	208372	10 52 02.1 +08 46 52	10 52 03.2 +08 46 44	6664	202(21)	1.66	12.6	2.06	100.2	9.59	1
5-351	5981	10 52 03.3 +10 08 52	10 52 03.9 +10 08 52	2722	256(1)	23.26	123.3	2.33	41.6	9.98	1
5-352	201240	10 52 10.9 +10 08 29	10 52 11.7 +10 08 23	9612	237(7)	0.89	5.5	2.13	142.3	9.63	2 *
5-353	208354	10 52 19.5 +09 05 22	10 52 17.7 +09 05 24	14472	197(7)	0.95	6.4	2.34	211.8	10.00	1
5-354	200645	10 52 26.4 +08 34 05	10 52 25.6 +08 33 26	6199	266(13)	0.85	6.6	1.77	93.6	9.24	1
5-355	5988	10 52 26.7 +10 32 52	10 52 26.0 +10 32 48	6496	186(14)	1.93	14.3	2.01	97.8	9.64	1
5-356	201662	10 52 27.4 +08 05 48	10 52 27.5 +08 05 38	6554	304(15)	2.81	18.1	1.99	98.7	9.81	1 *
5-357	5994	10 52 33.4 +10 00 52	10 52 33.4 +10 01 07	6389	352(5)	3.58	20.6	2.07	96.3	9.89	1
5-358	202236	10 52 36.5 +08 00 19	10 52 37.4 +08 00 24	6458	74(12)	0.88	10.7	2.10	97.3	9.29	1
5-359	202670	10 52 53.6 +11 31 06	10 52 55.3 +11 32 15	8444	134(4)	0.72	5.8	2.14	125.6	9.43	2
5-360	6004	10 52 58.9 +10 12 32	10 52 59.4 +10 12 36	9393	447(8)	4.08	19.6	2.01	139.2	10.27	1

TableA.1 – Continued

Source	AGC	HI Coords (J2000)	Opt Coords (J2000)	$cz_{\odot}$	$W50$ (ϵ_w)	F_c	S/N	rms	Dist	$\log M_{HI}$	Code
	#	hh mm ss.s+dd mm ss	hh mm ss.s+dd mm ss	km s^{-1}	km s^{-1}	Jy km s^{-1}		mJy	Mpc	$M_{\odot}$	
5-361	202671	10 53 16.0 +11 37 32	10 53 16.2 +11 38 20	8355	391(18)	1.21	7.0	1.81	124.3	9.64	1
5-362	208355	10 53 30.4 +08 39 31	10 53 33.1 +08 39 08	6194	137(18)	0.73	7.5	1.87	93.5	9.18	1 *
5-363	208357	10 53 32.3 +09 18 30	10 53 33.1 +09 19 09	8956	146(16)	0.67	6.5	1.91	133.0	9.45	1 *
5-364	6014	10 53 41.9 +09 43 45	10 53 42.7 +09 43 39	1133	94(3)	2.90	41.3	1.61	11.1	7.93	1
5-365	200661	10 54 27.7 +09 56 30	10 54 27.7 +09 56 59	9260	136(5)	1.03	9.0	2.19	137.3	9.66	1
5-366	200662	10 54 31.5 +11 26 59	10 54 31.1 +11 27 10	9472	291(8)	2.42	13.4	2.03	140.3	10.05	1
5-367	200663	10 54 34.5 +11 01 00	10 54 35.0 +11 00 47	9435	343(66)	1.31	6.9	2.28	139.8	9.78	2
5-368	208358	10 54 50.2 +09 39 52	10 54 49.5 +09 39 53	9788	155(8)	0.75	7.4	1.82	144.9	9.57	1
5-369	200670	10 54 54.3 +10 02 52	10 54 54.3 +10 02 50	8106	208(8)	3.10	24.0	2.00	120.8	10.03	1
5-370	205333	10 54 56.7 +09 52 52	10 54 56.6 +09 52 35	11030	24(11)	0.36	7.9	1.99	162.6	9.35	1 *
5-371	202673	10 54 57.0 +11 09 15	10 54 57.3 +11 10 06	14442	787(0)	2.16	9.5	1.91	211.3	10.36	1 *
5-372	208359	10 55 07.9 +09 49 52	10 55 08.6 +09 49 38	10978	102(9)	0.65	7.9	1.79	161.9	9.60	1 *
5-373	202676	10 55 19.0 +11 54 22	10 55 15.6 +11 54 11	14032	44(13)	0.24	4.4	1.76	205.4	9.38	2
5-374	208362	10 55 42.2 +09 41 04	10 55 40.8 +09 40 56	9707	166(5)	0.97	9.7	1.73	143.7	9.67	1
5-375	202678	10 55 45.9 +11 35 57	10 55 41.1 +11 36 24	11449	125(0)	0.42	5.1	1.73	168.5	9.45	2
5-376	202681	10 56 02.0 +11 26 22	10 56 04.4 +11 27 20	11670	271(33)	1.17	5.8	2.04	171.7	9.91	2
5-377	201030	10 56 05.2 +09 44 02	10 56 03.9 +09 44 22	9621	300(5)	1.98	16.2	1.58	142.5	9.98	1
5-378	6042	10 56 11.8 +09 45 44	10 56 15.4 +09 45 15	9921	568(12)	1.61	7.6	1.65	146.8	9.91	1 *
5-379	202464	10 56 14.4 +10 57 31	10 56 13.4 +10 57 46	6468	140(7)	0.99	9.3	1.99	97.4	9.34	1
5-380	208361	10 56 23.9 +08 49 30	10 56 26.5 +08 49 50	14682	287(10)	1.02	6.6	2.02	214.8	10.04	1
5-381	200696	10 56 32.0 +09 56 16	10 56 33.0 +09 56 02	9467	371(12)	1.91	10.5	2.10	140.3	9.95	1
5-382	208364	10 56 40.0 +09 25 00	10 56 41.0 +09 25 09	6255	97(3)	1.32	15.2	1.96	94.4	9.44	1
5-383	208365	10 56 44.0 +09 32 32	10 56 45.6 +09 32 25	6291	204(9)	1.42	10.1	2.20	94.9	9.48	1
5-384	208366	10 57 07.1 +09 36 22	10 57 06.5 +09 36 11	10333	125(22)	0.57	6.3	1.81	152.6	9.50	1

TableA.1 – Continued

Source	AGC	HI Coords (J2000)	Opt Coords (J2000)	$cz_{\odot}$	$W50$ (ϵ_w)	F_c	S/N	rms	Dist	$\log M_{HI}$	Code
	#	hh mm ss.s+dd mm ss	hh mm ss.s+dd mm ss	km s^{-1}	km s^{-1}	Jy km s^{-1}		mJy	Mpc	$M_{\odot}$	
5-385	200710	10 57 12.0 +08 27 23	10 57 11.2 +08 27 10	10919	64(9)	1.10	13.6	2.22	161.0	9.83	1
5-386	205061	10 57 28.2 +09 10 34	10 57 27.3 +09 10 28	2723	51(11)	0.42	6.2	2.10	41.5	8.23	1 *
5-387	200714	10 57 30.7 +08 17 46	10 57 31.9 +08 17 56	10412	161(34)	1.41	12.6	1.97	153.8	9.90	1
5-388	208367	10 57 34.8 +09 10 31	10 57 34.2 +09 10 37	9340	209(14)	1.32	9.8	2.06	138.5	9.78	1
5-389	200717	10 57 34.9 +08 20 38	10 57 36.4 +08 20 23	10970	437(59)	1.89	9.1	2.12	161.8	10.07	1
5-390	202237	10 57 36.6 +08 09 20	10 57 36.2 +08 08 58	9334	128(13)	0.71	6.4	2.19	138.4	9.51	1
5-391	203374	10 57 53.0 +08 09 51	10 57 53.8 +08 10 19	17049	93(14)	0.46	4.6	2.30	248.6	9.83	2
5-392	200728	10 58 00.0 +11 59 21	10 58 00.2 +11 59 13	10446	145(7)	1.13	10.4	1.80	154.2	9.80	1
5-393	203233	10 58 07.6 +09 30 32	10 58 05.4 +09 30 07	10181	71(10)	0.58	7.0	2.18	150.5	9.49	1
5-394	203381	10 58 17.2 +08 22 16	10 58 13.1 +08 20 53	10358	380(18)	1.24	7.2	1.97	153.0	9.84	1 *
5-395	203236	10 58 17.5 +09 38 12	10 58 17.8 +09 37 55	10201	271(6)	1.11	8.4	1.80	150.8	9.77	1
5-396	203383	10 58 19.8 +08 35 49	10 58 19.3 +08 36 12	10417	187(15)	0.78	5.4	2.36	153.9	9.64	2
5-397	203391	10 58 54.5 +08 00 28	10 58 54.8 +08 00 44	15242	292(8)	1.13	8.3	1.77	222.8	10.12	1 *
5-398	203240	10 58 59.4 +09 41 05	10 59 00.3 +09 40 40	10114	210(8)	0.92	7.6	1.86	149.5	9.69	1
5-399	208368	10 59 23.5 +08 36 13	10 59 25.5 +08 36 29	6228	63(10)	0.58	7.3	2.21	94.0	9.08	1
5-400	203395	10 59 27.5 +08 43 34	10 59 29.9 +08 42 33	10512	339(12)	1.01	5.3	2.31	155.2	9.76	2
5-401	203392	10 59 27.6 +08 07 06	10 59 26.8 +08 06 48	10444	289(23)	1.00	6.7	1.96	154.3	9.75	1
5-402	202239	10 59 39.7 +09 44 32	10 59 37.5 +09 44 38	9301	141(14)	0.71	7.5	1.76	137.9	9.50	1 *
5-403	6072	10 59 43.8 +10 04 30	10 59 44.5 +10 04 13	10646	212(7)	4.03	27.7	2.23	157.1	10.37	1
5-404	203397	10 59 44.6 +08 37 59	10 59 47.2 +08 38 44	10811	186(41)	0.89	5.9	2.48	159.5	9.73	2
5-405	200803	11 00 11.5 +10 21 52	11 00 09.9 +10 22 13	11018	241(5)	1.11	6.6	2.19	162.4	9.84	1
5-406	200805	11 00 22.9 +09 50 58	11 00 23.7 +09 50 23	9296	209(13)	1.22	8.8	2.15	137.8	9.74	1 *
5-407	213235	11 00 28.0 +11 37 26	11 00 27.8 +11 37 15	2835	138(2)	1.77	18.0	1.87	43.2	8.89	1
5-408	6086	11 00 34.4 +09 57 12	11 00 34.4 +09 57 22	9304	381(9)	2.18	7.7	2.27	137.9	9.99	1

TableA.1 – Continued

Source	AGC	HI Coords (J2000)	Opt Coords (J2000)	$cz_{\odot}$	$W50$ (ϵ_w)	F_c	S/N	rms	Dist	$\log M_{HI}$	Code
	#	hh mm ss.s+dd mm ss	hh mm ss.s+dd mm ss	km s^{-1}	km s^{-1}	Jy km s^{-1}		mJy	Mpc	$M_{\odot}$	
5-409	213651	11 00 37.6 +08 54 08	11 00 38.9 +08 54 23	10271	252(2)	1.68	13.5	1.75	151.8	9.96	1
5-410	213573	11 00 39.4 +09 13 41	11 00 39.8 +09 13 41	10723	195(24)	0.91	6.6	2.21	158.2	9.73	1
5-411	6091	11 00 40.1 +09 52 35	11 00 39.7 +09 52 34	10715	425(19)	3.12	17.0	1.92	158.1	10.26	1
5-412	6093	11 00 48.9 +10 43 50	11 00 47.9 +10 43 39	10806	134(5)	1.26	8.8	2.42	159.4	9.88	1
5-413	200817	11 00 52.2 +11 01 02	11 00 51.8 +11 00 46	8173	132(8)	2.07	13.7	2.36	121.8	9.86	1
5-414	213240	11 01 27.1 +11 53 08	11 01 28.6 +11 53 22	7959	357(17)	1.41	10.3	1.62	118.7	9.67	1
5-415	213054	11 01 27.9 +08 25 53	11 01 27.4 +08 25 14	9095	301(5)	1.31	8.3	2.04	135.0	9.75	1 *
5-416	213583	11 01 35.3 +09 23 22	11 01 35.3 +09 23 10	11826	89(9)	0.69	7.6	2.16	174.0	9.69	1
5-417	200844	11 01 55.6 +11 50 58	11 01 55.4 +11 50 54	14111	232(5)	2.57	23.0	1.63	206.6	10.41	1
5-418	200845	11 01 56.6 +10 17 42	11 01 56.4 +10 17 27	10417	264(7)	1.73	7.9	2.42	153.8	9.98	1
5-419	213056	11 01 59.5 +08 06 23	11 01 59.0 +08 06 32	9025	219(12)	1.64	11.6	2.13	134.0	9.84	1
5-420	213656	11 02 15.3 +08 32 13	11 02 12.6 +08 32 49	15036	343(6)	1.66	8.4	2.37	219.9	10.28	1 *
5-421	200855	11 02 23.9 +10 20 36	11 02 23.8 +10 20 37	11327	250(5)	1.30	7.1	2.07	166.8	9.93	1
5-422	200858	11 02 32.3 +09 59 42	11 02 28.6 +09 58 52	10709	325(41)	0.87	4.9	2.22	158.0	9.71	2
5-423	213058	11 02 33.1 +09 28 19	11 02 29.3 +09 28 49	8241	263(9)	0.87	4.9	2.45	122.8	9.49	2
5-424	215761	11 02 34.2 +09 28 54	11 02 34.0 +09 29 01	10486	253(12)	1.26	8.5	2.08	154.8	9.85	1
5-425	213662	11 02 42.7 +08 32 36	11 02 40.1 +08 32 40	14785	147(13)	0.55	4.2	2.38	216.3	9.78	2
5-426	202040	11 03 01.8 +08 02 53	11 03 01.7 +08 02 53	1359	96(4)	1.77	20.6	1.95	17.5	8.11	1
5-427	6120	11 03 13.1 +11 04 49	11 03 13.0 +11 04 34	6401	193(2)	5.65	50.8	1.79	96.4	10.09	1
5-428	6122	11 03 30.9 +11 07 22	11 03 32.4 +11 07 04	6394	75(5)	2.95	44.3	1.71	96.3	9.81	1
5-429	219116	11 03 35.5 +09 17 31	11 03 34.6 +09 17 29	8226	107(9)	0.88	8.5	2.21	122.6	9.49	1
5-430	213060	11 03 42.9 +08 52 16	11 03 39.1 +08 52 38	6384	154(23)	0.49	5.7	1.55	96.3	9.03	2
5-431	219117	11 03 45.1 +08 34 44	11 03 46.7 +08 34 19	1738	68(10)	0.65	8.1	2.17	17.5	7.67	1
5-432	213586	11 03 53.1 +09 08 22	11 03 51.4 +09 07 59	12171	154(30)	0.60	5.2	2.06	178.9	9.66	2 *

TableA.1 – Continued

Source	AGC	HI Coords (J2000)	Opt Coords (J2000)	$cz_{\odot}$	$W50$ (ϵ_w)	F_c	S/N	rms	Dist	$\log M_{HI}$	Code
	#	hh mm ss.s+dd mm ss	hh mm ss.s+dd mm ss	km s^{-1}	km s^{-1}	Jy km s^{-1}		mJy	Mpc	$M_{\odot}$	
5-433	212984	11 03 57.6 +10 06 29	11 03 58.6 +10 06 23	9907	216(7)	1.13	8.4	2.03	146.6	9.76	1
5-434	215235	11 03 59.8 +11 20 28	11 03 59.9 +11 20 51	2827	28(7)	0.42	8.8	1.95	43.0	8.26	1
5-435	213663	11 04 08.6 +08 27 30	11 04 08.7 +08 27 36	12814	193(8)	0.73	5.1	2.28	188.1	9.78	2
5-436	6130	11 04 09.2 +08 21 47	11 04 08.9 +08 22 06	8308	219(6)	2.82	20.3	2.10	123.8	10.01	1 *
5-437	215236	11 04 24.6 +10 15 50	11 04 21.7 +10 15 11	9314	218(11)	1.20	7.8	2.13	138.1	9.73	1
5-438	210023	11 04 26.3 +11 45 22	11 04 26.3 +11 45 21	777	44(3)	1.81	42.2	1.42	11.1	7.72	1
5-439	213241	11 04 31.6 +11 53 27	11 04 29.4 +11 53 38	13011	400(39)	1.21	8.2	1.65	190.8	10.02	1
5-440	212987	11 05 12.6 +10 26 52	11 05 11.6 +10 27 00	9220	112(6)	1.24	10.9	2.16	136.7	9.74	1
5-441	215237	11 05 24.6 +10 40 30	11 05 22.6 +10 39 53	9233	151(4)	0.79	5.9	2.37	136.9	9.54	1
5-442	210041	11 05 58.7 +08 20 50	11 05 58.3 +08 21 29	12306	483(51)	1.36	5.3	2.39	180.9	10.02	2
5-443	213588	11 06 07.4 +09 38 17	11 06 08.5 +09 38 15	12358	193(11)	0.75	6.6	1.82	181.6	9.77	1
5-444	213061	11 06 18.3 +08 28 28	11 06 17.0 +08 28 51	8155	86(6)	0.69	7.1	2.32	121.6	9.38	1 *
5-445	210048	11 06 28.2 +11 24 32	11 06 27.1 +11 24 49	9372	272(3)	1.24	6.4	2.22	138.9	9.75	2
5-446	213062	11 07 05.2 +09 48 08	11 07 06.0 +09 47 23	6254	39(3)	0.83	13.9	2.10	94.4	9.24	1
5-447	212990	11 07 10.8 +10 15 59	11 07 10.4 +10 16 13	9005	42(4)	2.12	23.1	2.22	133.7	9.95	1
5-448	213669	11 07 53.2 +08 20 23	11 07 52.4 +08 20 04	11457	374(7)	1.20	5.9	2.35	168.7	9.91	2
5-449	210073	11 08 19.0 +09 57 25	11 08 19.6 +09 57 02	12067	370(37)	1.93	10.5	2.14	177.4	10.16	1 *
5-450	210072	11 08 19.4 +10 03 09	11 08 19.6 +10 02 24	12255	398(27)	1.96	10.2	2.14	180.1	10.18	1 *
5-451	215242	11 08 22.8 +10 05 00	11 08 25.0 +10 04 36	9090	125(31)	0.74	7.0	2.10	134.9	9.50	1
5-452	211086	11 08 30.2 +10 48 29	11 08 29.9 +10 49 12	10978	277(13)	1.00	6.1	2.05	161.8	9.79	1
5-453	213590	11 08 30.5 +09 55 32	11 08 30.7 +09 55 19	12027	227(24)	1.54	9.8	2.31	176.8	10.05	1 *
5-454	213246	11 08 39.0 +11 56 46	11 08 35.3 +11 56 45	13910	198(9)	0.70	5.4	2.07	203.7	9.84	2
5-455	213671	11 08 41.6 +08 38 22	11 08 40.7 +08 38 33	11676	179(9)	0.68	5.5	2.07	171.9	9.68	2
5-456	213673	11 08 51.8 +08 26 44	11 08 52.7 +08 26 30	11760	286(22)	0.74	4.4	2.21	173.1	9.72	2

TableA.1 – Continued

Source	AGC	HI Coords (J2000)	Opt Coords (J2000)	$cz_{\odot}$	$W50$ (ϵ_w)	F_c	S/N	rms	Dist	$\log M_{HI}$	Code
	#	hh mm ss.s+dd mm ss	hh mm ss.s+dd mm ss	km s^{-1}	km s^{-1}	Jy km s^{-1}		mJy	Mpc	$M_{\odot}$	
5-457	215239	11 09 05.4 +10 10 02	11 09 03.6 +10 09 24	11916	122(2)	0.95	8.9	2.23	175.3	9.84	1
5-458	6197	11 09 09.4 +08 10 56	11 09 10.4 +08 11 08	11731	221(15)	1.86	13.5	2.08	172.7	10.12	1
5-459	210082	11 09 24.1 +10 50 12	11 09 23.2 +10 50 03	1555	66(3)	2.46	27.2	1.88	17.5	8.25	1
5-460	210084	11 09 25.9 +09 46 11	11 09 27.3 +09 46 34	7862	215(5)	1.45	10.3	2.13	117.4	9.67	1
5-461	213247	11 09 27.8 +11 26 33	11 09 28.4 +11 26 33	12881	240(2)	0.90	5.2	2.34	189.0	9.88	2
5-462	210096	11 09 48.9 +08 58 55	11 09 48.3 +08 59 39	8956	200(9)	0.63	5.3	1.90	133.0	9.42	2 *
5-463	6209	11 09 56.7 +10 43 12	11 09 55.9 +10 43 12	1584	204(6)	7.42	34.1	2.54	18.1	8.76	1
5-464	213596	11 10 19.1 +09 30 33	11 10 19.5 +09 29 55	13260	256(7)	0.94	6.6	1.99	194.5	9.92	1
5-465	210111	11 10 25.4 +10 07 22	11 10 25.1 +10 07 34	1320	60(3)	2.72	25.1	2.04	17.5	8.29	1
5-466	210123	11 10 44.1 +11 36 52	11 10 46.0 +11 36 42	12687	254(11)	2.15	14.0	1.77	186.2	10.24	1
5-467	213251	11 10 52.9 +11 04 29	11 10 51.5 +11 04 35	11594	176(10)	0.42	4.9	2.13	170.6	9.46	2
5-468	213064	11 10 54.3 +09 37 22	11 10 54.5 +09 37 19	1604	124(6)	3.26	39.5	1.65	17.5	8.37	1
5-469	210148	11 11 39.4 +09 41 40	11 11 39.0 +09 41 46	13847	164(20)	0.66	6.6	1.73	202.9	9.81	1
5-470	213603	11 11 58.1 +09 27 37	11 11 55.6 +09 28 20	14080	50(12)	0.34	4.9	2.15	206.2	9.53	2
5-471	210154	11 12 15.1 +08 37 47	11 12 15.4 +08 37 44	3308	193(2)	2.42	19.0	2.05	49.9	9.15	1
5-472	6245	11 12 41.1 +09 03 55	11 12 39.8 +09 03 21	1421	177(3)	1.29	11.0	1.96	17.5	7.97	1
5-473	213069	11 12 49.8 +09 31 22	11 12 50.2 +09 31 39	6250	140(9)	1.03	10.3	1.88	94.3	9.33	1
5-474	213609	11 12 50.1 +09 44 02	11 12 50.5 +09 43 16	14033	279(15)	0.95	6.7	1.91	205.5	9.98	2
5-475	6248	11 12 52.2 +10 11 59	11 12 51.7 +10 12 00	1286	26(3)	2.29	47.1	2.05	17.5	8.22	1
5-476	213257	11 13 10.3 +11 36 04	11 13 10.0 +11 36 04	11417	246(17)	1.04	8.5	1.74	168.1	9.84	1
5-477	210171	11 13 27.8 +10 29 05	11 13 28.3 +10 29 10	8885	153(7)	1.09	9.0	2.17	131.9	9.65	1 *
5-478	215240	11 13 54.1 +09 56 09	11 13 50.8 +09 57 39	1610	34(8)	0.45	7.6	2.18	17.5	7.51	1 *
5-479	213611	11 13 54.1 +09 38 45	11 13 55.5 +09 38 34	12370	160(4)	1.06	10.8	1.73	181.8	9.92	1
5-480	212824	11 13 57.5 +11 19 45	11 13 59.4 +11 19 49	2933	116(10)	2.14	21.3	2.07	44.5	9.00	1

TableA.1 – Continued

Source	AGC	HI Coords (J2000)	Opt Coords (J2000)	$cz_{\odot}$	$W50$ (ϵ_w)	F_c	S/N	rms	Dist	$\log M_{HI}$	Code
	#	hh mm ss.s+dd mm ss	hh mm ss.s+dd mm ss	km s^{-1}	km s^{-1}	Jy km s^{-1}		mJy	Mpc	$M_{\odot}$	
5-481	210180	11 14 44.3 +10 13 42	11 14 45.5 +10 13 29	13958	282(13)	1.24	7.5	2.19	204.4	10.09	1
5-482	213691	11 15 26.9 +08 43 28	11 15 26.6 +08 43 58	13892	201(19)	0.99	7.1	2.21	203.5	9.99	1
5-483	6288	11 16 03.6 +10 10 15	11 16 04.2 +10 09 44	5897	198(14)	2.23	16.5	2.15	89.3	9.62	1
5-484	6290	11 16 07.9 +11 02 59	11 16 08.3 +11 02 53	5880	207(5)	3.20	24.0	2.06	89.0	9.78	1
5-485	215241	11 17 02.2 +10 08 52	11 17 02.7 +10 08 36	1765	120(2)	1.80	16.9	2.16	17.5	8.11	1
5-486	215246	11 17 19.7 +11 26 37	11 17 19.1 +11 26 56	3059	43(8)	0.39	6.0	2.16	46.3	8.29	1 *
5-487	213277	11 17 27.0 +11 43 34	11 17 28.8 +11 42 49	6287	212(6)	0.95	9.1	1.61	94.8	9.30	1 *
5-488	213693	11 17 41.3 +08 46 34	11 17 43.2 +08 46 34	13503	217(20)	1.14	9.7	1.78	198.0	10.02	1 *
5-489	210228	11 17 51.1 +11 52 52	11 17 51.1 +11 53 07	5997	96(8)	0.76	10.6	1.62	90.6	9.17	1
5-490	215247	11 18 24.9 +11 54 22		12183	55(12)	0.45	6.9	1.95	179.0	9.53	1 *
5-491	213072	11 18 52.6 +09 37 44	11 18 52.7 +09 37 36	9278	46(3)	0.81	15.5	1.68	137.6	9.56	1
5-492	202257	11 19 14.5 +11 57 11	11 19 14.4 +11 57 07	861	51(2)	2.97	47.0	1.94	10.7	7.90	1
5-493	213073	11 19 25.9 +08 46 23	11 19 24.6 +08 46 29	8933	98(25)	0.76	9.2	1.84	132.7	9.50	1 *
5-494	213074	11 19 27.8 +09 35 57	11 19 28.1 +09 35 44	990	51(2)	1.95	38.3	1.57	13.7	7.94	1
5-495	213284	11 19 38.6 +11 26 26	11 19 38.7 +11 26 43	3029	90(21)	0.75	8.6	2.03	45.9	8.57	1
5-496	213292	11 21 12.5 +11 54 28	11 21 12.4 +11 54 53	11960	207(7)	1.51	10.8	1.84	175.8	10.04	1
5-497	213076	11 21 17.4 +09 09 07	11 21 17.5 +09 09 09	8981	188(4)	1.43	11.3	2.07	133.3	9.78	1
5-498	213294	11 21 36.9 +11 48 15	11 21 35.6 +11 48 09	11247	166(4)	0.73	7.3	1.70	165.6	9.67	1 *
5-499	213297	11 21 49.7 +11 53 52	11 21 49.6 +11 54 08	11148	233(28)	0.79	6.4	1.79	164.2	9.70	1 *
5-500	213010	11 21 57.8 +10 29 40	11 21 56.8 +10 29 55	4461	91(5)	0.90	9.6	2.20	66.2	8.97	1 *
5-501	210270	11 22 04.3 +08 23 13	11 22 02.0 +08 23 38	6364	283(11)	0.86	5.9	1.94	96.0	9.27	2
5-502	213511	11 22 25.3 +11 47 52	11 22 23.4 +11 47 38	1571	61(12)	0.40	4.9	1.66	17.5	7.46	2
5-503	213079	11 22 48.5 +08 51 47	11 22 47.4 +08 50 59	9427	84(9)	0.39	5.4	1.75	139.7	9.25	2
5-504	213081	11 23 00.9 +08 58 15	11 22 58.5 +08 57 34	9341	60(8)	0.31	5.3	1.70	138.5	9.15	2

TableA.1 – Continued

Source	AGC	HI Coords (J2000)	Opt Coords (J2000)	$cz_{\odot}$	$W50$ (ϵ_w)	F_c	S/N	rms	Dist	$\log M_{HI}$	Code
	#	hh mm ss.s+dd mm ss	hh mm ss.s+dd mm ss	km s^{-1}	km s^{-1}	Jy km s^{-1}		mJy	Mpc	$M_{\odot}$	
5-505	213083	11 23 28.2 +09 05 15	11 23 27.5 +09 04 25	9456	106(8)	0.58	5.1	2.47	140.1	9.43	2
5-506	6420	11 24 26.7 +11 20 34	11 24 26.2 +11 20 30	1059	255(2)	39.28	262.2	2.09	16.3	9.39	1
5-507	213305	11 25 17.5 +11 31 11	11 25 17.1 +11 31 48	14358	136(6)	0.97	7.8	2.17	210.1	10.00	1 *
5-508	6438	11 25 53.5 +09 59 05	11 25 53.5 +09 59 13	1156	50(5)	3.46	53.5	2.01	20.4	8.53	1
5-509	219119	11 26 02.9 +08 04 23	11 26 03.4 +08 04 32	1567	35(6)	0.44	9.4	1.69	25.8	7.84	1
5-510	213307	11 26 07.4 +11 15 47	11 26 06.5 +11 15 20	11060	137(23)	0.62	4.2	2.15	163.0	9.59	2
5-511	213085	11 26 32.0 +09 55 10	11 26 31.8 +09 55 16	9391	116(4)	1.14	10.7	2.19	139.2	9.72	1
5-512	213308	11 26 33.8 +11 53 32	11 26 31.8 +11 53 20	12395	193(8)	0.69	6.8	1.61	182.0	9.73	1
5-513	6449	11 26 34.3 +11 26 25	11 26 33.9 +11 26 22	3204	223(3)	9.50	70.4	2.02	48.3	9.72	1
5-514	210340	11 27 10.4 +08 43 39	11 27 11.0 +08 43 53	1046	45(2)	2.67	41.7	2.09	18.0	8.31	1
5-515	213086	11 27 12.7 +08 46 48	11 27 12.8 +08 47 17	6145	62(3)	1.12	14.4	2.18	92.8	9.36	1
5-516	213703	11 27 22.3 +08 15 23	11 27 23.8 +08 14 44	5724	169(9)	0.67	5.3	2.18	86.8	9.08	2
5-517	211420	11 28 11.8 +08 01 15	11 28 10.9 +08 00 37	6254	438(23)	1.53	9.2	1.70	94.4	9.51	1
5-518	213087	11 28 12.7 +09 48 15	11 28 14.0 +09 48 01	9321	222(13)	1.22	8.6	2.13	138.2	9.74	1
5-519	213311	11 28 13.0 +11 23 33	11 28 14.6 +11 23 40	4884	159(15)	1.34	12.0	1.98	72.1	9.21	1
5-520	6470	11 28 14.2 +09 08 52	11 28 14.8 +09 08 48	6311	380(8)	5.07	28.4	2.04	95.2	10.03	1 *
5-521	210354	11 28 14.6 +09 04 58	11 28 12.9 +09 03 44	6254	261(33)	4.05	26.6	2.11	94.4	9.93	1 *
5-522	6474	11 28 23.4 +09 24 39	11 28 24.0 +09 24 26	1716	408(2)	10.55	57.7	2.00	27.8	9.28	1
5-523	6475	11 28 34.7 +09 05 53	11 28 31.0 +09 06 14	6309	406(6)	6.43	33.1	2.14	95.2	10.14	1 *
5-524	219120	11 28 34.7 +08 17 53	11 28 35.7 +08 18 07	8112	68(10)	0.50	6.5	2.06	120.9	9.24	1
5-525	6477	11 28 37.1 +09 05 59	11 28 40.0 +09 05 55	6288	164(3)	4.95	41.5	2.07	94.9	10.02	1 *
5-526	210368	11 29 01.9 +09 06 03	11 29 00.5 +09 05 22	6287	149(33)	1.44	13.3	1.98	94.9	9.48	1 *
5-527	6482	11 29 03.9 +09 06 23	11 29 03.8 +09 06 41	6201	472(83)	1.86	9.0	1.96	93.6	9.58	1 *
5-528	6485	11 29 07.6 +08 59 19	11 29 06.5 +08 59 17	6216	477(9)	1.93	8.1	2.23	93.8	9.60	1

TableA.1 – Continued

Source	AGC	HI Coords (J2000)	Opt Coords (J2000)	$cz_{\odot}$	$W50$ (ϵ_w)	F_c	S/N	rms	Dist	$\log M_{HI}$	Code
	#	hh mm ss.s+dd mm ss	hh mm ss.s+dd mm ss	km s^{-1}	km s^{-1}	Jy km s^{-1}		mJy	Mpc	$M_{\odot}$	
5-529	6486	11 29 11.9 +11 52 10	11 29 12.3 +11 51 55	3230	113(3)	4.93	58.8	1.76	48.7	9.44	1
5-530	210372	11 29 17.6 +08 35 51	11 29 20.6 +08 36 09	8044	154(7)	1.25	7.4	3.02	120.0	9.63	1
5-531	213090	11 29 28.6 +10 37 25	11 29 27.6 +10 37 45	5855	35(3)	0.92	15.9	2.11	88.6	9.23	1
5-532	213092	11 29 38.4 +09 57 52	11 29 38.2 +09 58 03	5887	222(6)	1.40	11.2	1.86	89.1	9.42	1
5-533	213312	11 29 50.9 +11 58 09	11 29 51.0 +11 58 12	3229	79(21)	1.95	23.5	2.07	48.7	9.04	1
5-534	6498	11 30 08.2 +09 16 25	11 30 07.6 +09 16 36	1019	345(2)	41.38	216.2	2.30	17.2	9.46	1 *
5-535	213206	11 30 15.3 +10 55 59	11 30 15.8 +10 54 39	12818	221(8)	0.78	5.3	2.21	188.1	9.81	2
5-536	210391	11 30 29.0 +09 23 34	11 30 29.6 +09 23 16	6141	258(5)	1.88	12.9	2.03	92.8	9.58	1
5-537	213093	11 32 20.7 +08 51 04	11 32 21.9 +08 50 51	6220	73(42)	0.58	6.6	2.28	93.9	9.08	2
5-538	219128	11 32 43.0 +08 26 29	11 32 44.6 +08 26 14	12533	36(8)	0.56	6.9	2.94	184.1	9.65	1 *
5-539	213094	11 32 48.4 +08 43 45	11 32 50.4 +08 43 23	6242	228(21)	1.30	7.6	2.51	94.2	9.43	1
5-540	211092	11 33 26.0 +09 59 13	11 33 25.4 +09 59 00	6302	206(15)	1.12	7.7	2.26	95.0	9.38	1 *
5-541	210454	11 33 42.7 +10 05 02	11 33 44.0 +10 05 19	9161	366(22)	1.21	7.1	1.99	135.9	9.72	1
5-542	213095	11 33 47.8 +09 04 40	11 33 47.7 +09 04 16	6176	160(10)	0.79	6.0	2.33	93.3	9.21	1
5-543	213712	11 34 34.7 +08 15 05	11 34 33.3 +08 14 59	12479	133(12)	0.52	4.9	2.06	183.3	9.61	2 *
5-544	210470	11 34 48.7 +11 14 43	11 34 49.0 +11 15 00	10749	284(4)	1.54	10.1	2.02	158.5	9.96	1
5-545	213316	11 34 48.8 +11 46 14	11 34 48.0 +11 46 16	9527	187(4)	0.97	8.9	1.78	141.1	9.66	1
5-546	212838	11 34 54.9 +11 01 27	11 34 53.4 +11 01 10	881	22(2)	1.47	34.6	1.92	10.3	7.57	1
5-547	210474	11 35 02.1 +08 28 32	11 35 02.2 +08 28 25	8122	147(9)	1.44	8.2	3.22	121.1	9.70	1
5-548	213096	11 35 08.3 +10 33 42	11 35 08.9 +10 33 40	5914	40(11)	0.72	12.4	2.01	89.5	9.13	1
5-549	213713	11 35 11.8 +08 34 27	11 35 10.3 +08 34 26	8223	35(10)	0.36	4.4	3.04	122.5	9.10	2

The comments associated with the sources marked with an asterisk in column 12 of Table A.1 are given here:

5- 1: affected by rfi

5- 3: feature bisected by rfi, rfi tentatively interpolated out; params uncertain

5- 6: affected by rfi

5- 15: NGC2939=AGC5134 25 seconds away at 3344 km/s

5- 27: also possible but less likely opt counterpart 1′ to S

5- 28: on edge of band, ragged data

5- 30: near very strong continuum source

5- 31: blend with U5164 at 094049.7+113306

5- 32: ambiguous opt id: very blue object at 094105.2+105700 is possible but assigned to 094101.2+105642 because has matching opt cz

5- 39: star superimposed on top of optical image of counterpart

5- 40: disturbed system: blend of U5189, 094253.3+092939 (AGC191298) and 094242.9+092722 (AGC191865)

5- 61: v ragged data

5- 63: optical identification with tiny object is very tentative

5- 65: blue optical galaxy also nearby at 094711.6+100506 (AGC191853)

5- 67: poor centroiding because in region of ragged data

5- 76: equally likely optical counterpart at 094817.2+091044 (AGC712913)

5- 79: blend with optical galaxy at 0948448+105855 (AGC192046)

5- 85: affected by rfi, params uncertain

5- 90: affected by rfi, params uncertain

5-103: equally possible opt id at 095320.3+105539; blend?

5-105: AGC192525 (at 095329.7+083046) also in profile at cz 10740

5-110: opt id is tentative - HI centroid is off opt position by more than 1 arcmin (seems high for this s/n)

5-117: HI emission blended with IC578 (AGC5337)

5-124: v ragged data

5-141: crowded optical field, opt id somewhat ambiguous

5-156: equally likely optical counterpart at 100435.0+102424 (CGCG 065-049/AGC200031); blend?

5-157: also possible but less likely opt counterpart at 100442.5+102251 (AGC202289)

5-162: HI looks to be a blend of CGCG 065-053 (AGC200042) and opt galaxy at 1005259+114253 (AGC205066)

5-186: no identifiable opt counterpart, uncertain separation from MW HI, HVC

5-188: no identifiable opt counterpart, but s/n marginal

5-196: affected by rfi, params very uncertain

5-203: possibly affected by rfi; params somewhat uncertain

5-206: no identifiable optical counterpart

5-227: alternate opt id at 1024372+101650 (205096), assigned to 202371 because has matching opt cz

5-233: affected by rfi, params very uncertain

5-238: possible but less likely opt counterpart at 102639.7+105710 (AGC200380)

5-240: HI emission might be blended with that of opt galaxy at 102656.2+080908 (AGC201443) which is nearby and at similar cz

5-241: no identifiable optical counterpart, extended HVC

5-259: blend with emission of AGC202558 but recovery of this signal better than fair

5-260: part of crowded group in field, blend mainly with AGC200456 at

103310.3+115326 and AGC200466 at 103333.4+115217

5-263: part of crowded group in field, severely nasty blend with AGC200463 at 103332.6+115232, putative contribution from AGC200463 tentatively interpolated out; params very uncertain

5-264: part of crowded group in field, contact pair with AGC200466 at 103333.4+115217, severely nasty blend; params very uncertain

5-265: tight blend with AGC200466 and AGC200463

5-266: part of crowded group in field, blend mainly with AGC200466 at 103333.4+115217; params very uncertain

5-268: affected by rfi; params very uncertain

5-276: equally likely opt counterpart at 103656.3+104015 (AGC202411); HI looks to be a blend of the two

5-281: blend with CGCG 065-071=AGC200495 at 103721.7+094615

5-282: HI blended with that of opt gal at 103715.7+094936 (AGC202227)

5-283: on edge of bandpass, ragged data; params uncertain

5-286: affected by rfi; params uncertain

5-287: affected by rfi; params very uncertain

5-291: affected by rfi; params very uncertain

5-293: HVC extends over 15’

5-309: extended HI emission

5-316: affected by rfi, possible blend with AGC205470 at 104531.8+082923; params very uncertain

5-321: extended HI emission

5-323: part of the Leo Ring

5-327: blend with emission of AGC202645

5-334: ambiguous opt id; also possible at 104956.9+090400

5-342: possible blend with emission of gal at 105102.0+113734 (AGC202660)

5-352: HI emission blends with that of N3444 (AGC6004)

5-356: HI emission blends with gal at 105237.4+080024 (AGC202236)

5-362: possible but less likely opt counterpart at 105333.4+083834

5-363: affected by rfi; params very uncertain

5-370: blend with emission of AGC208359 at 105508.7+094936; params probably affected

5-371: ambiguous opt id; HI probably a blend

5-372: blend with emission of AGC205333 at 105456.6+095235; params probably affected

5-378: blended with AGC201030 at 105603.9+094422; params uncertain

5-386: alternate (equally likely) opt id at 105734.1+091037

5-394: poorly determined position and width

5-397: affected by rfi; params uncertain

5-402: affected by rfi; params uncertain

5-406: affected by rfi; params uncertain

5-415: affected by rfi; params mildly uncertain

5-420: affected by rfi; params very uncertain

5-432: HI emission a heavy blend of AGC213587 at 110352.1+090948 and AGC213586 at 110351.4+090759

5-436: affected by rfi; params mildly uncertain

5-444: ambiguous opt id: also possible at 110619.2+082856; blend?

5-449: part of triple system, mild blend with AGC210072=CGCG 067-009 at 110819.6+100224 and AGC213590 at 110830.7+095519

5-450: part of triple system, mild blend with AGC210073=CGCG 067-008 at 110819.6+095702 and AGC213590 at 110830.7+095519; params uncertain

5-453: part of triple system, mild blend with AGC210073=CGCG 067-008 at 110819.6+095702 and AGC210072=CGCG 067-009 at 110819.6+100224

5-462: affected by rfi; params very uncertain

5-477: affected by rfi; params very uncertain

5-478: large HI/opt position offset may be significant

5-486: for feature assigned opt id, SDSS gives unrealistic z=2.2

5-487: alternate opt id at 111728.5+114442

5-488: ambiguous opt id; also possible at 111736.5+084646 (AGC213692) and at 111743.2+084634 (AGC213693); blend?

5-490: no identifiable optical counterpart

5-493: affected by rfi; params uncertain

5-498: ambiguous opt id; also possible at 112137.4+114801; blend?

5-499: ambiguous opt id; also possible at 112151.48+115325.1

5-500: HI source in v close pair: ambiguous opt id; also possible at 112157.6+102956; blend?

5-507: ambiguous opt id; also possible at 112514.2+113148; blend?

5-520: part of crowded group in field, blend mainly with AGC210354 at 112812.9+090344, AGC6477 at 112840.0+090555, and AGC6475 at 112831.0+090614; params uncertain

5-521: part of crowded group in field, blend mainly with AGC6470 at 112814.8+090848, AGC6477 at 112840.0+090555, and AGC6475 at 112831.0+090614; params uncertain

5-523: part of crowded group in field, severely nasty blend with AGC6477 at 112840.0+090555, putative contribution from AGC6477 tentatively interpolated out; params very uncertain

5-525: part of crowded group in field, severely nasty blend with AGC6475 at

112831.0+090616; params uncertain

5-526: part of crowded group in field, severely nasty blend with AGC6482 at 112903.8+090641; params very uncertain

5-527: part of crowded group in field, severely nasty blend with AGC210368 at 112900.5+090522, putative contribution from AGC210368 tentatively interpolated out; params very uncertain

5-534: extended HI

5-538: ambiguous opt id; also possible at 113244.8+082544, params affected by rfi

5-540: evidence for extended HI

5-543: alternate opt id at 113435.7+081455

APPENDIX B

OPTICAL SPECTRA FOR SELECTED ALFALFA DWARFS

In this appendix we present the flux calibrated optical spectra for the HII regions of the spectroscopic sample. An overlap of 300 Å is shown for the spectra coming from the blue and red arms of the spectrograph to show the agreement in the continuum levels. Each spectrum is labeled with the AGC number associated with the galaxy containing the HII region, and when an 'a','b', or 'c' is present, multiple HII regions were observed within the same galaxy.

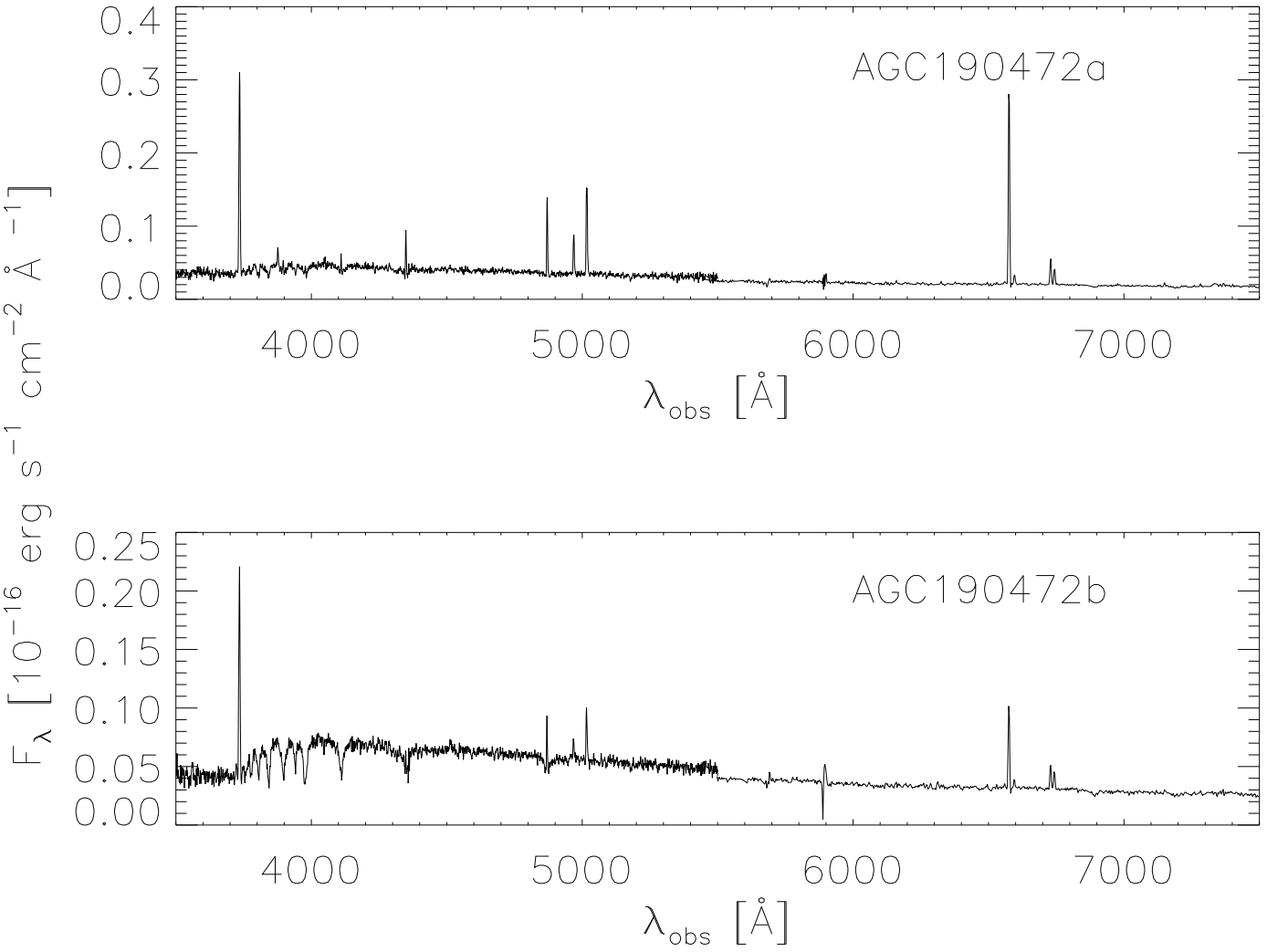
AGC190472a
AGC190472b
F_λ [10^{-16} erg s^{-1} cm^{-2} Å $^{-1}$]
λ_{obs} [Å]
0.4
0.3
0.2
0.1
0.0
0.25
0.20
0.15
0.10
0.05
0.00
4000
5000
6000
7000

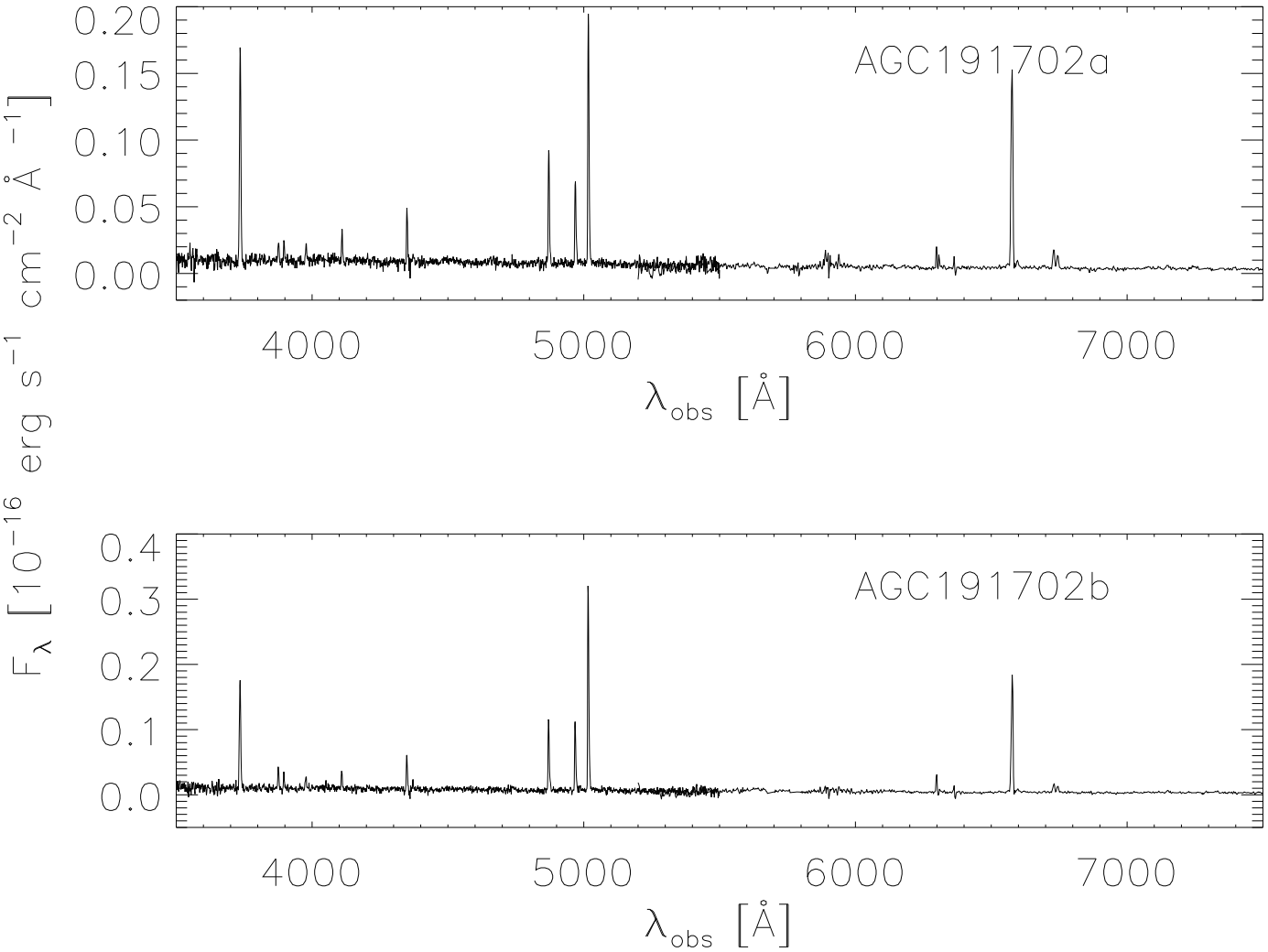
AGC191702a
AGC191702b
0.20
0.15
0.10
0.05
0.00
0.4
0.3
0.2
0.1
0.0
4000
5000
6000
7000
λ_{obs} [Å]
F_λ [10^{-16} erg s^{-1} cm^{-2} Å $^{-1}$]

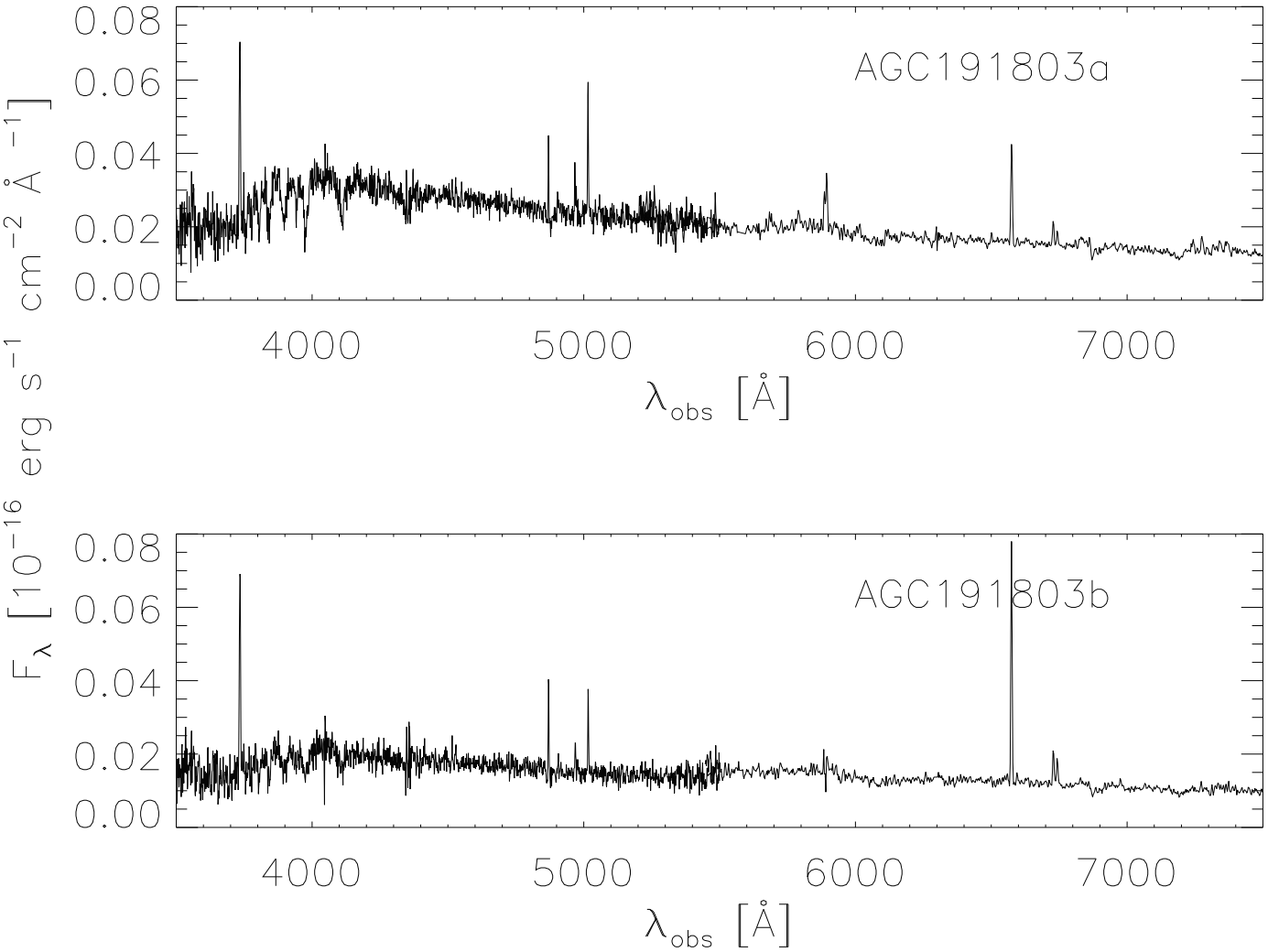
AGC191803a
AGC191803b
0.08
0.06
0.04
0.02
0.00
4000
5000
6000
7000
λ_{obs} [Å]
F_λ [10^{-16} erg s^{-1} cm^{-2} Å^{-1}]

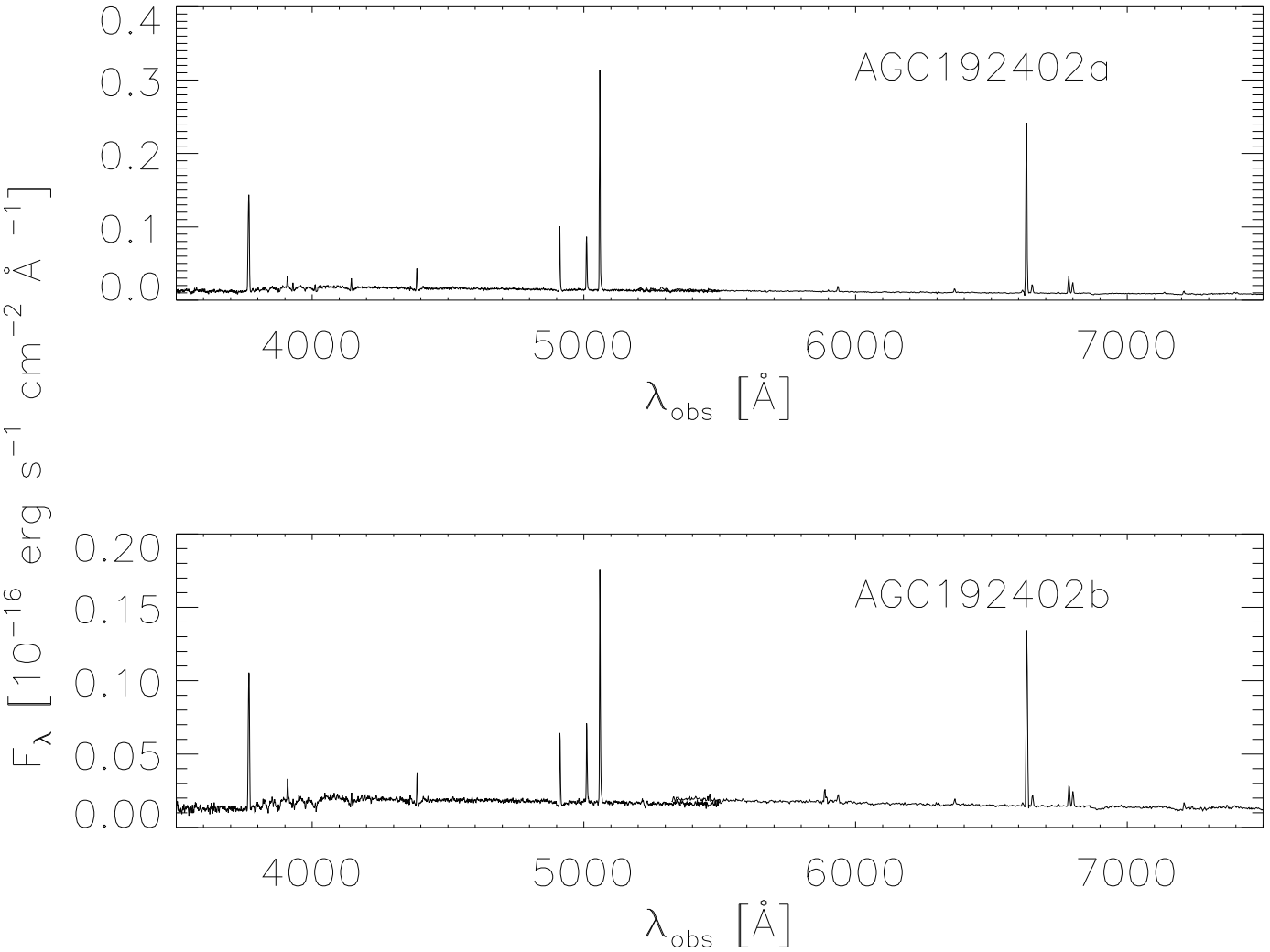
AGC192402a
AGC192402b
F_λ [10^{-16} erg s^{-1} cm^{-2} Å $^{-1}$]
λ_{obs} [Å]
0.4
0.3
0.2
0.1
0.0
0.20
0.15
0.10
0.05
0.00
4000
5000
6000
7000

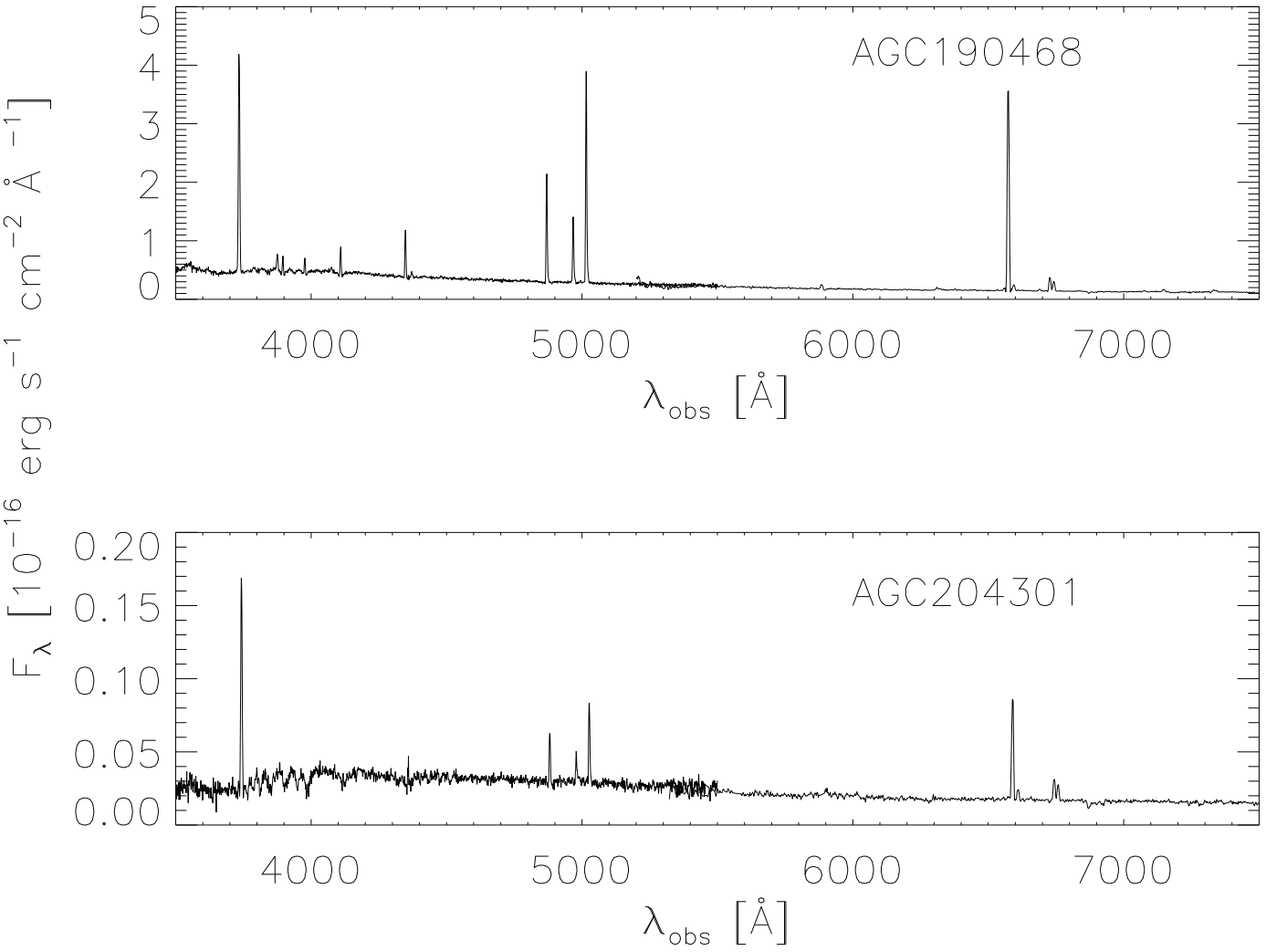
AGC190468
AGC204301
F_λ [10^{-16} erg s^{-1} cm^{-2} Å $^{-1}$]
λ_{obs} [Å]
0
1
2
3
4
5
0.00
0.05
0.10
0.15
0.20
4000
5000
6000
7000

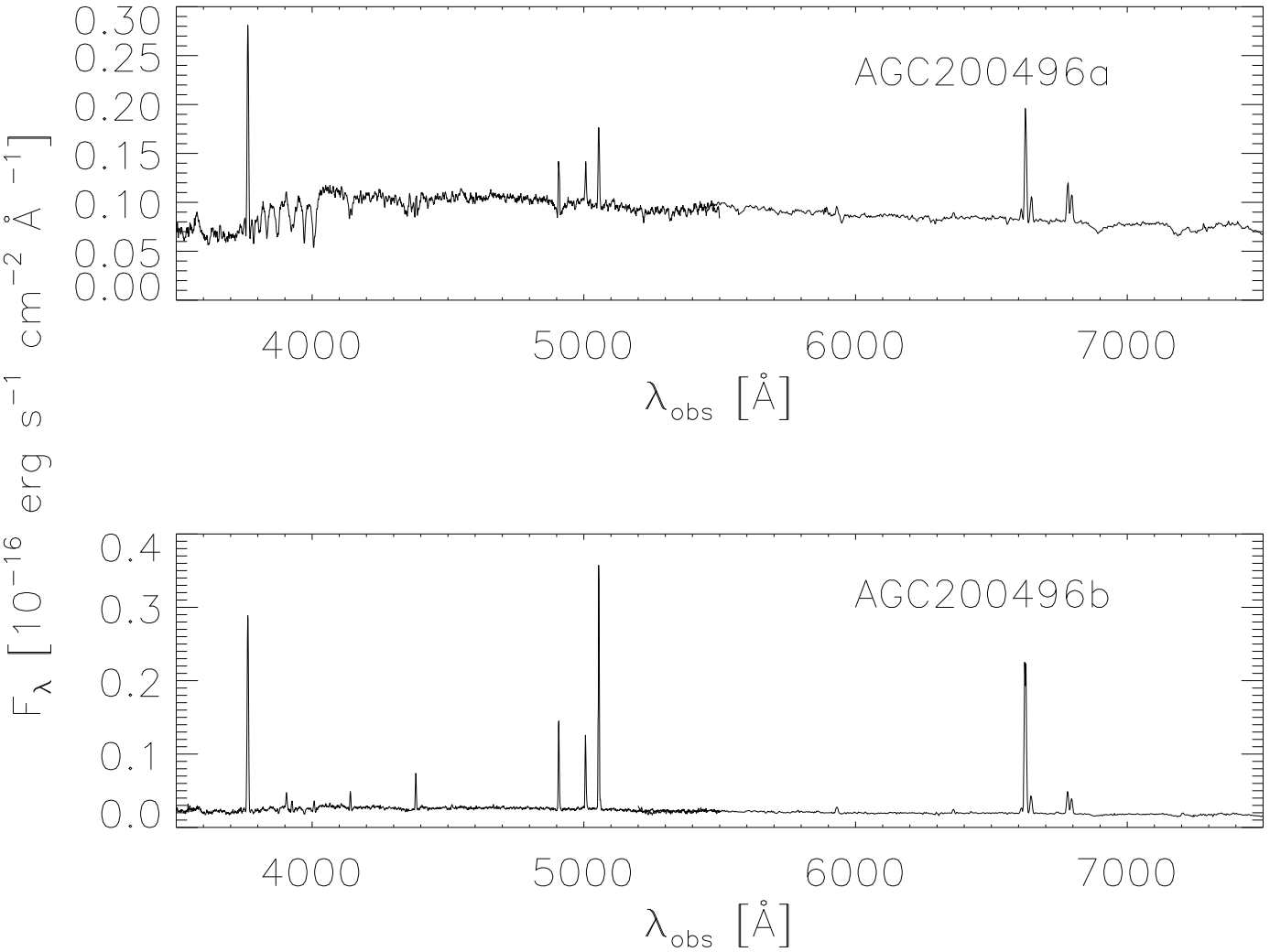
AGC200496a
AGC200496b
F_λ [10^{-16} erg s^{-1} cm^{-2} Å^{-1}]
λ_{obs} [Å]
0.30
0.25
0.20
0.15
0.10
0.05
0.00
0.4
0.3
0.2
0.1
0.0
4000
5000
6000
7000

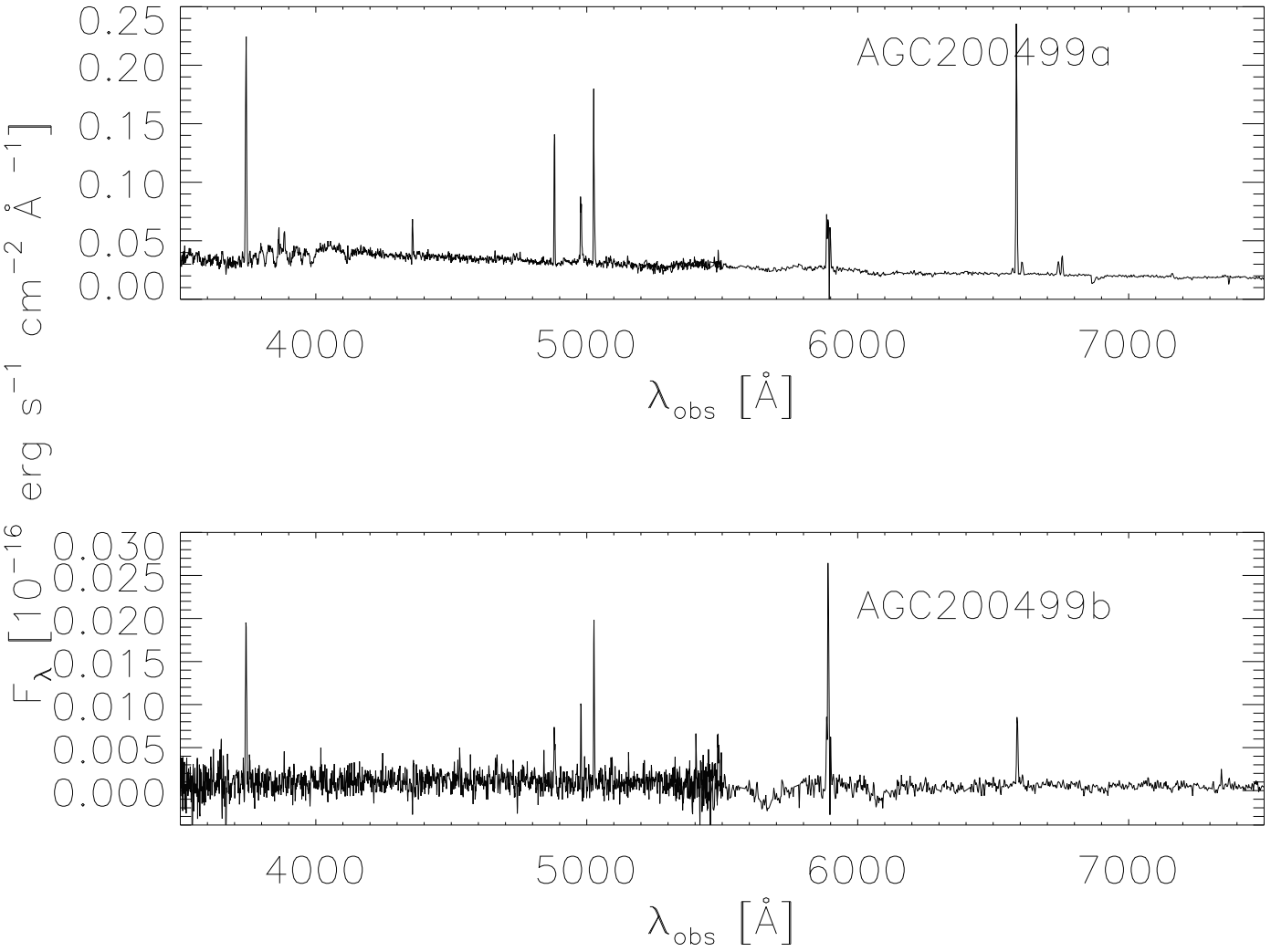
AGC200499a
AGC200499b
F_λ [10^{-16} erg s^{-1} cm^{-2} Å^{-1}]
λ_{obs} [Å]
0.25
0.20
0.15
0.10
0.05
0.00
0.030
0.025
0.020
0.015
0.010
0.005
0.000
4000
5000
6000
7000

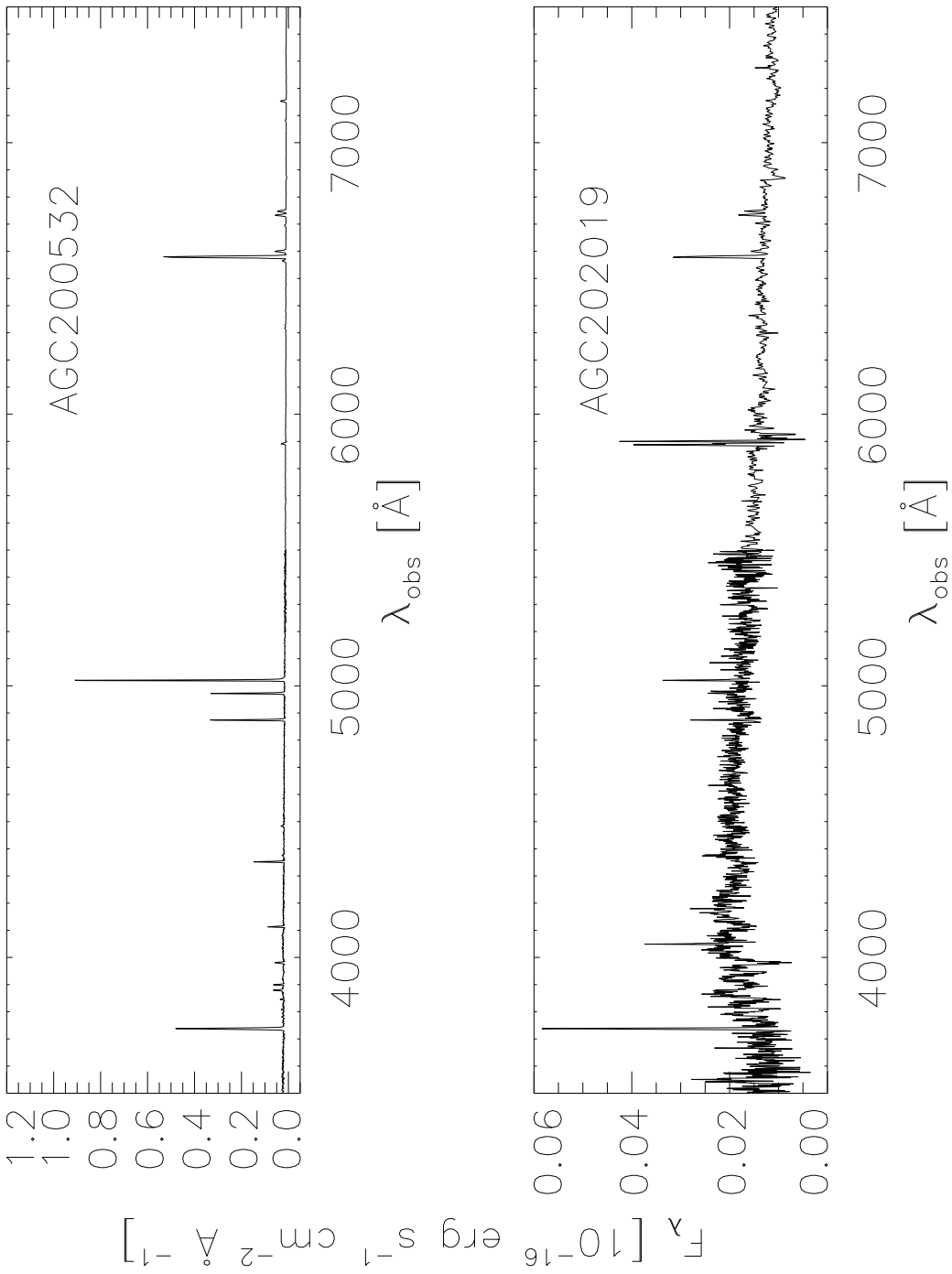
AGC200532
AGC202019
λ_{obs} [Å]
F_λ [10^{-16} erg s^{-1} cm^{-2} Å^{-1}]

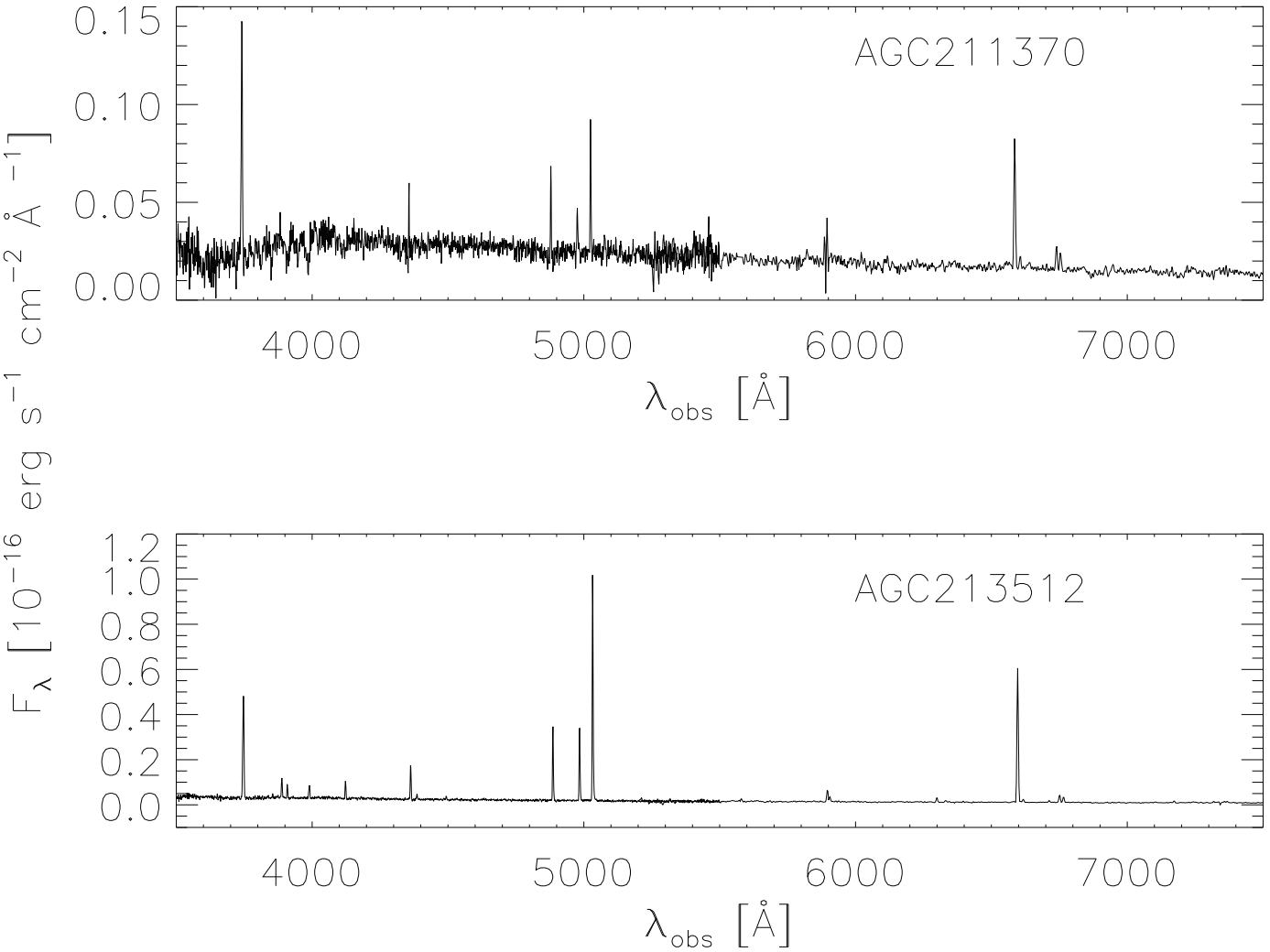
AGC211370
AGC213512
0.15
0.10
0.05
0.00
1.2
1.0
0.8
0.6
0.4
0.2
0.0
4000
5000
6000
7000
λ_{obs} [Å]
F_λ [10^{-16} erg s^{-1} cm^{-2} Å^{-1}]

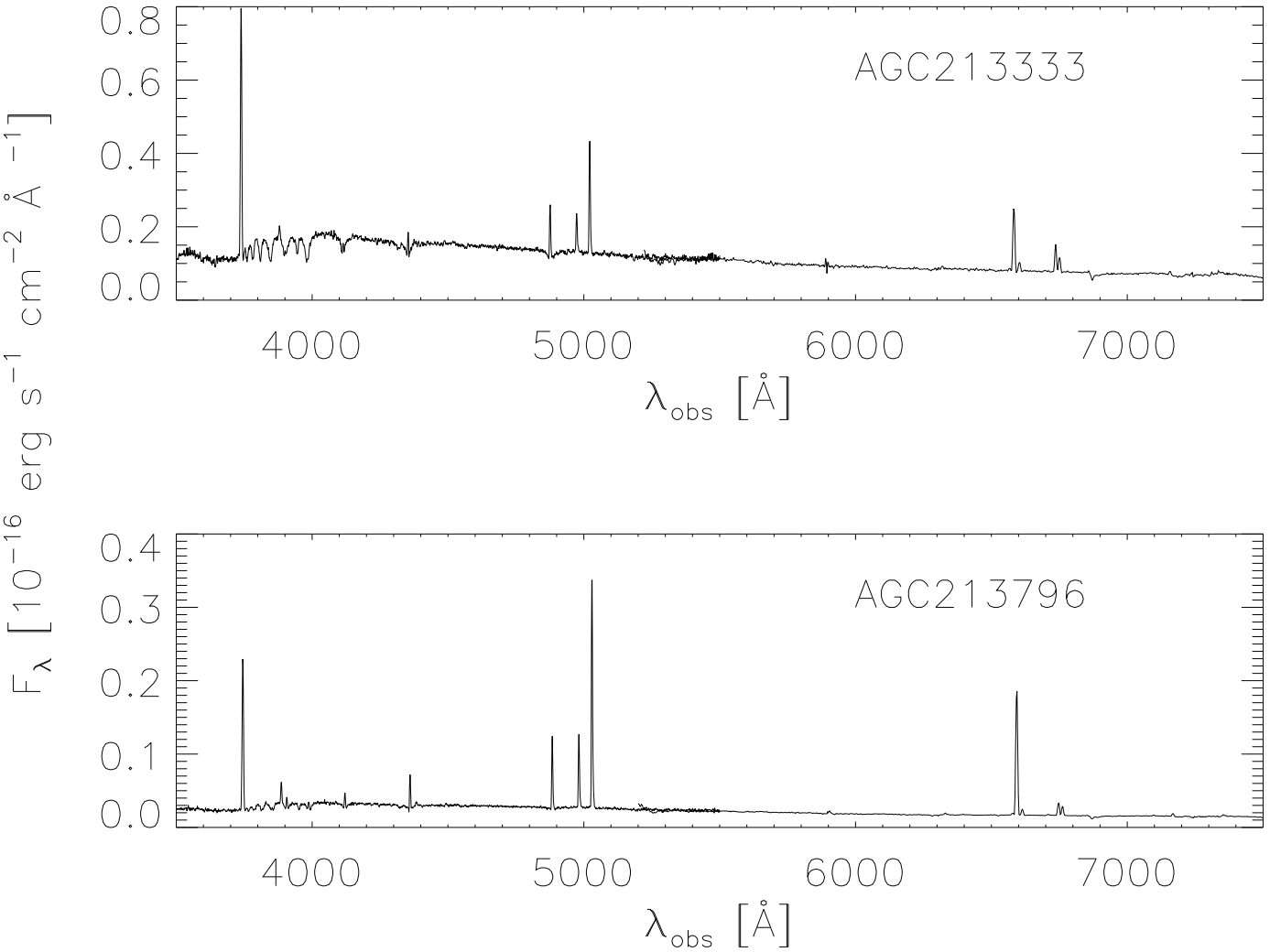
AGC213333
AGC213796
F_λ [10^{-16} erg s^{-1} cm^{-2} Å $^{-1}$]
λ_{obs} [Å]
0.0
0.2
0.4
0.6
0.8
0.1
0.3
4000
5000
6000
7000

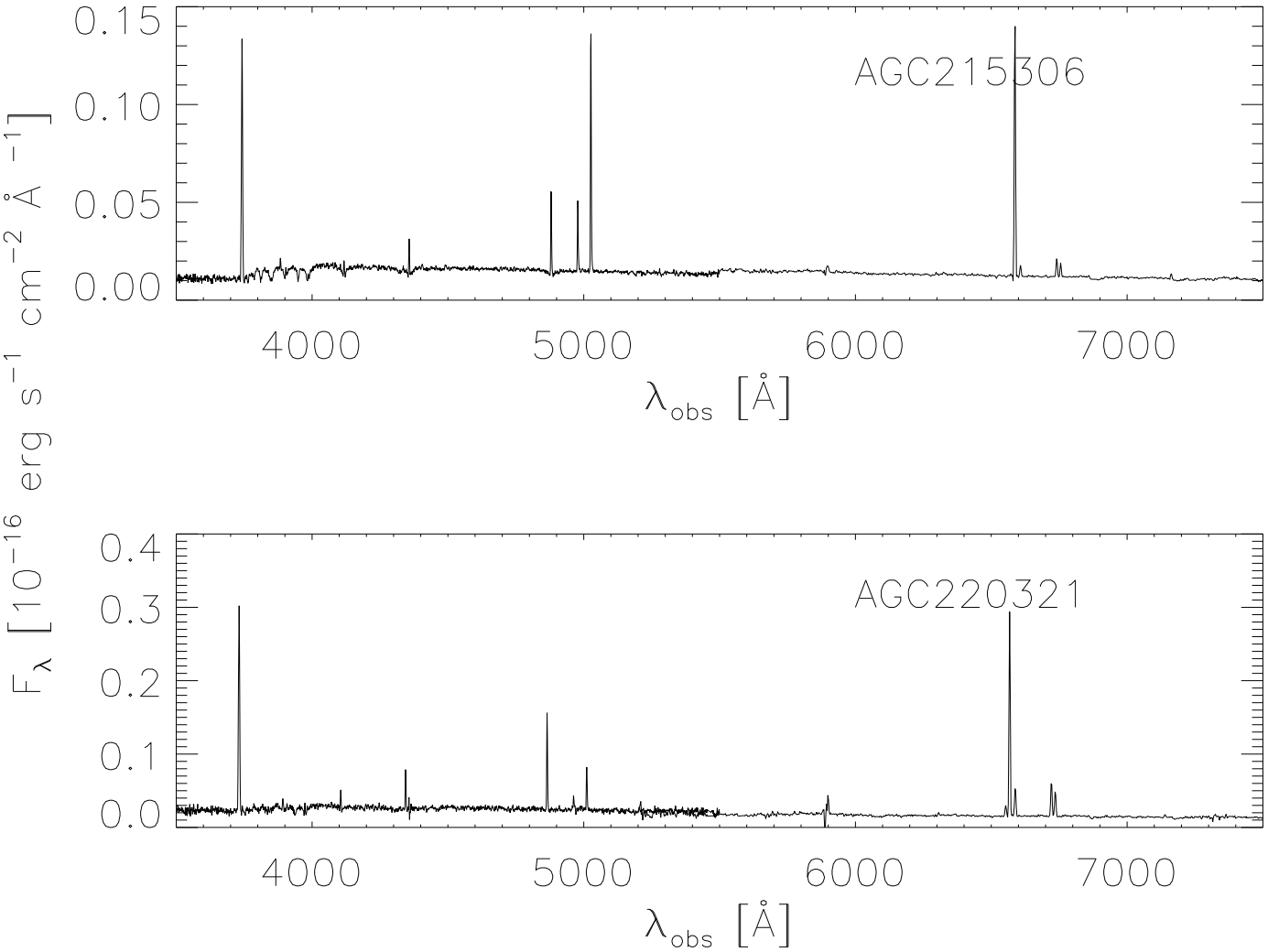
AGC215306
AGC220321
0.15
0.10
0.05
0.00
0.4
0.3
0.2
0.1
0.0
4000
5000
6000
7000
λ_{obs} [Å]
F_λ [10^{-16} erg s^{-1} cm^{-2} Å^{-1}]

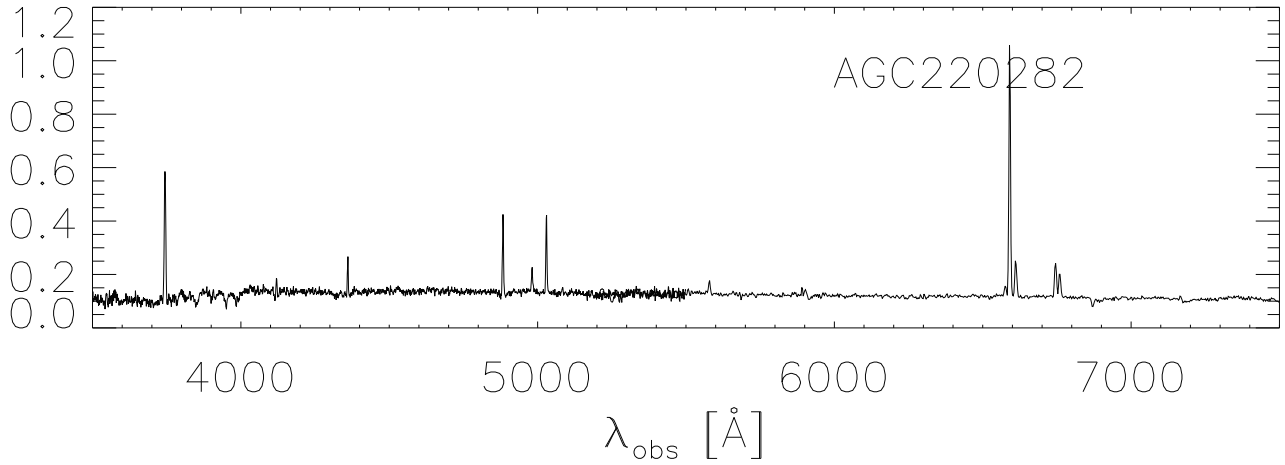
AGC220282
1.2
1.0
0.8
0.6
0.4
0.2
0.0
4000
5000
6000
7000
λobs [Å]

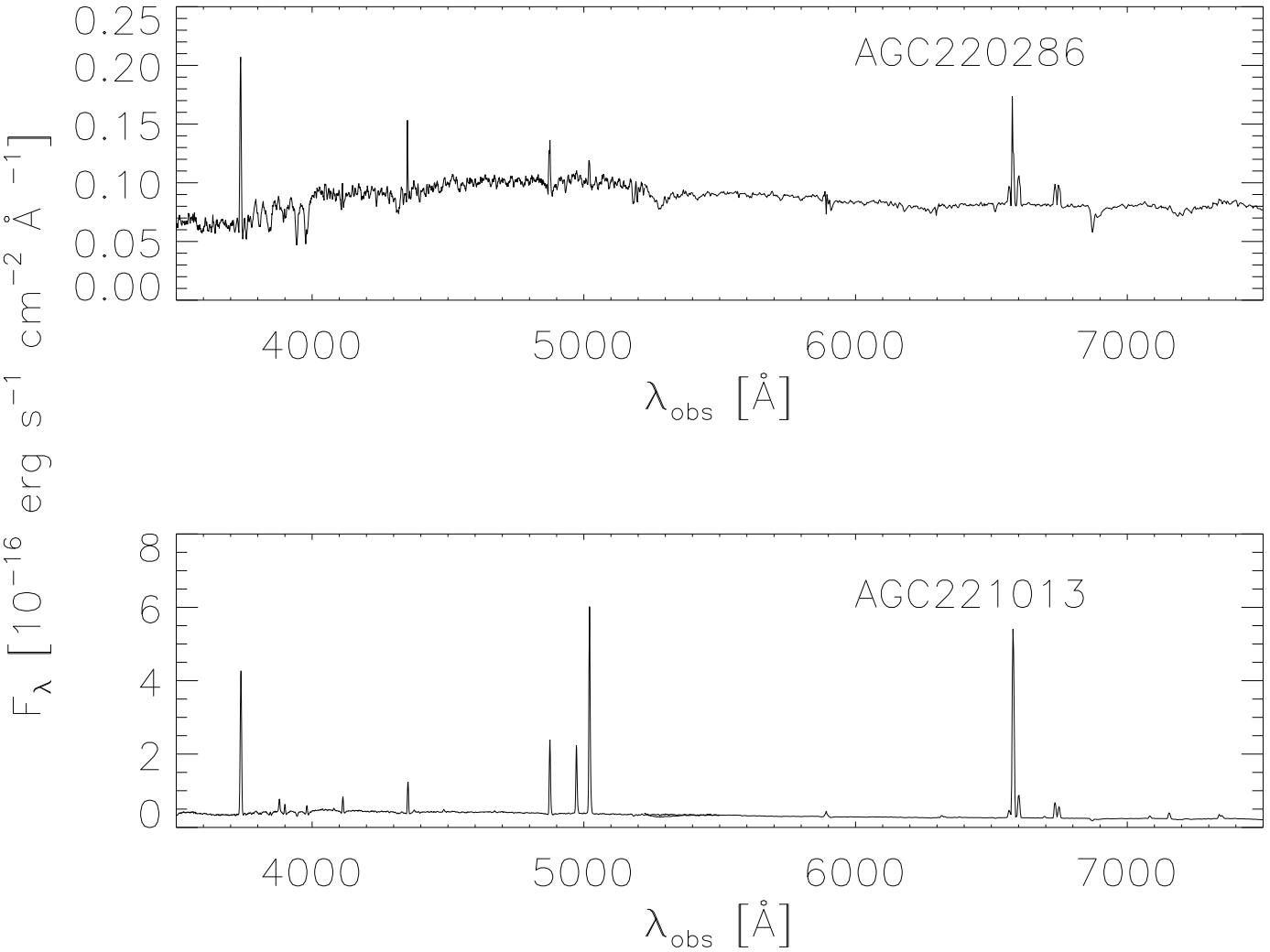
AGC220286
AGC221013
F_λ [10^{-16} erg s^{-1} cm^{-2} Å $^{-1}$]
λ_{obs} [Å]
0.25
0.20
0.15
0.10
0.05
0.00
8
6
4
2
0
4000
5000
6000
7000

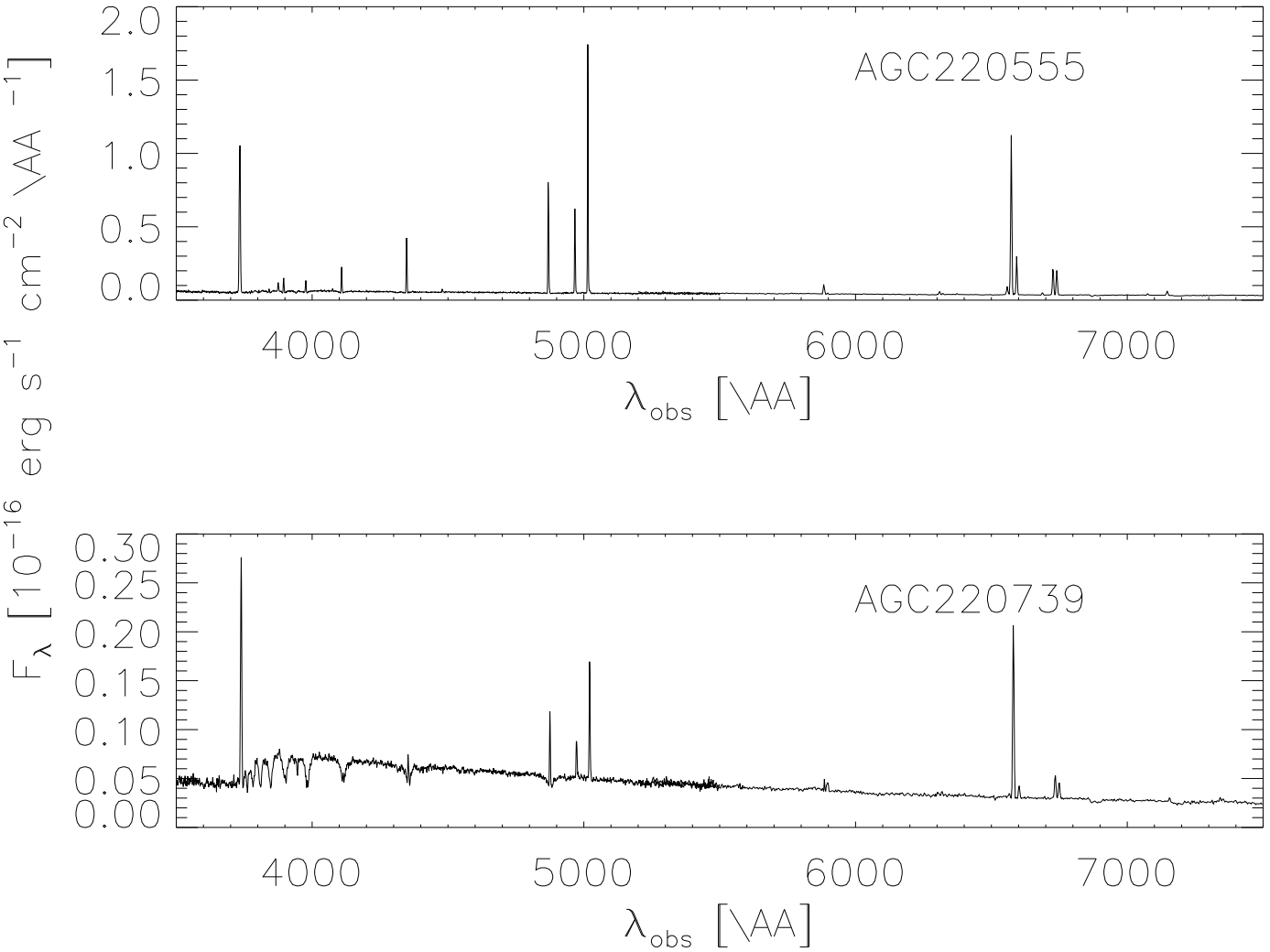
AGC220555
AGC220739
F_λ [10^{-16} erg s^{-1} cm^{-2} \AA $^{-1}$]
λ_{obs} [\AA]
2.0
1.5
1.0
0.5
0.0
0.30
0.25
0.20
0.15
0.10
0.05
0.00
4000
5000
6000
7000

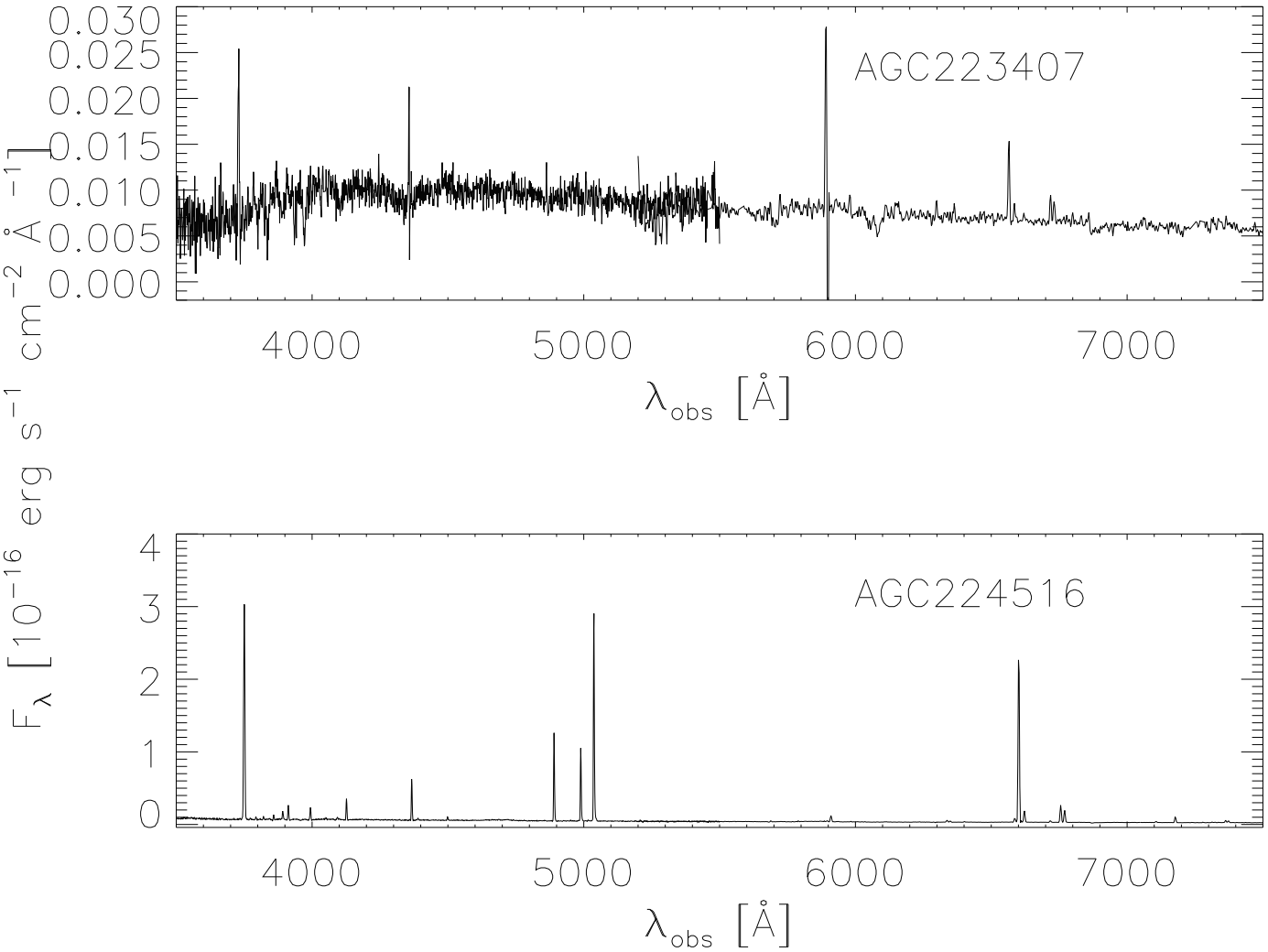
AGC223407
AGC224516
F_λ [10^{-16} erg s^{-1} cm^{-2} Å $^{-1}$]
λ_{obs} [Å]
0.030
0.025
0.020
0.015
0.010
0.005
0.000
4000
5000
6000
7000
4
3
2
1
0

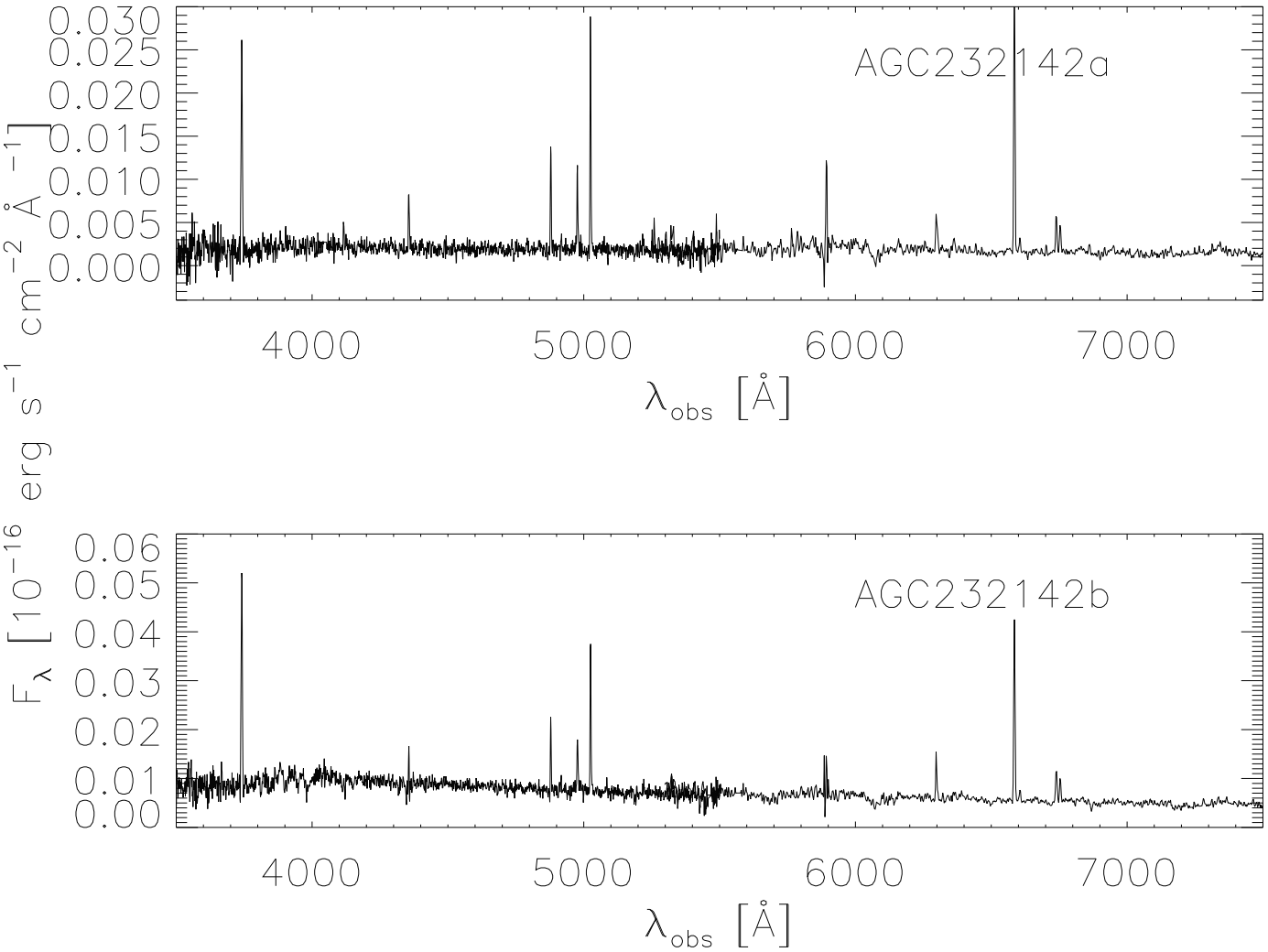
AGC232142a
AGC232142b
F_λ [10^{-16} erg s^{-1} cm^{-2} Å^{-1}]
λ_{obs} [Å]
0.030
0.025
0.020
0.015
0.010
0.005
0.000
0.06
0.05
0.04
0.03
0.02
0.01
0.00
4000
5000
6000
7000

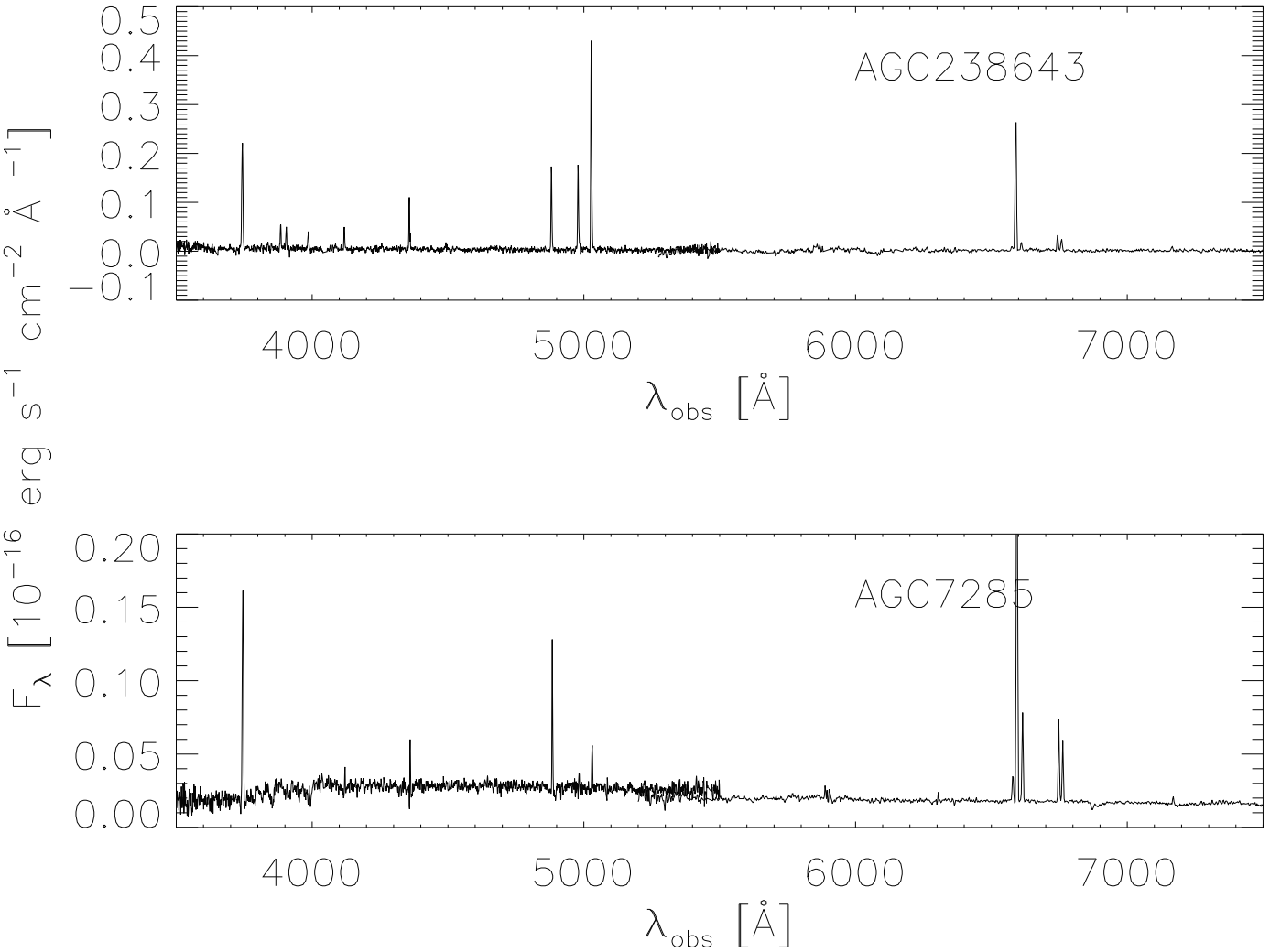
AGC238643
AGC7285
F_λ [10^{-16} erg s^{-1} cm^{-2} Å^{-1}]
λ_{obs} [Å]
0.5
0.4
0.3
0.2
0.1
0.0
−0.1
0.20
0.15
0.10
0.05
0.00
4000
5000
6000
7000

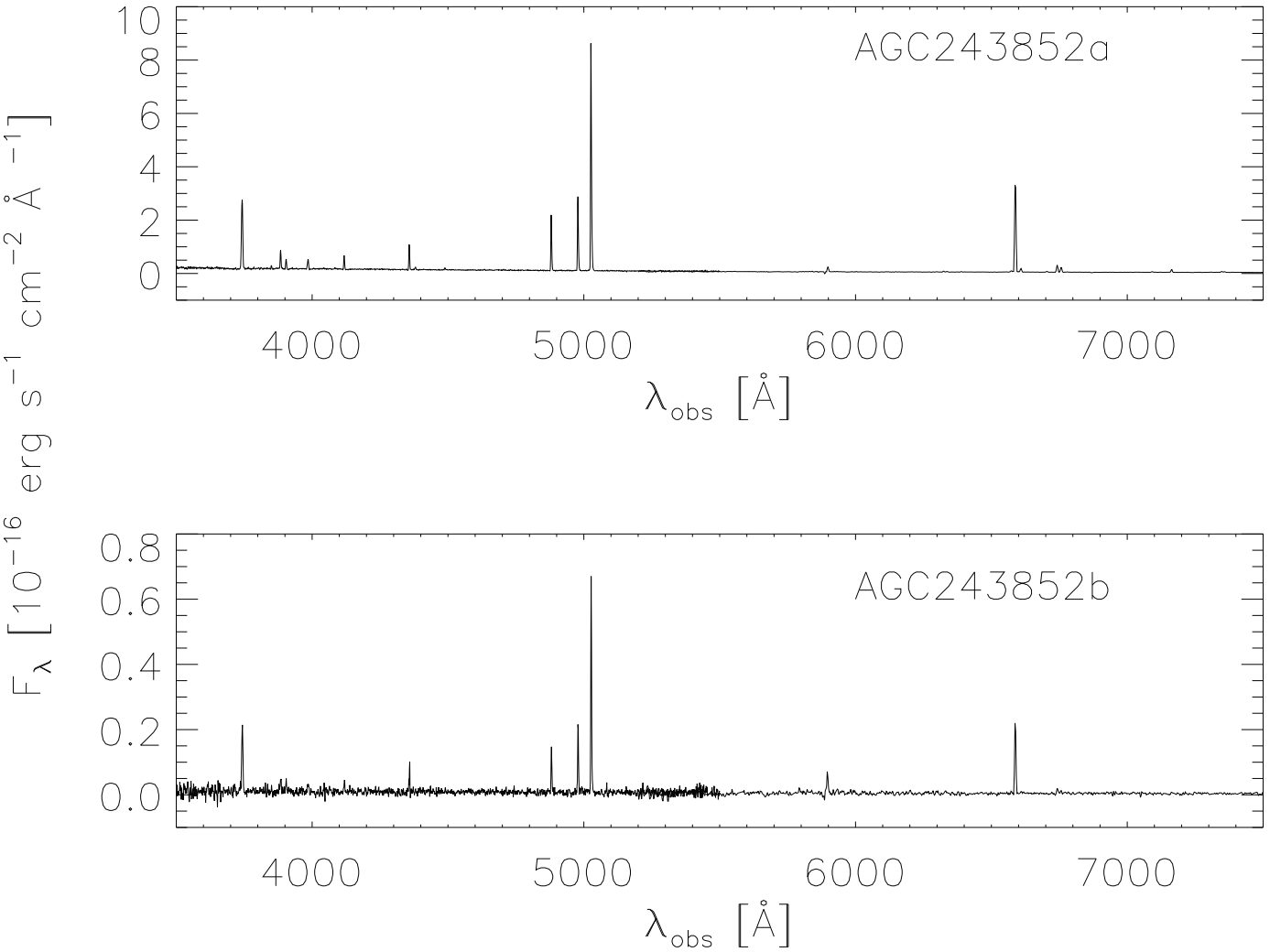
AGC243852a
AGC243852b
F_λ [10^{-16} erg s^{-1} cm^{-2} Å^{-1}]
λ_{obs} [Å]
0
2
4
6
8
10
0.0
0.2
0.4
0.6
0.8
4000
5000
6000
7000

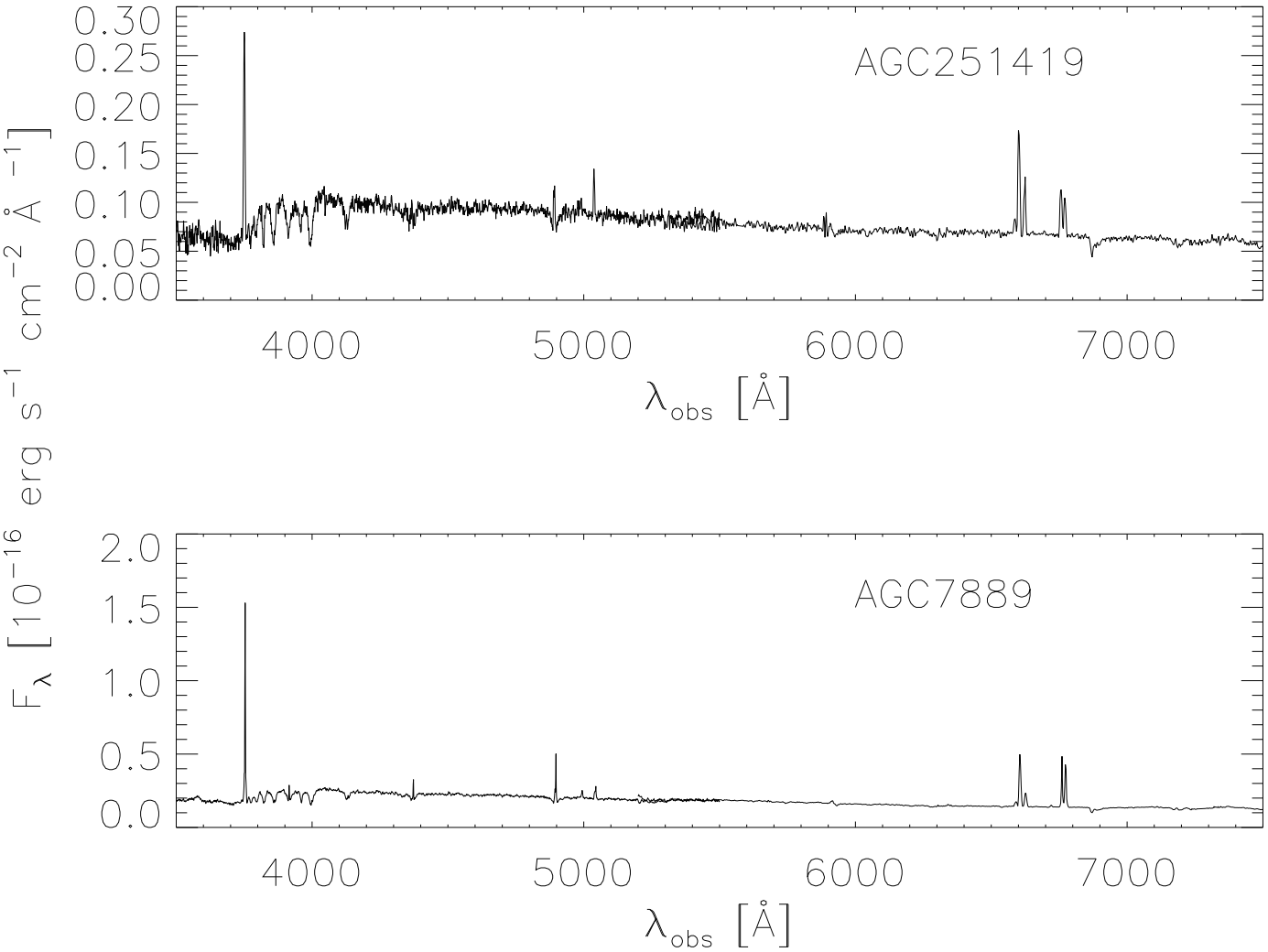
AGC251419
AGC7889
F_λ [10^{-16} erg s^{-1} cm^{-2} Å^{-1}]
λ_{obs} [Å]
0.30
0.25
0.20
0.15
0.10
0.05
0.00
2.0
1.5
1.0
0.5
0.0
4000
5000
6000
7000

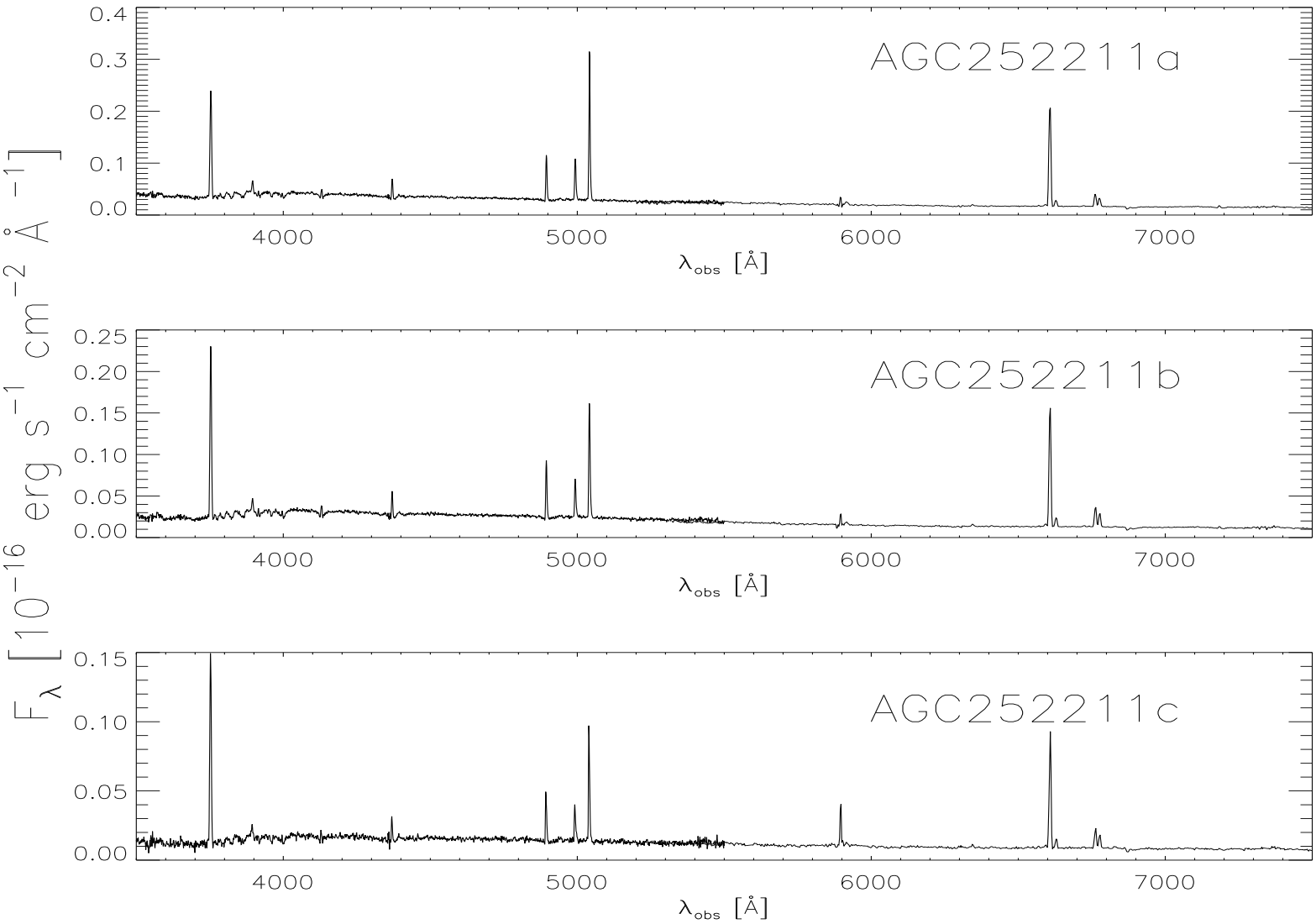
AGC252211a
AGC252211b
AGC252211c
F_λ [10^{-16} erg s^{-1} cm^{-2} Å $^{-1}$]
λ_{obs} [Å]
0.4
0.3
0.2
0.1
0.0
0.25
0.20
0.15
0.10
0.05
0.00
4000
5000
6000
7000

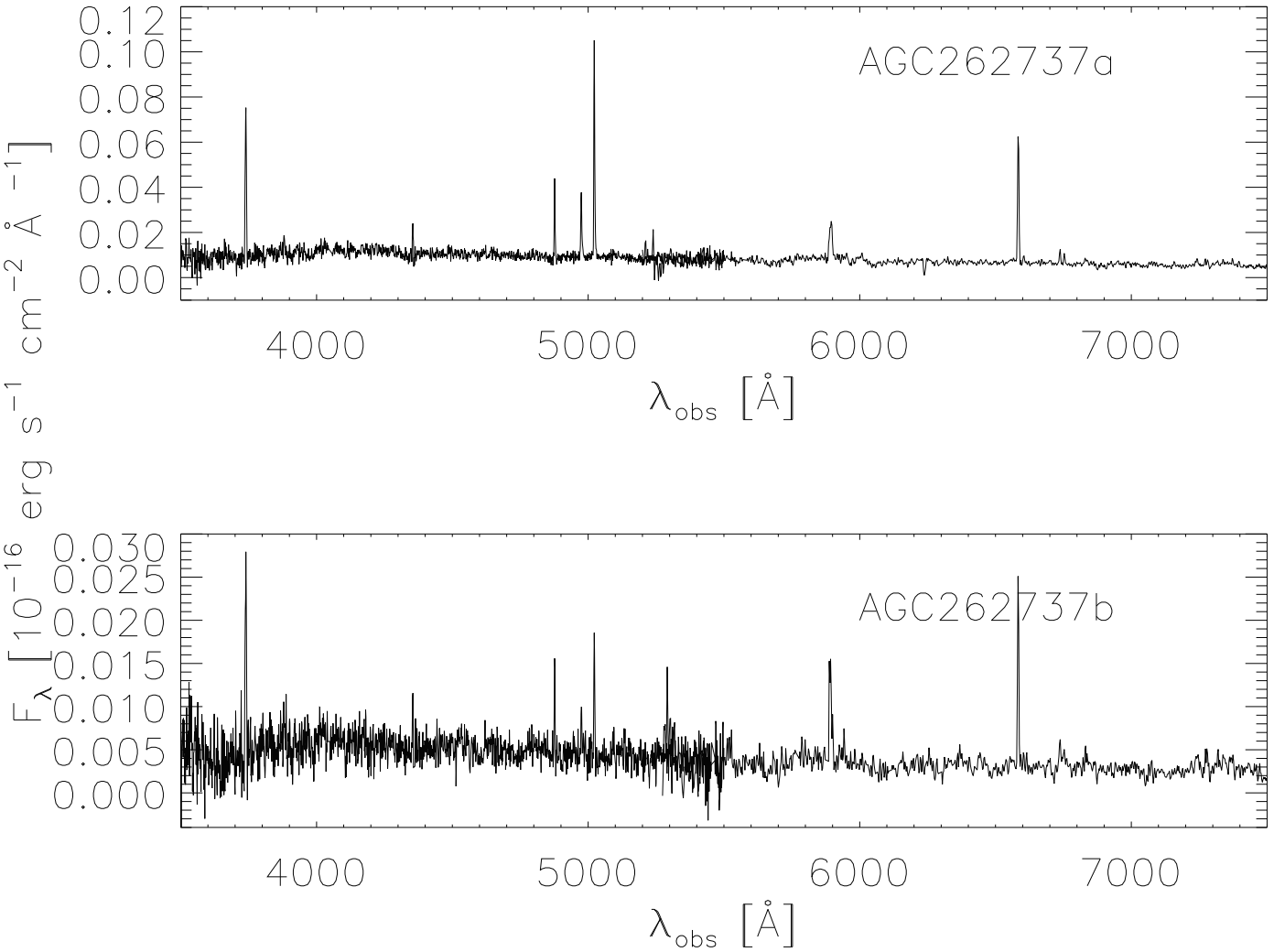
AGC262737a
AGC262737b
F_λ [10^{-16} erg s^{-1} cm^{-2} Å^{-1}]
λ_{obs} [Å]
0.12
0.10
0.08
0.06
0.04
0.02
0.00
0.030
0.025
0.020
0.015
0.010
0.005
0.000
4000
5000
6000
7000

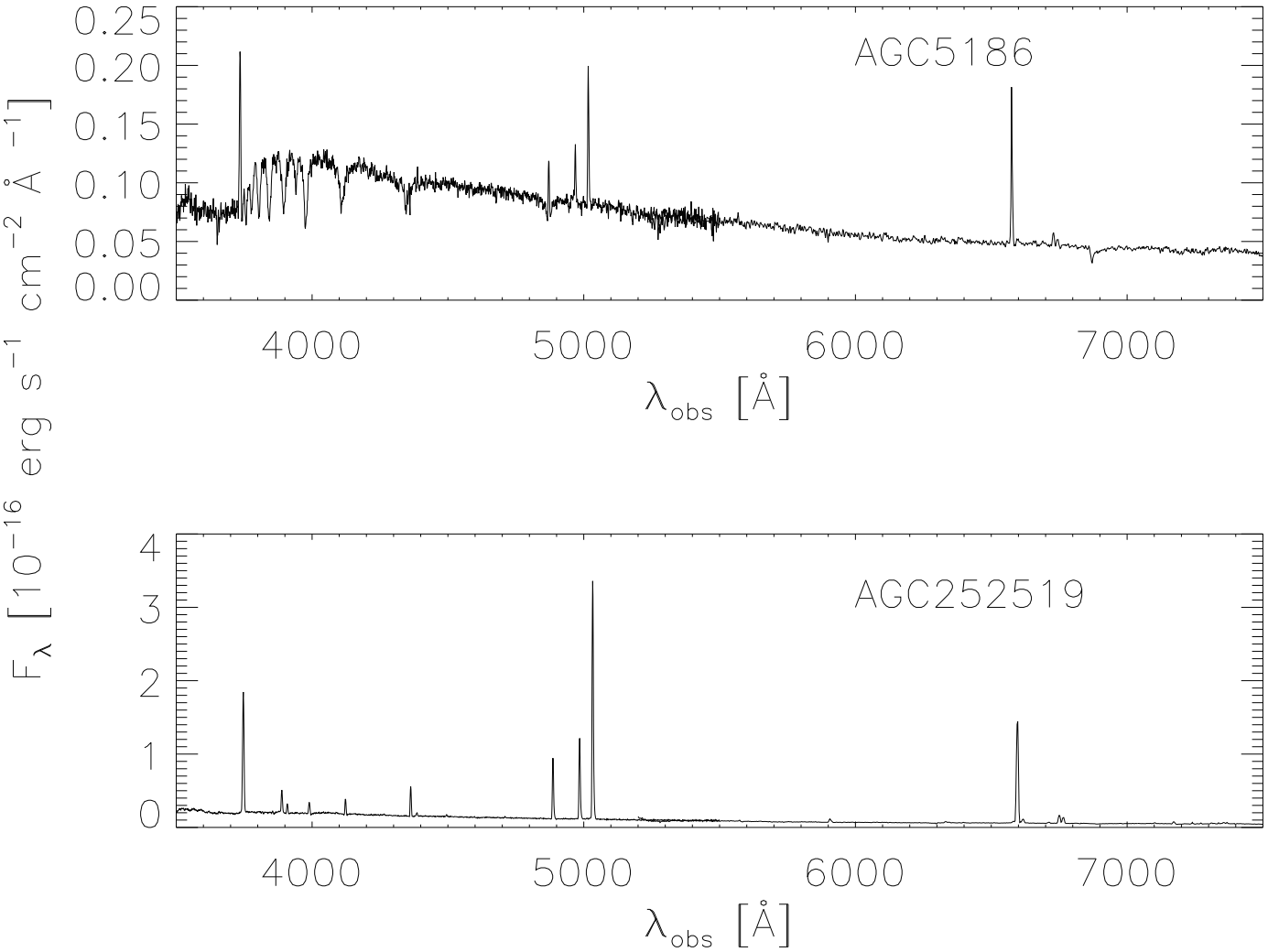
AGC5186
AGC252519
F_λ [10^{-16} erg s^{-1} cm^{-2} Å $^{-1}$]
λ_{obs} [Å]
0.25
0.20
0.15
0.10
0.05
0.00
4
3
2
1
0
4000
5000
6000
7000

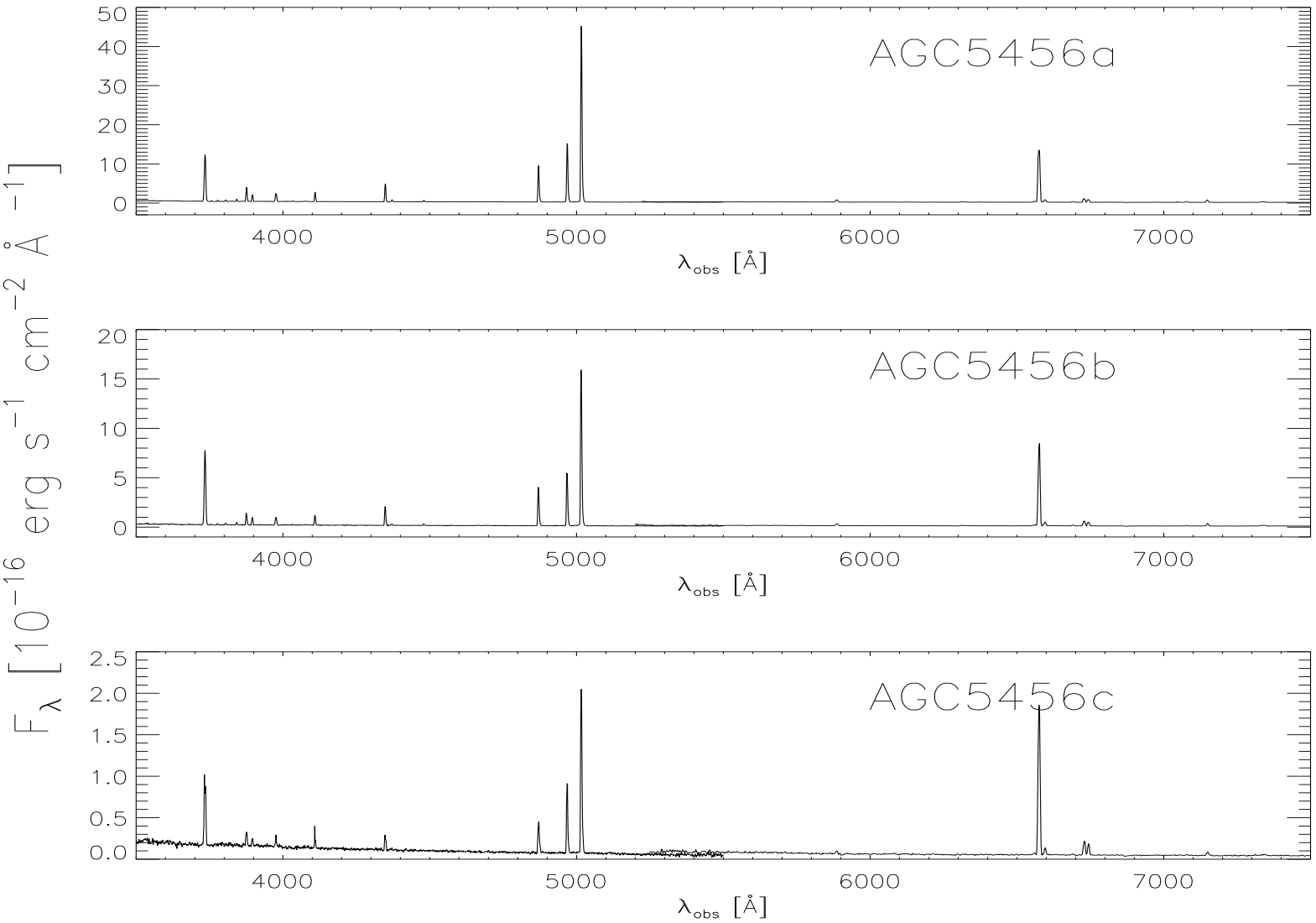
AGC5456a
AGC5456b
AGC5456c
F_λ [10^{-16} erg s^{-1} cm^{-2} Å $^{-1}$]
λ_{obs} [Å]
4000
5000
6000
7000

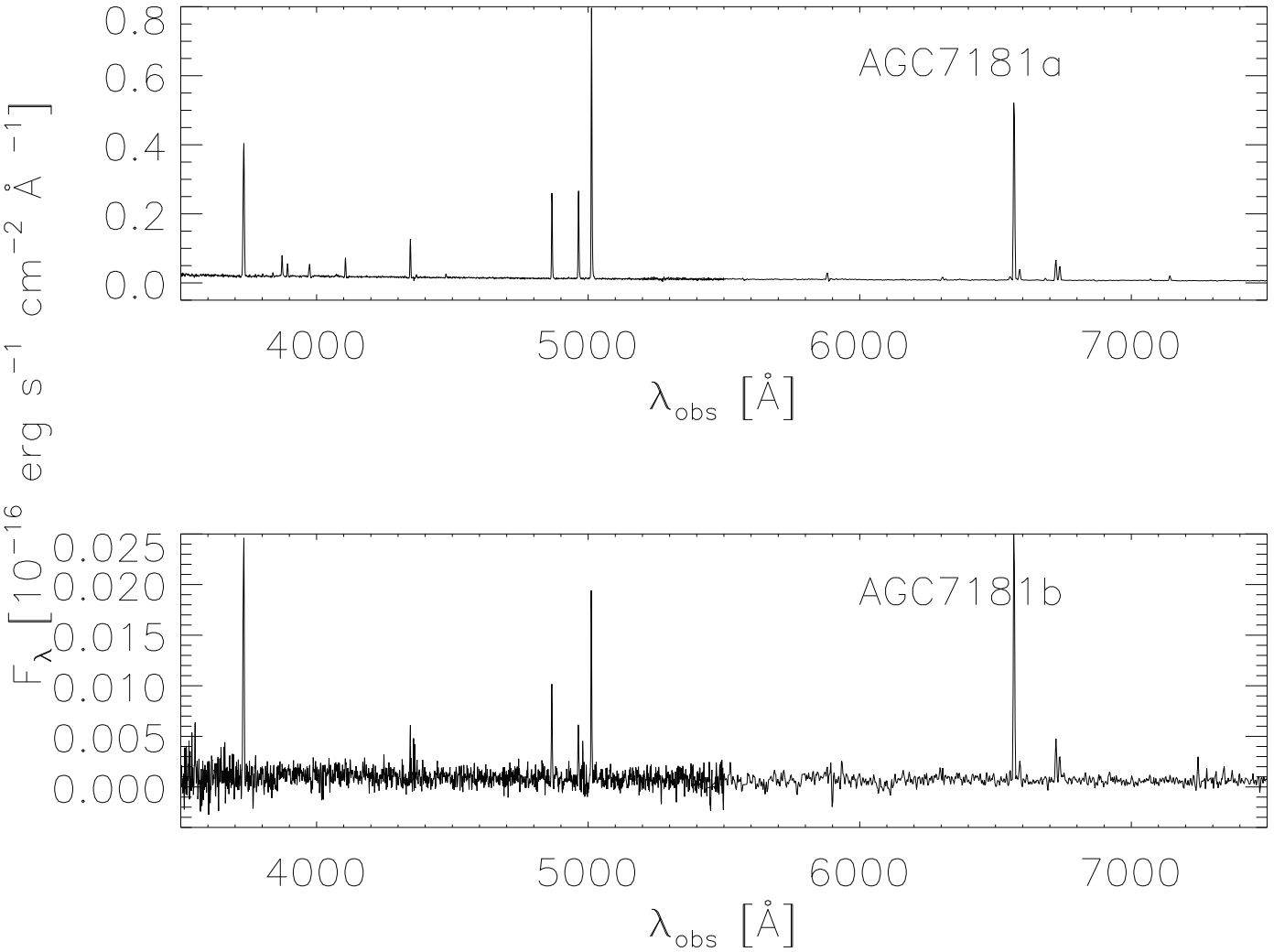
AGC7181a
AGC7181b
F_λ [10^{-16} erg s^{-1} cm^{-2} Å $^{-1}$]
λ_{obs} [Å]
0.0
0.2
0.4
0.6
0.8
0.000
0.005
0.010
0.015
0.020
0.025
4000
5000
6000
7000

BIBLIOGRAPHY

M. Aaronson and J. Mould. Infrared photometry and the comparative stellar content of dwarf spheroidals in the galactic halo. *ApJ*, 290:191–210, March 1985. doi: 10.1086/162973.

K. Abazajian, J. K. Adelman-McCarthy, M. A. Agüeros, S. S. Allam, K. S. J. Anderson, S. F. Anderson, J. Annis, N. A. Bahcall, I. K. Baldry, S. Bastian, A. Berlind, M. Bernardi, M. R. Blanton, J. J. Bochanski, Jr., W. N. Boroski, H. J. Brewington, J. W. Briggs, J. Brinkmann, R. J. Brunner, T. Budavári, L. N. Carey, F. J. Castander, A. J. Connolly, K. R. Covey, I. Csabai, J. J. Dalcanton, M. Doi, F. Dong, D. J. Eisenstein, M. L. Evans, X. Fan, D. P. Finkbeiner, S. D. Friedman, J. A. Frieman, M. Fukugita, B. Gillespie, K. Glazebrook, J. Gray, E. K. Grebel, J. E. Gunn, V. K. Gurbani, P. B. Hall, M. Hamabe, D. Harbeck, F. H. Harris, H. C. Harris, M. Harvanek, S. L. Hawley, J. Hayes, T. M. Heckman, J. S. Hendry, G. S. Hennessy, R. B. Hindsley, C. J. Hogan, D. W. Hogg, D. J. Holmgren, J. A. Holtzman, S.-i. Ichikawa, T. Ichikawa, Ž. Ivezić, S. Jester, D. E. Johnston, A. M. Jorgensen, M. Jurić, S. M. Kent, S. J. Kleinman, G. R. Knapp, A. Y. Kniazev, R. G. Kron, J. Krzesinski, D. Q. Lamb, H. Lampeitl, B. C. Lee, H. Lin, D. C. Long, J. Loveday, R. H. Lupton, E. Mannery, B. Margon, D. Martínez-Delgado, T. Matsubara, P. M. McGehee, T. A. McKay, A. Meiksin, B. Ménard, J. A. Munn, T. Nash, E. H. Neilsen, Jr., H. J. Newberg, P. R. Newman, R. C. Nichol, T. Nicinski, M. Nieto-Santisteban, A. Nitta, S. Okamura, W. O'Mullane, R. Owen, N. Padmanabhan, G. Pauls, J. Peoples, J. R. Pier, A. C. Pope, D. Pourbaix, T. R. Quinn, M. J. Raddick, G. T. Richards, M. W. Richmond, H.-W. Rix, C. M. Rockosi, D. J. Schlegel, D. P. Schneider, J. Schroeder, R. Scranton, M. Sekiguchi, E. Sheldon, K. Shimasaku, N. M. Silvestri, J. A. Smith, V. Smolčić, S. A. Snedden, A. Stebbins, C. Stoughton, M. A. Strauss,

M. SubbaRao, A. S. Szalay, I. Szapudi, P. Szkody, G. P. Szokoly, M. Tegmark, L. Teodoro, A. R. Thakar, C. Tremonti, D. L. Tucker, A. Uomoto, D. E. Vanden Berk, J. Vandenberg, M. S. Vogeley, W. Voges, N. P. Vogt, L. M. Walkowicz, S.-i. Wang, D. H. Weinberg, A. A. West, S. D. M. White, B. C. Wilhite, Y. Xu, B. Yanny, N. Yasuda, C.-W. Yip, D. R. Yocum, D. G. York, I. Zehavi, S. Zibetti, and D. B. Zucker. The Third Data Release of the Sloan Digital Sky Survey. *AJ*, 129:1755–1759, March 2005. doi: 10.1086/427544.

K. N. Abazajian, J. K. Adelman-McCarthy, M. A. Agüeros, S. S. Allam, C. Allende Prieto, D. An, K. S. J. Anderson, S. F. Anderson, J. Annis, N. A. Bahcall, C. A. L. Bailer-Jones, J. C. Barentine, B. A. Bassett, A. C. Becker, T. C. Beers, E. F. Bell, V. Belokurov, A. A. Berlind, E. F. Berman, M. Bernardi, S. J. Bickerton, D. Bizyaev, J. P. Blakeslee, M. R. Blanton, J. J. Bochanski, W. N. Boroski, H. J. Brewington, J. Brinchmann, J. Brinkmann, R. J. Brunner, T. Budavári, L. N. Carey, S. Carliles, M. A. Carr, F. J. Castander, D. Cinabro, A. J. Connolly, I. Csabai, C. E. Cunha, P. C. Czarapata, J. R. A. Davenport, E. de Haas, B. Dilday, M. Doi, D. J. Eisenstein, M. L. Evans, N. W. Evans, X. Fan, S. D. Friedman, J. A. Frieman, M. Fukugita, B. T. Gänsicke, E. Gates, B. Gillespie, G. Gilmore, B. Gonzalez, C. F. Gonzalez, E. K. Grebel, J. E. Gunn, Z. Györy, P. B. Hall, P. Harding, F. H. Harris, M. Harvanek, S. L. Hawley, J. J. E. Hayes, T. M. Heckman, J. S. Hendry, G. S. Hennessy, R. B. Hindsley, J. Hoblitt, C. J. Hogan, D. W. Hogg, J. A. Holtzman, J. B. Hyde, S.-i. Ichikawa, T. Ichikawa, M. Im, Ž. Ivezić, S. Jester, L. Jiang, J. A. Johnson, A. M. Jorgensen, M. Jurić, S. M. Kent, R. Kessler, S. J. Kleinman, G. R. Knapp, K. Konishi, R. G. Kron, J. Krzesinski, N. Kuropatkin, H. Lampeitl, S. Lebedeva, M. G. Lee, Y. S. Lee, R. F. Leger, S. Lépine, N. Li, M. Lima, H. Lin, D. C. Long, C. P. Loomis, J. Loveday, R. H. Lupton, E. Magnier, O. Malanushenko, V. Malanushenko, R. Mandelbaum,

B. Margon, J. P. Marriner, D. Martínez-Delgado, T. Matsubara, P. M. McGehee, T. A. McKay, A. Meiksin, H. L. Morrison, F. Mullally, J. A. Munn, T. Murphy, T. Nash, A. Nebot, E. H. Neilsen, H. J. Newberg, P. R. Newman, R. C. Nichol, T. Nicinski, M. Nieto-Santisteban, A. Nitta, S. Okamura, D. J. Oravetz, J. P. Ostriker, R. Owen, N. Padmanabhan, K. Pan, C. Park, G. Pauls, J. Peoples, W. J. Percival, J. R. Pier, A. C. Pope, D. Pourbaix, P. A. Price, N. Purger, T. Quinn, M. J. Raddick, P. R. Fiorentin, G. T. Richards, M. W. Richmond, A. G. Riess, H.-W. Rix, C. M. Rockosi, M. Sako, D. J. Schlegel, D. P. Schneider, R.-D. Scholz, M. R. Schreiber, A. D. Schwope, U. Seljak, B. Sesar, E. Sheldon, K. Shimasaku, V. C. Sibley, A. E. Simmons, T. Sivarani, J. A. Smith, M. C. Smith, V. Smolčić, S. A. Snedden, A. Stebbins, M. Steinmetz, C. Stoughton, M. A. Strauss, M. Subba Rao, Y. Suto, A. S. Szalay, I. Szapudi, P. Szkody, M. Tanaka, M. Tegmark, L. F. A. Teodoro, A. R. Thakar, C. A. Tremonti, D. L. Tucker, A. Uomoto, D. E. Vanden Berk, J. Vandenberg, S. Vidrih, M. S. Vogeley, W. Voges, N. P. Vogt, Y. Wadadekar, S. Watters, D. H. Weinberg, A. A. West, S. D. M. White, B. C. Wilhite, A. C. Wonders, B. Yanny, D. R. Yocum, D. G. York, I. Zehavi, S. Zibetti, and D. B. Zucker. The Seventh Data Release of the Sloan Digital Sky Survey. *ApJS*, 182:543–558, June 2009. doi: 10.1088/0067-0049/182/2/543.

J. K. Adelman-McCarthy, M. A. Agüeros, S. S. Allam, C. Allende Prieto, K. S. J. Anderson, S. F. Anderson, J. Annis, N. A. Bahcall, C. A. L. Bailer-Jones, I. K. Baldry, J. C. Barentine, B. A. Bassett, A. C. Becker, T. C. Beers, E. F. Bell, A. A. Berlind, M. Bernardi, M. R. Blanton, J. J. Bochanski, W. N. Boroski, J. Brinchmann, J. Brinkmann, R. J. Brunner, T. Budavári, S. Carliles, M. A. Carr, F. J. Castander, D. Cinabro, R. J. Cool, K. R. Covey, I. Csabai, C. E. Cunha, J. R. A. Davenport, B. Dilday, M. Doi, D. J. Eisenstein, M. L. Evans, X. Fan,

D. P. Finkbeiner, S. D. Friedman, J. A. Frieman, M. Fukugita, B. T. Gänsicke, E. Gates, B. Gillespie, K. Glazebrook, J. Gray, E. K. Grebel, J. E. Gunn, V. K. Gurbani, P. B. Hall, P. Harding, M. Harvanek, S. L. Hawley, J. Hayes, T. M. Heckman, J. S. Hendry, R. B. Hindsley, C. M. Hirata, C. J. Hogan, D. W. Hogg, J. B. Hyde, S.-i. Ichikawa, Ž. Ivezić, S. Jester, J. A. Johnson, A. M. Jorgensen, M. Jurić, S. M. Kent, R. Kessler, S. J. Kleinman, G. R. Knapp, R. G. Kron, J. Krzesinski, N. Kuropatkin, D. Q. Lamb, H. Lampeitl, S. Lebedeva, Y. S. Lee, R. F. Leger, S. Lépine, M. Lima, H. Lin, D. C. Long, C. P. Loomis, J. Loveday, R. H. Lupton, O. Malanushenko, V. Malanushenko, R. Mandelbaum, B. Margon, J. P. Marriner, D. Martínez-Delgado, T. Matsubara, P. M. McGehee, T. A. McKay, A. Meiksin, H. L. Morrison, J. A. Munn, R. Nakajima, E. H. Neilsen, Jr., H. J. Newberg, R. C. Nichol, T. Nicinski, M. Nieto-Santisteban, A. Nitta, S. Okamura, R. Owen, H. Oyaizu, N. Padmanabhan, K. Pan, C. Park, J. J. Peoples, J. R. Pier, A. C. Pope, N. Purger, M. J. Raddick, P. Re Fiorentin, G. T. Richards, M. W. Richmond, A. G. Riess, H.-W. Rix, C. M. Rockosi, M. Sako, D. J. Schlegel, D. P. Schneider, M. R. Schreiber, A. D. Schwope, U. Seljak, B. Sesar, E. Sheldon, K. Shimasaku, T. Sivarani, J. A. Smith, S. A. Snedden, M. Steinmetz, M. A. Strauss, M. SubbaRao, Y. Suto, A. S. Szalay, I. Szapudi, P. Szkody, M. Tegmark, A. R. Thakar, C. A. Tremonti, D. L. Tucker, A. Uomoto, D. E. Vanden Berk, J. Vandenberg, S. Vidrih, M. S. Vogeley, W. Voges, N. P. Vogt, Y. Wadadekar, D. H. Weinberg, A. A. West, S. D. M. White, B. C. Wilhite, B. Yanny, D. R. Yocum, D. G. York, I. Zehavi, and D. B. Zucker. The Sixth Data Release of the Sloan Digital Sky Survey. *ApJS*, 175:297–313, April 2008. doi: 10.1086/524984.

V. L. Afanasiev and O. K. Sil'chenko. The Leo Triplet: Common origin or late encounter? *A&A*, 429:825–836, January 2005. doi: 10.1051/0004-6361:20040311.

M. Asplund, N. Grevesse, A. J. Sauval, C. Allende Prieto, and D. Kiselman. Line formation in solar granulation. IV. [O I], O I and OH lines and the photospheric O abundance. *A&A*, 435:339–340, May 2005. doi: 10.1051/0004-6361:20034328e.

I. K. Baldry, K. Glazebrook, J. Brinkmann, Ž. Ivezić, R. H. Lupton, R. C. Nichol, and A. S. Szalay. Quantifying the Bimodal Color-Magnitude Distribution of Galaxies. *ApJ*, 600:681–694, January 2004. doi: 10.1086/380092.

I. K. Baldry, K. Glazebrook, T. Budavári, D. J. Eisenstein, J. Annis, N. A. Bahcall, M. R. Blanton, J. Brinkmann, I. Csabai, T. M. Heckman, H. Lin, J. Loveday, R. C. Nichol, and D. P. Schneider. The Sloan Digital Sky Survey u-band Galaxy Survey: luminosity functions and evolution. *MNRAS*, 358:441–456, April 2005. doi: 10.1111/j.1365-2966.2005.08799.x.

A. Baldwin, M. M. Phillips, and R. Terlevich. Erratum - Classification Parameters for the Emission-Line Spectra of Extragalactic Objects. *PASP*, 93:817–+, 1981. doi: 10.1086/130930.

J. E. Barnes and L. Hernquist. Formation of dwarf galaxies in tidal tails. *Nature*, 360:715–717, December 1992. doi: 10.1038/360715a0.

A. Begum and J. N. Chengalur. Kinematics of the faintest gas-rich galaxy in the Local Group: DDO210. *A&A*, 413:525–534, January 2004. doi: 10.1051/0004-6361:20031549.

A. Begum, J. N. Chengalur, I. D. Karachentsev, S. S. Kaisin, and M. E. Sharina. Gas distribution, kinematics and star formation in faint dwarf galaxies. *MNRAS*, 365:1220–1234, February 2006. doi: 10.1111/j.1365-2966.2005.09817.x.

E. F. Bell, D. H. McIntosh, N. Katz, and M. D. Weinberg. The Optical and Near-Infrared Properties of Galaxies. I. Luminosity and Stellar Mass Functions. *ApJS*, 149:289–312, December 2003. doi: 10.1086/378847.

V. Belokurov, D. B. Zucker, N. W. Evans, J. T. Kleyna, S. Koposov, S. T. Hodgkin, M. J. Irwin, G. Gilmore, M. I. Wilkinson, M. Fellhauer, D. M. Bramich, P. C. Hewett, S. Vidrih, J. T. A. De Jong, J. A. Smith, H.-W. Rix, E. F. Bell, R. F. G. Wyse, H. J. Newberg, P. A. Mayeur, B. Yanny, C. M. Rockosi, O. Y. Gnedin, D. P. Schneider, T. C. Beers, J. C. Barentine, H. Brewington, J. Brinkmann, M. Harvanek, S. J. Kleinman, J. Krzesinski, D. Long, A. Nitta, and S. A. Snedden. Cats and Dogs, Hair and a Hero: A Quintet of New Milky Way Companions. *ApJ*, 654:897–906, January 2007. doi: 10.1086/509718.

E. Bertin and S. Arnouts. SExtractor: Software for source extraction. *A&AS*, 117: 393–404, June 1996.

M. R. Blanton and S. Roweis. K-Corrections and Filter Transformations in the Ultraviolet, Optical, and Near-Infrared. *AJ*, 133:734–754, February 2007. doi: 10.1086/510127.

M. R. Blanton, J. Dalcanton, D. Eisenstein, J. Loveday, M. A. Strauss, M. SubbaRao, D. H. Weinberg, J. E. Anderson, Jr., J. Annis, N. A. Bahcall, M. Bernardi, J. Brinkmann, R. J. Brunner, S. Burles, L. Carey, F. J. Castander, A. J. Connolly, I. Csabai, M. Doi, D. Finkbeiner, S. Friedman, J. A. Frieman, M. Fukugita, J. E. Gunn, G. S. Hennessy, R. B. Hindsley, D. W. Hogg, T. Ichikawa, Ž. Ivezić, S. Kent, G. R. Knapp, D. Q. Lamb, R. F. Leger, D. C. Long, R. H. Lupton, T. A. McKay, A. Meiksin, A. Merelli, J. A. Munn, V. Narayanan, M. Newcomb, R. C. Nichol, S. Okamura, R. Owen, J. R. Pier, A. Pope, M. Postman, T. Quinn, C. M. Rockosi, D. J. Schlegel, D. P. Schneider, K. Shimasaku, W. A. Siegmund,

S. Smee, Y. Snir, C. Stoughton, C. Stubbs, A. S. Szalay, G. P. Szokoly, A. R. Thakar, C. Tremonti, D. L. Tucker, A. Uomoto, D. Vanden Berk, M. S. Vogeley, P. Waddell, B. Yanny, N. Yasuda, and D. G. York. The Luminosity Function of Galaxies in SDSS Commissioning Data. *AJ*, 121:2358–2380, May 2001. doi: 10.1086/320405.

M. R. Blanton, J. Brinkmann, I. Csabai, M. Doi, D. Eisenstein, M. Fukugita, J. E. Gunn, D. W. Hogg, and D. J. Schlegel. Estimating Fixed-Frame Galaxy Magnitudes in the Sloan Digital Sky Survey. *AJ*, 125:2348–2360, May 2003. doi: 10.1086/342935.

M. R. Blanton, R. H. Lupton, D. J. Schlegel, M. A. Strauss, J. Brinkmann, M. Fukugita, and J. Loveday. The Properties and Luminosity Function of Extremely Low Luminosity Galaxies. *ApJ*, 631:208–230, September 2005a. doi: 10.1086/431416.

M. R. Blanton, D. J. Schlegel, M. A. Strauss, J. Brinkmann, D. Finkbeiner, M. Fukugita, J. E. Gunn, D. W. Hogg, Ž. Ivezić, G. R. Knapp, R. H. Lupton, J. A. Munn, D. P. Schneider, M. Tegmark, and I. Zehavi. New York University Value-Added Galaxy Catalog: A Galaxy Catalog Based on New Public Surveys. *AJ*, 129:2562–2578, June 2005b. doi: 10.1086/429803.

G. R. Blumenthal, S. M. Faber, J. R. Primack, and M. J. Rees. Formation of galaxies and large-scale structure with cold dark matter. *Nature*, 311:517–525, October 1984. doi: 10.1038/311517a0.

F. Bournaud and P.-A. Duc. From tidal dwarf galaxies to satellite galaxies. *A&A*, 456:481–492, September 2006. doi: 10.1051/0004-6361:20065248.

G. Bruzual A. and S. Charlot. Spectral evolution of stellar populations using isochrone synthesis. *ApJ*, 405:538–553, March 1993. doi: 10.1086/172385.

P. Buyle, D. Michielsen, S. de Rijcke, J. Ott, and H. Dejonghe. The CO content of the Local Group dwarf irregular galaxies IC5152, UGCA438 and the Phoenix dwarf. *MNRAS*, 373:793–798, December 2006. doi: 10.1111/j.1365-2966.2006.11071.x.

K. Chiboucas, I. D. Karachentsev, and R. B. Tully. Discovery of New Dwarf Galaxies in the M81 Group. *AJ*, 137:3009–3037, February 2009. doi: 10.1088/0004-6256/137/2/3009.

A. Chung, J. H. van Gorkom, J. D. P. Kenney, and B. Vollmer. Virgo Galaxies with Long One-sided H I Tails. *ApJL*, 659:L115–L119, April 2007. doi: 10.1086/518034.

G. S. Da Costa, H. Jerjen, and A. Bouchard. ESO540-032: a Transition-Type Dwarf in the Sculptor Group. *ArXiv e-prints*, October 2007.

J. J. Dalcanton. The Metallicity of Galaxy Disks: Infall versus Outflow. *ApJ*, 658: 941–959, April 2007. doi: 10.1086/508913.

G. de Vaucouleurs. Astrofizika. *Astrofizika*, 3:571–+, 1967.

G. de Vaucouleurs. Supergalactic studies. III - The supergalactic distribution of nearby groups of galaxies. IV - Systematic orientation of galaxy clouds relative to the supergalactic plane. *ApJ*, 202:610–618, December 1975. doi: 10.1086/154014.

A. Dekel and J. Silk. The origin of dwarf galaxies, cold dark matter, and biased galaxy formation. *ApJ*, 303:39–55, April 1986. doi: 10.1086/164050.

K. E. Dellenbusch, J. S. Gallagher, III, and P. M. Knezek. H II Region Oxygen Abundances in Starbursting Transition Dwarf Galaxies. *ApJL*, 655:L29–L32, January 2007. doi: 10.1086/511678.

J. Diemand, M. Kuhlen, and P. Madau. Dark Matter Substructure and Gamma-Ray Annihilation in the Milky Way Halo. *ApJ*, 657:262–270, March 2007. doi: 10.1086/510736.

P.-A. Duc and I. F. Mirabel. Young tidal dwarf galaxies around the gas-rich disturbed lenticular NGC 5291. *A&A*, 333:813–826, May 1998.

P.-A. Duc, F. Bournaud, and F. Masset. A top-down scenario for the formation of massive Tidal Dwarf Galaxies. *A&A*, 427:803–814, December 2004. doi: 10.1051/0004-6361:20041410.

P.-A. Duc, J. Braine, U. Lisenfeld, E. Brinks, and M. Boquien. VCC 2062: an old tidal dwarf galaxy in the Virgo cluster? *A&A*, 475:187–197, November 2007. doi: 10.1051/0004-6361:20078335.

M. G. Edmunds and B. E. J. Pagel. On the composition of H II regions in southern galaxies. III - NGC 2997 and 7793. *MNRAS*, 211:507–519, December 1984.

G. Efstathiou. Suppressing the formation of dwarf galaxies via photoionization. *MNRAS*, 256:43P–47P, May 1992.

B. G. Elmegreen. Star Formation at Compressed Interfaces in Turbulent Self-gravitating Clouds. *ApJL*, 419:L29+, December 1993. doi: 10.1086/187129.

H. C. Ferguson and A. Sandage. Population studies in groups and clusters of galaxies. III - A catalog of galaxies in five nearby groups. *AJ*, 100:1–31, July 1990. doi: 10.1086/115486.

H. C. Ferguson and A. Sandage. Population studies in groups and clusters of galaxies. IV - Comparison of the luminosity functions and morphological-type distributions in seven nearby groups. *AJ*, 101:765–782, March 1991. doi: 10.1086/115721.

K. Flint, M. Bolte, and C. Mendes de Oliveira. The Missing Intermediate Luminosity Galaxies in the Leo I Group. *APSS*, 285:191–195, 2003. doi: 10.1023/A:1024646817568.

W. L. Freedman, B. F. Madore, B. K. Gibson, L. Ferrarese, D. D. Kelson, S. Sakai, J. R. Mould, R. C. Kennicutt, Jr., H. C. Ford, J. A. Graham, J. P. Huchra, S. M. G. Hughes, G. D. Illingworth, L. M. Macri, and P. B. Stetson. Final Results from the Hubble Space Telescope Key Project to Measure the Hubble Constant. *ApJ*, 553:47–72, May 2001. doi: 10.1086/320638.

M. Fukugita, T. Ichikawa, J. E. Gunn, M. Doi, K. Shimasaku, and D. P. Schneider. The Sloan Digital Sky Survey Photometric System. *AJ*, 111:1748–+, April 1996. doi: 10.1086/117915.

G. Gavazzi and A. Boselli. A UBVJHK Photometric Catalogue of 1022 Galaxies in nearby clusters (Special Issue). *Astrophysical Letters Communications*, 35:1–+, 1996.

M. Geha, M. R. Blanton, M. Masjedi, and A. A. West. The Baryon Content of Extremely Low Mass Dwarf Galaxies. *ApJ*, 653:240–254, December 2006. doi: 10.1086/508604.

M. J. Geller and J. P. Huchra. Groups of galaxies. III - The CfA survey. *ApJS*, 52: 61–87, June 1983. doi: 10.1086/190859.

R. Giovanelli and M. P. Haynes. A protogalaxy in the local supercluster. *ApJL*, 346:L5–L7, November 1989. doi: 10.1086/185565.

R. Giovanelli, M. P. Haynes, J. J. Salzer, G. Wegner, L. N. da Costa, and W. Freudling. Dependence on Luminosity of Photometric Properties of Disk Galaxies: Surface Brightness, Size, and Internal Extinction. *AJ*, 110:1059–+, September 1995. doi: 10.1086/117586.

R. Giovanelli, M. P. Haynes, B. R. Kent, P. Perillat, B. Catinella, G. L. Hoffman, E. Momjian, J. L. Rosenberg, A. Saintonge, K. Spekkens, S. Stierwalt, N. Brosch, K. L. Masters, C. M. Springob, I. D. Karachentsev, V. E. Karachentseva, R. A. Koopmann, E. Muller, W. van Driel, and L. van Zee. The Arecibo Legacy Fast ALFA Survey. II. Results of Precursor Observations. *AJ*, 130:2613–2624, December 2005a. doi: 10.1086/497432.

R. Giovanelli, M. P. Haynes, B. R. Kent, P. Perillat, A. Saintonge, N. Brosch, B. Catinella, G. L. Hoffman, S. Stierwalt, K. Spekkens, M. S. Lerner, K. L. Masters, E. Momjian, J. L. Rosenberg, C. M. Springob, A. Boselli, V. Charmandaris, J. K. Darling, J. Davies, D. G. Lambas, G. Gavazzi, C. Giovanardi, E. Hardy, L. K. Hunt, A. Iovino, I. D. Karachentsev, V. E. Karachentseva, R. A. Koopmann, C. Marinoni, R. Minchin, E. Muller, M. Putman, C. Pantoja, J. J. Salzer, M. Scodeggio, E. Skillman, J. M. Solanes, C. Valotto, W. van Driel, and L. van Zee. The Arecibo Legacy Fast ALFA Survey. I. Science Goals, Survey Design, and Strategy. *AJ*, 130:2598–2612, December 2005b. doi: 10.1086/497431.

R. Giovanelli, M. P. Haynes, B. R. Kent, A. Saintonge, S. Stierwalt, A. Altaf, T. Balonek, N. Brosch, S. Brown, B. Catinella, A. Furniss, J. Goldstein, G. L. Hoffman, R. A. Koopmann, D. A. Kornreich, B. Mahmood, A. M. Martin, K. L. Masters, A. Mitschang, E. Momjian, P. H. Nair, J. L. Rosenberg, and B. Walsh.

The Arecibo Legacy Fast ALFA Survey. III. H I Source Catalog of the Northern Virgo Cluster Region. *AJ*, 133:2569–2583, June 2007. doi: 10.1086/516635.

G. Giuricin, C. Marinoni, L. Ceriani, and A. Pisani. Nearby Optical Galaxies: Selection of the Sample and Identification of Groups. *ApJ*, 543:178–194, November 2000. doi: 10.1086/317070.

N. Y. Gnedin. Effect of Reionization on Structure Formation in the Universe. *ApJ*, 542:535–541, October 2000. doi: 10.1086/317042.

E. K. Grebel. Stellar Populations in the Local Group of Galaxies. In J. Mikolajewska and A. Olech, editors, *Stellar Astrophysics with the World's Largest Telescopes*, volume 752 of *American Institute of Physics Conference Series*, pages 161–174, March 2005. doi: 10.1063/1.1893349.

E. K. Grebel and J. S. Gallagher, III. The Impact of Reionization on the Stellar Populations of Nearby Dwarf Galaxies. *ApJL*, 610:L89–L92, August 2004. doi: 10.1086/423339.

E. K. Grebel, J. S. Gallagher, III, and D. Harbeck. The Progenitors of Dwarf Spheroidal Galaxies. *AJ*, 125:1926–1939, April 2003a. doi: 10.1086/368363.

E. K. Grebel, J. S. Gallagher, III, and D. Harbeck. The Progenitors of Dwarf Spheroidal Galaxies. *AJ*, 125:1926–1939, April 2003b. doi: 10.1086/368363.

M. Grossi, S. di Serego Alighieri, C. Giovanardi, G. Gavazzi, R. Giovanelli, M. P. Haynes, B. R. Kent, S. Pellegrini, S. Stierwalt, and G. Trinchieri. The Hi content of early-type galaxies from the ALFALFA survey. II. The case of low density environments. *A&A*, 498:407–417, May 2009. doi: 10.1051/0004-6361/200810823.

M. P. Haynes, R. Giovanelli, and M. S. Roberts. A detailed examination of the neutral hydrogen distribution in the Leo triplet NGC 3623, 3627, and 3628. *ApJ*, 229:83–90, April 1979. doi: 10.1086/156932.

M. P. Haynes, R. Giovanelli, J. J. Salzer, G. Wegner, W. Freudling, L. N. da Costa, T. Herter, and N. P. Vogt. The I-Band Tully-Fisher Relation for SC Galaxies: Optical Imaging Data. *AJ*, 117:1668–1687, April 1999. doi: 10.1086/300817.

M. P. Haynes, R. Giovanelli, and B. R. Kent. NGC 4254: An Act of Harassment Uncovered by the Arecibo Legacy Fast ALFA Survey. *ApJL*, 665:L19–L22, August 2007. doi: 10.1086/521188.

P. A. Henning, L. Staveley-Smith, R. D. Ekers, A. J. Green, R. F. Haynes, S. Juraszek, M. J. Kesteven, B. Koribalski, R. C. Kraan-Korteweg, R. M. Price, E. M. Sadler, and A. Schr"oder. H I-bright Galaxies in the Southern Zone of Avoidance. *AJ*, 119:2686–2698, June 2000. doi: 10.1086/301374.

J. E. Hibbard and J. C. Mihos. Dynamical Modeling of NGC 7252 and the Return of Tidal Material. *AJ*, 110:140–+, July 1995. doi: 10.1086/117502.

J. E. Hibbard, J. M. van der Hulst, J. E. Barnes, and R. M. Rich. High-Resolution H I Mapping of NGC 4038/39 ("The Antennae") and Its Tidal Dwarf Galaxy Candidates. *AJ*, 122:2969–2992, December 2001. doi: 10.1086/324102.

S. J. U. Higdon and J. L. Higdon. Spitzer Observations of Tidal Dwarf Galaxies. In J. Davies and M. Disney, editors, *IAU Symposium*, volume 244 of *IAU Symposium*, pages 356–357, May 2008. doi: 10.1017/S1743921307014251.

G. L. Hoffman, J. Glosson, G. Helou, E. E. Salpeter, and A. Sandage. H I detection survey of a complete magnitude-limited sample of dwarf irregular

galaxies in the Virgo Cluster area. *ApJS*, 63:247–264, February 1987. doi: 10.1086/191164.

D. W. Hogg, I. K. Baldry, M. R. Blanton, and D. J. Eisenstein. The K correction. *ArXiv Astrophysics e-prints*, October 2002.

I. D. Howarth. LMC and galactic extinction. *MNRAS*, 203:301–304, April 1983.

J. P. Huchra and M. J. Geller. Groups of galaxies. I - Nearby groups. *ApJ*, 257: 423–437, June 1982. doi: 10.1086/160000.

D. H. Hughes, P. N. Appleton, and J. M. Schombert. Far-infrared counterpart to the optical and H I plume in the Leo triplet of galaxies - NGC 3623, NGC 3627, and NGC 3628. *ApJ*, 370:176–183, March 1991. doi: 10.1086/169802.

D. A. Hunter, S. D. Hunsberger, and E. W. Roye. Identifying Old Tidal Dwarf Irregulars. *ApJ*, 542:137–142, October 2000. doi: 10.1086/309542.

M. J. Irwin, V. Belokurov, N. W. Evans, E. V. Ryan-Weber, J. T. A. de Jong, S. Koposov, D. B. Zucker, S. T. Hodgkin, G. Gilmore, P. Prema, L. Hebb, A. Begum, M. Fellhauer, P. C. Hewett, R. C. Kennicutt, Jr., M. I. Wilkinson, D. M. Bramich, S. Vidrih, H.-W. Rix, T. C. Beers, J. C. Barentine, H. Brewington, M. Harvanek, J. Krzesinski, D. Long, A. Nitta, and S. A. Snedden. Discovery of an Unusual Dwarf Galaxy in the Outskirts of the Milky Way. *ApJL*, 656:L13–L16, February 2007. doi: 10.1086/512183.

I. D. Karachentsev and V. E. Karachentseva. New Dwarf Galaxy Candidates in the Leo-I Group. *Astronomy Reports*, 48:267–274, April 2004. doi: 10.1134/1.1704672.

I. D. Karachentsev, M. E. Sharina, A. E. Dolphin, E. K. Grebel, D. Geisler, P. Guhathakurta, P. W. Hodge, V. E. Karachentseva, A. Sarajedini, and

P. Seitzer. Galaxy flow in the Canes Venatici I cloud. *A&A*, 398:467–477, February 2003. doi: 10.1051/0004-6361:20021598.

I. D. Karachentsev, V. E. Karachentseva, W. K. Huchtmeier, and D. I. Makarov. A Catalog of Neighboring Galaxies. *AJ*, 127:2031–2068, April 2004. doi: 10.1086/382905.

V. E. Karachentseva and I. D. Karachentsev. A list of new nearby dwarf galaxy candidates. *AAPS*, 127:409–419, February 1998. doi: 10.1051/aas:1998109.

G. Kauffmann, S. D. M. White, and B. Guiderdoni. The Formation and Evolution of Galaxies Within Merging Dark Matter Haloes. *MNRAS*, 264:201–+, September 1993.

G. Kauffmann, T. M. Heckman, S. D. M. White, S. Charlot, C. Tremonti, J. Brinchmann, G. Bruzual, E. W. Peng, M. Seibert, M. Bernardi, M. Blanton, J. Brinkmann, F. Castander, I. Csábai, M. Fukugita, Z. Ivezic, J. A. Munn, R. C. Nichol, N. Padmanabhan, A. R. Thakar, D. H. Weinberg, and D. York. Stellar masses and star formation histories for 1e5 galaxies from the Sloan Digital Sky Survey. *MNRAS*, 341:33–53, May 2003. doi: 10.1046/j.1365-8711.2003.06291.x.

R. C. Kennicutt, Jr. The Global Schmidt Law in Star-forming Galaxies. *ApJ*, 498: 541–+, May 1998. doi: 10.1086/305588.

B. R. Kent, R. Giovanelli, M. P. Haynes, A. Saintonge, S. Stierwalt, T. Balonek, N. Brosch, B. Catinella, R. A. Koopmann, E. Momjian, and K. Spekkens. Optically Unseen H I Detections toward the Virgo Cluster Detected in the Arecibo Legacy Fast ALFA Survey. *ApJL*, 665:L15–L18, August 2007. doi: 10.1086/521100.

B. R. Kent, R. Giovanelli, M. P. Haynes, A. M. Martin, A. Saintonge, S. Stierwalt, T. J. Balonek, N. Brosch, and R. A. Koopmann. The Arecibo Legacy Fast Alfa Survey. VI. Second HI Source Catalog of the Virgo Cluster Region. *AJ*, 136: 713–724, August 2008. doi: 10.1088/0004-6256/136/2/713.

E. J. Kibblewhite, M. G. M. Cawson, M. J. Disney, and S. Phillipps. An optical search for the intergalactic H I cloud in Leo. *MNRAS*, 213:111–115, March 1985.

A. Klypin, A. V. Kravtsov, O. Valenzuela, and F. Prada. Where Are the Missing Galactic Satellites? *ApJ*, 522:82–92, September 1999. doi: 10.1086/307643.

P. M. Knezek, K. R. Sembach, and J. S. Gallagher, III. Evolutionary Status of Dwarf "Transition" Galaxies. *ApJ*, 514:119–132, March 1999. doi: 10.1086/306921.

E. Komatsu, J. Dunkley, M. R. Nolta, C. L. Bennett, B. Gold, G. Hinshaw, N. Jarosik, D. Larson, M. Limon, L. Page, D. N. Spergel, M. Halpern, R. S. Hill, A. Kogut, S. S. Meyer, G. S. Tucker, J. L. Weiland, E. Wollack, and E. L. Wright. Five-Year Wilkinson Microwave Anisotropy Probe Observations: Cosmological Interpretation. *ApJS*, 180:330–376, February 2009. doi: 10.1088/0067-0049/180/2/330.

R. A. Koopmann, R. Giovanelli, M. P. Haynes, B. R. Kent, T. J. Balonek, N. Brosch, J. L. Higdon, J. J. Salzer, and O. Spector. A 500 kpc H I Extension of the Virgo Pair NGC 4532/DDO 137 Detected by the Arecibo Legacy Fast ALFA (ALFALFA) Survey. *ApJL*, 682:L85–L88, August 2008. doi: 10.1086/591124.

J. Köppen and M. G. Edmunds. Gas flows and the chemical evolution of galaxies

- III. Graphical analysis and secondary elements. *MNRAS*, 306:317–326, June 1999. doi: 10.1046/j.1365-8711.1999.02584.x.

J. Köppen, C. Weidner, and P. Kroupa. A possible origin of the mass-metallicity relation of galaxies. *MNRAS*, 375:673–684, February 2007. doi: 10.1111/j.1365-2966.2006.11328.x.

K. Kovac, T. A. Oosterloo, and J. M. van der Hulst. A blind HI survey in the Canes Venatici region. *ArXiv e-prints*, April 2009.

K. Kovač. *Searching for the lowest mass galaxies: an HI perspective*. PhD thesis, Kapteyn Institute, Groningen, Netherlands, 2007.

R. C. Kraan-Korteweg, W. van Driel, F. Briggs, B. Binggeli, and T. I. Mostefaoui. Nançay "blind" 21 CM line survey of the Canes Venatici group region. *A&AS*, 135:255–271, March 1999. doi: 10.1051/aas:1999175.

P. Kroupa, C. A. Tout, and G. Gilmore. The distribution of low-mass stars in the Galactic disc. *MNRAS*, 262:545–587, June 1993.

R. Kuzio de Naray, S. S. McGaugh, and W. J. G. de Blok. Oxygen abundances and chemical evolution in low surface brightness galaxies. *MNRAS*, 355:887–898, December 2004. doi: 10.1111/j.1365-2966.2004.08364.x.

H. Lee, M. L. McCall, and M. G. Richer. Uncovering Additional Clues to Galaxy Evolution. II. The Environmental Impact of the Virgo Cluster on the Evolution of Dwarf Irregular Galaxies. *AJ*, 125:2975–2997, June 2003. doi: 10.1086/375304.

J. Lequeux, M. Peimbert, J. F. Rayo, A. Serrano, and S. Torres-Peimbert. Chemical composition and evolution of irregular and blue compact galaxies. *A&A*, 80:155–166, December 1979.

A. Leroy, A. D. Bolatto, J. D. Simon, and L. Blitz. The Molecular Interstellar Medium of Dwarf Galaxies on Kiloparsec Scales: A New Survey for CO in Northern, IRAS-detected Dwarf Galaxies. *ApJ*, 625:763–784, June 2005. doi: 10.1086/429578.

D. N. C. Lin and S. M. Faber. Some implications of nonluminous matter in dwarf spheroidal galaxies. *ApJL*, 266:L21–L25, March 1983. doi: 10.1086/183971.

C. J. Lintott, K. Schawinski, A. Slosar, K. Land, S. Bamford, D. Thomas, M. J. Raddick, R. C. Nichol, A. Szalay, D. Andreescu, P. Murray, and J. Vandenberg. Galaxy Zoo: morphologies derived from visual inspection of galaxies from the Sloan Digital Sky Survey. *MNRAS*, 389:1179–1189, September 2008. doi: 10.1111/j.1365-2966.2008.13689.x.

T. Lisker, E. K. Grebel, and B. Binggeli. Virgo Cluster Early-Type Dwarf Galaxies with the Sloan Digital Sky Survey. I. On the Possible Disk Nature of Bright Early-Type Dwarfs. *AJ*, 132:497–513, August 2006. doi: 10.1086/505045.

C. T. Liu, P. Capak, B. Mobasher, T. A. D. Paglione, R. M. Rich, N. Z. Scoville, S. M. Tribiano, and N. D. Tyson. The Faint-End Slopes of Galaxy Luminosity Functions in the COSMOS Field. *ApJ*, 672:198–206, January 2008. doi: 10.1086/522361.

R. Lupton and Ž. Ivezić. Experience with SDSS: the Promise and Perils of Large Surveys. In P. K. Seidelmann and A. K. B. Monet, editors, *Astrometry in the Age of the Next Generation of Large Telescopes*, volume 338 of *Astronomical Society of the Pacific Conference Series*, pages 151–+, October 2005.

R. Lupton, J. E. Gunn, Z. Ivezić, G. R. Knapp, and S. Kent. The SDSS Imaging Pipelines. In F. R. Harnden, Jr., F. A. Primini, and H. E. Payne, editors, *As-*

tronomical Data Analysis Software and Systems X, volume 238 of *Astronomical Society of the Pacific Conference Series*, pages 269–+, 2001.

M.-M. Mac Low and A. Ferrara. Starburst-driven Mass Loss from Dwarf Galaxies: Efficiency and Metal Ejection. *ApJ*, 513:142–155, March 1999. doi: 10.1086/306832.

A. Mahdavi, N. Trentham, and R. B. Tully. The NGC 5846 Group: Dynamics and the Luminosity Function to Mr=-12. *AJ*, 130:1502–1515, October 2005. doi: 10.1086/444560.

L. N. Makarova and I. D. Karachentsev. CCD imaging of twenty nearby isolated irregular galaxies. *AAPS*, 133:181–196, December 1998. doi: 10.1051/aas:1998315.

D. C. Martin, J. Fanson, D. Schiminovich, P. Morrissey, P. G. Friedman, T. A. Barlow, T. Conrow, R. Grange, P. N. Jelinsky, B. Milliard, O. H. W. Siegmund, L. Bianchi, Y.-I. Byun, J. Donas, K. Forster, T. M. Heckman, Y.-W. Lee, B. F. Madore, R. F. Malina, S. G. Neff, R. M. Rich, T. Small, F. Surber, A. S. Szalay, B. Welsh, and T. K. Wyder. The Galaxy Evolution Explorer: A Space Ultraviolet Survey Mission. *ApJL*, 619:L1–L6, January 2005. doi: 10.1086/426387.

K. L. Masters. *Galaxy flows in and around the Local Supercluster*. PhD thesis, Cornell University, United States – New York, 2005.

K. L. Masters, R. Giovanelli, and M. P. Haynes. Internal Extinction in Spiral Galaxies in the Near-Infrared. *AJ*, 126:158–174, July 2003. doi: 10.1086/375758.

K. L. Masters, M. P. Haynes, and R. Giovanelli. The Impact of Distance Uncertainties on Local Luminosity and Mass Functions. *ApJL*, 607:L115–L118, June 2004. doi: 10.1086/422100.

M. L. Mateo. Dwarf Galaxies of the Local Group. *ARA&A*, 36:435–506, 1998. doi: 10.1146/annurev.astro.36.1.435.

J. Materne. The structure of nearby clusters of galaxies - Hierarchical clustering and an application to the Leo region. *A&A*, 63:401–409, February 1978.

A. W. McConnachie, N. Arimoto, M. Irwin, and E. Tolstoy. The stellar content of the isolated transition dwarf galaxy DDO210. *MNRAS*, 373:715–728, December 2006. doi: 10.1111/j.1365-2966.2006.11053.x.

S. S. McGaugh. H II region abundances - Model oxygen line ratios. *ApJ*, 380: 140–150, October 1991. doi: 10.1086/170569.

J. Melbourne, A. Phillips, J. J. Salzer, C. Gronwall, and V. L. Sarajedini. Metal Abundances of KISS Galaxies. II. Nebular Abundances of 12 Low-Luminosity Emission-Line Galaxies. *AJ*, 127:686–703, February 2004. doi: 10.1086/381067.

C. Mendes de Oliveira, H. Plana, P. Amram, C. Balkowski, and M. Bolte. Candidate Tidal Dwarf Galaxies Associated with Stephan's Quintet. *AJ*, 121:2524–2539, May 2001. doi: 10.1086/320390.

I. Meschin, C. Gallart, A. Aparicio, S. Cassisi, and A. Rosenberg. Cepheid Variable Stars in the Pegasus Dwarf Irregular Galaxy: Constraints on the Star Formation History. *AJ*, 137:3619–3631, March 2009. doi: 10.1088/0004-6256/137/3/3619.

M. Metz, P. Kroupa, and H. Jerjen. Discs of satellites: the new dwarf spheroidals. *MNRAS*, 394:2223–2228, April 2009a. doi: 10.1111/j.1365-2966.2009.14489.x.

M. Metz, P. Kroupa, C. Theis, G. Hensler, and H. Jerjen. Did the Milky Way Dwarf Satellites Enter The Halo as a Group? *ApJ*, 697:269–274, May 2009b. doi: 10.1088/0004-637X/697/1/269.

M. J. Meyer, M. A. Zwaan, R. L. Webster, L. Staveley-Smith, E. Ryan-Weber, M. J. Drinkwater, D. G. Barnes, M. Howlett, V. A. Kilborn, J. Stevens, M. Waugh, M. J. Pierce, R. Bhathal, W. J. G. de Blok, M. J. Disney, R. D. Ekers, K. C. Freeman, D. A. Garcia, B. K. Gibson, J. Harnett, P. A. Henning, H. Jerjen, M. J. Kesteven, P. M. Knezek, B. S. Koribalski, S. Mader, M. Marquarding, R. F. Minchin, J. O'Brien, T. Oosterloo, R. M. Price, M. E. Putman, S. D. Ryder, E. M. Sadler, I. M. Stewart, F. Stootman, and A. E. Wright. The HIPASS catalogue - I. Data presentation. *MNRAS*, 350:1195–1209, June 2004. doi: 10.1111/j.1365-2966.2004.07710.x.

G. Meynet and A. Maeder. Stellar evolution with rotation. VIII. Models at Z = 0.00001 and CNO yields for early galactic evolution. *A&A*, 390:561–583, August 2002. doi: 10.1051/0004-6361:20020755.

M. Mori and A. Burkert. Gas Stripping of Dwarf Galaxies in Clusters of Galaxies. *ApJ*, 538:559–568, August 2000. doi: 10.1086/309140.

L. Mortara and A. Fowler. Evaluations of Charge-Coupled Device / CCD / Performance for Astronomical Use. In *Society of Photo-Optical Instrumentation Engineers (SPIE) Conference Series*, volume 290 of *Society of Photo-Optical Instrumentation Engineers (SPIE) Conference Series*, pages 28–+, 1981.

J. B. Oke. Faint spectrophotometric standard stars. *AJ*, 99:1621–1631, May 1990. doi: 10.1086/115444.

J. B. Oke and J. E. Gunn. An Efficient Low Resolution and Moderate Resolution Spectrograph for the Hale Telescope. *PASP*, 94:586–+, June 1982. doi: 10.1086/131027.

D. E. Osterbrock and G. J. Ferland. *Astrophysics of gaseous nebulae and active galactic nuclei*. 2006.

N. Padmanabhan, D. J. Schlegel, D. P. Finkbeiner, J. C. Barentine, M. R. Blanton, H. J. Brewington, J. E. Gunn, M. Harvanek, D. W. Hogg, Ž. Ivezić, D. Johnston, S. M. Kent, S. J. Kleinman, G. R. Knapp, J. Krzesinski, D. Long, E. H. Neilsen, Jr., A. Nitta, C. Loomis, R. H. Lupton, S. Roweis, S. A. Snedden, M. A. Strauss, and D. L. Tucker. An Improved Photometric Calibration of the Sloan Digital Sky Survey Imaging Data. *ApJ*, 674:1217–1233, February 2008. doi: 10.1086/524677.

B. E. J. Pagel, E. A. Simonson, R. J. Terlevich, and M. G. Edmunds. The primordial helium abundance from observations of extragalactic H II regions. *MNRAS*, 255:325–345, March 1992.

W. J. Percival, S. Cole, D. J. Eisenstein, R. C. Nichol, J. A. Peacock, A. C. Pope, and A. S. Szalay. Measuring the Baryon Acoustic Oscillation scale using the Sloan Digital Sky Survey and 2dF Galaxy Redshift Survey. *MNRAS*, 381:1053–1066, November 2007. doi: 10.1111/j.1365-2966.2007.12268.x.

S. Phillipps, M. G. Edmunds, and J. I. Davies. A surface brightness-metallicity relation for dwarf galaxies - The effect of density thresholds for star formation? *MNRAS*, 244:168–172, May 1990.

L. S. Pilyugin. Oxygen abundances in dwarf irregular galaxies and the metallicity-luminosity relationship. *A&A*, 374:412–420, August 2001. doi: 10.1051/0004-6361:20010732.

L. S. Pilyugin and T. X. Thuan. Oxygen Abundance Determination in H II Re-

gions: The Strong Line Intensities-Abundance Calibration Revisited. *ApJ*, 631: 231–243, September 2005. doi: 10.1086/432408.

W. H. Press and P. Schechter. Formation of Galaxies and Clusters of Galaxies by Self-Similar Gravitational Condensation. *ApJ*, 187:425–438, February 1974. doi: 10.1086/152650.

C. J. Pritchet and S. van den Bergh. The Luminosity Distribution of Local Group Galaxies. *AJ*, 118:883–888, August 1999. doi: 10.1086/300977.

R. Rekola, H. Jerjen, and C. Flynn. New distances of unresolved dwarf elliptical galaxies in the vicinity of the Local Group. *A&A*, 437:823–835, July 2005. doi: 10.1051/0004-6361:20042198.

R. J. Reynolds, K. Magee, F. L. Roesler, F. Scherb, and J. Harlander. H-alpha scans of the intergalactic H I cloud in Leo. *ApJL*, 309:L9–L12, October 1986. doi: 10.1086/184750.

N. G. Roman, G. de Vaucouleurs, A. de Vaucouleurs, H. G. Corwin, Jr., R. J. Buta, G. Paturel, and P. Fouqué. *Third Reference Catalogue of Bright Galaxies (de Vaucouleurs, de Vaucouleurs, Corwin, Buta, Paturel, and Fouqué 1991). Documentation for the machine-readable version.* July 1991.

H. J. Rood and B. A. Williams. The intergalactic H I cloud in Leo - A simple modeling of the Spitzer-Baade collision event. *ApJ*, 288:535–550, January 1985. doi: 10.1086/162819.

J. L. Rosenberg and S. E. Schneider. The Arecibo Dual-Beam Survey: Arecibo and VLA Observations. *ApJS*, 130:177–199, September 2000. doi: 10.1086/317347.

J. L. Rosenberg and S. E. Schneider. The Arecibo Dual-Beam Survey: The H I Mass Function of Galaxies. *ApJ*, 567:247–257, March 2002. doi: 10.1086/338377.

A. H. Rots. Detection of a long H I plume emerging from NGC 3628. *AJ*, 83: 219–223, March 1978. doi: 10.1086/112195.

A. Saintonge. The Arecibo Legacy Fast ALFA Survey. IV. Strategies for Signal Identification and Survey Catalog Reliability. *AJ*, 133:2087–2096, May 2007a. doi: 10.1086/513515.

A. Saintonge. *Properties of low mass dwarf galaxies in the ALFALFA survey*. PhD thesis, Cornell University, 2007b.

A. Saintonge, R. Giovanelli, M. P. Haynes, G. L. Hoffman, B. R. Kent, A. M. Martin, S. Stierwalt, and N. Brosch. The Arecibo Legacy Fast Alfa Survey. V. The H I Source Catalog of the Anti-Virgo Region at $delta$ = +27deg. *AJ*, 135: 588–604, February 2008. doi: 10.1088/0004-6256/135/2/588.

S. Sakai, B. F. Madore, W. L. Freedman, T. R. Lauer, E. A. Ajhar, and W. A. Baum. Detection of the Tip of the Red Giant Branch in NGC 3379 (M105) in the Leo I Group Using the Hubble Space Telescope. *ApJ*, 478:49–+, March 1997. doi: 10.1086/303768.

A. Sandage and G. L. Hoffman. NGC 4286 and NGC 3377A - Galaxies with mixed morphologies between the dwarf Im and dE/dSO types. *ApJL*, 379: L45–L47, October 1991. doi: 10.1086/186150.

A. Sandage and G. A. Tammann. Steps toward the Hubble constant. V - The Hubble constant from nearby galaxies and the regularity of the local velocity field. *ApJ*, 196:313–328, March 1975. doi: 10.1086/153413.

K. Schawinski, C. Lintott, D. Thomas, M. Sarzi, D. Andreescu, S. P. Bamford, S. Kaviraj, S. Khochfar, K. Land, P. Murray, R. C. Nichol, M. J. Raddick, A. Slosar, A. Szalay, J. Vandenberg, and S. K. Yi. Galaxy Zoo: a sample of blue early-type galaxies at low redshift. *MNRAS*, 396:818–829, June 2009. doi: 10.1111/j.1365-2966.2009.14793.x.

D. J. Schlegel, D. P. Finkbeiner, and M. Davis. Maps of Dust Infrared Emission for Use in Estimation of Reddening and Cosmic Microwave Background Radiation Foregrounds. *ApJ*, 500:525–+, June 1998. doi: 10.1086/305772.

M. Schmidt. The Rate of Star Formation. *ApJ*, 129:243–+, March 1959. doi: 10.1086/146614.

S. E. Schneider. Neutral hydrogen in the M96 group - The galaxies and the intergalactic ring. *ApJ*, 343:94–106, August 1989. doi: 10.1086/167687.

S. E. Schneider, G. Helou, E. E. Salpeter, and Y. Terzian. Discovery of a large intergalactic H I cloud in the M96 group. *ApJL*, 273:L1–L5, October 1983. doi: 10.1086/184118.

S. E. Schneider, G. Helou, E. E. Salpeter, and Y. Terzian. Neutral hydrogen in small groups of galaxies. *AJ*, 92:742–765, October 1986. doi: 10.1086/114209.

S. E. Schneider, M. F. Skrutskie, P. B. Hacking, J. S. Young, R. L. Dickman, M. J. Claussen, E. E. Salpeter, J. R. Houck, Y. Terzian, B. M. Lewis, and M. A. Shure. Multifrequency survey of the intergalactic cloud in the M96 group. *AJ*, 97: 666–673, March 1989. doi: 10.1086/115012.

L. Searle and W. L. W. Sargent. Inferences from the Composition of Two Dwarf Blue Galaxies. *ApJ*, 173:25–+, April 1972. doi: 10.1086/151398.

O. K. Sil'chenko, A. V. Moiseev, V. L. Afanasiev, V. H. Chavushyan, and J. R. Valdes. The Leo I Cloud: Secular Nuclear Evolution of NGC 3379, NGC 3384, and NGC 3368? *ApJ*, 591:185–203, July 2003. doi: 10.1086/375315.

J. D. Simon and M. Geha. The Kinematics of the Ultra-faint Milky Way Satellites: Solving the Missing Satellite Problem. *ApJ*, 670:313–331, November 2007. doi: 10.1086/521816.

E. D. Skillman, R. C. Kennicutt, and P. W. Hodge. Oxygen abundances in nearby dwarf irregular galaxies. *ApJ*, 347:875–882, December 1989. doi: 10.1086/168178.

E. D. Skillman, R. J. Televich, R. C. Kennicutt, Jr., D. R. Garnett, and E. Terlevich. Spatially resolved optical and near-infrared spectroscopy of the low-metallicity galaxy UGC 4483. *ApJ*, 431:172–187, August 1994. doi: 10.1086/174476.

E. D. Skillman, D. J. Bomans, and H. A. Kobulnicky. Interstellar Medium Abundances in the Pegasus Dwarf Irregular Galaxy. *ApJ*, 474:205–+, January 1997. doi: 10.1086/303464.

E. D. Skillman, S. C^{o}t$'e$, and B. W. Miller. Star Formation in Sculptor Group Dwarf Irregular Galaxies and the Nature of "Transition" Galaxies. *AJ*, 125: 593–609, February 2003. doi: 10.1086/345964.

M. F. Skrutskie, M. A. Shure, and S. Beckwith. Limits on the infrared and visual luminosity of the intergalactic H I cloud in Leo. *ApJL*, 282:L65–L68, July 1984. doi: 10.1086/184306.

D. N. Spergel, R. Bean, O. Doré, M. R. Nolta, C. L. Bennett, J. Dunkley, G. Hinshaw, N. Jarosik, E. Komatsu, L. Page, H. V. Peiris, L. Verde, M. Halpern, R. S.

Hill, A. Kogut, M. Limon, S. S. Meyer, N. Odegard, G. S. Tucker, J. L. Weiland, E. Wollack, and E. L. Wright. Three-Year Wilkinson Microwave Anisotropy Probe (WMAP) Observations: Implications for Cosmology. *ApJS*, 170:377–408, June 2007a. doi: 10.1086/513700.

D. N. Spergel, R. Bean, O. Dor'e, M. R. Nolta, C. L. Bennett, J. Dunkley, G. Hinshaw, N. Jarosik, E. Komatsu, L. Page, H. V. Peiris, L. Verde, M. Halpern, R. S. Hill, A. Kogut, M. Limon, S. S. Meyer, N. Odegard, G. S. Tucker, J. L. Weiland, E. Wollack, and E. L. Wright. Three-Year Wilkinson Microwave Anisotropy Probe (WMAP) Observations: Implications for Cosmology. *ApJS*, 170:377–408, June 2007b. doi: 10.1086/513700.

C. M. Springob, M. P. Haynes, and R. Giovanelli. Morphology, Environment, and the H I Mass Function. *ApJ*, 621:215–226, March 2005. doi: 10.1086/427432.

C. M. Springob, K. L. Masters, M. P. Haynes, R. Giovanelli, and C. Marinoni. SFI++. II. A New I-Band Tully-Fisher Catalog, Derivation of Peculiar Velocities, and Data Set Properties. *ApJS*, 172:599–614, October 2007. doi: 10.1086/519527.

J. St-Germain, C. Carignan, S. C^{o}te, and T. Oosterloo. H I in the Field of the Dwarf Spheroidal/Irregular Galaxy PHOENIX. *AJ*, 118:1235–1244, September 1999. doi: 10.1086/301021.

S. Stierwalt, M. P. Haynes, R. Giovanelli, B. R. Kent, A. M. Martin, A. Saintonge, I. D. Karachentsev, and V. E. Karachentseva. The Arecibo Legacy Fast Alfa Survey. IX. The Leo Region HI Catalog, Group Membership, and the HI Mass Function for the Leo I Group. *AJ*, 138:338–361, August 2009. doi: 10.1088/0004-6256/138/2/338.

P. J. Storey and D. G. Hummer. Recombination line intensities for hydrogenic ions-IV. Total recombination coefficients and machine-readable tables for Z=1 to 8. *MNRAS*, 272:41–48, January 1995.

C. Stoughton, J. Adelman, J. T. Annis, J. Hendry, J. Inkmann, S. Jester, S. M. Kent, N. Kuropatkin, B. Lee, H. Lin, J. J. Peoples, R. Sparks, D. Tucker, D. Vanden Berk, B. Yanny, and D. Yocum. Data Processing Factory for the Sloan Digital Sky Survey. In J. A. Tyson and S. Wolff, editors, *Society of Photo-Optical Instrumentation Engineers (SPIE) Conference Series*, volume 4836 of *Society of Photo-Optical Instrumentation Engineers (SPIE) Conference Series*, pages 339–349, December 2002. doi: 10.1117/12.457014.

I. Strateva, Ž. Ivezić, G. R. Knapp, V. K. Narayanan, M. A. Strauss, J. E. Gunn, R. H. Lupton, D. Schlegel, N. A. Bahcall, J. Brinkmann, R. J. Brunner, T. Budavári, I. Csabai, F. J. Castander, M. Doi, M. Fukugita, Z. Győry, M. Hamabe, G. Hennessy, T. Ichikawa, P. Z. Kunszt, D. Q. Lamb, T. A. McKay, S. Okamura, J. Racusin, M. Sekiguchi, D. P. Schneider, K. Shimasaku, and D. York. Color Separation of Galaxy Types in the Sloan Digital Sky Survey Imaging Data. *AJ*, 122:1861–1874, October 2001. doi: 10.1086/323301.

M. A. Strauss, D. H. Weinberg, R. H. Lupton, V. K. Narayanan, J. Annis, M. Bernardi, M. Blanton, S. Burles, A. J. Connolly, J. Dalcanton, M. Doi, D. Eisenstein, J. A. Frieman, M. Fukugita, J. E. Gunn, Ž. Ivezić, S. Kent, R. S. J. Kim, G. R. Knapp, R. G. Kron, J. A. Munn, H. J. Newberg, R. C. Nichol, S. Okamura, T. R. Quinn, M. W. Richmond, D. J. Schlegel, K. Shimasaku, M. SubbaRao, A. S. Szalay, D. Vanden Berk, M. S. Vogeley, B. Yanny, N. Yasuda, D. G. York, and I. Zehavi. Spectroscopic Target Selection in the Sloan Digital

Sky Survey: The Main Galaxy Sample. *AJ*, 124:1810–1824, September 2002. doi: 10.1086/342343.

L. E. Strigari, J. S. Bullock, M. Kaplinghat, J. D. Simon, M. Geha, B. Willman, and M. G. Walker. A common mass scale for satellite galaxies of the Milky Way. *Nature*, 454:1096–1097, August 2008. doi: 10.1038/nature07222.

D. A. Thilker, J. Donovan, D. Schiminovich, L. Bianchi, S. Boissier, A. Gil de Paz, B. F. Madore, D. C. Martin, and M. Seibert. Massive star formation within the Leo 'primordial' ring. *Nature*, 457:990–993, February 2009. doi: 10.1038/nature07780.

T. X. Thuan. Near-infrared photometry and stellar populations in dwarf elliptical and irregular galaxies. *ApJ*, 299:881–895, December 1985. doi: 10.1086/163755.

J. L. Tonry, A. Dressler, J. P. Blakeslee, E. A. Ajhar, A. B. Fletcher, G. A. Luppino, M. R. Metzger, and C. B. Moore. The SBF Survey of Galaxy Distances. IV. SBF Magnitudes, Colors, and Distances. *ApJ*, 546:681–693, January 2001. doi: 10.1086/318301.

A. Toomre and J. Toomre. Galactic Bridges and Tails. *ApJ*, 178:623–666, December 1972. doi: 10.1086/151823.

N. Trentham and B. Tully. Dwarf Galaxies in the NGC 1023 Group. *ArXiv e-prints*, June 2009.

N. Trentham and R. B. Tully. The faint end of the galaxy luminosity function. *MNRAS*, 335:712–732, September 2002. doi: 10.1046/j.1365-8711.2002.05651.x.

R. B. Tully. Nearby groups of galaxies. II - an all-sky survey within 3000 kilometers per second. *ApJ*, 321:280–304, October 1987. doi: 10.1086/165629.

R. B. Tully, M. J. Pierce, J.-S. Huang, W. Saunders, M. A. W. Verheijen, and P. L. Witchalls. Global Extinction in Spiral Galaxies. *AJ*, 115:2264–2272, June 1998. doi: 10.1086/300379.

R. B. Tully, E. J. Shaya, I. D. Karachentsev, H. M. Courtois, D. D. Kocevski, L. Rizzi, and A. Peel. Our Peculiar Motion Away from the Local Void. *ApJ*, 676:184–205, March 2008. doi: 10.1086/527428.

E. L. Turner and J. R. Gott, III. Groups of galaxies. I. A catalog. *ApJS*, 32:409–427, November 1976. doi: 10.1086/190403.

L. van Zee. The Evolutionary Status of Isolated Dwarf Irregular Galaxies. II. Star Formation Histories and Gas Depletion. *AJ*, 121:2003–2019, April 2001. doi: 10.1086/319947.

L. van Zee and M. P. Haynes. Oxygen and Nitrogen in Isolated Dwarf Irregular Galaxies. *ApJ*, 636:214–239, January 2006. doi: 10.1086/498017.

L. van Zee, M. P. Haynes, and J. J. Salzer. Optical Colors and the Metallicities of Gas-Rich Quiescent Dwarf Galaxies. *AJ*, 114:2479–+, December 1997. doi: 10.1086/118661.

L. van Zee, J. J. Salzer, M. P. Haynes, A. A. O'Donoghue, and T. J. Balonek. Spectroscopy of Outlying H II Regions in Spiral Galaxies: Abundances and Radial Gradients. *AJ*, 116:2805–2833, December 1998. doi: 10.1086/300647.

L. van Zee, E. D. Skillman, and M. P. Haynes. Rotationally Supported Virgo Cluster Dwarf Elliptical Galaxies: Stripped Dwarf Irregular Galaxies? *AJ*, 128:121–136, July 2004. doi: 10.1086/421368.

L. E. van Zee. *Evolutionary Studies of Low Surface Brightness Dwarf Galaxies.* PhD thesis, AA(CORNELL UNIVERSITY.), 1996.

M. A. W. Verheijen, N. Trentham, B. Tully, and M. Zwaan. The HI Mass Function in Ursa Major. In J. E. Hibbard, M. Rupen, and J. H. van Gorkom, editors, *Gas and Galaxy Evolution*, volume 240 of *Astronomical Society of the Pacific Conference Series*, pages 507–+, 2001.

A. A. West. *HI selected galaxies in the Sloan Digital Sky Survey*. PhD thesis, University of Washington, United States – Washington, November 2005.

T. Wilding, P. Alexander, and D. A. Green. Neutral Hydrogen Observations of NGC3628. *MNRAS*, 263:1075–+, August 1993.

B. Willman, J. J. Dalcanton, D. Martinez-Delgado, A. A. West, M. R. Blanton, D. W. Hogg, J. C. Barentine, H. J. Brewington, M. Harvanek, S. J. Kleinman, J. Krzesinski, D. Long, E. H. Neilsen, Jr., A. Nitta, and S. A. Snedden. A New Milky Way Dwarf Galaxy in Ursa Major. *ApJL*, 626:L85–L88, June 2005. doi: 10.1086/431760.

O. I. Wong, E. V. Ryan-Weber, D. A. Garcia-Appadoo, R. L. Webster, L. Staveley-Smith, M. A. Zwaan, M. J. Meyer, D. G. Barnes, V. A. Kilborn, R. Bhathal, W. J. G. de Blok, M. J. Disney, M. T. Doyle, M. J. Drinkwater, R. D. Ekers, K. C. Freeman, B. K. Gibson, S. Gurovich, J. Harnett, P. A. Henning, H. Jerjen, M. J. Kesteven, P. M. Knezek, B. S. Koribalski, S. Mader, M. Marquarding, R. F. Minchin, J. O'Brien, M. E. Putman, S. D. Ryder, E. M. Sadler, J. Stevens, I. M. Stewart, F. Stootman, and M. Waugh. The Northern HIPASS catalogue - data presentation, completeness and reliability measures. *MNRAS*, 371:1855–1864, October 2006. doi: 10.1111/j.1365-2966.2006.10846.x.

N. Yasuda, M. Fukugita, V. K. Narayanan, R. H. Lupton, I. Strateva, M. A. Strauss, Ž. Ivezić, R. S. J. Kim, D. W. Hogg, D. H. Weinberg, K. Shimasaku, J. Loveday, J. Annis, N. A. Bahcall, M. Blanton, J. Brinkmann, R. J. Brunner,

A. J. Connolly, I. Csabai, M. Doi, M. Hamabe, S.-I. Ichikawa, T. Ichikawa, D. E. Johnston, G. R. Knapp, P. Z. Kunszt, D. Q. Lamb, T. A. McKay, J. A. Munn, R. C. Nichol, S. Okamura, D. P. Schneider, G. P. Szokoly, M. S. Vogeley, M. Watanabe, and D. G. York. Galaxy Number Counts from the Sloan Digital Sky Survey Commissioning Data. *AJ*, 122:1104–1124, September 2001. doi: 10.1086/322093.

D. G. York, J. Adelman, J. E. Anderson, Jr., S. F. Anderson, J. Annis, N. A. Bahcall, J. A. Bakken, R. Barkhouser, S. Bastian, E. Berman, W. N. Boroski, S. Bracker, C. Briegel, J. W. Briggs, J. Brinkmann, R. Brunner, S. Burles, L. Carey, M. A. Carr, F. J. Castander, B. Chen, P. L. Colestock, A. J. Connolly, J. H. Crocker, I. Csabai, P. C. Czarapata, J. E. Davis, M. Doi, T. Dombeck, D. Eisenstein, N. Ellman, B. R. Elms, M. L. Evans, X. Fan, G. R. Federwitz, L. Fiscelli, S. Friedman, J. A. Frieman, M. Fukugita, B. Gillespie, J. E. Gunn, V. K. Gurbani, E. de Haas, M. Haldeman, F. H. Harris, J. Hayes, T. M. Heckman, G. S. Hennessy, R. B. Hindsley, S. Holm, D. J. Holmgren, C.-h. Huang, C. Hull, D. Husby, S.-I. Ichikawa, T. Ichikawa, v Z. Ivezi'c, S. Kent, R. S. J. Kim, E. Kinney, M. Klaene, A. N. Kleinman, S. Kleinman, G. R. Knapp, J. Korienek, R. G. Kron, P. Z. Kunszt, D. Q. Lamb, B. Lee, R. F. Leger, S. Limmongkol, C. Lindenmeyer, D. C. Long, C. Loomis, J. Loveday, R. Lucinio, R. H. Lupton, B. MacKinnon, E. J. Mannery, P. M. Mantsch, B. Margon, P. McGehee, T. A. McKay, A. Meiksin, A. Merelli, D. G. Monet, J. A. Munn, V. K. Narayanan, T. Nash, E. Neilsen, R. Neswold, H. J. Newberg, R. C. Nichol, T. Nicinski, M. Nonino, N. Okada, S. Okamura, J. P. Ostriker, R. Owen, A. G. Pauls, J. Peoples, R. L. Peterson, D. Petravick, J. R. Pier, A. Pope, R. Pordes, A. Prosapio, R. Rechenmacher, T. R. Quinn, G. T. Richards, M. W. Richmond, C. H. Rivetta, C. M. Rockosi, K. Ruthmansdorfer, D. Sandford, D. J. Schlegel, D. P. Schneider, M. Sekiguchi,

G. Sergey, K. Shimasaku, W. A. Siegmund, S. Smee, J. A. Smith, S. Snedden, R. Stone, C. Stoughton, M. A. Strauss, C. Stubbs, M. SubbaRao, A. S. Szalay, I. Szapudi, G. P. Szokoly, A. R. Thakar, C. Tremonti, D. L. Tucker, A. Uomoto, D. Vanden Berk, M. S. Vogeley, P. Waddell, S.-i. Wang, M. Watanabe, D. H. Weinberg, B. Yanny, and N. Yasuda. The Sloan Digital Sky Survey: Technical Summary. *AJ*, 120:1579–1587, September 2000. doi: 10.1086/301513.

J. S. Young, L. J. Tacconi, and N. Z. Scoville. CO observations of the galaxies in the Leo triplet - NGC 3623, NGC 3627, and NGC 3628. *ApJ*, 269:136–146, June 1983. doi: 10.1086/161025.

L. M. Young and K. Y. Lo. The Neutral Interstellar Medium in Nearby Dwarf Galaxies. III. Sagittarius DIG, LGS 3, and PHOENIX. *ApJ*, 490:710–+, December 1997. doi: 10.1086/304909.

L. M. Young, E. D. Skillman, D. R. Weisz, and A. E. Dolphin. The Aptly Named Phoenix Dwarf Galaxy. *ApJ*, 659:331–338, April 2007. doi: 10.1086/512153.

D. Zaritsky, R. C. Kennicutt, Jr., and J. P. Huchra. H II regions and the abundance properties of spiral galaxies. *ApJ*, 420:87–109, January 1994. doi: 10.1086/173544.

X. Zhang, M. Wright, and P. Alexander. High-Resolution CO and H i Observations of the Interacting Galaxy NGC 3627. *ApJ*, 418:100–+, November 1993. doi: 10.1086/173374.

M. A. Zwaan, F. H. Briggs, D. Sprayberry, and E. Sorar. The H i Mass Function of Galaxies from a Deep Survey in the 21 Centimeter Line. *ApJ*, 490:173–+, November 1997. doi: 10.1086/304872.

M. A. Zwaan, M. J. Meyer, L. Staveley-Smith, and R. L. Webster. The HIPASS catalogue: $Omega_{HI}$ and environmental effects on the HI mass function of galaxies. *MNRAS*, 359:L30–L34, May 2005. doi: 10.1111/j.1745-3933.2005.00029.x.

F. Zwicky. Multiple Galaxies. *Ergebnisse der exakten Naturwissenschaften*, 29:344–385, 1956.